

University of Southampton Research Repository ePrints Soton

Copyright © and Moral Rights for this thesis are retained by the author and/or other copyright owners. A copy can be downloaded for personal non-commercial research or study, without prior permission or charge. This thesis cannot be reproduced or quoted extensively from without first obtaining permission in writing from the copyright holder/s. The content must not be changed in any way or sold commercially in any format or medium without the formal permission of the copyright holders.

When referring to this work, full bibliographic details including the author, title, awarding institution and date of the thesis must be given e.g.

AUTHOR (year of submission) "Full thesis title", University of Southampton, name of the University School or Department, PhD Thesis, pagination

UNIVERSITY OF SOUTHAMPTON
FACULTY OF ENGINEERING AND THE ENVIRONMENT
NATIONAL CENTRE FOR ADVANCED TRIBOLOGY

WEAR MODELLING OF DIAMOND-LIKE CARBON
COATINGS AGAINST STEEL IN DEIONISED WATER

Daniel Christopher Sutton
Rolls-Royce funded PhD Studentship

Thesis for the degree of Doctor of Philosophy
March 2014

UNIVERSITY OF SOUTHAMPTON

ABSTRACT

FACULTY OF ENGINEERING AND THE ENVIRONMENT

Doctor of Philosophy

WEAR MODELLING OF DIAMOND-LIKE CARBON COATINGS
AGAINST STEEL IN DEIONISED WATER

Daniel Christopher Sutton

Diamond-Like Carbon (DLC) coatings are thin protective surface coatings used to reduce friction and minimise wear in a wide range of applications. The focus of this work is the use of DLC coatings within Rolls-Royce's pressurised water reactors. A strong understanding of material behaviour in this environment is compulsory due to the stringent safety requirements of the nuclear industry.

Wear testing of a range of commercial DLC coatings against steel in water, and the dependence of the tribology on normal load, sliding distance, and environmental species, was examined. Wear depth was observed to increase with normal load, and increase non-linearly with sliding distance. Uniquely, it was suggested that the tribology of a DLC coating in water was controlled by the velocity accommodation mode (VAM) of the transfer layer. When interfacial sliding was the dominant VAM, the carbonaceous transfer layer was present at all times, and a low specific wear rate was observed. When shear and recirculation of debris was the dominant VAM, the carbonaceous transfer layer initially present was replaced by iron oxide species, and a high specific wear rate was observed as a result of a three-body mechanism involving hematite.

Two individual wear models were developed to predict the wear depth of a DLC coating sliding against steel in water. Each model represents a novel extension to the current literature regarding the modelling of wear. Firstly, an analytical differential equation was derived to predict the wear depth of a ball and a flat surface, in relation to any phenomenological law for wear volume. Secondly, a unique formulation of an incremental wear model for an arbitrary geometry was developed for a DLC coating which included the growth of a transfer layer. An efficient methodology was presented to allow fast integration of the equations whilst damping numerical instabilities. A comparison between the analytic and computational wear models showed a strong agreement in the model predictions, with a comparative error of less than 5 %.

Table of Contents

Abstract.....	I
Table of Contents	III
List of Figures.....	VII
List of Tables.....	XIII
List of Acronyms.....	XIV
Nomenclature.....	XVII
Declaration of Authorship.....	XXI
Acknowledgements.....	XXIII
Chapter 1. Introduction	1
1.1. Project outline	2
1.2. Project aims and objectives	3
1.3. Thesis structure	4
Chapter 2. Diamond-Like Carbon Coatings	7
2.1. Composition and deposition.....	8
2.1.1. Bonding configurations of carbon.....	9
2.1.2. Hydrogen content	10
2.1.3. Categorisation of DLC coatings	10
2.1.4. Deposition processes	12
2.2. Mechanical properties	15
2.2.1. Hardness, elastic modulus, and density	15
2.2.2. Residual stresses	17
2.2.3. Multi-layer and gradient coatings	18
2.2.4. Doping and alloying.....	18
2.3. Conclusion	19
Chapter 3. Tribology of Diamond-Like Carbon Coatings	21
3.1. Friction.....	22
3.1.1. Classical theories of friction	22

3.1.2.	Contributions to the friction of a DLC coating	23
3.1.3.	The effects of hydrogen	24
3.1.4.	The effects of doping and alloying.....	27
3.2.	Wear.....	29
3.2.1.	General wear mechanisms	29
3.2.2.	Graphitisation and transfer layer formation.....	30
3.2.3.	The effects of temperature	33
3.3.	Tribology in water	35
3.3.1.	The effects of an oxidising environment	35
3.3.2.	Tribochemistry of a DLC coating versus steel in water	39
3.4.	Conclusion	42
Chapter 4.	Modelling of Wear.....	45
4.1.	Contact modelling.....	46
4.2.	Archard's wear law	49
4.3.	Frictional energy dissipation	50
4.4.	Incremental wear models.....	54
4.5.	Lifetime prediction of DLC coatings	55
4.6.	Conclusion	59
Chapter 5.	Materials and Methods.....	61
5.1.	Experimental aims	62
5.2.	Materials.....	63
5.2.1.	Graphit-iC™ from Teer Coatings.....	63
5.2.2.	BALINIT® DLC STAR from Oerlikon Balzers.....	64
5.2.3.	Adamant® from Diamond Hard Surfaces.....	64
5.2.4.	AISI 4118H steel	64
5.2.5.	AISI 52100 steel.....	65
5.2.6.	AISI 440C steel	65
5.3.	Analysis techniques.....	66
5.3.1.	Surface roughness measurements and image capture	66
5.3.2.	Wear volume and wear depth measurements	66

5.3.3.	Hardness and elastic modulus measurements	67
5.3.4.	Bonding characterisation	68
5.3.5.	Scanning electron microscopy	68
5.4.	Reciprocating friction tests	68
5.4.1.	Plint TE77 tribometer	69
5.4.2.	Experimental set-up.....	69
Chapter 6.	Tribological Testing of DLC Coatings in Water	71
6.1.	Aims	72
6.2.	Mechanical characterisation	72
6.2.1.	Optical microscopy	72
6.2.2.	Surface roughness	73
6.2.3.	Hardness and elastic modulus	73
6.2.4.	Raman spectroscopy	75
6.3.	Reciprocating test matrix	76
6.4.	Friction and wear results	77
6.5.	Transfer layer analysis.....	80
6.5.1.	Optical microscopy	80
6.5.2.	SEM and EDX spectroscopy	82
6.5.3.	Raman spectroscopy	83
6.5.4.	Nanoindentation	85
6.6.	Discussion.....	86
6.7.	Conclusion	87
Chapter 7.	The Influence of Normal Load and Sliding Velocity on the Tribology of DLC Coatings in Water	89
7.1.	Aims	90
7.2.	Mechanical characterisation	90
7.2.1.	Surface images and surface roughness	91
7.2.2.	Scanning electron microscopy	91
7.3.	Reciprocating test matrix	94
7.4.	Results.....	95

7.4.1. Coefficient of friction.....	95
7.4.2. Wear depth.....	99
7.5. Conclusion	106
Chapter 8. A Functional Form for the Wear Depth of a Ball and a Flat Surface.....	107
8.1. Aims	108
8.2. Introduction.....	108
8.3. Derivation of the equations	111
8.4. Results.....	113
8.5. Extension to a time-dependent specific wear rate.....	116
8.6. Conclusion	118
Chapter 9. An Incremental Wear Model for Diamond-Like Carbon Coatings.....	121
9.1. Introduction.....	122
9.2. Methodology	123
9.2.1. Finite element model.....	123
9.2.2. Implementation of wear	125
9.3. Results.....	130
9.4. Discussion	133
9.4.1. Diffusion of the contact boundaries.....	133
9.4.2. The minimum wear depth condition	134
9.4.3. Comparison to the predictions of Chapter 8.....	135
9.4.4. Prediction of wear under different test conditions	137
9.5. Conclusion	138
Chapter 10. Conclusions and Future Work	141
10.1. Conclusions	142
10.1.1. Experimental conclusions	143
10.1.2. Modelling conclusions.....	145
10.2. Future work	148
Appendix A.....	XXV
Appendix B.....	XXXIX
Bibliography.....	LVI

List of Figures

Figure 1.1. A schematic of a pressurised water reactor from the United States Nuclear Regulatory Commission [2].	2
Figure 1.2. Flow-chart of the thesis.	5
Figure 2.1. The bonding structure in (a) graphite and (b) diamond [6].	9
Figure 2.2. A ternary phase diagram for DLC coatings [4].	10
Figure 2.3. A closed field unbalanced magnetron sputter ion plating system [12].	14
Figure 2.4. Hardness versus contact depth ratio for a 47 nm thick a-C:H coating deposited on a silicon wafer [18].	16
Figure 2.5. The density of a ta-C coating, a ta-C:H coating, and an a-C:H coating, as a function of sp^3 content [20].	16
Figure 3.1. The effect of water vapour pressure on the coefficient of friction for hydrogenated (black squares) and non-hydrogenated (white diamonds) DLC coatings [60].	25
Figure 3.2. The effect of the hydrogen / carbon ratio during the deposition of a DLC coating on the coefficient of friction in dry nitrogen [58].	26
Figure 3.3. The effect of sliding speed on the coefficient of friction of hydrogenated DLC coatings [62].	26
Figure 3.4. The coefficient of friction and specific wear rate of aluminium doped DLC coatings [70].	28
Figure 3.5. The velocity accommodation modes of a transfer layer; (a) shear and extrusion of loose debris, and (b) interfacial sliding.	31
Figure 3.6. Images of transfer layers formed during reciprocating sliding of a-C:H coatings against steel in (a) dry nitrogen, (b) ambient air, and (c) dry air [72].	32
Figure 3.7. Indentation hardness of two hydrogenated DLC coatings after annealing at a range of temperatures [84].	33
Figure 3.8. The coefficient of friction as a function of time at 25 °C, 120 °C, and 300 °C [89].	34
Figure 3.9. Thermo-gravimetric analysis (TGA) of a DLC coating as temperature increases at a rate of 15 °C per minute [90].	35
Figure 3.10. The effect of relative humidity and sliding speed on the specific wear rate of non-hydrogenated DLC coatings against tungsten carbide balls [95].	36
Figure 3.11. The effects of load, temperature, dissolved oxygen, and water pressure, on (top) the specific wear rate of a DLC coating, (middle) the specific wear rate of steel,	

and (bottom) the coefficient of friction, in the case of pure deionised water and quasi-tap water [97].	38
Figure 3.12. SEM images of transfer layers formed at (a-b) 20 °C, (c) 50 °C, and (d) 80 °C, in quasi-tap water at a 57 N normal load against stainless steel [97].	38
Figure 3.13. SEM images of wear scars for hydrogenated DLC coatings tested at (a) 0 %, (b) 50 %, and (c) 90 % relative humidity. An AES spectrum for each coating is shown in (d) [98].	39
Figure 3.14. An XPS C1s spectra of the DLC coating wear scar after testing against steel in (a) < 5 %, (b) 40 %, and (c) 100 % humidity environments [99].	40
Figure 3.15. A comparison between ToF-SIMS spectra inside and outside the wear track for an a-C:H coating sliding against steel in humid air [103].	41
Figure 4.1. The stress field in a coated surface resulting from a sliding sphere [105].	47
Figure 4.2. First principal stresses on the coating at the plane of symmetry are shown for (a) 5 N pre-load, (b) 5.3 N load and 0.06 mm displacement, (c) 10 N load and 1.2 mm displacement, and (d) 20 N load and 3.3 mm displacement [105].	47
Figure 4.3. Normal stress distributions between a flat DLC coating and a steel ball, for states (I), (II), and (III). Image is redrawn based on the original work of Fan and Diao [109].	48
Figure 4.4. Wear volume versus dissipated energy for a TiN coating under fretting conditions [116].	51
Figure 4.5. Normalised wear rate versus normalised entropy flow due to the diffusion of heat [124].	52
Figure 4.6. A contact simulation of a DLC coating ($R_a = 1.2 \mu\text{m}$) against a steel ball, compared to the Hertzian estimation of contact pressure [139].	56
Figure 4.7. Wear predictions of (a) a DLC coating (in percentage wear depth), and (b) a steel ball (in actual wear depth) as different influencing factors are included in the model. The predictions are compared to experiments [139].	57
Figure 4.8. A flow chart illustrating the routine to model wear in Abaqus [143].	58
Figure 4.9. A comparison of the predicted wear depth from the model to the actual wear depth measurements from experiments, plotted against the number of fretting cycles (600,000 fretting cycles relates to a sliding distance of 60 metres) [143, 144].	58
Figure 5.1. A schematic of the wear volume measurement of a worn surface profile using the TaiCaan profilometer.	67
Figure 5.2. A photograph of the Plint TE77 reciprocating tribometer.	69
Figure 5.3. A schematic of the Plint TE77 reciprocating tribometer.	70
Figure 6.1. Photographs of unworn surfaces at 10x magnification for (a) Graphit-iC™, (b) BALINIT® DLC STAR, (c) Adamant®, and (d) the AISI 4118H steel substrate.	73

Figure 6.2. Load – depth curves for the nanoindentation of (a) Graphit-iC™, (b) BALINIT® DLC STAR, and (c) Adamant®, using a Nanotest platform (Micro Materials Limited, Wrexham, UK).	74
Figure 6.3. Raman spectra for Graphit-iC™ (red), BALINIT® DLC STAR (blue) and Adamant® (green).....	75
Figure 6.4. Coefficient of friction of Graphit-iC™, BALINIT® DLC STAR, and Adamant® in distilled water for (a) 600 seconds, and (b) 3 hours. The contact potential in (b) is shown in black.....	78
Figure 6.5. Wear depth of (a) Graphit-iC™, BALINIT® DLC STAR, and Adamant®, and (b) AISI 52100 steel balls, in distilled water plotted against time.	79
Figure 6.6. Images of each AISI 52100 steel ball after sliding against Graphit-iC™, BALINIT® DLC STAR, and Adamant®, in distilled water for 30, 120, and 600 seconds.	81
Figure 6.7. (a) An optical image, and (b) a 3D model from surface profilometry measurements, of an AISI 52100 steel ball after 3600 seconds of sliding against BALINIT® DLC STAR in distilled water.	81
Figure 6.8. (top) An SEM image of wear debris on the AISI 52100 steel ball counterface after sliding for 3600 seconds against Graphit-iC™, and (bottom) EDX spectra taken at locations 1 and 2, as labelled.	82
Figure 6.9. (top) An SEM image of wear debris on the AISI 52100 steel ball counterface after sliding for 3600 seconds against BALINIT® DLC STAR, and (bottom) EDX spectra taken at locations 1 and 2, as labelled.....	82
Figure 6.10. (a) A BEI of an AISI 52100 steel ball after sliding against Adamant® for 600 seconds, and EDX maps showing (b) C (c) O, and (d) Fe distributions on the worn surface.	83
Figure 6.11. Raman spectra for transfer layers sliding against (a) Graphit-iC™, (b) BALINIT® DLC STAR, and (c) Adamant®, after 30, 120, 600, and 3600 seconds. (d) Raman spectra of magnetite, hematite, and maghemite [154, 155]. In each case, two spectra from different locations on the ball surface are shown (by solid and dotted lines) to represent the inhomogeneity of the transfer layer.	85
Figure 6.12. Load – depth curve for the nanoindentation of the transfer layer formed by BALINIT® DLC STAR after 3600 seconds.	86
Figure 7.1. (a) Image of Adamant® at 10x and 100x magnification; (b) Image of BALINIT® DLC STAR at 10x and 100x magnification; (c) Image of the AISI 440C steel surface at 10x and 100x magnification; (d) Image of the 6 mm diameter AISI 440C ball at 10x magnification.....	91

Figure 7.2. A cross-section of Adamant[®] as observed by secondary electron imaging at 8,000x magnification. The locations of two EDX area spectra are marked in white. 92

Figure 7.3. A cross-section of BALINIT[®] DLC STAR as observed using backscatter electron imaging at 8,000x magnification. The location of an EDX line spectrum is marked in white. 92

Figure 7.4. The weight percentage of (a) C, (b) N, (c) Fe, and (d) Cr, along the EDX line spectrum for BALINIT[®] DLC STAR. The x-axis represents depth from the top of the coating. 93

Figure 7.5. Test schedule for wear testing of BALINIT[®] DLC STAR and Adamant[®] against a 6 mm diameter AISI 440C ball on the TE77 reciprocating tribometer using a 2 mm stroke. 94

Figure 7.6. The coefficient of friction of Adamant[®] plotted against the normal load, at a frequency of 5 Hz (red circles), 10 Hz (green circles), and 20 Hz (blue circles). The predictions of the linear model (solid line) and associated 95 % prediction intervals (dashed lines) are plotted for each sliding frequency. 95

Figure 7.7. The coefficient of friction of BALINIT[®] DLC STAR plotted against the normal load for all frequency combinations (black circles). The predictions of the linear model (solid line) and associated 95 % prediction intervals (dashed lines) are shown as labelled..... 97

Figure 7.8. The average wear depth of Adamant[®] plotted against sliding distance, at a normal load of (a) 5 N, (b) 10 N, and (c) 20 N. Tests than ran at 5 Hz are shown in red, tests that ran at 10 Hz are shown in green, and tests that ran at 20 Hz are shown in blue. Error bars denote the error in the experimental measurements. 99

Figure 7.9. The average wear depth of (a) Adamant[®] and (b) AISI 440C steel plotted against sliding distance at a frequency of 5 Hz. Tests than ran at 5 N are shown in red, and tests that ran at 20 N are shown in blue. Error bars denote the error in the experimental measurements..... 101

Figure 7.10. The average wear depth of BALINIT[®] DLC STAR plotted against sliding distance, at a normal load of (a) 5 N, (b) 10 N, and (c) 20 N. Tests than ran at 5 Hz are shown in red, tests that ran at 10 Hz are shown in green, and tests that ran at 20 Hz are shown in blue. Error bars denote the error in the experimental measurements. 102

Figure 7.11. Predicted wear depth for BALINIT[®] DLC STAR (black line) and the associated 95 % confidence intervals (black dashed lines) and 95 % prediction interval (red dashed lines) plotted against load. Experimental data is plotted with a black circle. 103

Figure 7.12. The average wear depth of (a) BALINIT[®] DLC STAR and (b) AISI 440C steel plotted against sliding distance at a frequency of 5 Hz. Tests than ran at 5 N are shown in red, and tests that ran at 20 N are shown in blue. Error bars denote the error in the experimental measurements.104

Figure 8.1. A schematic of a ball-on-flat contact. The wear depth of the ball $w_{D,Ball}$ and the wear depth of the flat surface $w_{D,Flat}$ are labelled, as are the geometric parameters (namely stroke length l , contact radius a , ball radius r , and contact area A). Dashed lines represent the original unworn geometry.111

Figure 8.2. Contact radius (top-left), contact pressure (top-right), wear depth of the ball (middle-left), wear volume of the ball (middle-right), wear depth of the DLC coating (bottom-left), wear volume of the DLC coating (bottom-right), plotted against sliding distance. The black line represents the numerical solution, the red asterisks represent the model of Kauzlarich and Williams [159], and the black circles represent experimental data. Error bars are shown by black vertical lines and represent the error in measurement.....114

Figure 8.3. The specific wear rate (SWR) plotted against sliding distance for the ball (left), and BALINIT[®] DLC STAR (right). Experimental data is indicated by blue circles. The linear regression is given as a black line, and the exponential regression is given as a dashed red line.117

Figure 8.4. Contact radius (top-left), contact pressure (top-right), wear depth of the ball (middle-left), wear volume of the ball (middle-right), wear depth of BALINIT[®] DLC STAR (bottom-left), wear volume of BALINIT[®] DLC STAR (bottom-right), at a normal load of 5 N, plotted against sliding distance. The specific wear rate of the ball and BALINIT[®] DLC STAR is assumed to decrease exponentially. The black line represents the numerical solution, and the black circles represent experimental data. Error bars, shown by black vertical lines, represent the error in measurement.....117

Figure 9.1. (a) The actual test geometry, and (b) the model geometry, including the active region.....124

Figure 9.2. (a) A sketch of the active region of the ball, where the contact surface and the transfer layer height are defined by polynomials $C(s,t)$ and $h(s,t)$, and (b) the polynomial $h(s,t)$ which defines transfer layer thickness.....125

Figure 9.3. The procedure for modelling the wear of BALINIT[®] DLC STAR and AISI 440C steel ball using COMSOL Multiphysics 4.3 and LiveLink[™] for MATLAB[®]126

Figure 9.4. The prescribed growth of the transfer layer with time, according to a logistic function (see **Equation 9.5**) with logistic growth parameter $\kappa = 1/120 \text{ s}^{-1}$129

Figure 9.5. The model prediction of wear depth of (top) BALINIT[®] DLC STAR, and (bottom) an AISI 440C steel ball, during reciprocating sliding at a frequency of 5 Hz

and a normal load of 5 N. Growth of the transfer layer is prescribed, with a growth parameter of 0.0083. Error bars are shown by vertical lines and represent the error in measurement. 131

Figure 9.6. The model geometry during reciprocating sliding between BALINIT[®] DLC STAR and an AISI 440C steel ball at a frequency of 5 Hz and a normal load of 5 N. The surface of the DLC coating and AISI 440C steel ball are shown by a solid black line. The transfer layer is shown by a solid green line. 132

Figure 9.7. The numerical solution for contact pressure between BALINIT[®] DLC STAR and an AISI 440C steel ball, during reciprocating sliding at a frequency of 5 Hz and a normal load of 5 N. 132

Figure 9.8. The incremental wear model prediction of wear depth (solid line) compared to the differential equation of **Chapter 8** (dashed line) for (top) BALINIT[®] DLC STAR and (bottom) an AISI 440C steel ball, during reciprocating sliding at a frequency of 5 Hz and a normal load of 5 N. 136

Figure 9.9. The model prediction for wear depth of (top) BALINIT[®] DLC STAR, and (bottom) an AISI 440C steel ball, during reciprocating sliding at a frequency of 5 Hz and a normal load of 20 N. The model was fitted to the data at a normal load of 5 N. 137

Figure B.1. A flowchart to describe the dependencies of each script and function file within the incremental wear model..... XXXIX

List of Tables

Table 2.1. Keywords used in the literature review strategy.....	8
Table 2.2. An approximate categorisation of DLC coatings [4, 8, 9].....	11
Table 3.1. An approximate range for the coefficient of friction of different categorisations of DLC coating, in varying relative humidity, and in water.....	24
Table 3.2. The mechanical properties and tribological results of 7 commercially produced DLC coatings in a water environment at room temperature [59].	37
Table 5.1. Material properties of Graphit-iC™, BALINIT® DLC STAR, and Adamant®.	64
Table 5.2. Material properties of AISI 52100 steel, AISI 4118H steel, and AISI 440C steel.	65
Table 6.1. Test parameters for reciprocating tests of each DLC coating against a 6 mm diameter AISI 52100 steel ball using a 19 mm stroke.	76
Table 7.1. Parameters for wear testing of BALINIT® DLC STAR and Adamant® against 6 mm diameter AISI 440C steel balls on the TE77 reciprocating tribometer using a 2 mm stroke.....	94
Table 7.2. The observed range for the wear depth and specific wear rate across all load and frequency combinations, and the dependence of wear depth on normal load, sliding distance, and sliding frequency.....	105
Table 8.1. Two special cases of Equation 8.14, where specific wear rates vary linearly and exponentially with time.....	116
Table 9.1. A parametric sweep of d_c to assess the total solution time of the incremental wear model in comparison to the relative error of the averaged predictions for wear depth of BALINIT® DLC STAR and an AISI 440C steel ball.....	134
Table 9.2. A parametric sweep of opt to assess the total solution time of the incremental wear model in comparison to the relative error of the averaged predictions for wear depth of BALINIT® DLC STAR and an AISI 440C steel ball.....	135

List of Acronyms

a-C	Amorphous carbon
a-C/Cr	Chromium doped amorphous carbon
a-C:H	Hydrogenated amorphous carbon
a-C:H/Si	Silicon doped hydrogenated amorphous carbon
a-C:H/Ti	Titanium doped hydrogenated amorphous carbon
a-C:H/W	Tungsten doped hydrogenated amorphous carbon
AISI	American Iron and Steel Institute
Abaqus	Abaqus finite element software
AES	Auger electron spectroscopy
Al	Aluminium
Alicona InfiniteFocus	Alicona InfiniteFocus surface profilometer
BEI	Backscatter electron imaging
C	Carbon
CFUBMSIP	Closed field unbalanced magnetron sputter ion plating
Cr	Chromium
CrN	Chromium nitride
COMSOL	COMSOL Multiphysics 4.3 finite element software
C1s	Carbon 1s spectrum
CVD	Chemical vapour deposition
DLC	Diamond-like carbon
D-peak	Carbon peak present in Raman spectra at around 1350 cm ⁻¹ .
ECWR	Electron cyclotron wave resonance
EDX	Energy dispersive x-ray spectroscopy
eV	Electronvolt
F	Fluorine
FCVA	Filtered cathodic vacuum arc deposition
Fe	Iron
FEA	Finite element analysis
FeOOH	Iron (III) oxide-hydroxide
Fe(OH)₃	Iron (III) hydroxide
Fe₂O₃	Iron (III) oxide
Fe₃O₄	Iron (II, III) oxide, commonly named magnetite.
GB	Gigabyte

GDP	Gross domestic product
G-peak	Carbon peak present in Raman spectra at around 1570 cm ⁻¹
H	Hydrogen
HIPIMS	High power impulse magnetron sputtering
H₂O	Water
H₂¹⁸O	Isotope of water with 18 atomic mass units
LiveLink™	LiveLink™ for MATLAB® software
MATLAB®	Matrix Laboratory, MathWorks Inc.
MML	Micro Materials Laboratory
Mo	Molybdenum
mV	Millivolt
N	Nitrogen
NanoTest	Nanoindentation platform, Micro Materials Ltd.
nCATS	National Centre for Advanced Tribology at Southampton
NPL	National Physics Laboratory
O	Oxygen
O₂	Oxygen molecule
PECVD	Plasma enhanced chemical vapour deposition
PhD	Doctor of Philosophy
PLD	Pulsed laser deposition
PVD	Physical vapour deposition
PWR	Pressurised water reactor
RAM	Random access memory
Renishaw	Renishaw Raman spectrometer
RH	Relative humidity
SEM	Scanning electron microscopy
Si	Silicon
sp²	sp ² orbital hybridisation
sp³	sp ³ orbital hybridisation
SWR	Specific wear rate
ta-C	Tetrahedral amorphous carbon
ta-C:H	Hydrogenated tetrahedral amorphous carbon
TE77	Plint TE77 reciprocating tribometer
TGA	Thermo-gravimetric analysis
TaiCaan	TaiCaan profilometer, TaiCaan Technologies Europe
Ti	Titanium

TiC	Titanium carbide
TiN	Titanium nitride
ToF-SIMS	Time-of-flight secondary ion mass spectroscopy
UK	United Kingdom
VAM	Velocity accommodation mode
W	Tungsten
XPS	X-ray photoelectron spectroscopy
100Cr6	100Cr6 bearing steel
2D	Two-dimensional
3D	Three-dimensional
4118H	AISI 4118H steel
440C	AISI 440C stainless steel
52100	AISI 52100 steel
α-Fe₂O₃	Alpha phase of iron (III) oxide, commonly named hematite.
γ-Fe₂O₃	Gamma phase of iron (III) oxide, commonly named maghemite.

Nomenclature

a	Radius of contact	m
a_l	Estimated width of a Hertzian line contact	m
a_p	Estimated radius of a Hertzian point contact	m
a_0	Initial radius of contact	m
A	Apparent area of contact	m ²
A_r	Real area of contact	m ²
A_0	Ahhrenius constant	kg ² /m ² s ³
C	Surface position of the ball	m
C_0	Initial volume shrinkage of a ball	m ³
d	Sliding distance	m
d_C	Diffusion coefficient	m ² /s
dQ	Flow of heat into a system	J
D	Surface position of the DLC coating	m
E	Young's modulus	GPa
E_a	Activation energy	kJ/mol
E_{Ball}	Young's modulus of a ball	GPa
E_d	Energy dissipated	J
E_{DLC}	Young's modulus of a DLC coating	GPa
E_{Flat}	Young's modulus of a flat surface	GPa
E^*	Reduced elastic modulus	GPa
f	Sliding frequency	Hz
F	Frictional force	N
F_{Abr}	Abrasive component of the frictional force	N
h	Vector containing the height of a transfer layer	m
h_{max}	Maximum height of a transfer layer	m
h_{ox}	Thickness of an oxide layer	m
H	Hardness	GPa
$I(D)$	Intensity of the D-peak of a Raman spectra of carbon	1/cm
$I(G)$	Intensity of the G-peak of a Raman spectra of carbon	1/cm
J_i^j	Generalised thermodynamic flow	N/A
k	Specific wear rate	mm ³ /Nm
k_{Ball}	Specific wear rate of the ball	mm ³ /Nm

k_{DLC}	Specific wear rate of the DLC coating	mm^3/Nm
k_p	Parabolic oxidation rate constant	$\text{kg}^2/\text{m}^2\text{s}^3$
K	Dimensionless wear coefficient	dimensionless
l	Stroke length	m
L	Transition phase energy of diamond	J/kg
L_x	Length of surface profilometer scan in x-direction	m
L_y	Length of surface profilometer scan in y-direction	m
M_{Fe}	Mass of iron	kg
M_i	Number of phenomenological coordinates	dimensionless
M_{O_2}	Mass of oxygen	kg
n_i	Position of mesh nodes along a contact surface	m
N	Normal load	N
N_B	Number of dissipative degradation processes	dimensionless
p_i	Dissipative degradation process	N/A
$p_{i,j}$	Surface height	μm
P	Contact pressure	GPa
q_{fr}	Frictional power intensity	W/m^2
q_{pulse}	Energy pulse	J/m^2
r	Ball radius	m
R	Avogadro's gas constant	1/mol
R_a	Average surface roughness	μm
R^2	Coefficient of correlation	dimensionless
s	Material coordinate system	m
S	Total entropy production	J/K
S_i	Entropy production of a single irreversible process	J/K
t	Time	s
t_c	Time of contact between asperities	S
t_{ox}	Time for oxidation to occur	S
t_{max}	Total integration time	S
T	Temperature	K
T_0	Transition temperature of a DLC coating in a vacuum	K
v	Sliding velocity	m/s
v_H	Specific volume of a hydrogenated DLC coating	cm^3/g
$v_{H'}$	Specific volume of a non-hydrogenated DLC coating	cm^3/g
V_A	Volume above the surface	m^3

V_B	Volume below the surface	m^3
w_{Ball}	Wear depth of the ball	m
w_D	Wear depth	m
w_{DLC}	Wear depth of the DLC	m
$w_{D,Ball}$	Wear depth of a ball	m
$w_{D,Flat}$	Wear depth of a flat surface	m
w_i	Degradation measure of an irreversible process	N/A
w_V	Wear volume	m^3
W_V	Wear volume of a flat surface	m^3
$w_{V,Ball}$	Wear volume of a ball	m^3
$w_{V,Flat}$	Wear volume of a flat surface	m^3
x	Horizontal Cartesian coordinate	m
x_d	Horizontal displacement	m
X_i^j	Generalised thermodynamic force	N/A
y	Vertical Cartesian coordinate	m
Y_i^j	Generalised degradation force	N/A
α_{DLC}	Thermal expansion coefficient of a DLC coating	1/K
α_S	Thermal expansion coefficient of a substrate	1/K
α_1	Constant of a linear form for the specific wear rate	1/s
α_2	Constant of a linear form for the specific wear rate	dimensionless
β	Degradation coefficient	N/A
β_i	Degradation coefficient of a single irreversible process	1/s
β_1	Constant of an exponential form for the specific wear rate	1/s
β_2	Constant of an exponential form for the specific wear rate	dimensionless
δ	Slip distance	m
Δh	Wear depth at each contact node	m
ΔN	Relaxation parameter	dimensionless
ΔP	Change in pressure	GPa
Δt	Time-step	s
ΔT	Change in temperature	K
Δx	Surface scan resolution in the x-direction	m
Δy	Surface scan resolution in the y-direction	m
$\Delta \tau$	Time-step of the subroutine	s
κ	Logistic growth parameter	1/s
ϕ	Percentage sp^3 orbital hybridisation	dimensionless

μ	Coefficient of friction	dimensionless
ν	Poisson's ratio	dimensionless
ν_{Ball}	Poisson's ratio of a ball	dimensionless
ν_{DLC}	Poisson's ratio of a DLC coating	dimensionless
ν_{Flat}	Poisson's ratio of a flat surface	dimensionless
ρ	Density	g/cm ³
ρ_{Fe}	Density of iron	g/cm ³
$\sigma_{External}$	External residual stress	GPa
$\sigma_{Intrinsic}$	Intrinsic residual stress	GPa
$\sigma_{Residual}$	Total residual stress	GPa
$\sigma_{Thermal}$	Thermal residual stress	GPa
τ	Shear strength	GPa
ξ	Simplification factor	dimensionless
ζ_i^j	Phenomenological coordinate	N/A

Declaration of Authorship

I, Daniel Christopher Sutton, declare that the thesis entitled “**Wear Modelling of Diamond-Like Carbon Coatings against Steel in Deionised Water**” and the work presented in the thesis are both my own, and have been generated by me as the result of my own original research.

I confirm that:

- This work was done wholly or mainly while in candidature for a research degree at this University;
- Where any part of this thesis has previously been submitted for a degree or any other qualification at this University or any other institution, this has been clearly stated;
- Where I have consulted the published work of others, this is always clearly attributed;
- Where I have quoted from the work of others, the source is always given. With the exception of such quotations, this thesis is entirely my own work;
- I have acknowledged all main sources of help;
- Where the thesis is based on work done by myself jointly with others, I have made clear exactly what was done by others and what I have contributed myself;
- Parts of this work have been published as:

Journal Publications

- D.C. Sutton, G. Limbert, B. Burdett, and R.J.K. Wood, Interpreting the effects of interfacial chemistry on the tribology of diamond-like carbon coatings against steel in distilled water. *Wear*, **302**: p.918-928 (2013).
- D.C. Sutton, G. Limbert, D. Stewart, and R.J.K. Wood, The friction of diamond-like carbon coatings in a water environment. *Friction*, **1**(3): p.210-221 (2013).

- D.C. Sutton, G. Limbert, D. Stewart, and R.J.K. Wood, A functional form for wear depth of a ball and a flat surface. *Tribology Letters* 53(1): p.173-179 (2013).

Conference Presentations

- D.C. Sutton, G. Limbert, B. Burdett, and R.J.K. Wood, Interpreting the effects of interfacial chemistry on the tribology of diamond-like carbon coatings against steel in distilled water. Presented at:
 - The 19th International Conference on Wear of Materials, Portland, Oregon, USA, 14th – 18th April 2013.
 - Rolls-Royce Nuclear Materials, Chemistry, and Corrosion Research Conference, Derby, UK, 3rd October 2012.
- D.C. Sutton, G. Limbert, B. Burdett, and R.J.K. Wood, Diamond-like carbon coatings: Predicting the wear behaviour. Presented at:
 - Rolls-Royce Nuclear Materials, Chemistry, and Corrosion Research Conference, Derby, UK, 3rd November 2011.
 - Mission of Tribology, Institute of Mechanical Engineers, London, UK, 7th December 2011. **Awarded Mission of Tribology Award.**

Signed:

Date: 20th March 2014

Daniel Christopher Sutton

Acknowledgements

First and foremost, I would like to thank my PhD supervisors, Professor Robert Wood and Dr Georges Limbert. You allowed me free reign to follow my own ideas, and provided the advice and guidance required to hone them into a PhD thesis. Your support throughout the PhD project has been invaluable, and I sincerely thank you, initially, for the opportunity, and finally, for the experience.

This PhD project was fully funded by Rolls-Royce Plc. I would like to convey my appreciation to Mr Barry Burdett for the instigation of the project, and Dr Dave Stewart for his willingness to adopt the project. You have provided me with sage words of advice, and expert direction.

I have also benefited greatly from presenting at my first international conference (Wear of Materials 2013, in Portland, Oregon, USA) which would not have been possible without funding from the Tin Plate Workers alias Wire Workers Company of the City of London, for which I am greatly thankful.

Great appreciation goes to colleagues at the University of Southampton who have assisted me in the completion of this thesis. Specifically, I would like to thank Dr Terry Harvey, Dr John Walker, Dr Richard Cook, Dr Jurgita Zekonyte, and Dr Shuncaï Wang, for the training and assistance you provided when I required it. Ion Costisanu, your summer internship forms an essential component of this document, and I sincerely thank you for the assistance you provided at a critical time. Kind thanks goes to Dr Brian Mellor for being my internal examiner at each viva examination. Sue Berger, throughout the project you have had all the answers. Thank you for all your help. Additional thanks goes to Mr Steve Pilehard, for his assistance in the manufacture of various components, and his preparation of countless pins for the TE77. Maureen, I am in your debt, for the supply of tea, and a biscuit, every day at precisely 2:35 pm.

A special thank you goes to friends and colleagues who, each in their individual way, have supported me these past years. Academic influence is important, but this document would not be here without innumerable cups of coffee and bouldering sessions with friends. You are too many to mention, but you know who you are, and I wish you all the best for the future.

Lastly, and most importantly, I would like to thank my loved ones for being there, and for providing a safe haven, not just throughout the PhD project, but always. Robbie, you deserve your name on the front of your own thesis, but I hope you'll be happy with your name on the inside of mine. Verity, you could not have offered more care and support and positivity, and you kept me sane when my whole world was mad. Mum, your support has always been unwavering, and you might not want to read *every* word, but every word is there because of you.

Chapter 1. Introduction

Diamond-Like Carbon (DLC) coatings are thin protective tribological coatings known for their high hardness, low coefficient of friction, and high wear resistance. Rolls-Royce is interested in the general use of these coatings in their pressurised water reactors to extend component lifetimes in harsh conditions. The tribology of a DLC coating in this challenging environment is unknown, and research is required to understand the long-term material behaviour. This PhD project focuses on accelerated testing of DLC coatings in a deionised water environment, and predictive modelling of the wear of DLC coatings through their lifetime. This chapter introduces the main goals of the PhD project and the unique contributions to knowledge.

1.1. Project outline

Nuclear power continues to be a key constituent of the energy provisions of the United Kingdom (UK), and is essential to meeting the Government's objective of delivering a low-carbon, sustainable future. Around £60 billion is to be invested into a new nuclear build that could provide the UK with 16 – 75 GW of energy up to 2050 – corresponding to 12 new nuclear reactors built at sites across the country, and approximately 40 – 50 % of the total UK energy production, compared to just 20 % today [1]. Requirements of the new nuclear build, both short and long term, include: continuous improvements in safety; provision of the next generation of nuclear power stations; and cost reduction of nuclear power for customers and industrial consumers. To obtain these goals, new nuclear reactors will be required to operate for a longer lifetime, which places the focus on research and development of materials which are able to provide longer component lifetimes without compromising on safety.

The type of nuclear reactor we focus on in this thesis is a pressurised water reactor (PWR's) (see **Figure 1.1**), where the nuclear engine heats the primary coolant (specially processed demineralised deionised water) to temperatures above 300 °C. Due to the high pressure (15 – 16 MPa) in the primary system, water cannot boil. The heated water flows to a steam generator where its thermal energy diffuses to a secondary system (typically at a pressure of 6.2 MPa and a temperature of 275 °C) which generates steam and powers a steam turbine. This is a complex environment and the tribology of any components in the system need to be understood for long service to be reached.

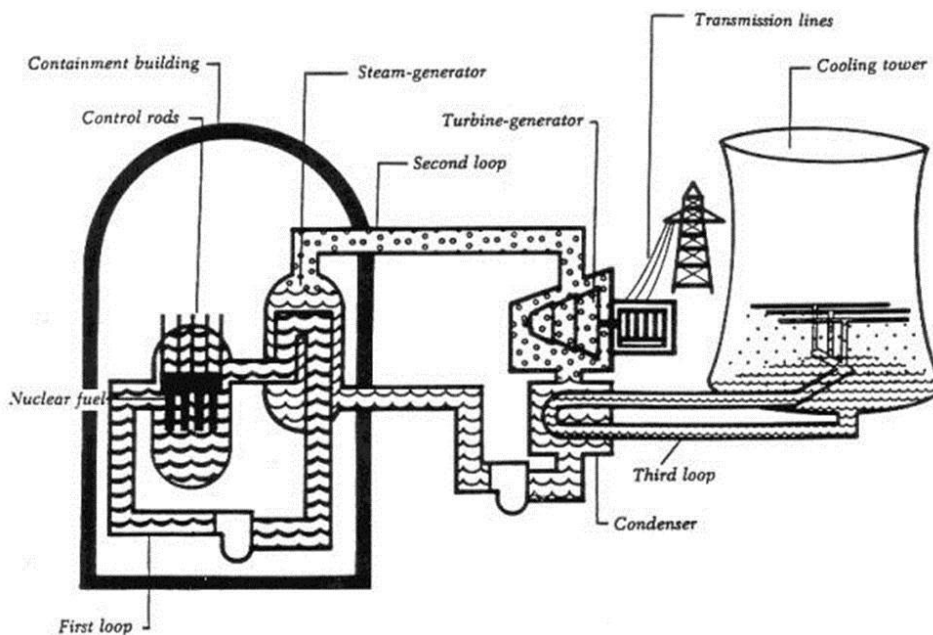


Figure 1.1. A schematic of a pressurised water reactor from the United States Nuclear Regulatory Commission [2].

Existing reactors were built decades ago, and a number of reactors currently in use are having their lifetimes extended to meet the energy requirements of the UK. The current generation of nuclear reactors were built before the advent of modern vacuum deposition techniques such as Plasma Enhanced Chemical Vapour Deposition (PECVD) or Physical Vapour Deposition (PVD). As a result, a new range of materials and surface treatments are now available to improve the tribology in a PWR. One particular new material that is the focus of this work is a Diamond-Like Carbon (DLC) coating.

DLC coatings are wear resistant coatings which display differing tribological behaviour depending on their chemical composition and mechanical properties [3, 4]. Advanced coating deposition techniques offer the potential to provide application specific solutions to minimise friction or wear whilst preserving macroscopic engineering tolerances. Some initial tests of DLC coatings in a PWR have shown promising results, and there is an interest in the introduction of DLC coatings to a PWR to solve some undisclosed tribological issues. To attain this goal, a greater understanding of the material behaviour and the coating wear mechanisms are required to have confidence in the survival of a DLC coating in service.

1.2. Project aims and objectives

This project examines the tribology of DLC coatings sliding against steel in a water environment. Both distilled and deionised water are used in the experiments in this thesis, and whilst they are an oversimplification of the PWR environment, the experiments act as a base from which a fundamental understanding of the tribological mechanisms can be built.

The main goals of the project are as follows:

- i. To increase understanding of the mechanisms of friction and wear between DLC coatings and steel in an aqueous environment.**
- ii. To evaluate the performance of UK commercially deposited DLC coatings sliding against steel in an aqueous environment.**
- iii. To develop a model to predict the wear of DLC coatings sliding against steel in an aqueous environment.**

To satisfy these goals, several commercial DLC coatings were obtained from surface engineering companies across the UK. Reciprocating sliding wear tests were performed

to assess the coefficient of friction and specific wear rate of each coating under the applied test conditions. A mechanical assessment of each coating was obtained using nanoindentation, and post-testing chemical analysis was performed using Raman spectroscopy. The effect of iron oxide formation on the tribology of DLC coatings was examined, particularly regarding the growth of a transfer layer.

The second stage of the project examined the consequence of varying test parameters on the tribology of the DLC coatings. A factorial experiment was designed to investigate how changes in normal load or sliding velocity affect the coefficient of friction and specific wear rate of a DLC coating and steel counterface. The results from these sliding wear tests provide a data set for subsequent wear modelling.

Two independent wear models were developed during the PhD project (both of which were validated by ball-on-flat reciprocating wear tests between a DLC coating and a steel ball in deionised water):

- **A geometric derivation of formulae to predict the wear depth of a ball and a flat surface through time as they slide against each other, in relation to any phenomenological law for wear volume.**
- **An incremental wear model developed using COMSOL Multiphysics 4.3 and LiveLink™ for MATLAB® to predict the evolution of contact surfaces of general system components due to the phenomenon of wear.**

This investigation has drawn on collaborations between the National Centre for Advanced Tribology at Southampton (nCATS), Rolls-Royce Nuclear, the National Physics Laboratory (NPL), and Micro Materials Laboratory (MML). The work is funded by Rolls-Royce Nuclear through a PhD studentship at the University of Southampton.

1.3. Thesis structure

The structure of the thesis is given by the flow chart in **Figure 1.2**. The thesis is split into three main sections; the literature review, the experimental work, and the wear modelling work.

Chapter 1 details the project aims and objectives, and provides an outline of the thesis structure. The importance of research into DLC coatings is explained in the context of the new build of nuclear reactors in the UK.

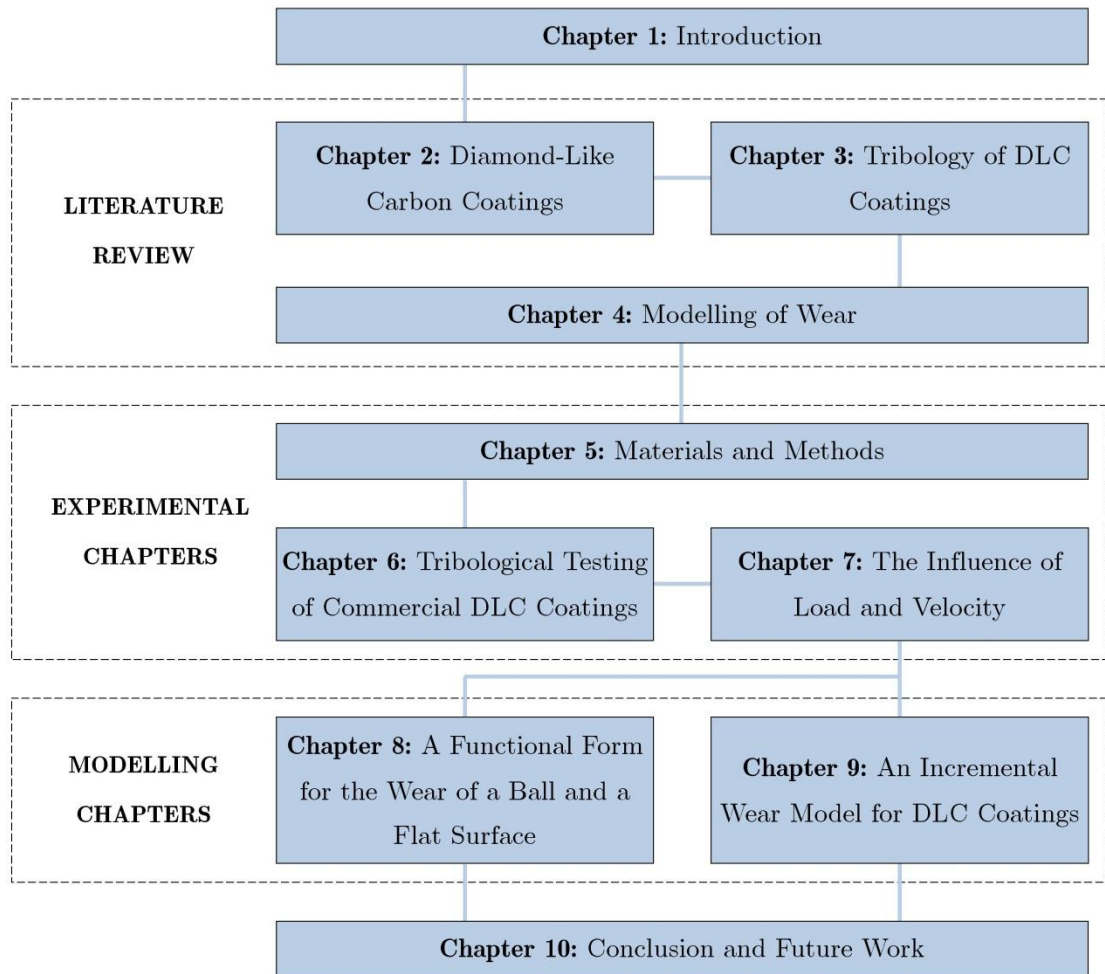


Figure 1.2. Flow-chart of the thesis.

Chapter 2 presents a review of the mechanical properties of DLC coatings. The chapter begins with the deposition of DLC coatings. Next, the link between the bonding structure of carbon atoms and the DLC coating mechanical properties is examined, in terms of hardness, elastic modulus, density, and residual stress.

Chapter 3 begins by considering the origins of friction, and the main contributions to the friction of a DLC coating. The hydrogen passivation mechanism of Erdemir [5] is presented. Next, the wear mechanisms of a DLC coating are discussed in terms of graphitisation and transfer layer formation. A special focus is placed on the tribology of DLC coatings in water, and the tribochemistry when DLC coatings slide against steel in water.

Chapter 4 examines the state of the literature regarding the modelling of wear, and begins with the introduction of Archard's wear law, frictional energy dissipation, and incremental wear models. Recent literature that models the lifetime prediction of DLC coatings is presented.

Chapter 5 provides a methodology for the measurement of friction and wear, and a discussion of the experimental aims (as guided by the literature review). Three

commercial DLC coatings are introduced, and their mechanical properties analysed using surface profilometry, nanoindentation, and Raman spectroscopy.

Chapter 6 presents results from the reciprocating tests of three commercial DLC coatings against AISI 52100 steel balls in distilled water. Friction and wear results are correlated to the dynamics of the transfer layer at the sliding interface. To examine the relationship between interfacial chemistry and the friction and wear, Electron Dispersive X-ray (EDX) spectroscopy and Raman spectroscopy are used.

Chapter 7 discusses the results from a factorial experiment designed to investigate the effect of normal load and sliding velocity on the coefficient of friction and specific wear rate of two commercially deposited DLC coatings sliding against an AISI 440C steel ball in deionised water.

Chapter 8 provides formulae that link a specific wear rate (often taken from experiments in the laboratory) to the wear depth of a ball and a flat surface as they slide against each other. The formulae remove previous limiting approximations made in the literature, and extend to the prediction of the wear depth of both contacting surfaces. The formulae derived are used to predict the wear depth of a DLC coating (BALINIT[®] DLC STAR from Oerlikon Balzers) and an AISI 440C steel ball as they slide against each other in deionised water.

Chapter 9 presents an incremental wear model, developed using COMSOL Multiphysics 4.3 and LiveLink[™] for MATLAB[®], to predict the evolution of contact surfaces due to the phenomenon of wear. The formulation can be applied to components of a generalised geometry. Of interest is the ball-on-flat reciprocating contact of a DLC coating (BALINIT[®] DLC STAR from Oerlikon Balzers) and an AISI 440C steel ball in deionised water.

Chapter 10 provides a summary of the key results of the thesis, and discusses the consequences in reference to PWR's. This chapter also examines future work needed to continue this research in terms of unanswered questions from experiments as well as potential extensions to the predictive models presented.

Chapter 2. Diamond-Like Carbon Coatings

This chapter introduces Diamond-Like Carbon coatings and their mechanical properties. An understanding of the mechanical properties of DLC coatings is vital to understand their tribological behaviour. A thorough review of the literature details their typical composition, common deposition methods, and how the bonding configuration of carbon affects the hardness, Young's modulus, and residual stress. Multi-layer coatings, and doping or alloying of DLC coatings are discussed.

This literature review aims to inform the experimental methodology and identify the types of DLC coating which will be selected for the sliding wear tests. The various sections of the literature review, and the relevant keywords used to identify relevant publications, are shown in **Table 2.1**.

Table 2.1. Keywords used in the literature review strategy.

Keywords	
Deposition parameters	Coating thickness; carbon bonding hybridisation; hydrogen content; dopants; interlayers; deposition process.
Mechanical properties	Hardness; elastic modulus; Poisson's ratio; density; roughness; residual stress; surface energy; deposition parameters.
Friction	Surface energy; adhesive friction; abrasive friction; contact conditions; environment; mechanical properties; transfer layer formation.
Wear	Graphitisation; oxidation; interfacial chemistry; contact conditions; environment; mechanical properties; transfer layer formation.
Transfer layer	Interfacial chemistry; adhesion; shear strength; volume of worn debris; abrasion; contact conditions; environment; mechanical properties.
Modelling of wear	Contact mechanics; Archard's wear law; frictional energy dissipation; incremental wear model; finite element analysis.

Tribology is the science and engineering of surfaces in relative motion, and their interactions in terms of friction, lubrication, and wear. There are many economic, industrial, and commercial advantages to be gained by the study of tribology, such as extended component lifetimes, higher reliability, and increased performance. The Jost report, published in 1966, marked the recognition of the economic value of tribology worldwide. The Jost report estimated that £515 million per annum (in 1966) was thought to be lost due to poor tribology. In today's terms, this represents £20 billion, approximately 1.3 % of the UK's GDP. Modern tribology is multidisciplinary, and has formed new areas of research such as nano- and bio-tribology. New materials provide new tribological behaviour, and so much research in tribology lies in the testing of new materials and their potential in various applications.

2.1. Composition and deposition

The mechanical properties of a DLC coating are governed by a number of important factors. Fundamentally, the deposition method is a crucial factor in defining the mechanical and tribological properties of a DLC coating. The mechanical properties may vary depending on the bonding configuration of carbon within the DLC coating, as

well as varying as a function of coating thickness. The development of multi-layered coatings, or inclusion of dopants within the carbon matrix, alters the properties of DLC coatings further, and there is much research into understanding the tribology of this. The following subsections consider the bonding configurations of carbon, the hydrogen content, a general categorisation of types of DLC coatings, and an overview of the deposition processes.

2.1.1. Bonding configurations of carbon

Allotropy is the property of a chemical element to exist in various different forms, due to its possible bonding configurations. Carbon atoms bond in three configurations: tetrahedral, trigonal, and linear [4]. A trigonal configuration is two-dimensional, and has three sp^2 hybridised orbitals and a 2p orbital. Each carbon atom forms three sigma bonds with neighbouring carbon atoms using the sp^2 orbitals. The 2p orbital forms a pi-bond perpendicular to the surface of the plane. Graphite, see **Figure 2.1 (a)**, is the most common allotrope of carbon and the most thermodynamically stable. The configuration leads to two-dimensional sheets of covalently bonded carbon atoms. A delocalisation of pi-bond electrons between the layers of graphite leads to its electrical conductivity. A tetrahedral configuration, by definition, comprises of four sigma bonds. A carbon atom must have four sp^3 hybridised orbitals which overlap with nearby orbitals of other carbon atoms to form four sigma bonds. Diamond, shown in **Figure 2.1 (b)**, is an allotrope of carbon that forms in a tetrahedral lattice. Strong covalent bonds (sigma-bonds) between atoms provide the characteristic high hardness and thermal conductivity of diamond.

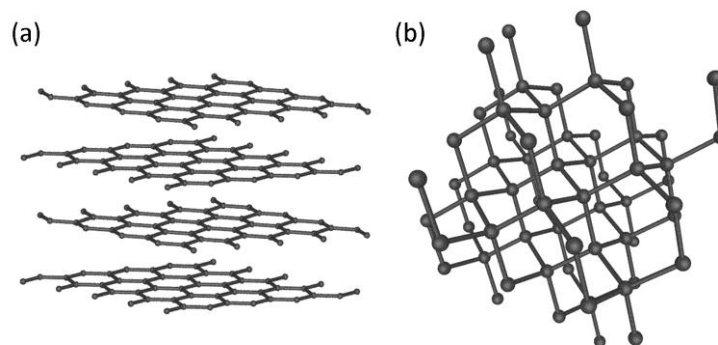


Figure 2.1. The bonding structure in (a) graphite and (b) diamond [6].

A DLC coating in its simplest form is comprised purely of amorphous carbon; that is carbon atoms bonded without any long-range crystalline structure. It can be deposited via a range of highly energetic processes which lead to an irregular bonding configuration that is not thermodynamically optimal. The number of sp^2 and sp^3 hybridisations of carbon in a DLC coating is governed by the deposition process, and

the ratio of the two affects the mechanical and tribological properties of the coating. In the literature, the percentage of sp^2 and sp^3 hybridised orbitals of carbon in a DLC coating are referred to the sp^2 and sp^3 content respectively.

2.1.2. Hydrogen content

As mentioned in the previous subsection, DLC coatings are comprised mainly of carbon atoms, bonded in sp^2 and sp^3 bonding hybridisations. Depending on the deposition process they may also contain hydrogen atoms, either chemically bonded to a carbon atom, or trapped within interstitials in the coating. DLC coatings are often categorised as hydrogenated or non-hydrogenated coatings. The hydrogen content might vary from 0 % up to 60 %, and this greatly affects the properties of a DLC coating, in terms of tribological behaviour [5] as well as the mechanical properties of the coating.

Hydrogen stabilises the sp^3 bonding hybridisation in a DLC coating [7]. As a DLC coating forms, intrinsic stresses arise due to the forced bonding of nearby carbon atoms. With the introduction of hydrogen, carbon atoms are able to bond to local hydrogen atoms, acting to relax the carbon network and stabilise the sp^3 structure of the DLC coating. If the hydrogen content is too high, most of the sp^3 bonds are C – H bonds and not C – C bonds, resulting in a DLC coating with a reduced hardness.

2.1.3. Categorisation of DLC coatings

This section outlines the different categorisations of DLC coatings, in terms of their carbon bonding hybridisation, hydrogen content, and mechanical properties. A ternary phase diagram is often used to outline the various types of DLC coatings. It was first presented by Jacob and Moller [7] for hydrogenated amorphous carbon (a-C:H) coatings and hydrogenated tetrahedral amorphous carbon (ta-C:H) coatings, and later was updated by Robertson [4] to include sputtered amorphous carbon (a-C) coatings, tetrahedral amorphous carbon (ta-C) coatings, and graphitic carbon coatings. The ternary phase diagram of Robertson [4] is shown in **Figure 2.2**.

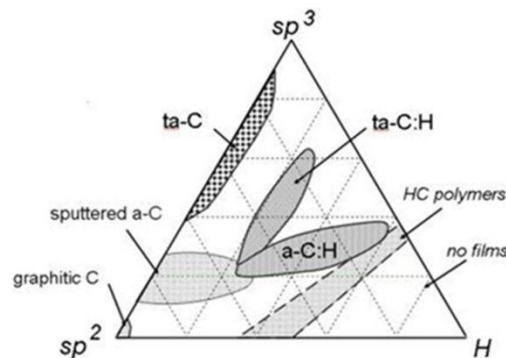


Figure 2.2. A ternary phase diagram for DLC coatings [4].

A general categorisation of DLC coatings, as presented in the literature, is given in **Table 2.2**. The mechanical properties of a DLC coating in terms of sp^3 content, hydrogen content, density, hardness, and Young's modulus, are compared to those of graphite and diamond.

Table 2.2. An approximate categorisation of DLC coatings [4, 8, 9].

	sp^3 Content (%)	Hydrogen Content (%)	Density (g/cm ³)	Hardness (GPa)	Young's Modulus (GPa)
Graphite	0	0	2.267	0.2 – 2	10
Diamond	100	0	3.515	100	1000
a-C	0 – 5	0	1.9 – 2.2	10 – 20	100 – 200
a-C:H soft	60	40 – 60	1.2 – 1.6	< 10	–
a-C:H hard	40	20 – 40	1.6 – 2.2	10 – 30	100 – 300
ta-C	80 – 88	0	2.2 – 3.2	50 – 80	300 – 500
ta-C:H	70	25 – 30	1.7 – 2.4	< 50	< 300

i. Non-hydrogenated amorphous carbon (a-C)

Non-hydrogenated amorphous carbon coatings can be produced by a variety of sputtering techniques such as unbalanced magnetron sputtering (discussed in **Section 2.1.4**). These coatings are rich in sp^2 bonded carbon, and generally the microstructure contains local regions of graphite-like carbon bonded within the amorphous carbon matrix. The sp^3 content is generally very low. These non-hydrogenated DLC coatings have a Young's modulus between 100 and 200 GPa, and a hardness between 10 and 20 GPa.

ii. Hydrogenated amorphous carbon (soft and hard a-C:H)

Hydrogenated amorphous carbon coatings are typically split into two groups; hard a-C:H coatings which contain 20 – 40 % hydrogen atoms, and soft a-C:H coatings which contain 40 – 60 % hydrogen atoms [9]. Soft a-C:H coatings are typically produced by a plasma enhanced chemical vapour deposition (PECVD) process (as discussed in **Section 2.1.4**). The high hydrogen content of these coatings relaxes the carbon matrix and results in a lower density (1.2 – 1.6 g/cm³) and lower hardness (<10 GPa). Hard a-C:H coatings are produced either by PECVD, or by sputtering of graphite in a hydrogenated atmosphere. They contain higher intrinsic stresses than a soft a-C:H coating, and have a higher hardness (10 – 30 GPa) than soft a-C:H coatings. The Young's modulus typically varies over the range 100 – 300 GPa.

iii. Tetrahedral amorphous carbon (ta-C)

Tetrahedral amorphous carbon coatings are highly dense non-hydrogenated coatings with a predominance of sp^3 bonded carbon. This type of DLC coating has a hardness value in the range of 50 – 80 GPa, and Young’s modulus in the range 300 – 500 GPa. It can be produced via filtered cathodic vacuum arc (FCVA) deposition process, or by pulsed laser deposition (PLD).

iv. Hydrogenated tetrahedral amorphous carbon (ta-C:H)

Hydrogenated tetrahedral amorphous carbon coatings, as the name suggests, show a high sp^3 content. The high sp^3 content is possible due to modern plasma techniques such as electron cyclotron wave resonance (ECWR), which will be discussed in **Section 2.1.4**. The density (1.7 – 2.4 g/cm³), hardness (< 50 GPa), and Young’s modulus (< 300 GPa) of these coatings, compared to ta-C coatings, is slightly reduced due to the inclusion of hydrogen.

2.1.4. Deposition processes

DLC coatings are deposited, fundamentally, by the collision of carbon ions with a substrate. The ions reach the surface of the substrate with high energy, allowing them to bond in irregular configurations, which result in the characteristic amorphous structure. Deposition of DLC coatings above a few micrometres in thickness is uncommon due to thermal and intrinsic residual stresses which accumulate during the deposition process.

The strong mechanical properties of DLC coatings result from a carbon matrix with a large proportion of sp^3 hybridisation. The proportion of sp^3 bonded carbon in a DLC coating is dependent on the energy per incident ion [10]. Consider an ion approaching the surface of a non-hydrogenated coating; if it has a relatively small energy, perhaps 50 eV, it cannot penetrate the surface and so finds an optimal position on the surface to bond in the unconstrained (and lower energy state) sp^2 alignment. If the carbon ion has a relatively high energy, the ion may penetrate into the bulk of the DLC coating and cause subsurface growth. This results in a dense sp^3 region within the amorphous carbon coating.

The proportion of sp^3 bonded carbon atoms in a non-hydrogenated DLC coating increases with the average energy per incident carbon ion only until a critical point after which the proportion of sp^3 bonded carbon atoms will begin to decrease [4, 10]. This is because a high energy carbon ion will have enough energy to transform the subsurface region into the sp^2 ground state, through a mass relaxation of the atoms.

Optimal conditions for sp^3 growth have been shown to be in the region of 100 eV per carbon ion [10]. Commercially produced coatings are typically optimised to allow for faster deposition (i.e. high energy per carbon ion) and idealised mechanical properties, specific to application.

During the deposition of hydrogenated DLC coatings, a decline in the hydrogen content is observed as the ion energy is increased. This is due to the production of hydrogen gas. The proportion of sp^3 hybridised carbon is at a maximum at zero ion energy (since a large proportion of the sp^3 hybridised carbon atoms are resultant from C – H bonding). The maximum hardness and Young’s modulus coincides with the maximum number of C – C bonds, at some intermediate value of the average ion energy – which is dependent on the source gas chemistry.

Methods for the deposition of DLC coatings fall into two categories; **Physical Vapour Deposition** (PVD) and **Chemical Vapour Deposition** (CVD). Some common methods for the deposition of DLC coatings are outlined below.

i. Ion beam deposition

An ion beam may be used to deposit a DLC coating onto a substrate by bombarding the surface with ions [4, 11]. This results in a physical rearrangement of the atoms, and alters the formation process and mechanical properties of the coating. Typically, carbon ions are produced through sputtering of a graphite cathode.

ii. Magnetron sputtering

DLC coatings are often deposited by sputtering of a graphite target with argon ions, resulting in positively charged carbon ions. A negative bias can be applied to the substrate to control the energy per incident ion so as to optimise the hardness and elastic modulus of the coating. This technique is used to produce non-hydrogenated coatings.

Closed field unbalanced magnetron sputter ion plating (CFUBMSIP) [12] is an advanced magnetron sputter technique that uses magnets to increase ion bombardment on the surface and prevent ions from escaping towards other targets such as the chamber walls (see **Figure 2.3**). The sputtering process has the disadvantage that it is line-of-sight, and subsequently it is hard to coat complex geometries. In addition, the proportion of ionised carbon to neutral carbon is quite small in comparison to a CVD technique, which results in coatings with a lower hardness [4]. Conversely, it allows for directional coating of specific sections.

High-power impulse magnetron sputtering (HIPIMS) is a magnetron sputtering technique which uses high power density impulses to provide a better degree of

ionisation and higher coating density. As a result, HIMPIIMS deposited DLC coatings have a higher hardness and Young's modulus than conventional PVD deposited DLC coatings.

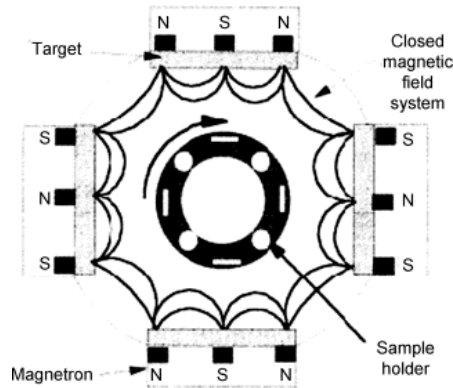


Figure 2.3. A closed field unbalanced magnetron sputter ion plating system [12].

iii. Pulsed Laser Deposition

Pulsed laser deposition (PLD) uses a laser to vaporise the graphite target into intense plasma. The laser pulse causes the plasma to expand towards the substrate creating a high energy per incident ion. Tetrahedral amorphous coatings have been produced in this manner at up to 80 % sp^3 bonded carbon [13].

iv. Filtered Cathodic Vacuum Arc Deposition

Cathodic vacuum arc deposition relies on a high current, low voltage electric arc to vaporize a cathode target, resulting in a vapour flux which, directed by magnetrons, deposits onto the substrate to form a thin surface coating. This process relies on the high power density of the arc to ionise the coating. This technique is able to produce high density ta-C coatings [4].

v. Plasma Enhanced Chemical Vapour Deposition (PECVD)

The CVD process produces high quality coatings through the reaction of source gases on the substrate surface [11]. The plasma enhanced chemical vapour deposition (PECVD) process creates plasma between electrodes, to assist the deposition process. For DLC coatings, the precursor gases are normally hydrocarbons. The major advantages of this method are the quality of the coatings produced, and the ability to coat components multi-directionally. A disadvantage is the temperature at which these processes occur, which can limit many conventional substrates from being used. Depending on the carbon / hydrogen ratio of the source gas used, the hydrogen content of the DLC coating will vary [5].

vi. Electron Cyclotron Wave Resonance

Electron cyclotron wave resonance (ECWR) is an advanced technique that has been used for the deposition of ta-C:H coatings [14]. The technique uses electron cyclotron wave resonance, a phenomenon observed in plasma physics by superimposing a static magnetic field and an electromagnetic field at some resonant frequency, to produce high density plasma at a fast deposition rate.

2.2. Mechanical properties

The mechanical properties that a DLC coating exhibits are dependent on the composition and bonding structure of the coating, and are dependent on the deposition method as a result. In particular, it is informative to see how the hardness and density vary with sp^3 content and hydrogen content. Accumulation of intrinsic residual stress is an issue, and the inclusion of various elements within DLC coatings has been shown to alter the mechanical properties and lower the residual stresses.

2.2.1. Hardness, elastic modulus, and density

Hardness is defined as the resistance of a solid material to plastic deformation. The hardness of a thin film material is measured using nanoindentation, since any macroscopic indentation would bias the results due to the mechanical effects of the substrate material, and is calculated as a ratio of applied load to plastically deformed area. The elastic modulus is defined as the gradient of the stress – strain curve whilst under elastic deformation. Using nanoindentation, it is possible to use the load – displacement curve to estimate values for Young’s modulus and hardness, based on the method developed by Oliver and Pharr [15, 16]. One should take caution however since this method does not allow for pile-up around the indenter and may result in an over-estimation of elastic properties as a result. Additionally, the known shape of the indenter is crucial in obtaining accurate values, so nanoindentation equipment should be calibrated regularly.

For DLC coatings, it is known that hardness and elastic modulus generally increase with sp^3 content [8], but the exact relationship between hardness and sp^3 content varies depending on deposition techniques and deposition parameters, hydrogen content, and density. The approximate hardness of different types of DLC coatings are shown in **Table 2.2**. Ferrari et al. [17] relate Young’s modulus E to the sp^3 content ϕ of a ta-C coating. The elastic modulus varies non-linearly according to $E = 478.5(\phi + 0.4)^{3/2}$.

Generally, for a relatively thick coating, a nanoindentation of approximately 10 % of the coating thickness allows for accurate determination of hardness, while removing the effect of the hardness of the substrate from the load – displacement curve. Lemoine et al. [8, 18, 19] explain that for extremely thin coatings, a nanoindentation of 10 % of the coating thickness is not feasible, so they present a model to allow estimation of the coatings elastic properties. They have shown how the measured hardness of a 47 nm thick a-C:H coating changes with indentation depth, see **Figure 2.4**. A model was developed to account for the substrate effect, as well as blunting of the tip [18]. As a result, bulk hardness of the ta-C coating and silicon can be extracted as a function of indentation depth.

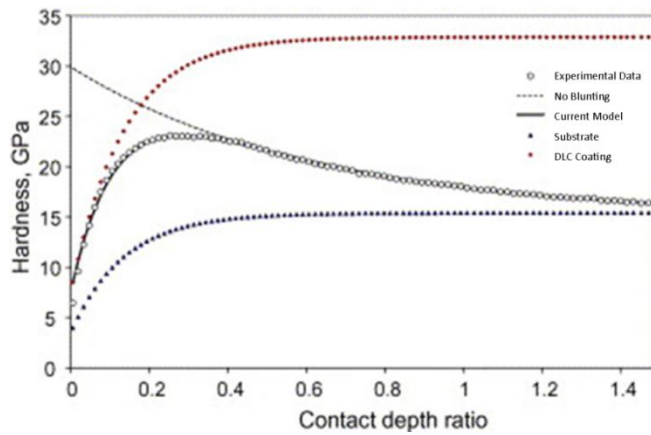


Figure 2.4. Hardness versus contact depth ratio for a 47 nm thick a-C:H coating deposited on a silicon wafer [18].

The density of a DLC coating (see **Figure 2.5**) is related strongly to the sp^3 content [9, 17, 20]. For ta-C coatings, the density increase is linear and can be described as $\rho = 1.92 + 1.37\phi$ [17]. Hydrogenated coatings show a lower density; for ta-C:H a similar linear relationship is observed, however for a-C:H coatings the density deviates from a linear relationship as the sp^3 content is increased beyond a critical point. This is because the majority of sp^3 bonds are terminated with hydrogen, resulting in less C – C bonding in the carbon matrix.

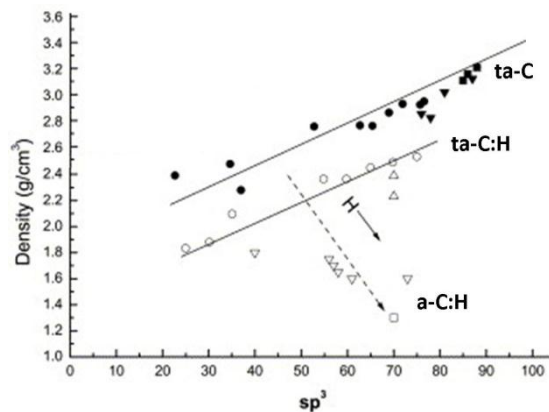


Figure 2.5. The density of a ta-C coating, a ta-C:H coating, and an a-C:H coating, as a function of sp^3 content [20].

2.2.2. Residual stresses

Residual stresses appear in DLC coatings as a consequence of the energetic deposition process [21]. These residual stresses cause delamination of DLC coatings, and limit the coating thickness to a few micrometres. Residual stress accumulates (see **Equation 2.1**) as a combination of **thermal stress**, due to differences between deposition temperature and operation temperature, and **intrinsic stress**, due to the changes in microstructure, or the growth of defects [22]. Additionally, **extrinsic stresses** may develop, perhaps due to permanent surface deformations, or microstructural change due to a surface reaction.

$$\sigma_{\text{Residual}} = \sigma_{\text{Intrinsic}} + \sigma_{\text{Thermal}} + \sigma_{\text{Extrinsic}} \quad (2.1)$$

Intrinsic stresses in a DLC coating may develop during the deposition process, due to the coating microstructure. When incident carbon ions have sufficient energy to penetrate the DLC coating surface, local regions of sp^3 bonded carbon develop. The carbon matrix in a DLC coating is stiff, and the formation of tetrahedrally bonded carbon imparts a local compressive stress. If the energy per incident ion is increased further, a subsurface transformation of the local bonding structure occurs resulting in decreased intrinsic stress [10]. Deposition techniques such as pulsed laser deposition aim to reduce intrinsic stress in this way [13].

Thermal stresses develop due to the difference in deposition temperature and the operation temperature of the DLC coating, the difference between the thermal expansion coefficients of the DLC coating and the substrate, and the elastic properties of the coating. The magnitude of thermal stress is given by **Equation 2.2** [21], where E_{DLC} and ν_{DLC} are the Young's modulus and Poisson's ratio of the DLC coating, ΔT is the change in temperature, and α_{DLC} and α_s are the thermal expansion coefficients of the DLC coating and the substrate, respectively.

$$\sigma_{\text{Thermal}} = \frac{E_{DLC}}{1 - \nu_{DLC}} (\alpha_s - \alpha_{DLC}) \Delta T \quad (2.2)$$

Minimising residual stress is important to prevent mechanical failure. The major component of stress within a DLC coating is intrinsic stress [21], so much effort has gone into optimising parameters in current deposition technologies to reduce intrinsic stress. Intrinsic stress is known to vary as a function of the bias voltage [23, 24], power density [25, 26], and gas precursor [23]. Additionally, by including metal or non-metal dopants into a DLC coating, the intrinsic stress may be reduced [27].

2.2.3. Multi-layer and gradient coatings

In order to minimise residual stress and deposit coatings with strong adhesion, changes may be made to the deposition process such as reducing the bias voltage, but this often sacrifices the desirable material properties of a DLC coating. An alternative solution is to look for methods by which the adhesion of a DLC coating to a substrate can be maximised without making modifications to the coating itself. Deposition of an adhesion layer between the DLC coating and the substrate has been shown to lower local changes in stress [28]. Deposition of a thin layer of a suitable element such as titanium (Ti) or silicon (Si) provides strong interfacial bonding by chemical reaction with the substrate material. The DLC coating is then deposited on top of the interlayer, providing enhanced adhesion [29]. Modern deposition techniques allow for the deposition of multi-layer and gradient coatings with strong adhesion to a range of substrates.

2.2.4. Doping and alloying

The composition of a DLC coating can be optimised in order to reduce intrinsic stress. Doping and alloying of DLC coatings is common practise either to improve a particular property of the coating to ensure its survival in a specific environment, or to achieve some extra functionality. In this manner, intrinsic stress can be reduced, and properties such as hardness, surface energy, and biocompatibility can be tailored to application [30, 31]. DLC coatings are typically doped with elements such as fluorine (F), silicon (Si), oxygen (O) or nitrogen (N). Common metal dopants include titanium (Ti), tungsten (W), and chromium (Cr).

For instance, doping of a-C:H coatings with Si has been shown to increase the mechanical hardness [27]. Residual stress was shown to decrease with the inclusion of silicon [27, 32]. Nitrogen doped DLC coatings are used for the protection of hard discs [33], and have been reported to lower internal stress [34] and increase thermal stability [35]. Metal doped coatings can decrease internal stresses and improve adhesion [30]. Reduction of internal stresses, and improved wear resistance, has been observed with the inclusion on Ti or Cr as a dopant [30].

Wang et al. [36] consider the effects of a Ti dopant, Ti interlayer, and Ti gradient layer on internal stress in DLC coatings. A Ti interlayer on a Si substrate causes an increase in residual stress, due to a mismatch between the coefficients of thermal expansion. A Ti interlayer on a steel substrate shows a decrease in residual stress. Doping with Ti caused a decrease in residual stress, through a reduction in the sp^3 content in the coating.

The surface of a hydrogenated DLC coating is typically passivated by hydrogen atoms, whereas non-hydrogenated coatings tend to chemisorb environmental gases such as water vapour. Therefore hydrogen content strongly affects the surface energy of a DLC coating [37]. Tagawa et al. [38] examined the surface energy of PECVD deposited coatings. The contact angle increased from 77° to 97° with increased hydrogen content from 0 % to 45 %. The surface energy of magnetron sputtered DLC coatings is very low - with a contact angle in the range $120 - 139^\circ$ varying based on the proportion of sp^3 bonding [39]. A linear decrease in surface energy was observed for a-C:H coatings doped with increasing amounts of Si or F [29]. This behaviour was related to the loss of sp^2 hybrids on the surface, since Si and F are unable to form double bonds. Inclusion of O or N increased the surface energy at a similar rate. Metal containing a-C coatings were deposited using FCVA to test the hydrophobicity of coatings. Nitrogen (N) decreased the contact angle, but inclusion of aluminium (Al) improved the hydrophobic character of the coating. Ali et al. [40] showed that surface energy decreased as Cr content increased in PECVD deposited coatings.

2.3. Conclusion

Diamond-Like Carbon (DLC) coatings are composed primarily of amorphously bonded carbon atoms. They can be deposited via a range of CVD and PVD processes, which lead to particular groupings based upon their mechanical properties. These groupings are known in the literature as **amorphous carbon** (a-C) coatings, **hydrogenated amorphous carbon** (a-C:H) coatings, **tetrahedral amorphous carbon** (ta-C) coatings, and **hydrogenated tetrahedral amorphous carbon** (ta-C:H) coatings.

It is clear from the literature review that the mechanical properties of a DLC coating depend strongly on the particular deposition process, and the resulting carbon bonding microstructure and hydrogen content, not to mention the addition of dopants and interlayers. The proportion of sp^3 hybridisations in the carbon matrix is controlled by the energy per incident ion. For ta-C and ta-C:H coatings, this correlates directly with high hardness, however for a-C and a-C:H coatings there exists a critical point where the hardness reaches a maximum before decreasing non-linearly. This is due to the termination of sp^3 bonds with hydrogen, resulting in a decrease in coating density. The hydrogen content can be varied by using different source gases, and has been shown to stabilise sp^3 bonding in a DLC coating, but generally causes a reduction in coating hardness.

Residual stresses develop within DLC coatings from the deposition process. Intrinsic stresses develop due to regions of compressively stressed tetrahedrally bonded carbon

atoms, but these can be relaxed using a high energy per carbon ion, or through doping of the coating with elements such as Ti, Cr, or Si. Thermal stresses develop due to differences between thermal expansion coefficients of the coating and substrate, but these can be relieved through deposition of a thin interlayer with an intermediate thermal expansion coefficient.

A lot is understood regarding the link between the deposition of DLC coatings and their mechanical properties. Modern coatings manufacturers are able to optimise deposition parameters such as the bias voltage to adjust the mechanical properties of a DLC coating as required. The commercial DLC coatings used in this thesis are presented in **Chapter 5**.

Chapter 3. Tribology of Diamond-Like Carbon Coatings

This chapter concerns the tribology of Diamond-Like Carbon coatings. It has been mentioned that Diamond-Like Carbon coatings are of interest to industry in a protective capability due to their advantageous mechanical properties. Additionally, they are of interest due to their excellent tribological properties which can provide a low coefficient of friction (less than 0.01) and low specific wear rate (less than 10^{-8} mm³/Nm) in a wide range of applications. These coatings display differing tribological behaviour depending on their chemical composition and mechanical properties. Additionally, the tribology of a DLC coating is strongly affected by the environment.

This chapter begins by reviewing the general theories of friction and wear and the key contributions to the tribology of a DLC coating. Next, the focus is placed on the tribology of DLC coatings in water; the development of a transfer layer is examined, as well as the interfacial chemistry of a DLC coating sliding against steel in water.

3.1. Friction

On an atomic scale, friction arises due to the electromagnetic forces between elementary particles [41]. From a thermodynamic viewpoint, friction is the energy dissipated due to irreversible processes of heat conduction, chemical reactions, and structural transformations (e.g. plastic deformations, surface fracture, or delamination) [42, 43]. Lastly, and most commonly, friction is understood on a macroscopic scale in terms of the force needed to overcome various adhesive and abrasive processes and initiate or continue motion.

3.1.1. Classical theories of friction

Da Vinci (1452 – 1519) postulated a relationship between the frictional force F needed to move a block over a flat surface, and the normal load N . He defined the friction coefficient μ as a ratio between the two (see **Equation 3.1**) [41].

$$\mu = \frac{F}{N} \quad (3.1)$$

Later, Amontons declared that the frictional force was not only proportional to the normal force, but that friction was independent of the apparent area of contact between surfaces. In 1699, Coulomb defined static friction as the force needed to overcome adhesive forces and initiate motion, and dynamic friction as the force needed to continue the motion. He suggested a third law, namely that dynamic friction and sliding velocity were independent. In many cases these laws have been shown to not hold.

Bowden and Tabor [44] showed that the coefficient of friction is related to the shear strength of the softest material in the contact. The tangential force required to break the asperity junctions is the product of the real area of contact A_r and the shear strength τ of the material. The contact pressure P is defined as the force per unit area.

$$\mu = \frac{F}{N} = \frac{A_r \tau}{N} = \frac{\tau}{P} \quad (3.2)$$

For soft metals, a low tangential force is required to overcome the adhesive forces at asperity contacts but there will be a large area of contact resulting in intermediary values of friction. For soft coatings on a hard substrate, there would be low shear strength and a small area of contact suggesting a low coefficient of friction. In a real contact, the situation is more complicated and several contributions to friction have to be considered. For instance friction might vary according to **Equation 3.3**, based on Bowden and Tabor's result.

$$F = A_r \tau + F_{Abr} \quad (3.3)$$

The first term is the adhesive friction, due to real contact between the surfaces. The second term is the abrasive component of friction. This will vary based on the extent of surface deformation or ploughing, which is related to the surface roughness.

3.1.2. Contributions to the friction of a DLC coating

The friction of a DLC coating depends on a number of intrinsic and extrinsic factors. The deposition method, chemical composition, and roughness, all strongly affect the coefficient of friction of a DLC coating. Additionally, the coefficient of friction is sensitive to the test environment, the counterface material, the interfacial chemistry, and the formation of a transfer layer. The formation of a transfer layer is discussed in detail in **Section 3.2.2**.

Fontaine et al. [45] considers friction of DLC coatings to be a combination of three main mechanisms:

- **Adhesion occurs due to interactions between surfaces; atomic bonding, Van der Waals forces, capillary forces, and electrostatic forces. Adhesive friction in a DLC coating is related to the chemical species at the interface.**
- **Abrasion concerns the degradation of a surface due to the wearing action of hard asperities or hard particles trapped in the wear track. This type of friction is due to mechanical actions, and varies based on the DLC coatings mechanical properties and surface roughness.**
- **A low shear strength layer of wear debris called a transfer layer provides DLC coatings with a low coefficient of friction [46-49]. The shearing component of friction accumulates from the energy required to cause plastic deformation to the transfer layer.**

An extensive number of reviews and publications on the tribology of DLC coatings are available in the literature [4, 28, 50-52]. The coefficient of friction can vary considerably for different types of DLC coating in different environments, and understanding of this has advanced considerably in recent years.

3.1.3. The effects of hydrogen

The sensitivity of the coefficient of friction to the test environment and to the chemical composition of the DLC coating can be illustrated by considering the effects of hydrogen on the coefficient of friction of DLC coatings in dry and humid air. **Table 3.1** outlines the approximate range for the coefficient of friction in varying relative humidity (RH), and in water, for a-C, a-C:H, and ta-C coatings.

Table 3.1. An approximate range for the coefficient of friction of different categorisations of DLC coating, in varying relative humidity, and in water.

Coefficient of Friction			
	< 5 % RH	5 – 100 % RH	Water
a-C	0.3 – 0.8 [5, 53]	0.1 – 0.2 [54]	0.07 – 0.1 [53]
a-C:H	0.003 – 0.3 [5, 54, 55]	0.02 – 0.5 [53, 54, 56]	0.01 – 0.7 [53]
ta-C	0.4 – 0.8 [54, 57]	0.08 – 0.12 [47, 53]	0.07 [57]

- **In dry air / vacuum, the coefficient of friction of non-hydrogenated coatings is often very large ($\mu > 0.3$) as a result of strong adhesive forces between opposing surfaces [5].**
- **In dry air / vacuum, the coefficient of friction of hydrogenated coatings is typically low, with $\mu < 0.003$ observed for highly hydrogenated a-C:H coatings deposited from methane gas at high ion energy [58].**
- **In humid air, for both hydrogenated and non-hydrogenated coatings, the coefficient of friction is typically in the range 0.02 – 0.2 due to the adsorption of environmental species to the surface which control adhesion [5].**
- **In water, the coefficient of friction of non-hydrogenated coatings is typically low ($0.07 < \mu < 0.1$) [59]. In water, the coefficient of friction of hydrogenated coatings varies widely ($0.01 < \mu < 0.7$) [53]. The tribology of DLC coatings in water is discussed in detail in Section 3.3.**

It has been mentioned in **Section 3.1.2** that adhesion is a main contributor to the coefficient of friction of DLC coatings. Specifically, Erdemir [5, 58] suggested that

adhesive bonding can occur between neighbouring carbon atoms, due to dangling sigma bonds on the DLC coating surface. The occurrence of such atomic bonding leads to large adhesive forces and therefore a large coefficient of friction. In the case of a hydrogenated DLC coating, hydrogen atoms are bonded covalently to many of the available carbon atoms. This reduces the number of available sigma bonds, leading to reduced adhesion. Reduced adhesion implies a lower coefficient of friction. For non-hydrogenated coatings, the passivation of a DLC coating surface by hydrogen cannot occur since there is no hydrogen present within the coating microstructure, and as a result a high coefficient of friction is observed in an inert environment.

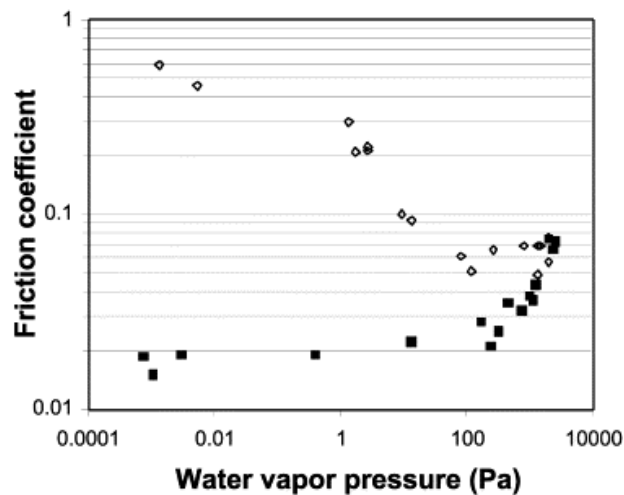


Figure 3.1. The effect of water vapour pressure on the coefficient of friction for hydrogenated (black squares) and non-hydrogenated (white diamonds) DLC coatings [60].

The surface of a DLC coating may adsorb environmental species such as water vapour. In high humidity, the adsorption of water vapour to the surface of a non-hydrogenated DLC coating results in a reduction in the coefficient of friction. This is due to the passivation of the sigma bonds on the DLC coating surface by the environmental species. However, for hydrogenated DLC coatings, an increased coefficient of friction is observed in a humid environment. This is due to the preferential adsorption of water to the DLC coating surface, displacing the hydrogen that is initially present. The coefficient of friction is controlled by the oxidative species adsorbed to the surface of the DLC coating, and not by the intrinsic properties of the DLC coating, and therefore the coefficient of friction of both hydrogenated and non-hydrogenated DLC coatings is similar in high humidity. The mechanism described above is illustrated in **Figure 3.1** where the effect of water vapour partial pressure on the coefficient of friction of hydrogenated and non-hydrogenated DLC coatings is shown [60]; the coefficient of friction of hydrogenated coatings increases from 0.015 to 0.06 as water vapour partial pressure increases, the coefficient of friction of non-hydrogenated coatings decreases from 0.7 to 0.06 as water vapour partial pressure increases.

To further investigate the tribology of hydrogenated DLC coatings, Fontaine et al. [45, 61] varied the partial pressure of hydrogen in a vacuum. At the beginning of the test, the coefficient of friction was shown to be initially very low ($\mu < 0.005$) regardless of the initial hydrogen partial pressure. As each test progressed, the hydrogen partial pressure was reduced to an ultra-high vacuum, and the initially low coefficient of friction increased to 0.3. The rate at which this increase in friction occurred was directly linked to the initial hydrogen partial pressure, and was due to the failure of the DLC coating to sustain a hydrogen passivated surface.

Erdemir [58] revealed a trend between the friction of DLC coatings and the source gas used during deposition (see **Figure 3.2**). DLC coatings which were deposited with a higher ratio of hydrogen atoms to carbon atoms showed a lower coefficient of friction than those deposited using a low ratio of hydrogen atoms to carbon atoms. This was due to a higher proportion of hydrogen terminated sigma bonds, minimising the number of adhesive interactions between opposing surfaces.

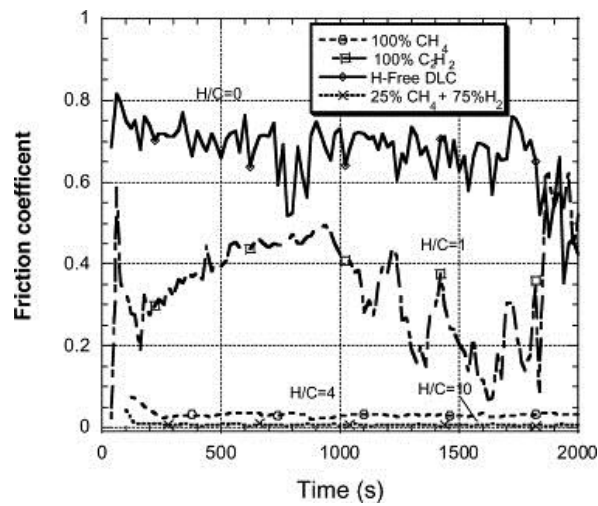


Figure 3.2. The effect of the hydrogen / carbon ratio during the deposition of a DLC coating on the coefficient of friction in dry nitrogen [58].

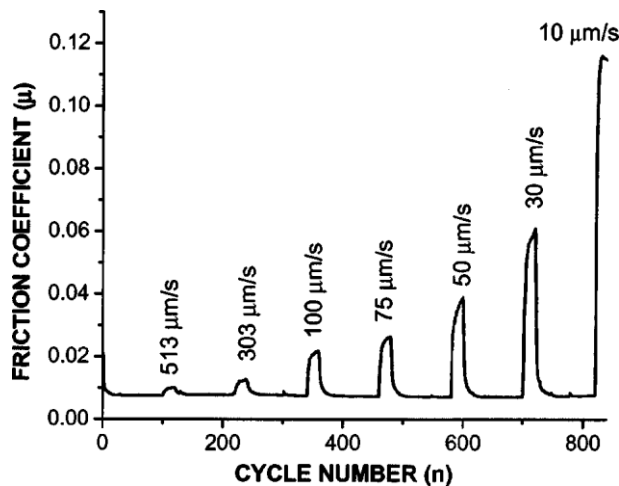


Figure 3.3. The effect of sliding speed on the coefficient of friction of hydrogenated DLC coatings [62].

Sliding velocity was shown to affect the coefficient of friction of a hydrogenated DLC coating [62]. The coefficient of friction was observed to increase non-linearly with sliding velocity (see Figure 3.3), and this was explained in terms of adhesive interactions on atomic level; for a small sliding velocity there was time for many atomic bonds to form between surfaces, causing a large frictional resistance, whereas for a large sliding velocity there was less time for atomic bonds to form, causing a reduction in the coefficient of friction.

3.1.4. The effects of doping and alloying

The tribological properties of a DLC coating are dependent on the bonding in the carbon matrix, the hydrogen content, and the inclusion of metal or non-metal dopants or interlayers. The tribology of Si, F, N, and metal containing DLC coatings have been reviewed previously [30, 63].

i. Silicon doped DLC coatings

The tribology of silicon (Si) doped a-C:H coatings against steel in ambient air was investigated by Oguri et al. [64]. Sliding wear tests identified a reduced coefficient of friction of 0.04 in comparison to a coefficient of friction of 0.12 for undoped coatings. Gilmore et al. [65] examined a range of commercial and in-house DLC coatings with varying Si content, and found a reduction in the coefficient of friction at high humidity against both steel and DLC coated counterfaces, however an increase in wear rate was also observed with increased Si content. Hioki et al. [66] deposited Si and O doped DLC coatings using ion beam assisted deposition, and showed a low coefficient of friction ranging between 0.04 – 0.07 against steel in ambient air. Donnet [63] stated that the environmental dependency of the tribology of a DLC coating is reduced with the addition of Si.

ii. Fluorine doped DLC coatings

Sanchez – Lopez and Fernandez [30] presented a review of the tribology of fluorine (F) doped DLC coatings. The inclusion of F in DLC coatings is thought to force carbon into a sp^3 hybridisation, reducing the number of dangling bonds, and decreasing the surface energy. Fluorine doped DLC coatings have also shown to have a reduced density [29]. DLC coatings containing both F and Si have been deposited by Miyamoto et al. [67] and showed good tribological properties along with strong adhesion to the substrate.

iii. Nitrogen doped DLC coatings

Nitrogen doped DLC coatings are commonly used in hard discs. Incorporation of N was seen to decrease the amount of sp^3 bonding in a DLC coating [63], which was related to an increase in surface energy [29]. The inclusion of N is complex, and there is a wide spread in reported coefficients of friction and wear for these coatings [30].

iv. Alloyed DLC coatings

A range of metals have been alloyed with DLC coatings, usually by magnetron sputtering in the presence of a hydrocarbon gas. The primary advantage of doping a DLC coating with metal is to decrease the internal stress of the coating, and therefore decrease the risk of coating delamination. Metals are deposited either as nanocrystalline droplets of pure metal, or as carbides within the carbon matrix.

Chromium doped a-C coatings (with high friction in a vacuum environment) showed a decreasing coefficient of friction with increasing humidity [68]. Dai et al. [69, 70] observed a decrease in residual stress with the inclusion of Al and Ti in DLC coatings, via a hybrid ion beam deposition method. Incorporation of Ti above a critical percentage (10 – 13 %) led to a carbide structure within the carbon matrix, and friction and wear increased as a result. Addition of Al showed a decrease in friction but an increase in wear rate (see **Figure 3.4**).

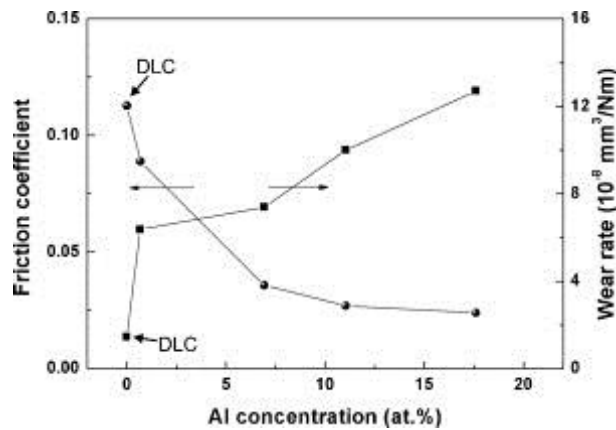


Figure 3.4. The coefficient of friction and specific wear rate of aluminium doped DLC coatings [70].

This section has outlined the basic mechanisms of friction, and the main contributions to the friction of a DLC coating. The effects of the coating microstructure and chemical composition of the DLC coating has been discussed in reference to the literature. In the next section, the general wear mechanisms of a DLC coating are examined, as well as the processes of graphitisation and transfer layer formation.

3.2. Wear

Wear is the removal of material due to the relative motion of surfaces. The phenomenon of wear is extremely complex since it concerns the deformation and failure of surfaces on a variety of length scales, and varies fundamentally based on material properties and chemical and structural changes. Wear is propagated by mechanical stresses, as well as by environmental conditions. The first part of this section examines some general wear mechanisms of coatings. Next, the known wear mechanisms of a DLC coating in terms of graphitisation and transfer layer formation are discussed in reference to the literature. Finally, the effects of temperature on the graphitisation process are examined.

3.2.1. General wear mechanisms

The two most important wear mechanisms in the context of DLC coatings are adhesive and abrasive wear.

- **Adhesive wear is loss of material that occurs as a result of adhesive forces. The graphitisation of a DLC coating is an example of an adhesive wear process.**
- **Abrasive wear occurs when a hard surface moves relative to a soft surface, causing removal of the soft material by plastic deformation. Two-body abrasion concerns the relative motion of two surfaces, whereas three-body abrasion concerns the interactions of hard particles in the contact region.**

Holmberg et al. [71] presented a generalised approach to understanding the mechanical wear mechanisms of coatings. They consider mechanical processes over a range of length scales, as well tribochemical effects and material transfer.

- **Macro-mechanical wear can be evaluated based upon the stress distribution in the contact, the generation and subsequent dynamics of wear debris, and elastic and plastic deformation.**
- **At a micro-mechanical level, the stress behaviour of asperity contacts, and the formation of wear debris are of importance.**
- **On a nano-mechanical scale, the interactions between colliding atoms and molecules govern the macroscopic properties.**

Aside from a purely mechanical consideration of the wear process, the effect of chemical reactions, as well as the formation of a third-body such as a transfer layer, must be considered [46-49].

3.2.2. Graphitisation and transfer layer formation

When a DLC coating moves relative to another surface, wear occurs to both surfaces at the contacting asperities. The process by which a DLC coating wears is graphitisation, and is a degradation of the amorphous structure of the carbon matrix to the sp^2 hybridisation (which is more energetically stable than the sp^3 hybridisation). Graphitisation occurs when the carbon matrix is mechanically broken by stresses exerted by a sliding motion, and is accelerated by high temperatures generated during sliding [53].

The graphitisation of a DLC coating has often been examined using Raman spectroscopy to understand changes to the bonding structure of the DLC coating before and after wear [47, 48, 56, 72]. Raman spectra of a DLC coating are characterised by two sharp peaks around 1570 cm^{-1} and 1350 cm^{-1} , called the G- and D-peak, respectively [73]. The G-peak arises in crystalline graphite from the in-plane stretching of sp^2 hybridised carbon and is present in all DLC coatings, whereas the D-peak arises from the breathing modes of sp^2 bonded carbon in a six fold aromatic ring and relates to disorder. The graphitisation of the DLC coating is shown by an increase in the intensity of the D-peak [53, 74].

A transfer layer develops through adhesive transfer of wear debris from a DLC coating onto a counterface. Transfer layers have been reported since the advent of DLC coatings [75] and have been linked to a low coefficient of friction [56].

Investigations into the tribology of DLC coatings show that the formation of a transfer layer is common [46, 47, 76-78]. Transfer layers have been shown to increase in thickness with increased sliding velocity and normal load [53], and can develop in ambient air as well as in a humid atmosphere [57], or in water [59]. The strength of adhesion of a transfer layer to a counterface depends on the counterface material as well as the test environment.

The formation of a transfer layer as a third body limits contact between opposing surfaces. As a result, the tribology of the surfaces is controlled by the properties of the transfer layer. The theory of Bowden and Tabor [44] states that the coefficient of friction is proportional to the shear strength of the transfer layer.

It has been discussed that the formation of a transfer layer is beneficial, but the conditions under which a transfer layer will develop are unknown. Scharf and Singer [48,

79-81] investigated the mechanisms by which transfer layers form for a range of commercial DLC coatings using *in situ* Raman spectroscopy and optical microscopy to demonstrate how the third body governs the tribology.

Scharf and Singer [48, 79-81] characterised the dynamic motion of a transfer layer in terms of the velocity accommodation mode (VAM):

- **Shearing and extrusion of loose debris** (see Figure 3.5 (a)); wear debris from a DLC coating may loosely shear between two surfaces. Some are lost from the contact region entirely. This may lead to further contact between surfaces increasing two-body wear.
- **Interfacial sliding** (see Figure 3.5 (b)); wear particles from a DLC coating may adhere to the counterface. This static transfer layer prevents two-body wear between surfaces and acts as a sacrificial layer which limits contact between surfaces.

In any contact, both processes are likely to occur simultaneously in local regions. The formation of a static transfer layer through interfacial sliding will depend on the local contact pressure and temperature distribution, as well as third-body chemistry.

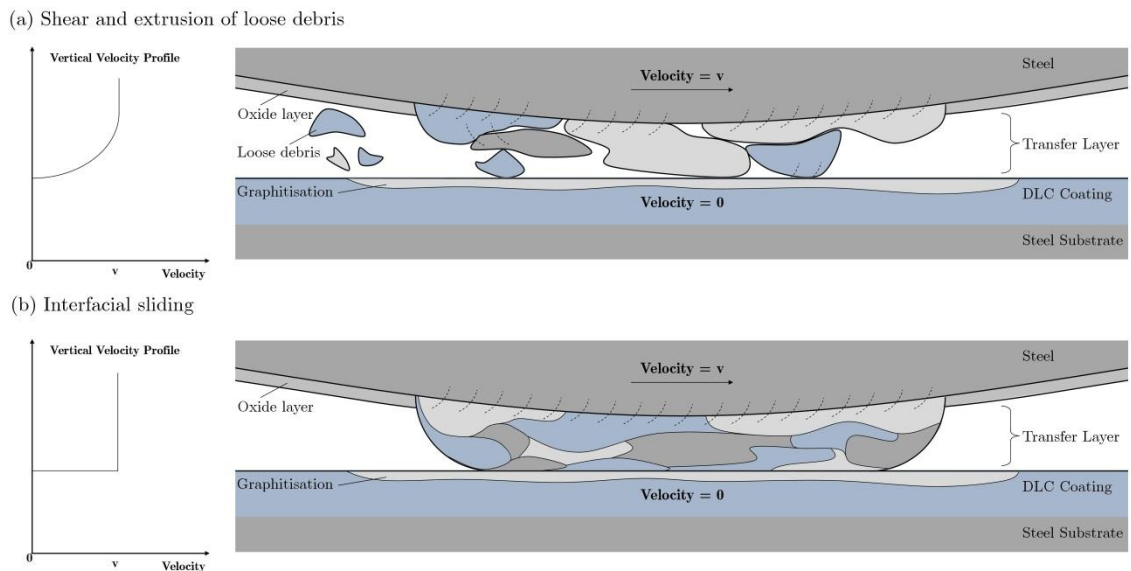


Figure 3.5. The velocity accommodation modes of a transfer layer; (a) shear and extrusion of loose debris, and (b) interfacial sliding.

The velocity profile through the transfer layer is shown on the left of **Figure 3.5** for each VAM. In each case the ball moves with velocity v and the DLC coating is static. In the case of interfacial sliding the transfer layer is perfectly adhered to the ball so a two-body motion occurs, and the velocity drops discontinuously at the transfer layer /

DLC coating interface. In **Figure 3.5 (a)**, detached particles shear between the steel ball and the DLC coating, so the velocity decreases gradually with depth from the ball to the DLC coating.

Scharf and Singer [48, 79-81] examined the VAM of a transfer layer during a reciprocating sliding test of a DLC coating against a sapphire ball in dry ($< 5\%$ RH) air. An initially high coefficient of friction of 0.25 dropped rapidly to 0.05 and remained constant for the next 300 cycles. The *in situ* optical images showed how a transfer layer developed and remained static on the ball surface. The VAM was interfacial sliding between surfaces. *In situ* Raman spectra showed a development of the intensity of the D-peak as the test continued, indicating graphitisation of the DLC coating. Later in the test, a spike in the coefficient of friction was observed, which was related (by optical microscopy) to a partial loss of the transfer layer. Subsequently, the transfer layer was regenerated, and interfacial sliding resumed.

In other work [80], Scharf and Singer showed the dependence of the VAM of a transfer layer on the relative humidity. In dry air, a a-C:H/W coating showed a high wear rate and interfacial sliding and shear and extrusion of debris were observed as VAMs. In ambient air, a thick transfer layer was observed and interfacial sliding and a lower wear rate was observed. This work demonstrated how the tribological behaviour of a DLC coating was controlled by the VAM of the third body. The formation of a transfer layer provided low and steady friction, while the magnitude of the steady state coefficient of friction was controlled by the environment.

The formation of a transfer layer was investigated by Sanchez-Lopez et al. [72], who examined hydrogenated and non-hydrogenated DLC coatings worn against steel balls in ambient air, dry air, and dry nitrogen environments. The lowest friction was observed for a hydrogenated DLC coating in dry nitrogen, where a transfer layer was observed on the ball surface (see **Figure 3.6 (a)**). Images of the transfer layers in ambient air and dry air environments are shown in **Figure 3.6 (b)** and **Figure 3.6 (c)**, respectively.

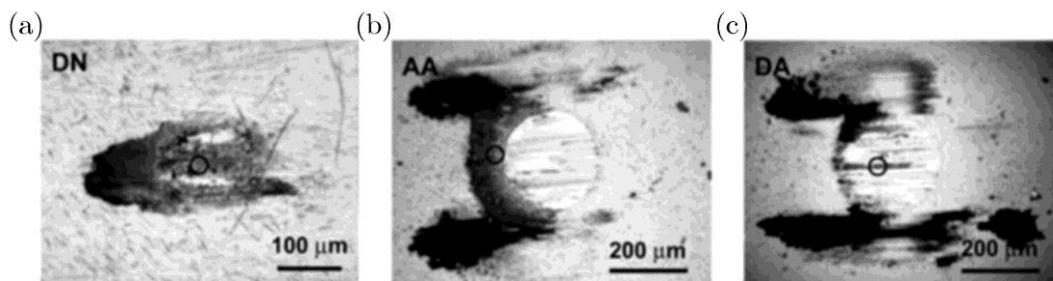


Figure 3.6. Images of transfer layers formed during reciprocating sliding of a-C:H coatings against steel in (a) dry nitrogen, (b) ambient air, and (c) dry air [72].

Raman spectra of the transfer layers shown in **Figure 3.6** suggested an increase in ordering and intensity of sp^2 bonded carbon (relating to increased graphitisation of the carbonaceous material) in dry nitrogen, where a low coefficient of friction and low wear was observed; suggesting that in dry nitrogen the dominant VAM was interfacial sliding.

Recently, the effect of surface roughness on the formation of a transfer layer was examined by Shaha et al. [82, 83]. Titanium carbide incorporated a-C coatings with a range of surface roughness were worn against 100Cr6 steel balls in humid air. The coefficient of friction increased with the surface roughness of the DLC coating. The formation of a transfer layer was retarded by the increased roughness of a DLC coating, due to abrasive ploughing which caused removal of the transferred material.

3.2.3. The effects of temperature

The hardness of a DLC coating is related to the sp^3 bonding hybridisation of carbon atoms in the coating. The sp^3 bonding hybridisation is metastable, and an increase in temperature promotes graphitisation, leading to a loss in hardness. The wear resistance of a DLC coating is therefore strongly dependent on the temperature.

The thermal stability of a-C:H coatings was investigated by Ito et al. [84] where DLC coatings were annealed at a range of temperatures up to 600 °C. DLC coatings annealed above 400 °C showed a lower mechanical hardness, which was due to the process of graphitisation (see **Figure 3.7**). Two otherwise identical DLC coatings with different hydrogen contents showed the same graphitisation temperature.

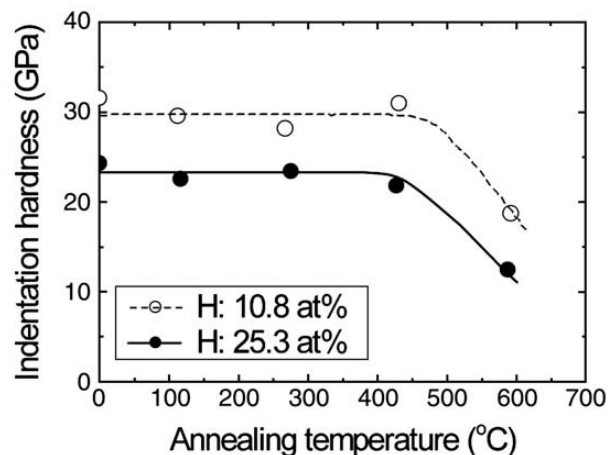


Figure 3.7. Indentation hardness of two hydrogenated DLC coatings after annealing at a range of temperatures [84].

Ronkainen et al. [53] showed that graphitisation occurred in the range 300 – 600 °C for a-C:H coatings, whereas ta-C:H coatings showed thermal stability above 700 °C. This is due to the dense microstructure of a ta-C coating. They estimated the temperature rise at the interface due to sliding to be in the range 100 – 300 °C, which was too low to

promote graphitisation [85, 86], and concluded that graphitisation of a DLC coating must be attenuated by local strains.

The high temperature tribology of three DLC coatings (a-C, a-C:H, and a-C:H/Ti) against steel was investigated by Krumpiegl et al. [87] who observed high wear rates leading to failure at 200 °C. Vanhulsel et al. [88] ran wear tests on an a-C:H coating after annealing the coatings at a range of temperatures up to 300 °C. The wear rate was larger for DLC coatings annealed at a higher temperature. The coefficient of friction decreased with increased annealing temperature, due to the formation of a thick transfer layer. Konca and co-workers [89] tested an a-C coating against aluminium alloy at a range of temperatures up to 300 °C (see **Figure 3.8**) and observed an increase in the coefficient of friction with increasing annealing temperature. A large wear rate was measured at 300 °C.

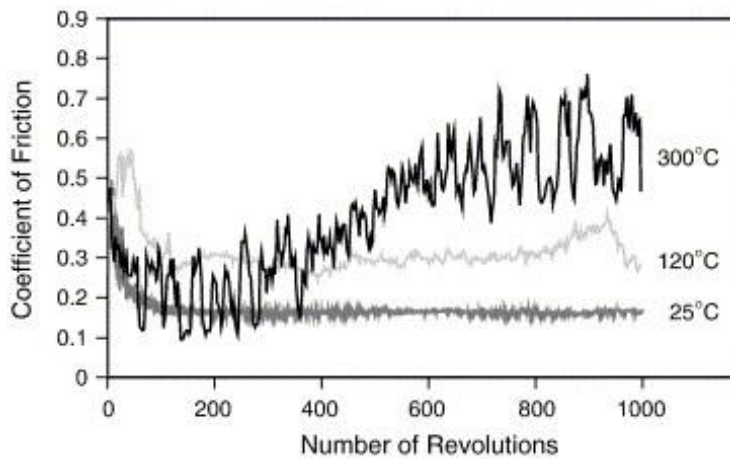


Figure 3.8. The coefficient of friction as a function of time at 25 °C, 120 °C, and 300 °C [89].

To further understand the graphitisation process of DLC coatings, a-C:H coatings with a Ti interlayer were annealed using thermo-gravimetric analysis (TGA) [90]. TGA spectra (see **Figure 3.9**) showed a weight loss due to the oxidation of carbon at 350 °C, followed by an increase in weight as the Ti interlayer oxidised at 450 °C. The hardness of the coating decreased significantly between 200 °C and 400 °C, and Raman spectra showed an increase in the intensity of the D-peak, which is associated with graphitisation.

It is clear that at high temperature, the specific wear rate of a DLC coating increases due to graphitisation of the DLC coating (which results in a loss of hardness). This critical temperature is dependent on the deposition method. The graphitisation process is directly related to the temperature, and is promoted by mechanical stresses. Differing behaviour is observed for the coefficient of friction at high temperature, and is thought to be related to the transfer layer formation and the counterface material.

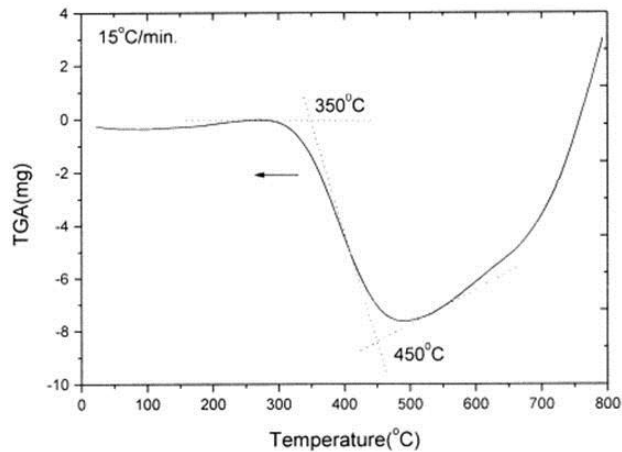


Figure 3.9. Thermo-gravimetric analysis (TGA) of a DLC coating as temperature increases at a rate of 15 °C per minute [90].

This section has focussed on the graphitisation of DLC coatings and the formation of a transfer layer. The velocity accommodation mode (VAM) of a transfer layer was shown to correlate to the tribological behaviour. Lastly, the effects of temperature on the tribology of DLC coatings are introduced. It is clear that the tribology of a DLC coating is sensitive to the test environment, so the focus moves inwards now to the tribology of a DLC coating in water.

3.3. Tribology in water

DLC coatings are known for their low friction and high wear resistance, yet the properties of a DLC coating are sensitive to the environment and counterface, and good tribological properties are not always realised. This section focuses on the tribology of DLC coatings in a water environment, and examines recent literature from experimental tests in an aqueous environment, and specifically the tribochemistry of a DLC coating when sliding against a steel counterface in water.

3.3.1. The effects of an oxidising environment

A non-hydrogenated DLC coating shows a high coefficient of friction in an inert environment due to the presence of sigma bonds on the DLC coating surface, which cause high adhesion. A hydrogenated DLC coating shows a very low coefficient of friction in an inert environment (such as dry air) due to the passivation of sigma bonds on the DLC coating surface by hydrogen atoms (see **Section 3.1.3**).

- **In water, for hydrogenated DLC coatings, the hydrogen passivation mechanism of Erdemir [5, 58] is replaced by the preferential adsorption of the most polar molecules onto the DLC surface [91], and as a consequence the tribology is**

controlled by the molecular species at the interface as opposed to the hydrogen content of the coating.

- In water, for non-hydrogenated DLC coatings, adsorption of oxidative species onto the unpassivated DLC coating surface provides a similar coefficient of friction to that of a hydrogenated coating [60].

The partial pressure of oxygen was not observed to affect the coefficient of friction of hydrogenated DLC coatings, however the partial pressure of water vapour caused the coefficient of friction to increase from 0.01 to above 0.1 [92]. Kim et al. [93] confirmed that the coefficient of friction of hydrogenated DLC coatings were most sensitive to water vapour, and insensitive to the presence of oxygen and nitrogen. This was explained in terms of adsorption of polar groups onto the surfaces of the DLC coating and wear debris. Transfer layers were analysed using optical microscopy and the thickness and homogeneity of a transfer layer was seen to decrease with an increase in water vapour partial pressure [92].

The coefficient of friction of an a-C:H/Cr coating sliding against ultra-high molecular weight polyethylene under water lubrication began at 0.3 and dropped slowly over several hundred metres of sliding to a steady state value of 0.1 [94]. Using EDX, two different transfer layers were observed; an initial layer composed of Fe, O, C, and Cr, which probably formed during the initial high friction sliding, and a 200 nanometre thick carbonaceous layer which was attributed to the low friction and low wear in the later stage of the test.

Jiang and co-workers [95] showed a decrease in the wear rate of a non-hydrogenated DLC coating with humidity (see **Figure 3.10**). Analysis of the wear debris using SEM revealed large wear debris in low RH, in contrast to very fine debris observed in water. Rabinowicz [96] proposed that the size of wear debris during sliding was proportional to the surface energy, therefore Jiang et al. [95] suggest that the adsorption of water to a DLC coating surface causes a reduction in surface energy [28].

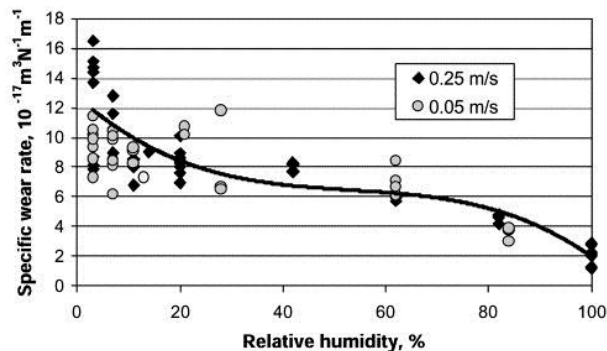


Figure 3.10. The effect of relative humidity and sliding speed on the specific wear rate of non-hydrogenated DLC coatings against tungsten carbide balls [95].

Ronkainen and Holmberg [59] investigated a range of commercial hydrogenated and non-hydrogenated DLC coatings in reciprocating sliding wear tests in water against alumina balls at a normal load of 5 N. **Table 3.2** shows a summary of their results. Non-hydrogenated vacuum arc coatings showed excellent wear resistance, which was suggested to be due to their high hardness. The use of Si as a dopant reduced the specific wear rate compared to an a-C:H coating with no dopant. The authors suggest that hydrogenated coatings are susceptible to a higher specific wear rate in water, but that this can be remedied with the use of dopants and/or multilayers.

Table 3.2. The mechanical properties and tribological results of 7 commercially produced DLC coatings in a water environment at room temperature [59].

Coating	Deposition Method	Hydrogen Content	Friction Coefficient	Wear Rate ($\times 10^{-6}$ mm ³ /Nm)	Transfer Layer
a-C:H	PECVD	25 – 40 %	0.05	Coating failed	Yes
a-C:H/Si	PECVD	\approx 30 %	0.06	0.2	No
a-C:H/W	Magnetron sputtering	\approx 10 %	0.08	0.3	Yes
a-C/Cr	Magnetron sputtering	\approx 0 %	0.12	2	Yes
a-C:H/Si	Ion beam	\approx 10 %	0.07	0.2	Yes
ta-C	Vacuum arc	\approx 0 %	0.03	Immeasurable	No
a-C	Vacuum arc	\approx 0 %	0.04	Immeasurable	No

Uchidate et al. [97] explored the tribology of a magnetron sputtered DLC coating against steel in distilled water. Using an autoclave they varied the dissolved oxygen concentration, pressure, temperature, and load, in order to understand the effects on the tribology. An experimental design methodology was used to decrease the number of tests required. The specific wear rate of the DLC coating (see **Figure 3.11 (a)**) was shown to increase dramatically with temperature but less so in deionised water. The wear to the steel ball (see **Figure 3.11 (b)**) was shown invariant to environmental changes although was generally higher in pure water. The coefficient of friction (see **Figure 3.11 (c)**) was higher in quasi-tap water in all tests, and was much larger at 80 °C. Analysis of ball by optical microscopy (see **Figure 3.12**) and Auger electron spectroscopy (AES) identified a relatively thick (500 nm) transfer layer formed at 20 °C. Chemical mapping showed the transfer layer consisted of mostly Fe, C and O. At high temperature this transfer layer was not present, and this can be linked to the high specific wear rate.

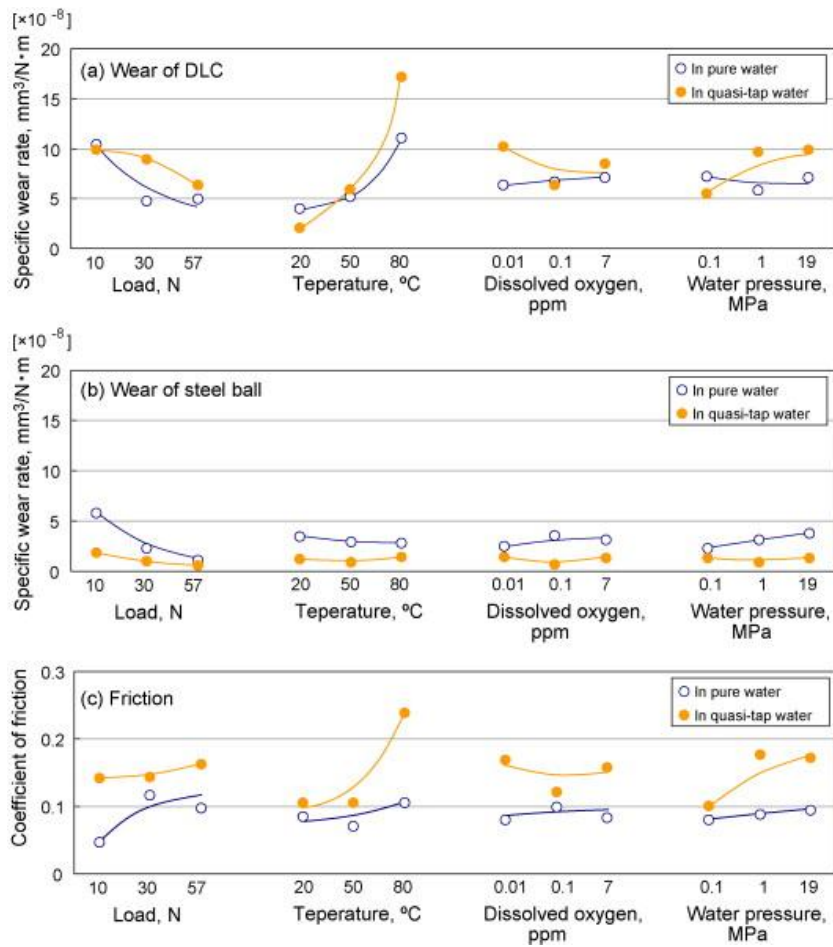


Figure 3.11. The effects of load, temperature, dissolved oxygen, and water pressure, on (top) the specific wear rate of a DLC coating, (middle) the specific wear rate of steel, and (bottom) the coefficient of friction, in the case of pure deionised water and quasi-tap water [97].

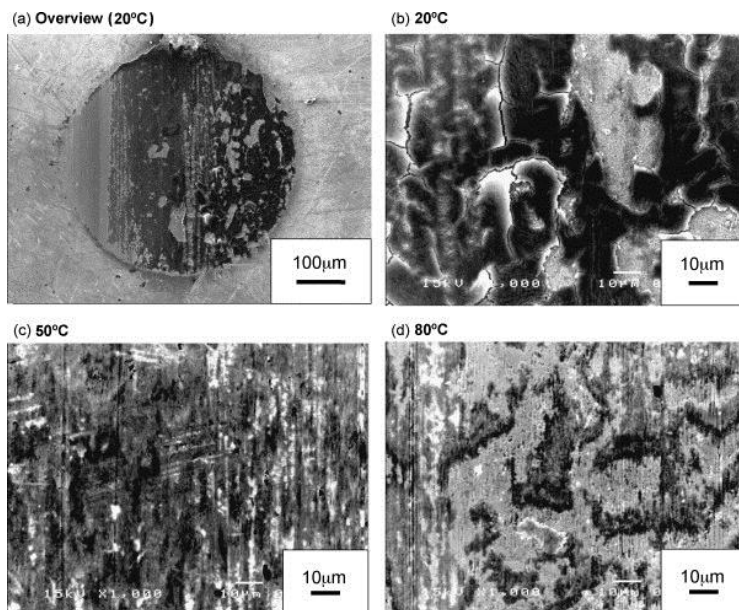


Figure 3.12. SEM images of transfer layers formed at (a-b) 20 °C, (c) 50 °C, and (d) 80 °C, in quasi-tap water at a 57 N normal load against stainless steel [97].

3.3.2. Tribochemistry of a DLC coating versus steel in water

The tribochemistry of a DLC coating sliding against a counterface will be dependent on the bonding structure of the DLC coating, the counterface material, and the environment in which the sliding occurs. The focus is placed on the tribochemistry of a DLC coating sliding against a steel counterface in water; an in-depth review of the tribochemistry in this environment is presented.

- **During the initial stages of sliding, surfaces are typically non-conformal, and a large contact pressure will cause high wear to both surfaces. Severe abrasive wear of steel is expected due to the high relative hardness of a DLC coating.**
- **Subsequently, a transfer layer will develop in the contact, composed of worn debris from steel and the DLC coating. The mechanical motion between surfaces will result in tribochemical reactions involving water. In the case of steel, this will result in the growth of an iron oxide layer.**

To investigate the tribology of a hydrogenated DLC coating against steel, Park et al. [98] ran sliding wear tests in dry and humid air. With increasing humidity, the coefficient of friction increased from 0.025 (at 0 % RH) to 0.2 (at 90 % RH). SEM images showed that the size and agglomeration of the wear debris increased with humidity (see **Figure 3.13 (a – c)**). AES spectra (see **Figure 3.13 (d)**) identified more Fe-rich debris at high humidity, suggesting that the high friction observed was a result of tribochemical reactions between the steel ball and the DLC coating.

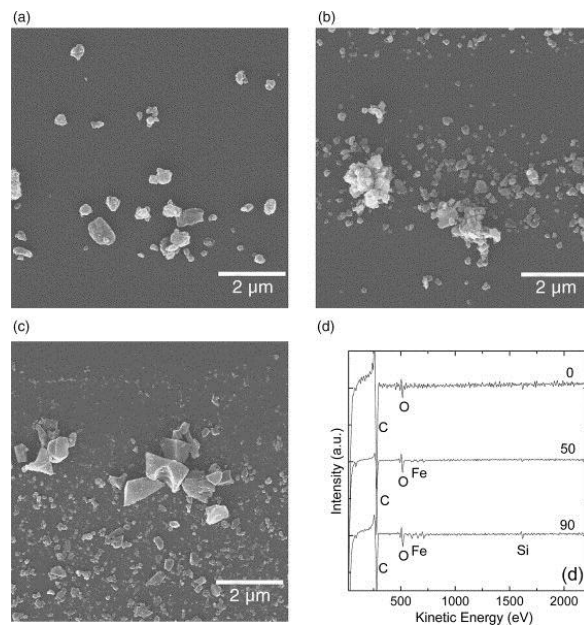


Figure 3.13. SEM images of wear scars for hydrogenated DLC coatings tested at (a) 0 %, (b) 50 %, and (c) 90 % relative humidity. An AES spectrum for each coating is shown in (d) [98].

Li et al. [99, 100] extended the work of Park et al. [98] to investigate the tribochemical reactions that occur between a hydrogenated DLC coating and steel in a humid environment. SEM images revealed that increased humidity inhibited the development of a transfer layer, resulting in high friction. The authors used x-ray photoelectron spectroscopy (XPS) (see **Figure 3.14**) to analyse the tribochemical reactions that occurred on the DLC coating wear scar at various relative humidity. At $< 5\%$ RH (see **Figure 3.14 (a)**), the XPS spectrum identified C – C, C – H, C – O, and C = O bonding, which was identical to the spectrum of the unworn coating. Oxygen on the DLC coating surface was absorbed from the atmosphere. At 40 % RH (**Figure 3.14 (b)**), O – C = O bonding was observed, relating to a carboxylic acid. At 100 % RH (see **Figure 3.14 (c)**), Fe – C bonding was observed, showing that tribochemical reactions had occurred directly between the DLC coating and steel counterface.

The following reaction mechanism was proposed [99, 100]; mechanical cracking of the DLC coating surface during sliding due to shear (breaking of C – C and C – H bonds), resulting in the production of macro-radicals which react with the local environment.

- **In a humid environment, frictional shear of the surface of a DLC coating will cause the carbon matrix to crack and react with water, resulting in the formation of C – O, C = O, and O – C = O functional groups.**
- **Against steel, frictional shear of the surface of a DLC coating will lead to cross-linking of Fe and C (resulting in high adhesion), and potential termination of Fe – C bonds on the surface of the DLC coating.**

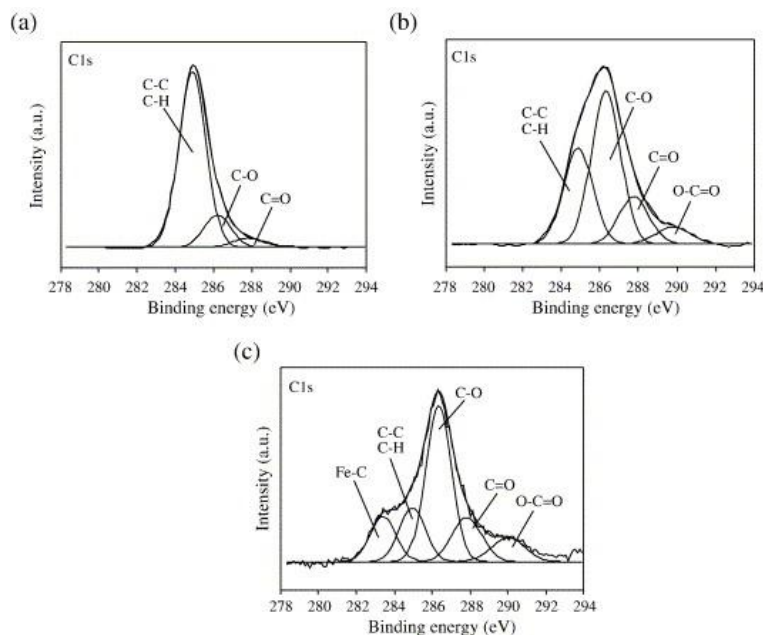
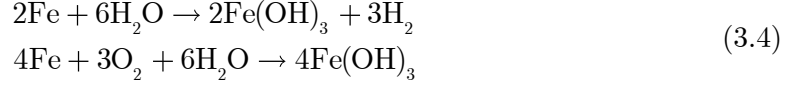
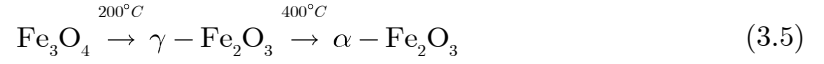


Figure 3.14. An XPS C1s spectra of the DLC coating wear scar after testing against steel in (a) $< 5\%$, (b) 40 %, and (c) 100 % humidity environments [99].

The root of adhesion in a DLC coating is the formation and breaking of atomic bonds. Against steel, the formation of Fe – C bonding between surfaces led to high friction [99]. Additionally, oxidation of steel in water will lead to formation of various iron oxides which may influence the tribology. Specifically, Li et al. [99] suggest possible chemical reactions between Fe, O₂, and H₂O, (see **Equation 3.4**) that will produce Fe(OH)₃, which may oxidise further to form Fe₂O₃, Fe₃O₄, and FeOOH.



Previous observations of Fe₃O₄ during the oxidation of steels in water has been linked to higher speeds and temperatures than hematite (α -Fe₂O₃) [101]. The transition of Fe₃O₄ to maghemite (γ -Fe₂O₃), and then to hematite, is well established under sufficiently high temperature or pressure, see **Equation 3.5** [102].



Fukui et al. [103] used Time-of-Flight Secondary Ion Mass Spectroscopy (ToF-SIMS) to further investigate the tribology of DLC coatings sliding against steel in humid air. During ToF-SIMS analysis, the compounds in a specimen are destroyed by primary ion irradiation so the results do not directly indicate the existence of some compound, rather the fragment pattern of secondary ions suggests the chemical composition and bonding structure of the bulk. Analysis of wear scars showed that debris was typically 50 – 400 nm in size. Transfer layers were very thin and inhomogeneous.

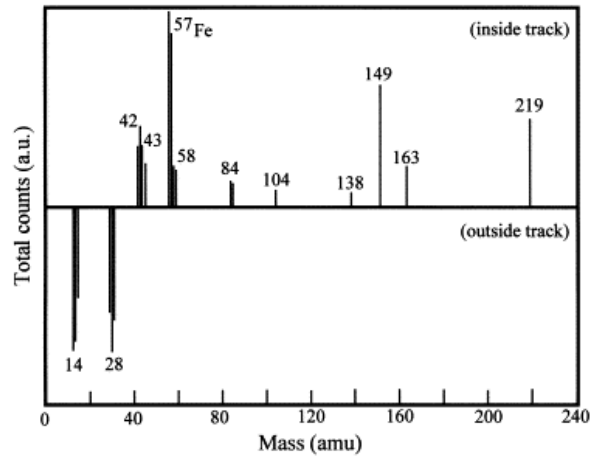


Figure 3.15. A comparison between ToF-SIMS spectra inside and outside the wear track for an a-C:H coating sliding against steel in humid air [103].

Figure 3.15 shows the ToF-SIMS spectra inside and outside the wear scar on the surface of the DLC coating. The presence of hydrocarbon macromolecules was detected

inside the wear track (suggested by the large atomic mass numbers) suggesting polymerisation occurs as the transfer layer forms, whereas outside the worn track the spectrum showed low order mass fragments. Of importance is the presence of Fe inside the wear track, which agrees with the oxidation mechanisms proposed by Li et al [99, 100].

Wu et al. [104] used a stable isotopic tracer (H_2^{18}O) to investigate the role of water in tribochemical reactions between a DLC coating and steel. ToF-SIMS spectra of the wear scar of the DLC coating were used to confirm that oxygen atoms chemically bonded to the carbon matrix of the DLC coating are the result of tribochemical reactions between water molecules and the DLC coating surface.

3.4. Conclusion

The friction of a DLC coating is dependent on a number of factors, both intrinsic to the coating in terms of carbon bonding microstructure and chemical composition, and extrinsic in terms of test environment, counterface, and interfacial chemistry. The hydrogen content of a DLC coating controls the frictional behaviour in an inert environment, where surface passivation by hydrogen atoms provides low friction. Non-hydrogenated coatings show a high coefficient of friction in an inert environment. In a humid environment, the tribology of a DLC coating is controlled by adsorption of polar species onto the surface – leading to similar values for the coefficient of friction regardless of the hydrogen content of the DLC coating.

A DLC coating wears through the process of graphitisation – a degradation of the carbon matrix to the sp^2 hybridisation. Adhesive transfer of wear debris from a DLC coating onto a counterface may lead to the growth of a transfer layer, a thin graphitic layer of material that promotes low wear and low friction. The effects of the environment, and mechanical parameters, on the evolution of this transfer layer were examined.

Velocity accommodation modes (VAMs) were used to describe the interfacial motion of a transfer layer, and were linked to the tribology observed in experimental tests. The VAM was either shearing and extrusion of debris (detached wear particles from a DLC coating may loosely shear between two surfaces), or interfacial sliding (wear particles from a DLC coating may adhere to the counterface preventing two body wear between surfaces and acting as a sacrificial layer). Interfacial sliding typically leads to a low coefficient of sliding and low specific wear rate.

At a high temperature (300 – 600 °C) the specific wear rate of a-C:H coatings increases due to graphitisation, which results in a loss of hardness. Tetrahedral amorphous

carbon coatings show a higher thermal stability due to a different carbon microstructure. The graphitisation process is directly related to the temperature, and is promoted by mechanical stresses.

In **Section 3.3**, the tribology of DLC coatings in water was examined. Ronkainen and Holmberg [59] tested a range of DLC coatings deposited via different methods against steel in water. The lowest specific wear rate observed was for a non-hydrogenated DLC coating deposited by pulsed vacuum arc discharge. Uchidate et al. [97] ran sliding wear tests on a magnetron sputtered DLC coating in water using an autoclave and varied the dissolved oxygen content and water pressure. The specific wear rate was observed to increase with temperature, but the dissolved oxygen content was not a significant parameter.

During sliding, a transfer layer often develops in the contact, composed of worn debris from steel and the DLC coating. Mechanical sliding between surfaces will result in tribochemical reactions involving water, and in the case of steel will lead to the growth of an iron oxide layer. In water, EDX spectroscopy showed the presence of Fe, O, Cr, and C in the transfer layer. XPS showed the formation of C – O, C = O, O – C = O, and Fe – C functional groups on the wear scar of the DLC coating [99]. Bonding between Fe and C was the reason for high adhesion when a transfer layer is not present. The tribology of a DLC coating is subtle, and depends on a number of factors. The literature suggests that the tribology is controlled by the environmental species present, and the VAM of the transfer layer. The experiments in **Chapter 6** are designed based on the findings of this literature review in this chapter.

Chapter 4. Modelling of Wear

In this chapter a focus is placed on the modelling of wear. To enhance understanding of the tribology of a DLC coating, models have been developed in the literature to better predict coating lifetime, explain complex interfacial phenomena, and decipher the mechanisms of wear. Whilst the focus of this work is on the lifetime prediction of a DLC coating, various approaches in the literature regarding the modelling of wear are explored.

The focus of the **Section 4.1** is contact modelling of DLC coatings using finite element analysis (FEA). FEA may be applied to understand failure mechanisms in DLC coatings such as surface cracking or delamination. Next, Archard's equation for wear volume is presented, and following this the frictional dissipation of energy and its relationship to wear volume is discussed. Last, and most important, is the development of incremental wear models, and the lifetime prediction of a DLC coating.

4.1. Contact modelling

Finite element analysis (FEA) is a useful tool to understand and predict mechanisms of failure for advanced surface coatings. Stress analyses are essential in the prediction of a coatings performance in terms of delamination or surface fracture. Holmberg et al. [105-107] simulated the stress field in a coated surface resulting from a sliding sphere and compared this to the experimental results from a scratch test of a diamond ball on a TiN coating [105]. The thin TiN coating was modelled as linearly elastic, and the substrate as elastic-plastic with strain hardening. The ball was assumed to be rigid.

Figure 4.1 shows a schematic of the deformations of the surface. The stresses in a TiN coating were assumed to be a combination of four mechanisms:

- **Frictional force (causing compressive stress at the front of the tip, and tensile stresses due to the pulling force behind the tip).**
- **Elastic and plastic deformation (sliding leaves a trail of plastically deformed material, and material pile-up in front of the tip).**
- **Bulk plasticity (identified by maximum and minimum tensile stresses).**
- **Residual stress (a result of the deposition process of the TiN coating).**

The first principal stresses of the coating are shown in **Figure 4.2** for (a) a normal load of 5 N prior to sliding, (b) a normal load of 5.3 N and 0.06 mm displacement, (c) a normal load of 10 N and 1.2 mm displacement, and (d) a normal load of 20 N and 3.3 mm displacement. In **Figure 4.2 (a)**, a compressive stress (shown in blue) is evident directly beneath the contact region. A tetra-armed tensile stress is present around the contact [108]. As sliding distance and normal load were increased, a tensile residual stress developed as a result of plastic deformation. **Figure 4.2 (c)** demonstrates two areas of residual stress; one on the plane of symmetry and the other off the plane of symmetry and closer to the contact (where surface analysis showed cracks developed).

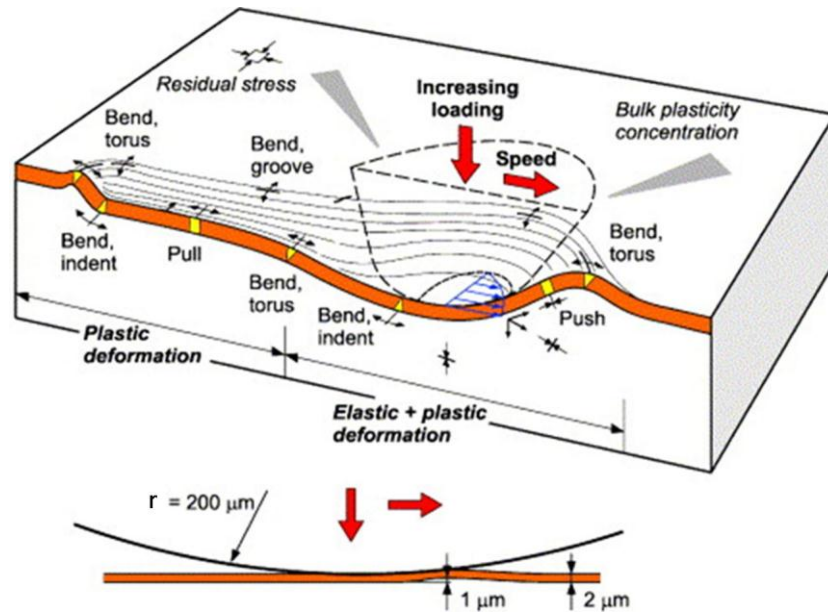


Figure 4.1. The stress field in a coated surface resulting from a sliding sphere [105].

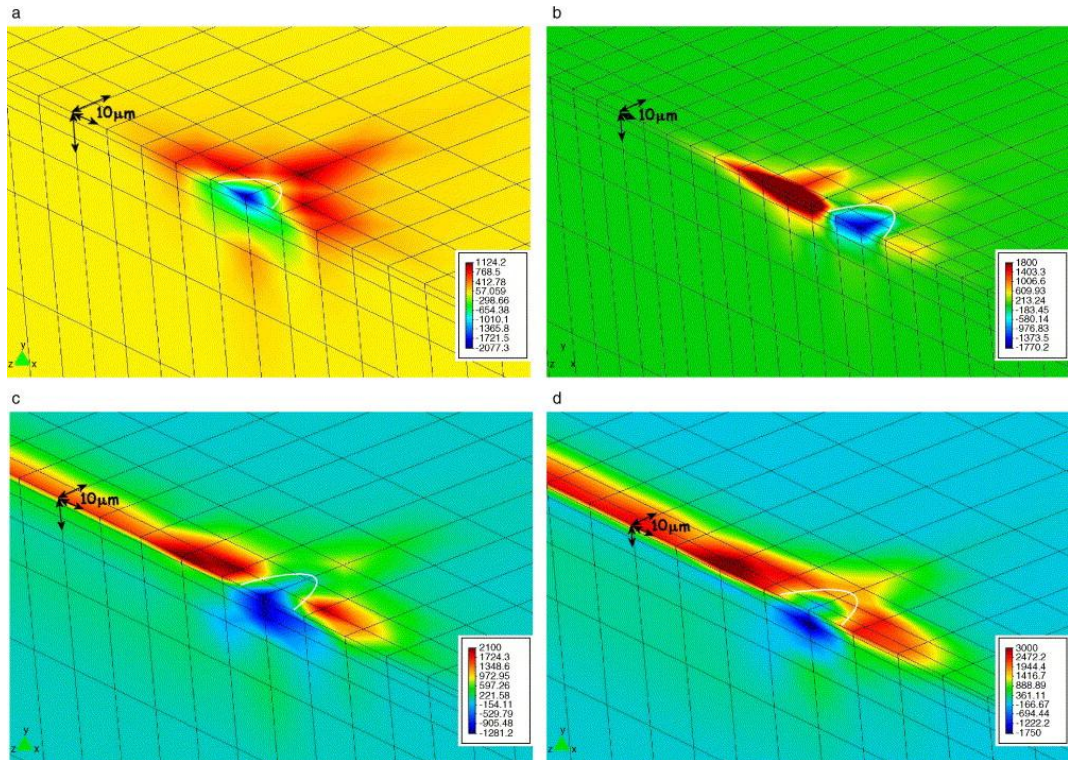


Figure 4.2. First principal stresses on the coating at the plane of symmetry are shown for (a) 5 N pre-load, (b) 5.3 N load and 0.06 mm displacement, (c) 10 N load and 1.2 mm displacement, and (d) 20 N load and 3.3 mm displacement [105].

In a second paper, Holmberg et al. [106] extend their analysis to consider the effects of coating thickness and material parameters on the stress distribution. Results showed that a thinner coating caused little change to the amount of plastic deformation but that it caused a decrease in the magnitude of the tensile stress. Varying the Young's modulus showed that a stiffer coating was less likely to suffer surface cracking that a

flexible coating – suggesting that more attention should be paid to optimising the elastic properties of a coating, as opposed to changing coating thickness, in order to increase wear resistance. The third part of Holmberg et al. [107] considered the effects of residual stress on the crack formation of a TiN coating. A residual compressive stress in the TiN coating was shown to increase the maximum tensile stress by 10 – 50 %. At the same time, compressive stresses under the tip were increased.

The formation of a transfer layer in a finite element was modelled by Fan and Diao [109] for the pin-on-disc contact of sputtered a-C coatings against a steel ball. Based on experimental results, the contact stresses were evaluated in a two-dimensional (2D) quasistatic model for three states: (I) an unworn ball, (II) a worn ball as the transfer layer developed, and (III) steady-state sliding with a transfer layer. The normal stress in the sliding direction for each state is shown in **Figure 4.3**. Each normal stress distribution is comprised of a tensile region behind the contact and a compressive stress beneath the contact, in agreement with Holmberg et al [107]. The magnitude of the tensile stress was greatest in state (I), and was reduced by 70 % in state (III) due to the increased contact area. The maximum shear stress also decreased dramatically from state (I) to state (III) due to a lower coefficient of friction when a transfer layer was present [109].

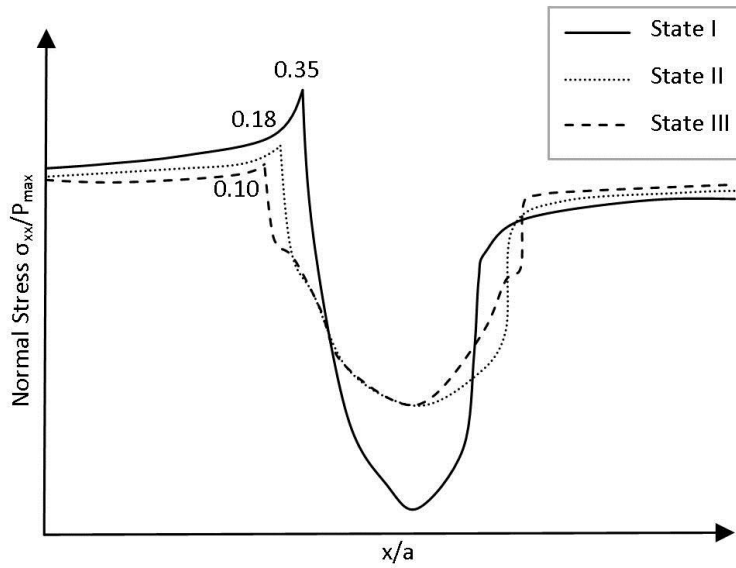


Figure 4.3. Normal stress distributions between a flat DLC coating and a steel ball, for states (I), (II), and (III). Image is redrawn based on the original work of Fan and Diao [109].

4.2. Archard's wear law

Archard [110, 111] presented a method for the estimation of wear volume in any particular tribological situation, for both adhesive and abrasive contacts. Assuming that wear occurs in hemispherical volumes at each asperity contact, that the contact pressure at an asperity contact equals the yield pressure of the softer material, and that the area of contact is constant, Archard derived the following expression for wear volume w_v as a function of the total sliding distance d , normal load N , material hardness of the softer material H , and dimensionless wear coefficient K .

$$w_v = K \frac{Nd}{H} \quad (4.1)$$

The dimensionless wear coefficient is related to the average probability of asperity wear occurring, and is used to measure the severity of the wear regime. More commonly used is the specific wear rate k (see **Equation 4.2**), which relates the wear coefficient to the hardness of the material. In the case of mild wear, the specific wear rate is usually given over the range $10^{-8} - 10^{-4} \text{mm}^3/\text{Nm}$.

$$k = \frac{K}{H} \quad (4.2)$$

Archard's wear law [110, 111] predicts linearity between the volume of wear and the product of load and sliding distance, but for many materials this has been shown not to be the case. For example, transitions between wear mechanisms or changes in surface chemistry may affect the evolution of wear volume with respect to time.

In the case of DLC coatings, a transfer layer composed of wear debris from the DLC coating is often known to adhere to the counterface material, which limits contact between the DLC coating and the counterface, thus lowering the specific wear rate as the contact ensues [3].

Prior to Archard's estimation of wear volume in a tribological contact, Preston [112] suggested that the rate of change of wear depth should vary proportionally to the contact pressure P and the sliding velocity v . In **Equation 4.3**, w_D denotes the wear depth of either surface, and k denotes the specific wear rate.

$$\frac{dw_D}{dt} = kPv \quad (4.3)$$

The models of Archard and Preston cannot be directly compared unless a relationship between wear depth and wear volume is known. In particular, if the area of contact between the surfaces remains constant throughout the test, then the two formulations can be expressed in a comparable rate form. Of course, in many real life applications and in many common test geometries such as a ball-on-flat contact, the area of contact cannot be assumed constant, and this has an effect on the prediction of the wear volume of both surfaces.

4.3. Frictional energy dissipation

The frictional energy produced between two surfaces is given as the product of the frictional force and the sliding distance. In 1965, Matveesky [113] related the flow of frictional energy in a system to wear volume via the concept of frictional power intensity q_{fr} . The frictional power intensity (**Equation 4.4**) is the rate at which frictional energy flows into a contact per unit area A .

$$q_{fr} = \frac{\mu N v}{A} \quad (4.4)$$

Later, Plint [114] modified the concept to include the estimated time of contact t_c for the surfaces. A factor of 1/2 was introduced to account for an equal flow of energy into each contacting surface. The energy pulse criterion was used in relation to the wear of gear teeth, and is defined in **Equation 4.5**.

$$q_{pulse} = \frac{\mu N v}{2A} t_c \quad (4.5)$$

The wear volume of hard coatings during fretting was shown by Fouvry et al. [115] to be linearly proportional to the cumulative energy dissipated. The total frictional energy was evaluated by summing the area inside the force – displacement curve during each cycle (see **Equation 4.6**).

$$E_d = \sum_t Fd \quad (4.6)$$

Later, Huq and Celis [116] show the validity of the method for the wear of unidirectional and bidirectional ball-on-flat tests. For varying relative humidity, they measure the volumetric wear of TiN coatings against alumina balls. They observed that the wear volume was linear with time, in agreement with Archard's law, and reduced with an increase in relative humidity.

A plot of wear volume against dissipated energy (see Figure 4.4) showed that the wear volume (which varied with RH) could be predicted using only the dissipated energy, independent of the RH of the room or the length of the test.

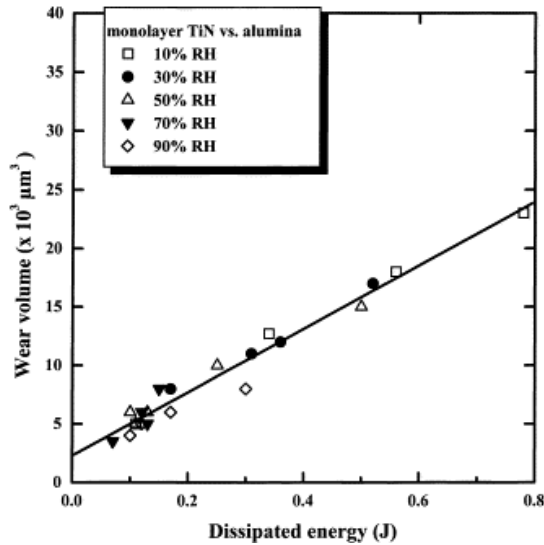


Figure 4.4. Wear volume versus dissipated energy for a TiN coating under fretting conditions [116].

Conservation of energy tells us that the flow of energy into the system through friction must equal the flow of energy out of the system. Energy leaves the system through the production of wear debris, but also leaves via structural and chemical changes, as well as by the dissipation of heat. The assumption that the wear rate is proportional to the frictional energy that flows into the system requires that the effects of chemical and structural changes, and heat dissipation, remain approximately constant during the duration of the test. Although this may be approximately true in a steady-state situation, it is generally an oversimplification.

From a thermodynamic viewpoint the wear of two surfaces is a non-equilibrium process due to the transfer of heat and mass across the boundaries of the system. The process of wear is irreversible, and so in order to quantify the characteristics of the system it is useful to consider the concept of entropy. Entropy quantifies the amount of disorder in a system. It is a thermodynamic quantity which is conserved in any system at equilibrium, but increases monotonically within an irreversible system. Entropy has been used to predict the direction and speed of a chemical reaction, the flow of heat in a system, and the efficiency of an engine. The process of wear is irreversible, and therefore acts to increase the entropy of the system.

Pioneering research into entropic theories of friction and wear were suggested by Klamecki [117-120] and Zmitrowicz [121-123] in the 1980s. These theories are complex and recently a more empirical route has been taken to measure wear. Doelling et al. [124] demonstrated that wear of machinery components can be correlated with the flow

of entropy. Using a calorimeter, the flow of heat into the system dQ and the surface temperature T were measured, and the entropy production S was calculated (see **Equation 4.7**).

$$S = \int \frac{dQ}{T} dt \quad (4.7)$$

If wear volume w_v is a function of the flow of entropy, then using Archard's equation it follows that the wear rate is linearly proportional to the rate of entropy production (see **Equation 4.8**).

$$\frac{dw_v}{dt} = \frac{kT}{\mu} \frac{dS}{dt} \quad (4.8)$$

As a result of this, wear volume can be plotted against the entropy flow that is measured (see **Figure 4.5**). The figure is normalised by scaling each axis to have a maximum value of one.

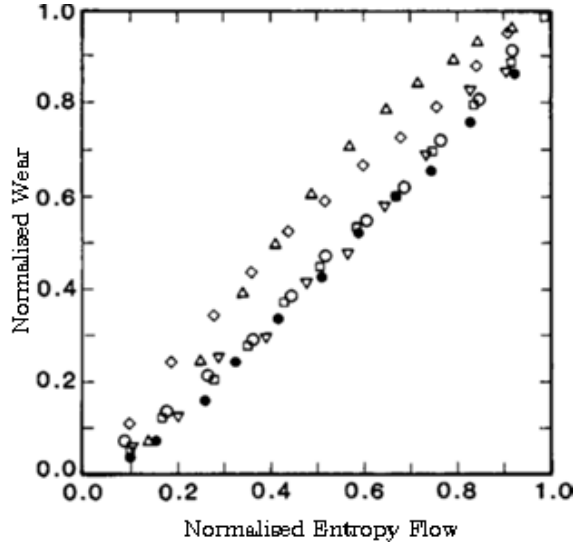


Figure 4.5. Normalised wear rate versus normalised entropy flow due to the diffusion of heat [124].

A more generalised formulation of the entropy production is presented by Bryant [42, 125] in terms of the degradation – entropy theorem. The theorem aims to establish a suitable framework for the wear, or degradation, of a tribological system as the sum of any number of degradation mechanisms. Irreversible thermodynamic systems may be expressed in terms of generalised forces X_i^j and generalised flows J_i^j [126]. Each force drives a flow, and in turn each flow may depend on numerous forces. Bryant's theorem states that for N_B dissipative degradation processes, such as the dissipation of heat or the plastic deformation of a solid, defined as $p_i = p_i(\zeta_i^1, \zeta_i^2, \dots, \zeta_i^{M_i})$ and each dependent on M_i phenomenological coordinates ζ_i^j , the degradation measure $w_i(p_1, p_2, \dots, p_{N_B})$ of each

irreversible process can be defined in terms a linear combination of the components of entropy production in the system. In **Equation 4.9**, β_i denotes the degradation coefficients which are defined at a later point.

$$\frac{dw_i}{dt} = \sum_{j=1}^{N_B} \beta_i \frac{d}{dt} S_i(p_i(\varsigma_i^j)) \quad (4.9)$$

The entropy that is produced as a result of each irreversible process depends on thermodynamics flows and forces [127] and is defined within the formulation of irreversible thermodynamics [126] by **Equation 4.10**.

$$\frac{dS_i}{dt} = \sum_{j=1}^{M_i} X_i^j J_i^j \quad (4.10)$$

Degradation mechanisms are defined as processes that degrade the functionality of a material. The rate of each degradation process is given in terms of thermodynamic degradation forces Y_i^j by **Equation 4.11**.

$$\frac{dw_i}{dt} = \sum_{j=1}^{M_i} Y_i^j J_i^j \quad (4.11)$$

The degradation coefficients β_i are defined in **Equation 4.12**, and measure the rate at which entropy is generated for each individual process.

$$\beta_i = \left(\frac{dw_i}{dS} \right)_{p_i} = \frac{Y_i^j}{X_i^j} \quad (4.12)$$

The above theory of Bryant [42, 125] presents a rigid approach to the prediction of wear as a function of irreversible processes. As an example, the energy dissipated due to friction might be assumed to be the only irreversible process that occurs. If the degradation measure is wear volume w_V , then the wear rate is given as follows.

$$\frac{dw_V}{dt} = \beta \frac{dS}{dt} = \beta \left(\frac{1}{T} \frac{dQ}{dt} \right) = \beta \left(\frac{\mu N v}{T} \right) \quad (4.13)$$

The thermodynamic flow is equal to the sliding velocity, and the thermodynamic force is equal to $\mu N / T$. The degradation coefficient can be related to the specific wear coefficient of Archard, using **Equations 4.1 – 4.2** and **Equation 4.13** as follows.

$$\beta = \frac{kT}{\mu} \quad (4.14)$$

4.4. Incremental wear models

Whilst Archard's wear law [110, 111] is a well-known model for the prediction of wear volume, the design engineer is interested in changes in tolerance, related directly to wear depth, which vary as a function of component geometry. Archard's wear law does not account for an increasing contact area, and therefore a more advanced approach for the prediction of wear of a general geometry is required.

An increasingly common methodology for the prediction of wear is the incremental wear model.

- **The model invokes an iterative procedure where the pressure distribution between contacting surfaces is evaluated in some manner, and used to calculate the wear depth at discrete points on the surface according to Preston's wear law (see Equation 4.3).**
- **The geometry of each surface is updated, from which a new contact pressure distribution may be evaluated.**
- **A finite difference discretisation is used to integrate forward in time and evaluate wear.**

The contact pressure distribution is most commonly evaluated using a finite element model [128-133], although other models exist such as the boundary element model [134, 135], Winkler model [136, 137], or Hertzian contact model [138]. Here focus is placed on the computational prediction of wear using finite element analyses.

The first incremental wear model using a finite element analysis to evaluate the pressure distribution was provided by Johansson [128] in the context of fretting wear, and followed up by Podra and Andersson [129] who presented a simulation of sliding wear. Both papers noted the presence of numerical error – specifically, artificial spikes in the pressure distribution. A limitation on the maximum wear depth in any one time-step was imposed to reduce the magnitude of the numerical error. The size of the time step is directly proportional to the wear depth, and thus it was noted that too large a time step may cause numerical instabilities. Of course, too short a time-step leads to computational inefficiency. Oqvist [130] increased the size of the time-step in the early stages of wear to decrease the solution time and noted that the error in the scheme was below 10 % when compared to a numerically stable integration.

Hegadekatte et al. [132] describe these numerical instabilities in terms of the dispersive components of the integrated pressure distribution. Mukras et al. [133] comment that

dispersive numerical errors grow from sharp boundaries at the edge of the contact region. The reason for this is that most numerical integration schemes, such as the widely used forward Euler method, are derived from a truncation of the Taylor series where continuity is a requirement. Discretisation of the geometry as a coarse mesh may break this criterion, and lead to the generation of numerical error.

To reduce the solution time an extrapolation technique may be used where the same finite element solution is used for several iterations to calculate wear. This approximation saves a lot of computation, but leads to the amplification of any discontinuity on the contact region. An optimisation technique is suggested by Mukras et al. [133] to iteratively vary the magnitude of the extrapolation, to optimise the speed of the integration whilst minimising numerical error. Mukras et al. [133] also suggest the use of parallel computation such that different processors solve identical finite element models at the same time, for a range of parameter values which represent different stages of the oscillatory motion.

4.5. Lifetime prediction of DLC coatings

Wear models for the prediction of the lifetime of a DLC coating are required in order to provide confidence in the material solution in the long term. This section presents two recent wear models which assess the wear behaviour of DLC coatings. These papers provide a basis for the modelling of DLC coatings against steel in distilled water in **Chapter 9**.

Steiner et al. [139] modelled the wear behaviour of DLC coatings using dissipated energy, and attempted to include effects of (I) surface roughness, (II) oxidation, and (III) graphitisation.

Ball-on-flat testing of various DLC coatings against a 100Cr6 ball in ambient air showed an initially severe wear regime, followed by a mild wear regime. The wear volume was demonstrated to be dependent on the normal load, but invariant to changes in sliding velocity.

(I) Surface roughness

The authors observed that severe plastic deformation of the ball occurs in the first few sliding cycles, as a result of the high contact pressure and abrasive nature of the DLC coating. Using half-space theory and considering the surface roughness of the DLC coating surface, the contact pressure was evaluated (see **Figure 4.6**). The results were compared to a Hertzian analysis.

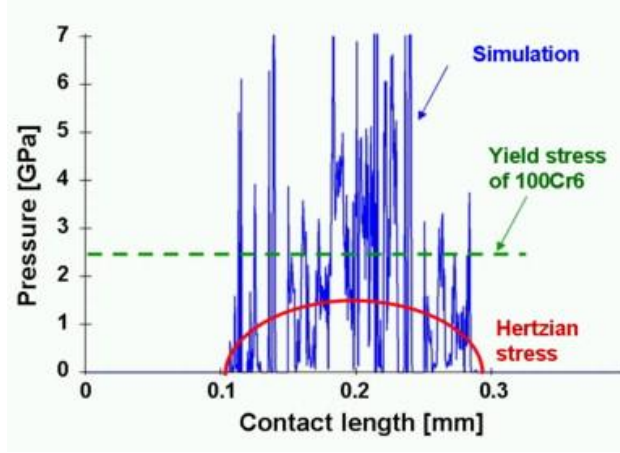


Figure 4.6. A contact simulation of a DLC coating ($R_a = 1.2 \mu\text{m}$) against a steel ball, compared to the Hertzian estimation of contact pressure [139].

(II) Oxidation

An oxide layer was observed on the ball surface; approximately 500 nm deep, and composed mainly of Fe_2O_3 . The growth of an oxide layer on steel was investigated by Quinn [140]. Assuming that oxidation occurs at asperity contacts, Steiner et al. [139] suggested that frictional heating would cause the growth of an oxide layer up to some critical thickness – at which point the oxide layer would be mechanically lost. Lim and Ashby [141] investigated the formation of an oxide layer on steel when frictional heating was not significant. The thickness of an oxide layer h_{ox} was estimated by **Equation 4.15** (assuming parabolic oxidation kinetics).

$$\frac{dh_{ox}}{dt} = \frac{2M_{Fe}}{3\rho_{Fe}M_{O_2}} \frac{1}{v} \sqrt{\frac{k_p}{t_{ox}}} \quad (4.15)$$

In **Equation 4.15**, M_{Fe} and ρ_{Fe} are the mass and density of iron, M_{O_2} is the mass of oxygen, v is the sliding velocity, k_p is the parabolic oxidation rate, and t_{ox} is the total time for oxidation to occur. The value of k_p was calculated by the following Arrhenius expression.

$$k_p = A_0 e^{-E_a/RT} \quad (4.16)$$

The Arrhenius equation predicts the rate at which a chemical reaction will occur. In **Equation 4.16**, A_0 is the Arrhenius constant, E_a is the activation energy of the oxidation process, R is Avogadro's gas constant, and T is the temperature.

(III) Graphitisation

The graphitisation of the DLC coating is modelled as a phase transformation from sp^3 to sp^2 bonded carbon according to the Clapeyron law. Le Huu et al. [142] used the

transition phase energy of diamond, L , in order to predict a phase transformation at $127 - 167$ °C, according to **Equation 4.17**.

$$T = T_0 e^{\frac{v_{H'} - v_H}{L} \Delta P} \quad (4.17)$$

Equation 4.17 uses the transition temperature of a coating in a vacuum T_0 , and the specific volume of a hydrogenated v_H and non-hydrogenated $v_{H'}$ coating. The pressure change ΔP was given as the difference between the Hertzian contact pressure and the pressure of the ambient atmosphere.

Using all the above, Steiner et al. [139] were able to predict the wear rate of the DLC coating, and ball counterface in ambient air. The results from the model are shown in **Figure 4.7**, showing how the accumulation of dissipated energy, and then roughness, then the oxide layer, and then graphitisation, affects the overall prediction of wear depth. The model fits the experimental data (red squares) reasonably well.

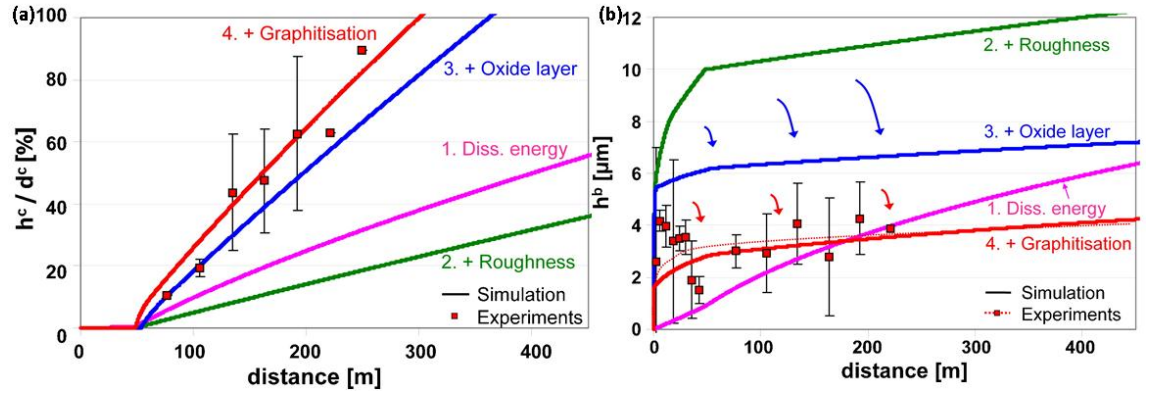


Figure 4.7. Wear predictions of (a) a DLC coating (in percentage wear depth), and (b) a steel ball (in actual wear depth) as different influencing factors are included in the model. The predictions are compared to experiments [139].

Mohd Tobi et al. [143, 144] considered an incremental wear model to predict the gross slip fretting wear of a $2 \mu\text{m}$ thick W doped DLC coating deposited on a $1.5 \mu\text{m}$ thick CrN layer in a cylinder-on-flat configuration in ambient air.

A finite element model was used to calculate the contact pressure distribution between surfaces and evaluate wear. Preston's equation was used to measure the local wear $\Delta h(x, t)$ at every node in contact (see **Equation 4.18**).

$$\Delta h(x, t) = kP(x, t)\delta(x, t)\Delta N \quad (4.18)$$

In **Equation 4.18**, the contact pressure $P(x, t)$ and slip distance $\delta(x, t)$ were defined at each contact node. The specific wear coefficient k was measured experimentally, and was defined on a global level as $1.1 \times 10^{-6} \text{ mm}^3/\text{Nm}$ within the DLC coating, and $0.13 \times$

$10^{-6} \text{ mm}^3/\text{Nm}$ within the CrN layer. The coefficient of friction was assumed to be constant ($\mu = 0.3$). The finite element model used linear quadrilateral elements, and used a single layer of elements to represent the DLC coating. Following previous formulations, to save computational time, a finite element model was evaluated every ΔN iterations. The flow chart in **Figure 4.8** illustrates the methodology for the simulation of wear.

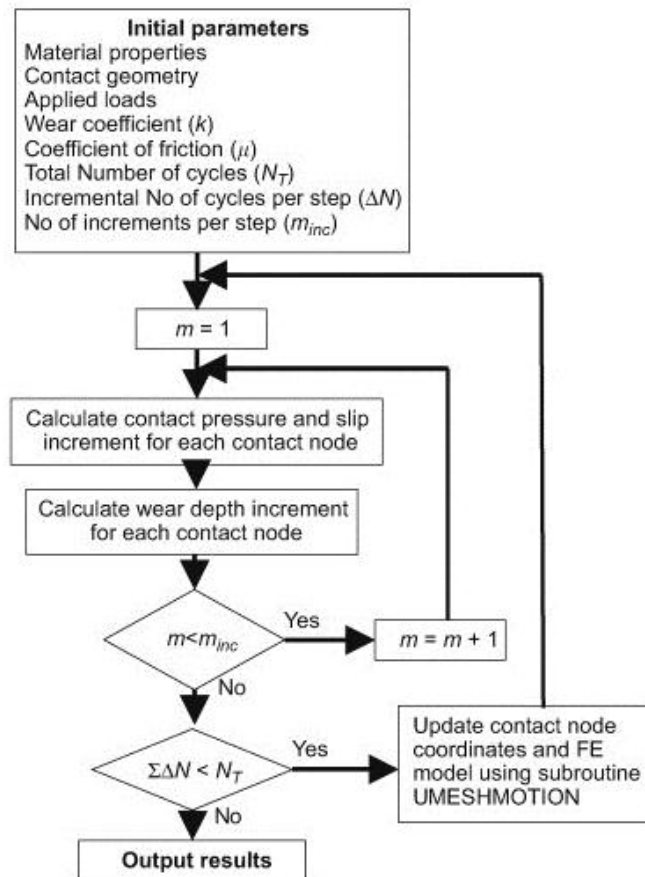


Figure 4.8. A flow chart illustrating the routine to model wear in Abaqus [143].

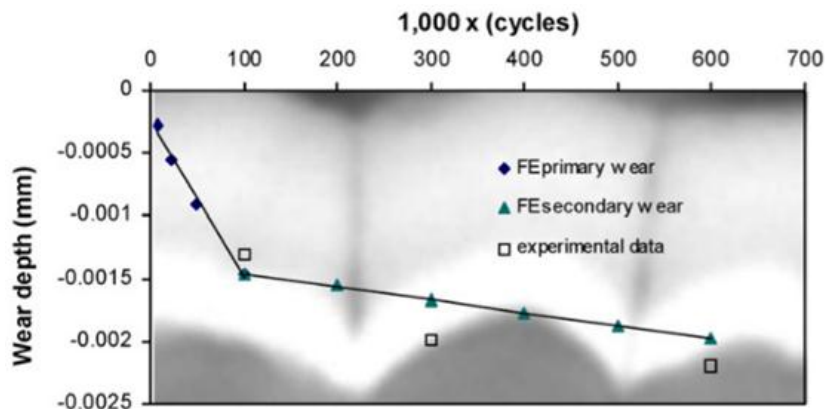


Figure 4.9. A comparison of the predicted wear depth from the model to the actual wear depth measurements from experiments, plotted against the number of fretting cycles (600,000 fretting cycles relates to a sliding distance of 60 metres) [143, 144].

Experimentally, the DLC coating was observed to wear through after approximately 100,000 fretting cycles. This was confirmed using EDX and cross-sectional analysis using the SEM. Following this, fretting wear to the CrN layer was observed, and this occurred at a reduced rate. The wear depth predicted by the incremental wear model compares well to the actual wear depth measurements (see **Figure 4.9**), to within 90 % of the measured wear depth.

Importantly, Mohd Tobi et al. [144] predicted the service life of a DLC coating across a wide range of normal loads and displacements. The wear depth of a DLC coating (as a ratio of the coating thickness t_c) was given by a power law formulation (see **Equation 4.19**), where N represents the normal load applied, and d represents the total sliding distance. The subscript *test* represents the data from the original fretting test from which the power law was fitted.

$$\frac{w_D}{t_c} = 0.364 \left(\frac{dN}{dN_{test}} \right)^{0.71} \quad (4.19)$$

The expression above may be manipulated to predict the sliding distance at which a coating may be predicted to fail, under the assumption that the test is under gross slip fretting conditions and that there is a low risk of tensile fracture. Additional wear data obtained for different normal load (350 – 700 N) and displacement (20 – 60 μm) combinations was used to validate **Equation 4.19**.

4.6. Conclusion

Chapter 4 concentrated on the modelling of wear. Firstly, the use of finite element models to evaluate stress distributions of coatings was discussed. Considering the effects of plastic deformation and residual stresses, a contact model was used to predict the location of surface cracking due to tensile stresses of a TiN coating during a scratch test [105-107]. Fan and Diao [109] presented the first FEA model to include a transfer layer. Three quasistatic models were constructed to represent three stages of pin-on-disc testing. As the transfer layer developed, the pressure distribution decreased and the magnitude of shear stress dropped considerably.

Secondly, Archard's wear law was introduced, as well as the concept of frictional energy dissipation. The energy dissipated due to friction was shown to be linearly related to the wear of hard coatings in different environments. Bryant's degradation – entropy theorem [42] provided a generalised framework to link the production of entropy through irreversible processes to degradation mechanisms such as wear.

Incremental wear models were shown to offer many advantages, such as prediction of spatially-resolved wear profiles, and applicability to a generalised geometry, however they are known to suffer from numerical error.

- Artificial spikes in the pressure distribution were observed that were suggested to be dispersive numerical errors resultant from discontinuity of surfaces (as a result of the discretisation of the geometry as a finite element mesh) [133].
- A limitation on the maximum wear depth in any one time-step was suggested to reduce the magnitude of the numerical error [128, 129].
- Oqvist [130] noted that the magnitude of numerical error was below 10 % when compared to a numerically stable integration.
- To reduce the solution time an extrapolation technique used the same finite element solution to calculate wear for several iterations.

Incremental wear models are discussed in more detail in Chapter 9, where an incremental wear model for DLC coatings in deionised water is developed.

The final section examined some recent literature to provide predictions of DLC coating lifetime. Steiner et al. [139] implemented a wear model to estimate wear depth of the DLC coating as a function of the dissipated energy, oxidation of the steel counterface, and graphitisation of the DLC coating. They validated their model with sliding wear tests for a DLC coating against a steel ball. Mohd Tobi et al. [143, 144] presented an incremental wear model for a multi-layer DLC / CrN coating. The model predictions closely matched the experimental data. An expression for the lifetime prediction of a DLC coating under gross slip fretting conditions was given based on a governing power law which was validated by experiments.

Chapter 5. Materials and Methods

This chapter introduces three commercial DLC coatings, and defines methodologies for the measurement of surface roughness, coating hardness, Young's modulus, bonding structure, wear volume, and wear depth. Methodologies are provided for the set-up and running of the reciprocating sliding tests.

Section 5.1 outlines the main experimental aims. **Section 5.2** details the test materials used in this thesis, including three commercially deposited DLC coatings. **Section 5.3** describes the acquisition of data regarding surface roughness, wear volume and wear depth, hardness, Young's modulus, bonding structure, and SEM images. In **Section 5.4**, the reciprocating tribometer and experimental tests are described in detail.

5.1. Experimental aims

Driven by the findings of the literature review and to align with the research objectives of Rolls-Royce, the main aims of this experimental work are given as follows:

- i. To evaluate the performance of DLC coatings commercially available in the UK sliding against steel in an aqueous environment.
- ii. To increase understanding of the mechanisms of friction and wear that occur when DLC coatings slide against steel balls in an aqueous environment including the effects of iron oxides on transfer layer formation.
- iii. To understand the effect of varying load and sliding velocity on the coefficient of friction and wear depth of each surface.
- iv. To provide a data set to validate the wear models presented in Chapter 8 and Chapter 9 of this thesis.

The first two aims outlined above are examined in **Chapter 6** where three commercial DLC coatings are worn against steel balls in a reciprocating setup, to examine the friction, wear, and mechanisms of transfer layer formation. The final two aims are considered in **Chapter 7** where different load and velocity combinations are compared to the tribological response.

A key requirement of the work is that a range of DLC coatings deposited by the UK industry are tested in water. The use of industry coatings is of specific interest to Rolls-Royce, since the deposition of components will be outsourced to UK suppliers, however the research has a more widespread interest to UK industry in general. The tribology of DLC coatings in water must be evaluated by means of sliding wear tests and compared to the literature. The friction and wear measurements will provide a data set to inform subsequent wear modelling (in **Chapter 8** and **Chapter 9**).

The use of distilled or deionised water is an over-simplification of the environment in a PWR; however it forms a solid and justifiable base from which to build an

understanding of the dominant tribological mechanisms. Gaining an understanding in this simplified environment will aid understanding of the tribology of a DLC coating in a PWR environment during later wear testing at Rolls-Royce. Additionally, this initial work will aid the implementation of a wear model, and allow for extension of the wear model to predict DLC coating behaviour in a PWR environment.

Finally, the data from the experiments will inform a model which can predict the lifetime behaviour of a DLC coating against steel in water. The model aims to predict the initiation of failure of DLC coatings, based upon a locally defined form of Archard's wear law. The model is implemented in COMSOL Multiphysics 4.3 using the LiveLink™ for MATLAB® framework. The model is presented in detail in **Chapter 9**.

5.2. Materials

This project considers three commercial DLC coatings; **Graphit-iC™** from Teer Coatings, **BALINIT® DLC STAR** from Oerlikon Balzers, and **Adamant®** from Diamond Hard Surfaces. Details of the deposition process and the coating material parameters are provided in **Table 5.1**.

Three different steels are used in this work – in **Chapter 6** the DLC coatings are deposited onto AISI 4118H steel disks and AISI 52100 steel is used as a counterface material in the form of a 6 mm ball. The literature review identified that a DLC coating and steel ball sliding in water led to strong adhesion between surfaces, so an AISI 52100 steel is used to examine the wear mechanisms and potential effects of iron oxide formation on the tribology of DLC coatings in water and in particular on the transfer layer formation. In **Chapter 7**, AISI 440C steel is used as both the substrate, and counterface material in the form of a 6 mm ball. This is a more realistic material that is commonly used in a PWR environment. The material properties of the steels are provided in **Table 5.2**.

5.2.1. Graphit-iC™ from Teer Coatings

Graphit-iC™ (Teer Coatings, Droitwich, WR9 9AS) is a Cr doped magnetron sputtered coating produced using a closed field unbalanced magnetron sputter ion plating (CFUBMSIP) system [12]. A Cr interlayer, followed by a Cr / C gradient layer, is used to maximise adhesion. The DLC coating itself is doped with 5 % Cr and is composed primarily sp² hybridised carbon. In distilled water, in-house tests showed a specific wear rate of 2.3×10^{-8} mm³/Nm under a 10 N load in water [145]. **Table 5.1** gives the material parameters of the Graphit-iC™ coating.

5.2.2. BALINIT[®] DLC STAR from Oerlikon Balzers

BALINIT[®] DLC STAR (Oerlikon Balzers, Milton Keynes, MK7 8AT) is a metal-free hydrogenated DLC coating produced through a PECVD method. The coating is predominantly sp³ bonded. A Cr layer followed by a chromium nitride (CrN) interlayer is used to enhance adhesion and provide load support. The material parameters of the BALINIT[®] DLC STAR coating are given in **Table 5.1**.

5.2.3. Adamant[®] from Diamond Hard Surfaces

Adamant[®] (Diamond Hard Surfaces, Northampton, NN12 8EQ) is a hydrogenated DLC coating produced through a low temperature PECVD deposition process. The Adamant[®] coating is 6.9 μm thick, and is mainly sp³ bonded. The material parameters can be found in **Table 5.1**.

Table 5.1. Material properties of Graphit-iC[™], BALINIT[®] DLC STAR, and Adamant[®].

	Graphit-iC[™]	BALINIT[®] DLC STAR	Adamant[®]
Manufacturer	Teer Coatings	Oerlikon Balzers	Diamond Hard Surfaces
Deposition Method	CFUBMSIP	PECVD	PECVD
Composition	a-C/Cr	a-C:H	a-C:H
Layer Structure	Cr/C gradient layer	Cr/CrN interlayer	N/A
Carbon Hybridisation	Primarily sp ²	Primarily sp ³	Primarily sp ³
Coating Thickness (μm)	1.5 [‡]	1.1 / 0.5 / 1.5 [‡]	6.9 [‡]
Roughness (μm)	0.097 ± 0.002 [†]	0.098 ± 0.002 [†]	0.075 ± 0.002 [†]
Hardness (GPa)	13.1 ± 1.1*	20.1 ± 2.7*	21.3 ± 0.6*
Young's Modulus(GPa)	155 ± 9*	212 ± 17*	191 ± 3*
Poisson's Ratio	0.22 [146]	0.22 [146]	0.22 [146]
Density (g/cm³)	2.5 [147]	2.5 [147]	2.5 [147]
Specific Heat Capacity (J/gK)	0.97 [148]	0.97 [148]	0.97 [148]
Thermal Conductivity (W/mK)	3.18 [147, 149]	3.18 [147, 149]	3.18 [147, 149]

[‡]Based on SEM analysis (Section 7.2.2). [†]From surface profilometry (Section 6.2.2). *Based on nanoindentation tests (Section 6.2.2).

5.2.4. AISI 4118H steel

AISI 4118H steel (see **Table 5.2**) is a standard Cr – Mo low alloy steel composed of (in weight percentage) 0.17 – 0.23 % carbon, 0.60 – 1.00 % manganese, 0.30 – 0.70 %

chromium, 0.08 – 0.15 % molybdenum, 0.035 % phosphorus, 0.040 % sulphur, 0.15 – 0.30 % silicon, and iron to balance. AISI 4118H steel was used as a substrate material for all three DLC coatings in **Chapter 6**.

5.2.5. AISI 52100 steel

AISI 52100 steel (see **Table 5.2**) is a high carbon low alloy bearing steel composed of (in weight percentage) 0.98 – 1.10 % carbon, 0.25 – 0.45 % manganese, 1.30 – 1.60 % chromium, 0.025 % phosphorus, 0.025 % sulphur, 0.15 – 0.35 % silicon, and iron to balance. AISI 52100 steel balls of 6 mm diameter were used as a counterface material for all three DLC coatings in **Chapter 6**.

5.2.6. AISI 440C steel

AISI 440C steel (see **Table 5.2**) is a high carbon martensitic stainless steel composed of (in weight percentage) 0.95 – 1.20 % carbon, 1.00 % manganese, 16.00 – 18.00 % chromium, 0.04 % phosphorus, 0.75 % manganese, 0.03 % sulphur, 1.00 % silicon, and iron to balance. AISI 440C steel balls of 6 mm diameter were used as a counterface material, and AISI 440C steel flats were used as a substrate material, for all three DLC coatings in **Chapter 7**.

Table 5.2. Material properties of AISI 52100 steel, AISI 4118H steel, and AISI 440C steel.

	AISI 52100 steel	AISI 4118H steel	AISI 440C steel
Roughness (μm)	0.1 [†]	0.1 [†]	0.06 [†]
Hardness (GPa)	7.57 [150]	7.47 \pm 0.3*	4.51 – 5.51 [‡]
Young's Modulus (GPa)	203.4 [150]	210.4 \pm 19.3*	190 – 210 [‡]
Poisson's Ratio	0.27 – 0.30 [150]	0.285 – 0.295 [‡]	0.275 – 0.285 [‡]
Density (g/m^3)	7.81 [150]	7.8 – 7.9 [‡]	7.7 – 7.9 [‡]
Specific Heat (W/mK)	0.475 [150]	0.46 – 0.50 [‡]	0.45 – 0.50 [‡]
Thermal Conductivity (J/gK)	46.6 [150]	42 – 48 [‡]	23 – 27 [‡]
Yield Strength (GPa)	2.03 [150]	0.320 – 0.420 [‡]	0.405 – 0.495 [‡]

[†]From surface profilometry (**Section 6.2.2**). *Based on nanoindentation tests (**Section 6.2.2**). [‡]CES EduPack 2013 software.

It is important to consider the likelihood that each steel substrate will yield plastically. A Hertzian contact analysis may be applied for each commercial DLC coating and steel ball, and the magnitude of the shear stress may be estimated as a result. This can be compared to the yield strength to determine the likelihood of subsurface plastic deformation. This is estimated for AISI 52100 steel in **Section 6.3**.

5.3. Analysis techniques

In this section the analysis techniques required to investigate the materials discussed above are introduced. In each sub-section, the test equipment and a precise methodology for obtaining data are discussed.

5.3.1. Surface roughness measurements and image capture

Surface profilometry techniques are used in order to obtain values for the surface roughness of each material. The Alicona InfiniteFocus (Alicona Imagine GmbH, Raaba, Austria) provides high resolution images and accurate 3D surface profiles, which allow for accurate determination of surface roughness measurements.

Surface roughness measurements are obtained by scanning a suitably large representative area of a surface ($> 1 \text{ mm}^2$ to ensure sufficient data points) using the Alicona InfiniteFocus, and using the auto-plane function to remove any tilt from the surface scan and to zero the average height of the surface scan. The average surface roughness may then be evaluated according to **Equation 5.1**, where $p_{i,j}$ is the surface height at each point (i, j) , L_x and L_y are the length of the surface profilometer scan in x- and y-directions, and Δx and Δy are the scan resolution in the x- and y-directions.

$$R_a = \frac{\Delta x \Delta y}{L_x L_y} \sum_i \sum_j |p_{i,j}| \quad (5.1)$$

Due to the large region the measurements are taken from, measurements are typically shown to be repeatable to $\pm 0.002 \text{ }\mu\text{m}$.

5.3.2. Wear volume and wear depth measurements

The TaiCaan profilometer (TaiCaan Technologies Europe, Southampton, UK) is used to measure the wear volume of the DLC coating wear scars. The TaiCaan profilometer uses a confocal laser to scan a surface and provide a set of (x, y, z) coordinates that describe the surface geometry. Wear volume measurements may be made by comparing the height of a clean flat surface surrounding a wear scar to the height distribution of the wear scar itself. A script coded in MATLAB[®] (MathWorks Inc., Natick, MA, USA) is used to remove any tilt from the surface scan, and to zero the average height of the surface scan, and then evaluate wear volume. The wear volume w_v is given by **Equation 5.2**, where Δx and Δy are the scan resolution in the x- and y-directions.

$$w_v = \sum_i \sum_j p_{i,j} \Delta x \Delta y \quad (5.2)$$

The total wear volume is shown schematically in **Figure 5.1** as the difference of the volume below the surface (V_B) and the volume above the surface (V_A). Far from the location of the wear scar, where the coating has a well-defined roughness, the wear volume measurements average zero. Wear depth measurements are a secondary output of the MATLAB[®] script which measures the maximum wear depth and average wear depth of the surface scan.

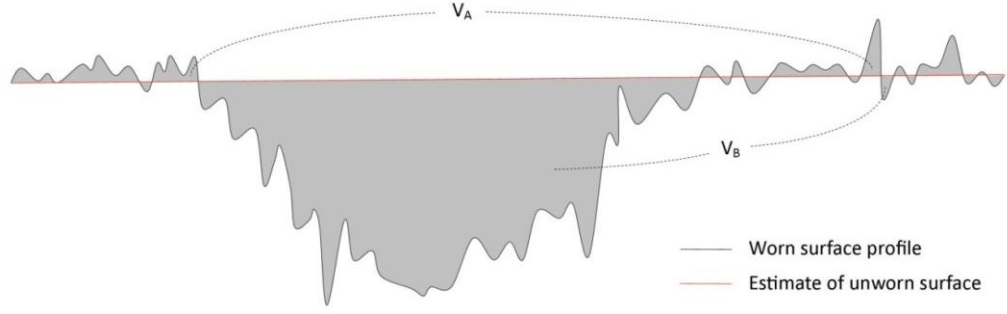


Figure 5.1. A schematic of the wear volume measurement of a worn surface profile using the TaiCaan profilometer.

In the case of a ball, the wear volume is evaluated by measurements of the wear scar radius. The wear scar radius is measured from images taken by the Alicona InfiniteFocus (see **Section 5.3.1**). In each case, 8 separate measurements are taken for the wear scar radius and the average value is quoted. The wear volume w_V may then be evaluated using the spherical cap formula (see **Equation 5.3**), where w_D is the maximum wear depth, r is the ball radius, and a is the wear scar radius.

$$w_V = \frac{\pi w_D}{6} (3a^2 + w_D^2), \text{ where } w_D = r - \sqrt{r^2 - a^2} \quad (5.3)$$

The wear volume measurement methodology using the spherical cap formulae was validated by comparison to wear volume measurements using the Alicona InfiniteFocus (see **Section 5.3.1**). The measurements from both approaches compared well to each other, and therefore the spherical cap formula was considered a suitable method for acquisition of wear volume data.

5.3.3. Hardness and elastic modulus measurements

Hardness and elastic modulus measurements may be obtained using nanoindentation, which is discussed in the context of DLC coatings in **Section 2.2.1**. In this thesis, the mechanical properties are measured using a NanoTest platform (Micro Materials Limited, Wrexham, UK). Nanoindentations use a Berkovich indenter, and thermal drift corrections are always performed pre- and post-indent. When indenting a DLC coating,

the maximum indent should be below 10 % of the coating thickness to minimise the dependence of measurements on the substrate material.

5.3.4. Bonding characterisation

Raman spectroscopy is used to characterise the bonding within a material. It relies on the inelastic scattering of monochromatic light; the light interacts with molecules within a sample causing a quantitative shift in the energy of the photons, which yields information about the vibrational and rotational modes within a material.

In this work, a Renishaw spectrometer (National Physics Laboratory, Teddington, UK) is used to determine the proportion of sp^3 bonding within the commercially deposited DLC coatings, and also to evaluate the chemical bonding within a transfer layer, in **Chapter 6**. A 514 nm laser with a 1 μm spot-size is used to record spectra over a range of 100 – 2000 cm^{-1} with an operating power of 4 mW.

5.3.5. Scanning electron microscopy

Scanning electron microscopy (SEM) uses a high energy electron beam to scan a surface, providing extremely high-resolution images compared to conventional light microscopy. In this thesis, all analyses are performed using a JSM 6500F SEM (JEOL Limited, Tokyo, Japan), which uses an accelerating voltage of 15 kV to provide a magnification of up to 500,000x, with a resolution of 1.5 nm.

Energy dispersive x-ray (EDX) spectroscopy (Oxford Inca 300, Abingdon, UK) identifies the chemical constituents of a sample by analysing x-ray patterns deflected from a specified location. Backscatter electron imaging (BEI) provides a high-resolution image, similar to SEM, however when using BEI, elements with a higher atomic number are shown to be brighter than those with a low atomic number.

5.4. Reciprocating friction tests

Reciprocating friction tests are performed using the Plint TE77 reciprocating tribometer (Phoenix Tribology Ltd, Kingsclere, RG20 4SW). In this thesis, reciprocating friction tests are used to analyse the performance of a selection of DLC coatings from industry in distilled and deionised water, and to assess the effect of varying load and velocity on the tribological output. The next section provides a description of the Plint TE77 reciprocating tribometer and its capability.

5.4.1. Plint TE77 tribometer

The Plint TE77 reciprocating tribometer can be used to assess the frictional performance of materials in a point, line, or area contact. The machine has the capability to provide a normal load of up to 1000 N, as well as a sliding frequency of up to 50 Hz. A stainless steel reservoir can be mounted on to the machine to allow testing in any variety of lubricants. A stainless steel reservoir is fixed to a heater block to allow testing at temperatures up to 250 °C. Temperature can be measured by means of a thermocouple fixed to the specimen. Additionally, a contact potential of 50 mV may be applied to record variations in voltage based on changes in the conductance. This provides a method to monitor the formation of chemical films, breakdown of non-conducting layers, or formation of oxide layers. The Plint TE77 tribometer is shown in **Figure 5.2**.



Figure 5.2. A photograph of the Plint TE77 reciprocating tribometer.

5.4.2. Experimental set-up

In this thesis, the Plint TE77 reciprocating tribometer is used in a ball-on-flat set-up with a 6 mm diameter steel ball sliding against a flat DLC coating deposited on a steel substrate. The composition of the steels used varies throughout the work, and are described in detail at the beginning of **Section 5.2**. **Figure 5.3** shows the set-up of the machine.

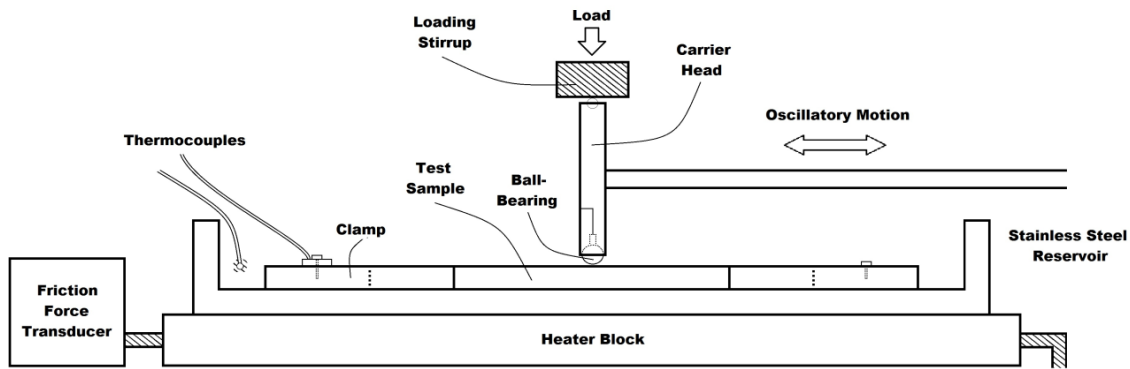


Figure 5.3. A schematic of the Plint TE77 reciprocating tribometer.

Initially, the test reservoir, each DLC coating, and each steel ball, is cleaned in isopropanol for 20 minutes using an ultrasonic bath, before rinsing and cleaning using deionised water for 10 minutes. A DLC coating is fixed within the stainless steel reservoir, and the reservoir is filled with distilled or deionised water to submerge the test samples. A steel ball is attached to the carrier head. Two thermocouples are attached to the machine; one to the stainless steel reservoir, and one to the sample clamp. Both are used to measure the bulk temperature of the water.

The test reservoir is electrically insulated from the carrier head and drive shaft. This allows an electric potential to be applied to the carrier head, and if both the ball and flat materials are electrical conductors, then variations in this voltage throughout the test may be used to detect the build-up of non-conducting material in the contact. In this thesis, contact potential measurements are recorded continuously using a voltage of 50 mV. Clearly steel is electrically conductive, and therefore the conductance of each DLC coating is the important variable. Graphite is electrically conductive, whereas diamond is electrically insulating. The conductance of a DLC coating depends on the sp^3 content of the coating. In this work, we expect Graphit-iC™ to be electrically conductive, and Adamant® and BALINIT® DLC STAR to be electrically insulating. The contact potential measurements of Graphit-iC™ are therefore of primary interest.

Chapter 6. Tribological Testing of DLC Coatings in Water

This chapter presents the tribological testing of three commercial DLC coatings against AISI 52100 steel in distilled water. An analysis of the DLC coating mechanical properties is presented initially. Next, a test matrix for reciprocating sliding tests is detailed as guided by the literature review. The post-test analysis examines the friction and wear of the DLC coatings, and presents analyses of the transfer layers using Raman spectroscopy and nanoindentation. The velocity accommodation mode (VAM) of the transfer layer is shown to control the tribology of a DLC coating.

Section 6.1 introduces the aims of this chapter. **Section 6.2** describes a mechanical characterisation of the DLC coatings. Next, **Section 6.3** considers the reciprocating test set-up and test matrix is detailed. **Section 6.4** presents the results from the reciprocating sliding tests, and **Section 6.5** discusses an analysis of the protective role of transfer layer using Raman spectra.

6.1. Aims

The main aims of this chapter are as follows:

- i. To evaluate the performance of UK commercially deposited DLC coatings sliding against steel in an aqueous environment.
- ii. To increase understanding of the mechanisms of friction and wear which occur when DLC coatings slide against steel balls in an aqueous environment, including the effect of iron oxides on the velocity accommodation mode.

The chapter focuses on the tribological testing of three commercial DLC coatings that were introduced in **Chapter 5**. Each DLC coating is deposited on AISI 4118H steel disks, and slides against an AISI 52100 steel ball in distilled water.

6.2. Mechanical characterisation

The following subsections image each DLC coating and a typical AISI 4118H substrate, and measure the surface roughness, hardness, elastic modulus, and bonding structure of the DLC coatings.

6.2.1. Optical microscopy

Each AISI 4118H steel substrate was polished on a lapping machine using diamond grit, moving gradually from 25 μm to 1 μm diamond grit until the desired surface roughness was attained. The surface of the AISI 4118H steel is shown in **Figure 6.1 (d)**. Images of each DLC coating (obtained from the Alicona InfiniteFocus profilometer) are shown in **Figure 6.1 (a) – (c)** at 10x magnification. All coatings are dark grey in colour. On Graphit-iCTM and BALINIT[®] DLC STAR, scratches from the underlying substrate are evident due to the conformity of the thin coating to the AISI 4118H substrate. There are defects visible on the surface, which are relics from deposition. The surface of Adamant[®] appears to be near featureless, although some defects are observed.

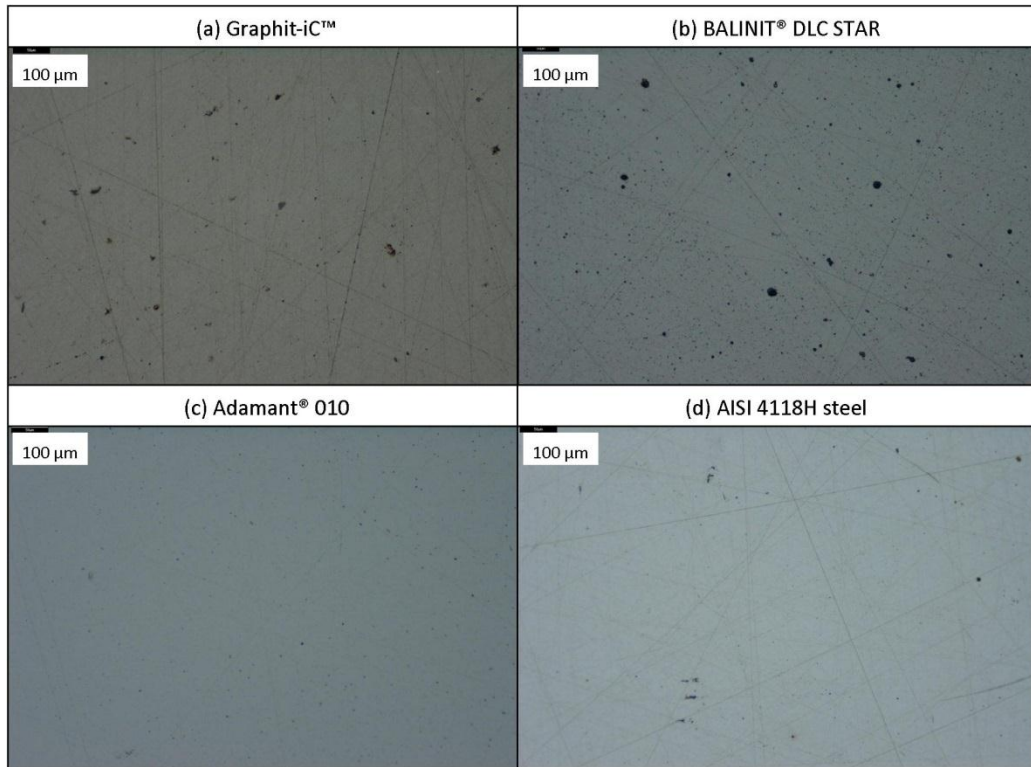


Figure 6.1. Photographs of unworn surfaces at 10x magnification for (a) Graphit-iC™, (b) BALINIT® DLC STAR, (c) Adamant®, and (d) the AISI 4118H steel substrate.

6.2.2. Surface roughness

Surface roughness measurements of the DLC coatings were taken using the Alicona InfiniteFocus according to the methodology described in **Section 5.3.1**, to a tolerance of 0.002 μm . Graphit-iC™ was measured to have an average surface roughness of 0.097 μm , BALINIT® DLC STAR was measured to have an average surface roughness of 0.098 μm , and Adamant® was measured to have an average surface roughness of 0.075 μm . The average surface roughness of the AISI 4118H steel substrates was measured to be 0.100 μm . Adamant® is thicker than Graphit-iC™ and BALINIT® DLC STAR, and as a result is less conformal to the substrate, resulting in a lower average surface roughness.

6.2.3. Hardness and elastic modulus

Hardness and elastic moduli of the DLC coatings were measured using nanoindentation. Nanoindentations were performed according to the methodology described in **Section 5.3.3**, and trial testing was performed to identify suitable load / depth for the indents so as to avoid influence from the mechanical properties of the substrate. Indentations were approximately 100 nm for Graphit-iC™ and BALINIT® DLC STAR, and 300 nm for Adamant® due to a higher coating thickness. The AISI 4118H steel was

indented to a depth of 600 nm. Indentations to peak loads of 3 – 50 mN were performed over 20 seconds of loading time, held for 2 seconds, and then unloaded over 20 seconds. Thermal drift corrections were performed pre- and post-indent.

Figure 6.2 shows the load – depth curves for each DLC coating. Relatively high surface roughness caused some scatter in the response for Graphit-iC™ and BALINIT® DLC STAR; however Adamant® showed impressive mechanical consistency across a wide load / depth range. **Table 5.1** details the hardness and elastic modulus of the DLC coatings. Graphit-iC™ was measured to have a hardness of 13.1 GPa, compared to a hardness of 20.1 GPa and 21.3 GPa for BALINIT® DLC STAR and Adamant®, respectively. The hardness of DLC coatings is known to increase with sp^3 content [4], and Graphit-iC™ is documented to have lower sp^3 content than BALINIT® DLC STAR and Adamant®, in agreement with the hardness results obtained here. Assuming a Poisson’s ratio of 0.22 [146], elastic moduli were calculated from the measured reduced moduli. Graphit-iC™ displayed an elastic modulus of 155 GPa, in comparison to BALINIT® DLC STAR and Adamant® which showed an elastic modulus of 212 GPa and 191 GPa, respectively.

The hardness of AISI 4118H steel was measured to be 7.47 GPa, and the elastic modulus was measured to be 210.4 GPa. The hardness of AISI 52100 steel balls is 7.57 GPa, and the elastic modulus is 203.4 GPa [150].

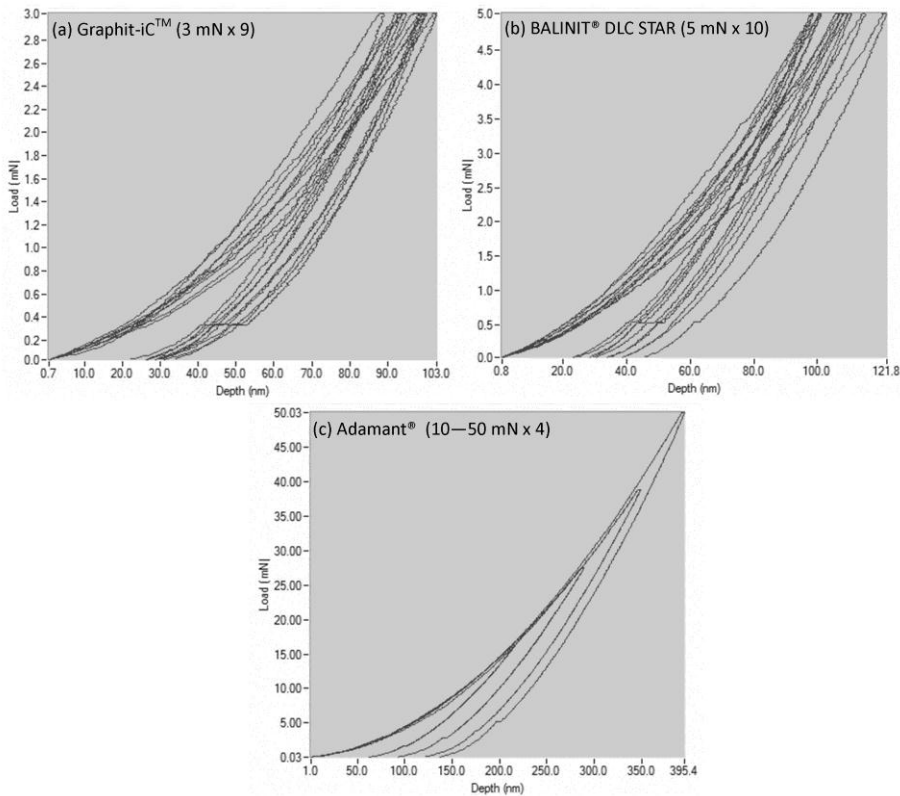


Figure 6.2. Load – depth curves for the nanoindentation of (a) Graphit-iC™, (b) BALINIT® DLC STAR, and (c) Adamant®, using a Nanotest platform (Micro Materials Limited, Wrexham, UK).

6.2.4. Raman spectroscopy

Raman spectroscopy of the as-deposited DLC coatings was performed on a Renishaw spectrometer (National Physics Laboratory, Teddington, UK) according to the methodology outlined in **Section 5.3.4**.

Typically, a Raman spectrum of a DLC coating is comprised of two carbon peaks at around 1580 cm^{-1} and $1330 - 1380\text{ cm}^{-1}$, called the G-peak and D-peak, respectively [73, 151]. These peaks show changes in position and intensity based upon structural changes. The G-peak is related to the bonding and stretching of sp^2 bonded atoms. The D-peak arises from breathing modes of sp^2 bonded atoms in six-fold aromatic rings, and is observed only in the presence of disorder. The $I(D)/I(G)$ ratio measures the degree of disorder within a DLC coating.

Figure 6.3 shows the Raman spectra of each DLC coating. Graphit-iCTM has the highest $I(D)/I(G)$ ratio, at 0.83. This is suggested to be due to the higher percentage of sp^2 bonding in this magnetron sputtered DLC coating. BALINIT[®] DLC STAR shows the lowest $I(D)/I(G)$ ratio at 0.73 compared to 0.77 for Adamant[®]. BALINIT[®] DLC STAR and Adamant[®] were both deposited via a PECVD process, and an approximate relationship exists between sp^3 content and $I(D)/I(G)$ ratio [73]. The sp^3 content of both these coatings can be estimated at 35 – 50 %.

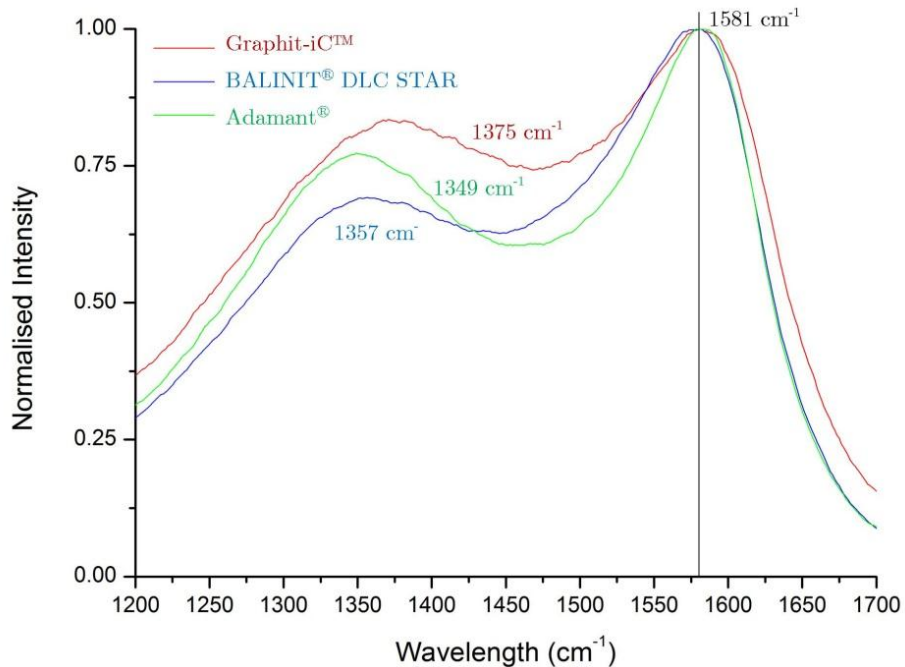


Figure 6.3. Raman spectra for Graphit-iCTM (red), BALINIT[®] DLC STAR (blue) and Adamant[®] (green).

6.3. Reciprocating test matrix

The reciprocating friction tests are detailed in **Table 6.1**. Every test runs in distilled water at room temperature against a 6 mm diameter AISI 52100 steel ball. In each case two identical tests are performed, from which the repeatability of tests can be judged.

Table 6.1. Test parameters for reciprocating tests of each DLC coating against a 6 mm diameter AISI 52100 steel ball using a 19 mm stroke.

Parameter	Values	Equivalent Machine Parameter Values
Mean Contact Pressure	0.98 – 1.10 GPa*	5 N
Sliding Velocity	0.076 m/s	2 Hz
Time	30 s, 120 s, 600 s, 3600 s, 10800 s	N/A

*Contact pressure calculated using a Hertzian analysis.

Suitable experimental parameters were suggested by the work of Ronkainen et al. [59] who tested DLC coatings of different compositions in water using a ball-on-flat contact. Using a maximum contact pressure of 0.92 GPa and a sliding velocity of 0.004 m/s the DLC coatings varied from immeasurable wear to complete coating failure. A Hertzian contact analysis using a normal load of 5 N for each commercial DLC coating and a 6 mm diameter AISI 52100 steel ball provides a contact pressure of 0.98 – 1.10 GPa, depending on the coating elastic modulus. The maximum shear stress is in the range 0.29 – 0.33 GPa, and occurs 24 μm below the surface. The maximum shear stress is far from the coating / substrate interface which reduces the risk of delamination. Thus a 5 N load is chosen as a suitable normal load for testing. The sliding velocity is set at 0.076 m/s, representing a 2 Hz reciprocating frequency at the maximum stroke of 19 mm. Analysis of the elastohydrodynamic lubrication regime using the equations of Hamrock and Dowson [152] confirm that this results in boundary lubrication at this sliding velocity. This is due to the poor lubricious properties of water.

Of interest is the investigation of the wear mechanisms of a DLC coating against steel, and the influences of the distilled water environment on the formation of a transfer layer. Therefore it is important to investigate the early stages of transfer layer formation. Additionally, the performance of commercially deposited DLC coatings needs to be evaluated which requires longer tests. Therefore a range of test times from 30 seconds up to 3 hours were chosen.

The reciprocating sliding tests ran according to the methodology described in **Section 5.4**. The coefficient of friction and contact potential were measured continuously throughout the test, whereas wear was measured at the end of each test, using the Alicona surface profilometer.

6.4. Friction and wear results

Figure 6.4 (a) shows the evolution of the coefficient of friction for each DLC coating during a 600 second friction test against AISI 52100 steel in distilled water. The coefficients of friction observed in this work are typical for DLC coatings in a water environment [59, 97]. Initially, Graphit-iC™ (red) had a large coefficient of friction, due to strong adhesion between the surfaces as a result of the high proportion of sp² bonding, and lack of hydrogen in the coating. The surface is composed of clusters of sp² bonded carbon, formed of cleavage faces with low surface energy, and edge faces with a high surface energy. The edge faces are very reactive and high adhesion with the steel surface is experienced as a result [5]. As the test continued, the coefficient of friction decreased to 0.23. This was shown to be repeatable behaviour via multiple tests. The fall in friction occurred as a transfer layer formed in the contact composed of worn debris from the DLC coating and steel ball. BALINIT® DLC STAR (green) and Adamant® (blue) show relatively steady coefficients of friction (see **Figure 6.4 (a)**). BALINIT® DLC STAR had an average coefficient of friction of 0.23, and Adamant® had a coefficient of friction of 0.14 which increased slightly to 0.17 throughout the test. Both these coatings are hydrogenated, and if a DLC coating is hydrogenated then the surface suffers limited adhesive interactions (by the hydrogen passivation mechanism of Erdemir [5]).

Longer friction tests ran for each DLC coating (see **Figure 6.4 (b)**) and the contact potential was measured continuously during each test (as identified by a black line). For Graphit-iC™ (red), an initially high coefficient of friction was followed by a decrease in the coefficient of friction as a transfer layer formed. The contact potential confirmed the presence of non-conducting material in the contact, and an increase in friction was observed, which is suggested to be caused by tribochemical reactions involving the wear debris of each surface and water and shear of the wear debris in the contact. Following this, Graphit-iC™ showed a decreasing coefficient of friction, possibly due to the gradual shear of debris from the contact region. BALINIT® DLC STAR (green) shows a similar behaviour to Graphit-iC™ initially. An increase in friction followed by a gradual decline in friction was observed. The increase in friction is suggested to be caused by tribochemical reactions and shear of the wear debris in the contact, and the decrease in friction is suggested to be due to the loss of debris from the contact region. After approximately 80 minutes of sliding, there was a sudden increase in the coefficient of friction to 0.50. A similar occurrence was observed in the work of Uchidate et al. [97] for hydrogenated DLC coatings and was unexplained, and also was observed in the work of Fontaine et al. [153] for hydrogenated DLC coatings

sliding in ultra-high vacuum. It is theorised that high adhesion occurs between the DLC coating and the steel ball, due to loss of the transfer layer. This theory is backed up by the subsequent decline in the contact potential measurements. Adamant[®] showed an initial increase in the coefficient of friction, followed by very smooth frictional behaviour throughout the rest of the test. The coefficient of friction was not affected by tribological interactions with steel.

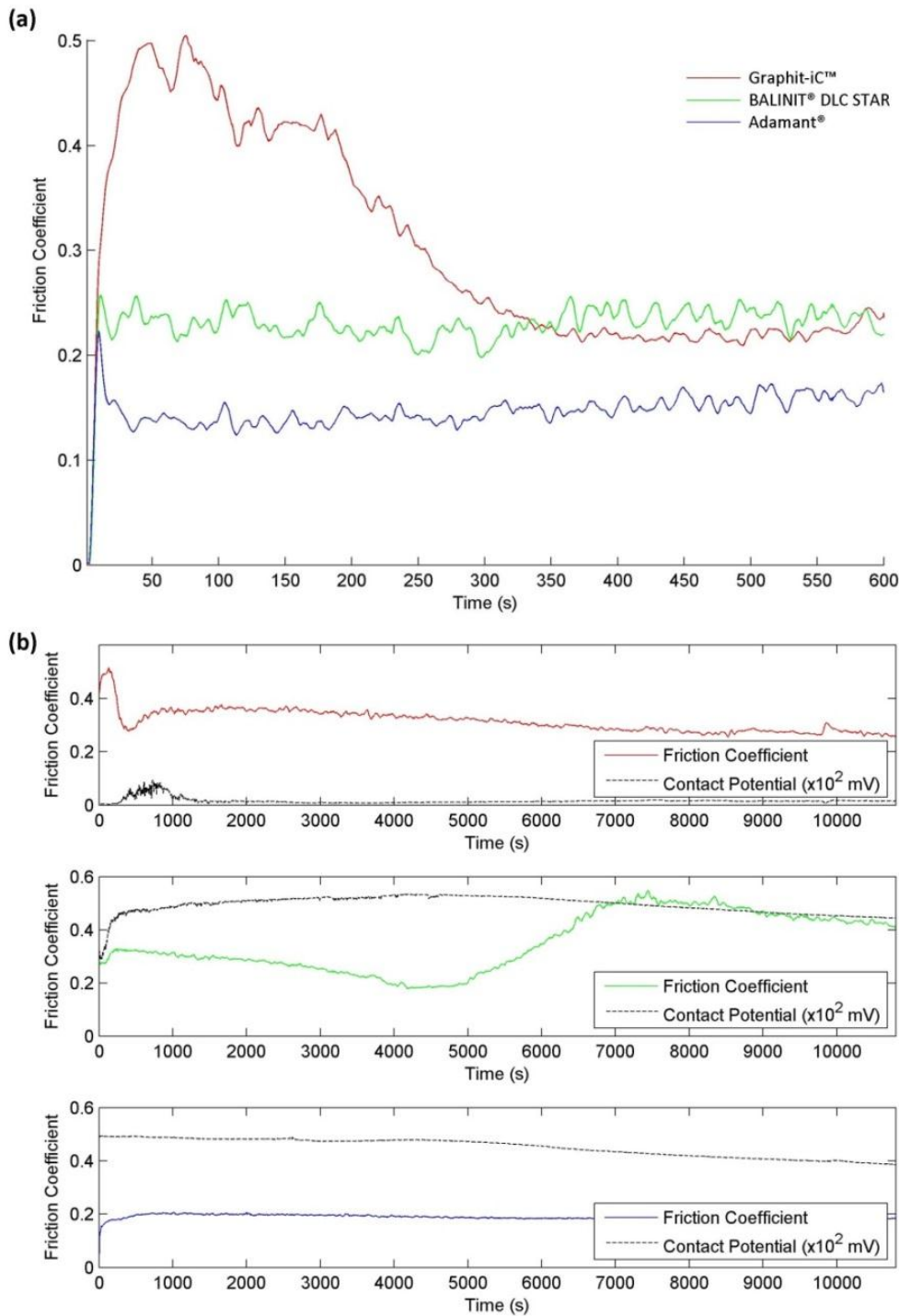


Figure 6.4. Coefficient of friction of Graphit-iC[™], BALINIT[®] DLC STAR, and Adamant[®] in distilled water for (a) 600 seconds, and (b) 3 hours. The contact potential in (b) is shown in black.

The average wear depth of each DLC coating (measured using the procedure described in **Section 5.3.2**) is shown in **Figure 6.5 (a)**. Graphit-iC™ and BALINIT® DLC STAR showed a maximum wear depth of 0.13 μm and 0.11 μm after 600 seconds, relating to a specific wear rate (SWR) of $2.2 \times 10^{-6} \text{ mm}^3/\text{Nm}$ and $1.8 \times 10^{-6} \text{ mm}^3/\text{Nm}$, respectively. A large amount of wear occurred during the first 120 seconds of testing, due to an initially high contact pressure between non-conformal surfaces. No wear was measurable for Adamant™ which showed extreme wear resistance, suggesting a specific wear rate of order $10^{-8} \text{ mm}^3/\text{Nm}$.

The steel balls showed a higher wear depth than their DLC counterparts (see **Figure 6.5 (b)**). BALINIT® DLC STAR caused the most wear to the steel counterface, whereas Graphit-iC™ and Adamant® caused lower wear to the steel counterface. It has been observed previously that the wear rate of a counterface in water is dependent on the hardness of the DLC coating [53], and so the high wear depth against BALINIT® DLC STAR in comparison to Graphit-iC™ is not surprising. Adamant® has a similar hardness to BALINIT® DLC STAR, so the low wear depth of the steel ball is unexpected.

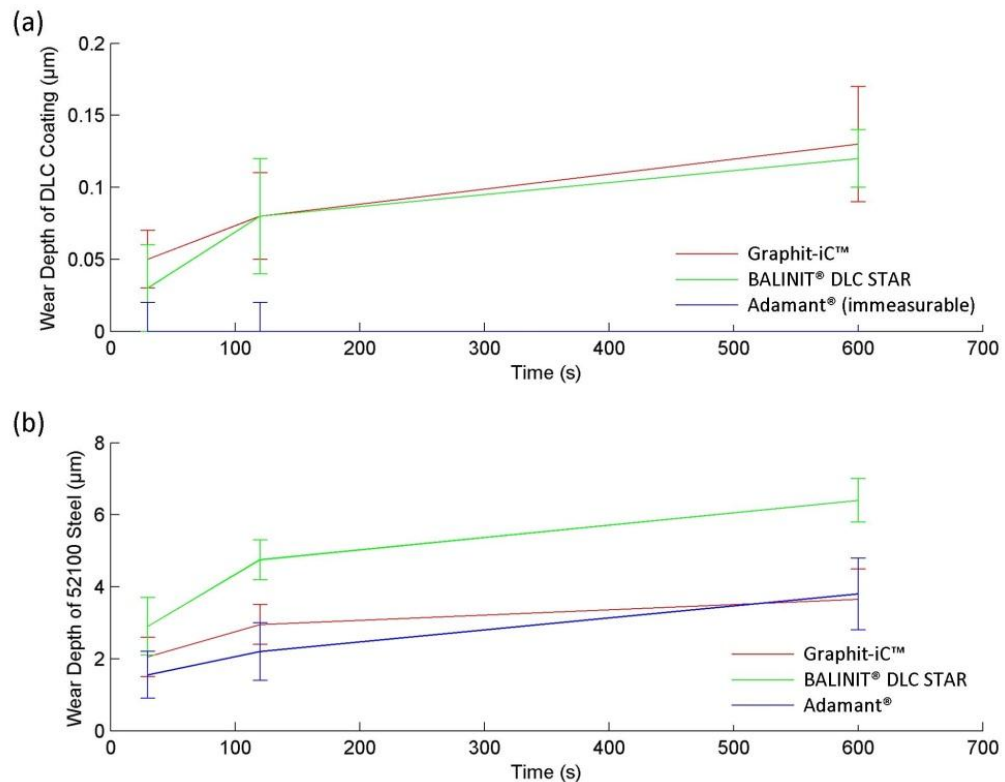


Figure 6.5. Wear depth of (a) Graphit-iC™, BALINIT® DLC STAR, and Adamant®, and (b) AISI 52100 steel balls, in distilled water plotted against time.

6.5. Transfer layer analysis

The tribology of each DLC coating can be linked to the formation and stability of a transfer layer on the surface of the AISI 52100 steel ball. The work of Scharf and Singer [48, 79-81] have related the velocity accommodation mode (VAM) of a transfer layer to the tribological response of DLC coatings (see **Section 3.2.2**). The following subsections discuss results from optical microscopy, SEM, EDX spectroscopy, Raman spectroscopy, and nanoindentation of a transfer layer.

6.5.1. Optical microscopy

Figure 6.6 shows the ball surfaces after 30, 120, and 600 seconds of wear against each DLC coating. There is no evidence of wear debris for Graphit-iC™ after 30 seconds and this coincides with the high coefficient of friction observed in the sliding tests. After 120 seconds, a large deposit of wear debris is seen in the contact. Tests that ran for 600 seconds show that a transfer layer has formed in the contact, and contact potential measurements during this time confirmed the presence of non-conducting material in the contact. The optical image at this time clearly shows abrasive grooves present on the steel surface, as well as a shearing of worn debris from the contact region, at the top and bottom of the image. The growth of a transfer layer is responsible for the reduction in friction during this initial stage. Similar abrasive grooves are evident on the surface of the ball when tested against BALINIT® DLC STAR for all test times, and the shearing of worn debris from the contact is clearly evident after 600 seconds. A thick and stable transfer layer is unable to grow due to extrusion of debris from the contact. A 3D profile of the ball surface after 3600 seconds can be seen in **Figure 6.7**. Adamant™ shows a stable transfer layer at all test times. Little evidence of shear of debris from the region was observed. This correlates with the low and stable coefficient of friction observed for this coating.

The velocity accommodation mode (VAM) [48, 79-81] of the transfer layer for each DLC coating tested was identified as follows:

- **For Graphit-iC™ and BALINIT® DLC STAR, the dominant VAM is shear of the transfer layer, potentially followed by circulation and re-attachment of the wear debris.**
- **For Adamant®, the dominant VAM is interfacial sliding. This is the reason for the low coefficient of friction, and low specific wear rate of both surfaces.**

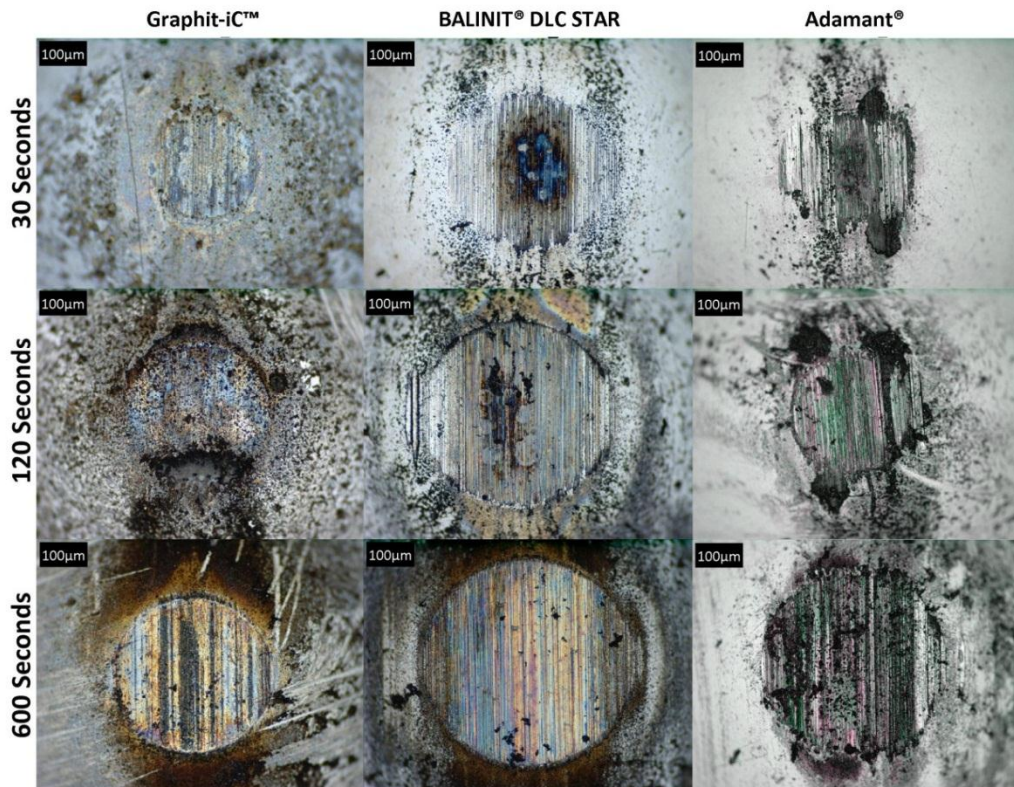


Figure 6.6. Images of each AISI 52100 steel ball after sliding against Graphit-iC™, BALINIT® DLC STAR, and Adamant®, in distilled water for 30, 120, and 600 seconds.

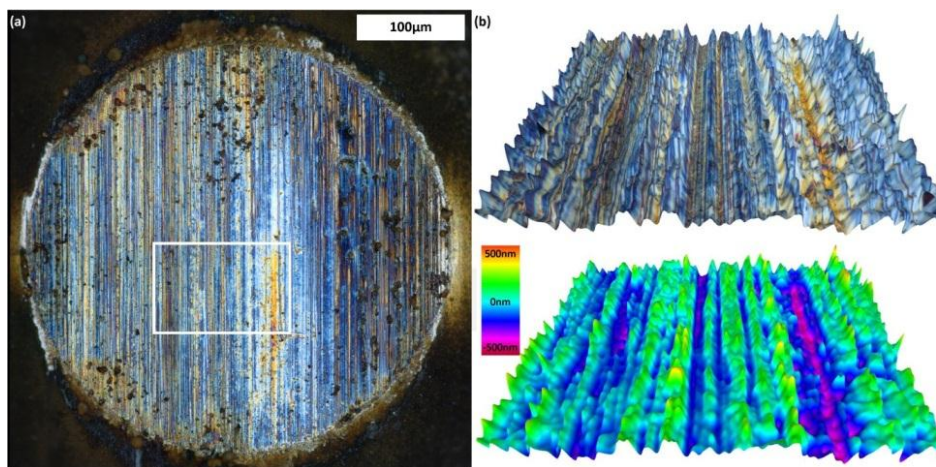


Figure 6.7. (a) An optical image, and (b) a 3D model from surface profilometry measurements, of an AISI 52100 steel ball after 3600 seconds of sliding against BALINIT® DLC STAR in distilled water.

For Graphit-iC™ and BALINIT® DLC STAR, an increase in friction was observed (see **Figure 6.5 (b)**) and it was hypothesised that this was due to tribochemical reactions and shear of the wear debris in the contact. A subsequent decrease in friction was related to the shearing and loss of material from the interface. The optical images obtained suggest that the dominant VAM is shear for these coatings, confirming our initial hypothesis.

6.5.2. SEM and EDX spectroscopy

To investigate the chemical species present at the interface, EDX spectroscopy was used to identify the chemical elements present in the transfer layer. **Figure 6.8** shows an SEM image of the transfer layer after 3600 seconds of sliding against Graphit-iC™. EDX spectra at two locations show that the debris contains C, O, and Fe, suggesting oxidation of the wear debris through tribochemical reactions with water have occurred during sliding. Similarly, **Figure 6.9** shows an SEM image of the transfer layer after 3600 seconds of sliding against BALINIT® DLC STAR. EDX spectra at two locations show that the debris contains O, C, and Fe.

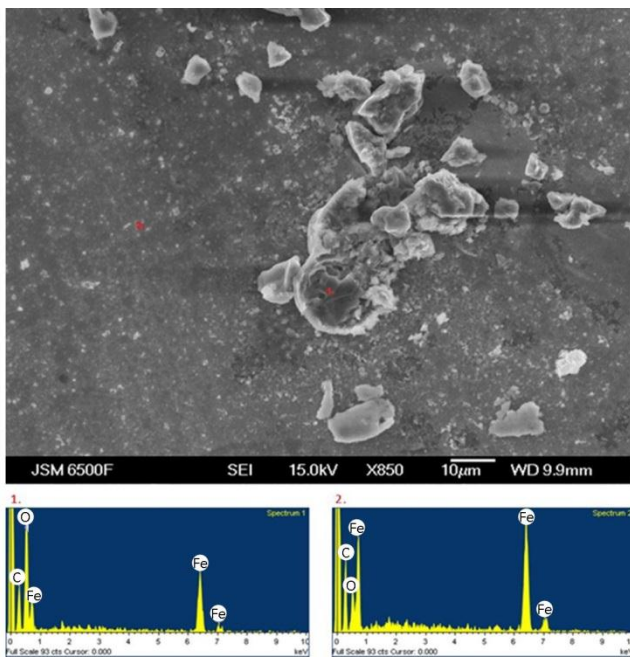


Figure 6.8. (top) An SEM image of wear debris on the AISI 52100 steel ball counterface after sliding for 3600 seconds against Graphit-iC™, and (bottom) EDX spectra taken at locations 1 and 2, as labelled.

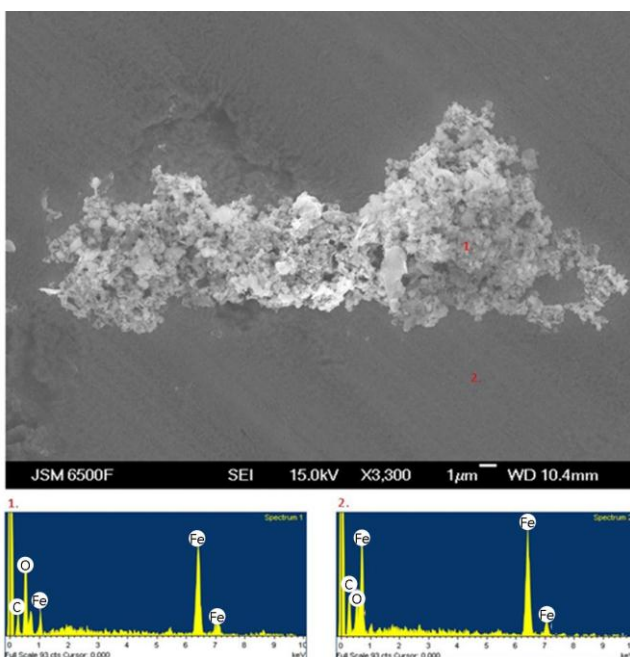


Figure 6.9. (top) An SEM image of wear debris on the AISI 52100 steel ball counterface after sliding for 3600 seconds against BALINIT® DLC STAR, and (bottom) EDX spectra taken at locations 1 and 2, as labelled.

Figure 6.10 shows a BEI of the transferred material after sliding against Adamant™ for 600 seconds. Analysis of the debris using EDX analysis (see **Figure 6.10 (b) – (d)**) shows the presence of C, O, and Fe. The transfer layer is composed mainly of O and C, and Fe is primarily observed in the steel bulk.

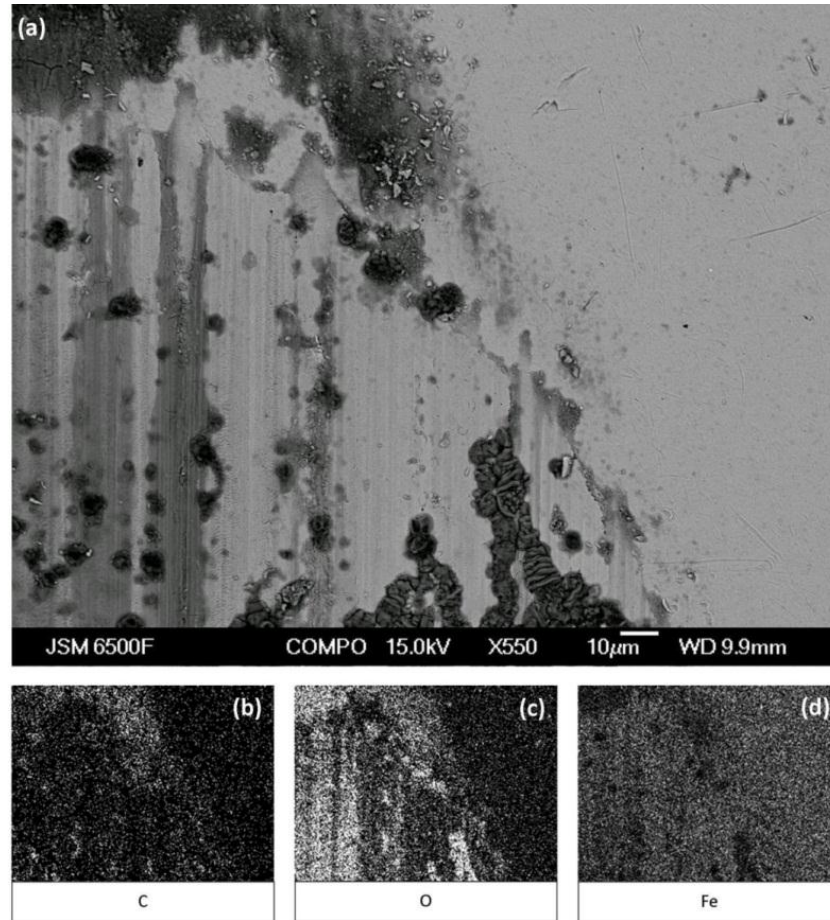


Figure 6.10. (a) A BEI of an AISI 52100 steel ball after sliding against Adamant® for 600 seconds, and EDX maps showing (b) C (c) O, and (d) Fe distributions on the worn surface.

It has been mentioned that the VAM of the transfer layer controls the tribology, but the influence of tribochemical reactions is currently unclear. EDX spectra show the presence of C and O in the transfer layer of each DLC coating, but the presence of Fe in the transfer layer is uncertain (as the EDX spectra may have detected it from the bulk steel).

6.5.3. Raman spectroscopy

Raman spectra of the transfer layers formed on AISI 52100 steel balls after sliding against each DLC coating in distilled water are shown in **Figure 6.11**, for tests which ran for 30, 120, 600, and 3600 seconds. For each sample, two typical Raman spectra of the transfer layer are shown to more fully represent surface state since a large degree of inhomogeneity was noted.

To assist in the interpretation of the Raman spectra, **Figure 6.11 (d)** shows typical Raman spectra of **magnetite** (Fe_3O_4), **hematite** ($\alpha\text{-Fe}_2\text{O}_3$), and **maghemite** ($\gamma\text{-Fe}_2\text{O}_3$); magnetite has peaks in its spectra at around 310 cm^{-1} , 532 cm^{-1} , and 667 cm^{-1} , hematite has peaks in its spectra at around 227 cm^{-1} , 245 cm^{-1} , 293 cm^{-1} , 414 cm^{-1} , 497 cm^{-1} , 612 cm^{-1} and 1321 cm^{-1} , and maghemite has peaks in its spectra at around 350 cm^{-1} , 505 cm^{-1} , and is characterised by the double peak at 660 (710) cm^{-1} .

The spectra taken from the transfer layer formed from Graphit-iCTM (see **Figure 6.11 (a)**) after a 30 second test is composed of carbon and magnetite. After a 120 second test, the spectra showed the presence of carbon, magnetite, and hematite. After a 3600 seconds test, the Raman spectra potentially shows the presence of maghemite. Magnetite and maghemite share peaks around 600 cm^{-1} meaning it is difficult to distinguish between these. A critical observation is that the intensity of the carbon peaks decreased at the test time was increased – suggesting a loss of the carbonaceous transfer layer. BALINIT[®] DLC STAR shows similar behaviour to Graphit-iCTM. There was initially a large volume of carbon on the ball surface, as seen from the high intensity of the spectra in **Figure 6.11 (b)**, but this reduced as the test continued. The presence of hematite is observed initially, but only magnetite is observed towards the end of the test. The spectra taken from the transfer layer formed from AdamantTM (see **Figure 6.11 (c)**) shows the presence of magnetite and hematite in all tests. Moreover, the presence of carbon in the transfer layer is constant.

Raman spectra have provided us with an insight into how the chemical species in a transfer layer vary over time.

- **For Graphit-iCTM and BALINIT[®] DLC STAR, a decrease in the intensity of the carbon peaks and an increase in the intensity of the iron oxide species present are observed with increasing test time. This suggests that as the test continued, the carbonaceous transfer layer was replaced by iron oxide species.**
- **For Adamant[®], the intensity of carbon peaks in the Raman spectra was constant, implying a carbonaceous transfer layer was present at all test times.**

In this work, no firm conclusions can be presented regarding the type of iron oxide on the surface and its correlation to test conditions. This is partially due to the inhomogeneity of the transfer layer.

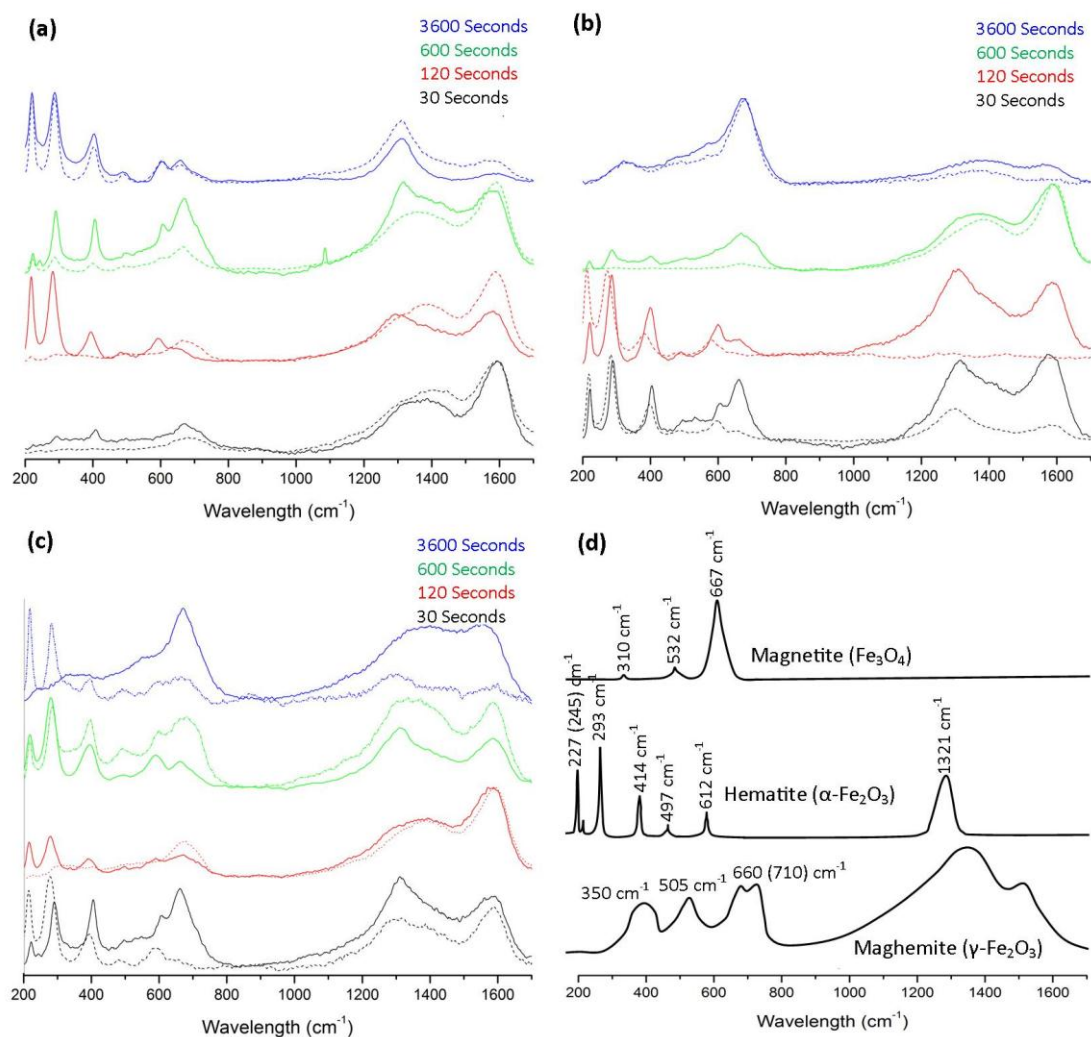


Figure 6.11. Raman spectra for transfer layers sliding against (a) Graphit-iCTM, (b) BALINIT® DLC STAR, and (c) Adamant®, after 30, 120, 600, and 3600 seconds. (d) Raman spectra of magnetite, hematite, and maghemite [154, 155]. In each case, two spectra from different locations on the ball surface are shown (by solid and dotted lines) to represent the inhomogeneity of the transfer layer.

6.5.4. Nanoindentation

The Raman spectra of Graphit-iCTM and BALINIT® DLC STAR (presented in **Section 6.5.3**) showed that the carbonaceous transfer layer was replaced by iron oxide species as the test time increased. Additionally, Graphit-iCTM and BALINIT® DLC STAR showed a higher specific wear rate than Adamant™ (see **Section 6.4**). Therefore, to understand the effect of iron oxide species on the tribology, nanoindentation of a transfer layer (formed from BALINIT® DLC STAR after 3600 seconds) was performed to obtain the hardness and elastic modulus of the iron oxide species present on the surface. The thickness of the transfer layer / oxide layer was not measured but an estimation of 150 – 200 nm thickness is justified [71], suggesting that an indentation depth of 15 – 20 nm was required.

The load – depth curves shown in **Figure 6.12** are mechanically consistent. A load of 0.4 mN led to an indentation depth of 14 – 16 nm, after an initial load of 0.03 mN was applied to tackle the high surface roughness. The small indentation depth and high surface roughness of the transfer layer meant indentations were difficult to obtain.

The hardness of the wear debris was measured as 14.3 ± 2.7 GPa, and the Young's modulus was measured as 415 ± 75 GPa.

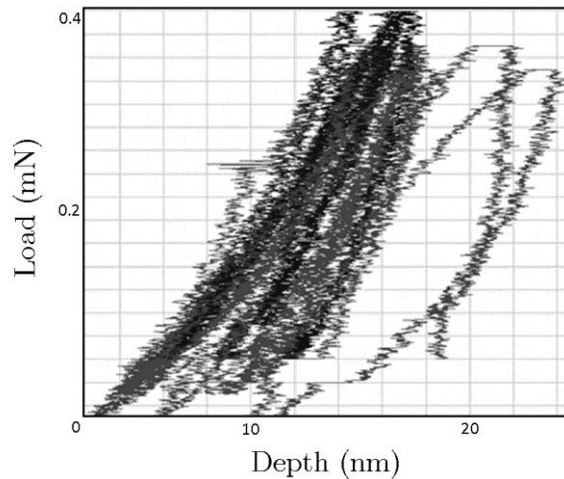


Figure 6.12. Load – depth curve for the nanoindentation of the transfer layer formed by BALINIT[®] DLC STAR after 3600 seconds.

6.6. Discussion

The tribology of each DLC coating can be linked to the velocity accommodation mode (VAM) of the transfer layer (see **Section 3.2.2**). For Adamant[®], the VAM was interfacial sliding, as identified by optical microscopy (see **Figure 6.6**) where a transfer layer was observed at all times. The coefficient of friction was low (0.19), and was constant throughout a 3 hour wear test. No wear of Adamant[®] was measurable, suggesting a specific wear rate of order 10^{-8} mm³/Nm. For Graphit-iC[™] and BALINIT[®] DLC STAR, the VAM was shear and extrusion of debris, as identified by optical microscopy (see **Figure 6.6**) where the shearing of worn debris from the contact region was clearly observed. The coefficient of friction was higher in general and varied throughout each test (as discussed in **Section 6.4**). The specific wear rates of Graphit-iC[™] and BALINIT[®] DLC STAR were measured to be 2.2×10^{-6} mm³/Nm and 1.8×10^{-6} mm³/Nm, respectively.

Raman spectroscopy was used to identify the tribochemistry of the transfer layers – to probe for an explanation to the differing behaviour observed between Adamant[®], and Graphit-iC[™] and BALINIT[®] DLC STAR. Raman spectra of the transfer layers formed

after sliding against Adamant[®] showed the presence of carbonaceous species in the transfer layer throughout each test. This is suggested to be because the VAM of the transfer layer was interfacial sliding, and no shear of wear debris occurred. The transfer layer is thought to protect the DLC surface by acting as a solid lubricant layer. Conversely, Raman spectra of the transfer layers formed after sliding against Graphit-iC[™] and BALINIT[®] DLC STAR identified that the carbonaceous transfer layer was eventually replaced by iron oxide species. This is due to the VAM of the transfer layer, which was shear and extrusion of debris. Magnetite is brittle and can easily be sheared, however hematite is a hard iron oxide and had an abrasive nature [156]. As a result of this, it is theorised that the high specific wear rate that was observed for these DLC coatings is due to a three-body mechanism involving hematite. Nanoindentation showed the hardness of the oxide layer to be 14.3 GPa.

6.7. Conclusion

This chapter evaluated the performance of UK commercially deposited DLC coatings sliding against steel in distilled water. The focus of the work was to increase understanding of the mechanisms of friction and wear, with a focus on the effect of iron oxide species on the formation of a transfer layer.

The following conclusions are drawn from the experimental testing of commercial DLC coatings:

- **The tribology was controlled by the velocity accommodation mode (VAM) of the transfer layer – either interfacial sliding, or shear and re-circulation of debris.**
- **When interfacial sliding was the dominant VAM, a carbonaceous transfer layer was present at all times (as identified by Raman spectroscopy). This was the case for Adamant[®], and a low coefficient of friction and low specific wear rate was observed as a result.**
- **When shear was the dominant VAM, the carbonaceous transfer layer was lost from the contact region and was replaced by iron oxide species (as identified by Raman spectroscopy). This was the case for Graphit-iC[™] and BALINIT[®] DLC STAR. A three-body abrasive wear mechanism involving hematite particles was suggested to be responsible for the high specific wear rate of Graphit-iC[™] and**

BALINIT[®] DLC STAR in comparison to Adamant[™]. Nanoindentation identified the hardness of the hematite particles to be 14.3 GPa.

- The AISI 52100 steel counterface wore proportionally to the hardness of each DLC coating, except in the case of Adamant[®] when a carbonaceous transfer layer led to reduced wear.
- Further tests are needed in order to draw conclusions from the presence of hematite, magnetite, and maghemite, at the interface. Variations in contact pressure and sliding speed could influence the distribution of species at the interface, and influence the tribological properties as a result.
- Further study is needed to understand which parameters affect the VAM, and govern whether or not interfacial sliding will occur. Important parameters might be the deposition method, hardness, or surface roughness of the DLC coating.
- The work in this chapter has focused on a normal load of 5 N and a sliding velocity of 0.076 m/s, and different tribological behaviour may be observed under different test conditions.

Chapter 7. The Influence of Normal Load and Sliding Velocity on the Tribology of DLC Coatings in Water

This chapter extends the experimental testing described in **Chapter 6** to consider the effect of varying the normal load and sliding velocity on the tribology of two commercial DLC coatings against AISI 440C balls in deionised water. Further experimental testing is essential to assess the critical parameters that control the formation and decay of a transfer layer, and to understand the dependence of the coefficient of friction and wear depth on the normal load and sliding velocity. The results of this chapter will also provide a data set for wear modelling in **Chapter 8** and **Chapter 9**. This work considers BALINIT[®] DLC STAR and Adamant[®] only to reduce the number of experimental tests required.

Section 7.1 introduces the main goals of the chapter as guided by the literature review and research objectives of Rolls-Royce. **Section 7.2** provides a characterisation of the DLC coatings and AISI 440C steel balls using optical microscopy and SEM. **Section 7.3** introduces the matrix of tests on the Plint TE77 reciprocating tribometer, and **Section 7.4** presents the friction and wear results.

7.1. Aims

Driven by the findings of the literature review and the research aims of Rolls-Royce, the main goals of this chapter are given as follows:

- i. To understand the changes in the coefficient of friction and the wear depth when the normal load and sliding velocity are varied, for DLC coatings sliding against steel under water-lubrication.
- ii. To provide a data set to validate the predictive wear models presented in Chapter 8 and Chapter 9.

The previous chapter discusses the importance of the velocity accommodation mode (VAM) of the transfer layer on the resulting tribology. This chapter aims to see how variations in normal load and sliding velocity affect the VAM of each DLC coating. Only BALINIT[®] DLC STAR and Adamant[®] are considered in this chapter due to the large number of tests necessary to obtain reliable data. Each DLC coating is deposited on flat AISI 440C steel, and will slide against an AISI 440C steel ball in deionised water. A summer intern student named Ion Costisanu performed the majority of the tests for BALINIT[®] DLC STAR.

7.2. Mechanical characterisation

BALINIT[®] DLC STAR and Adamant[®] are deposited on AISI 440C steel flats. A full mechanical characterisation of BALINIT[®] DLC STAR and Adamant[®] is provided in **Section 6.2** regarding hardness, elastic modulus, thickness, surface roughness, bonding structure, and hydrogen content. Their mechanical properties are detailed in **Table 5.1**. AISI 440C steel is used throughout this chapter as a substrate material for the DLC coatings, and also as a counterface in the form of a 6 mm diameter steel ball. The use of AISI 440C steel is justified as it is commonly used in PWR applications. Details regarding the composition of AISI 440C steel are given in **Section 5.2.6**, and the mechanical properties are provided in **Table 5.2**.

7.2.1. Surface images and surface roughness

BALINIT[®] DLC STAR and Adamant[®] were deposited on to AISI 440C steel flats. Surface roughness measurements of the DLC coatings and the AISI 440C steel flats were taken using the Alicona InfiniteFocus according to the methodology described in **Section 5.3.1**. The AISI 440C steel flats had a surface roughness of 0.060 μm . BALINIT[®] DLC STAR had an average surface roughness of 0.060 μm , and Adamant[®] had an average surface roughness of 0.058 μm . Images of Adamant[®] and BALINIT[®] DLC STAR are shown in **Figure 7.1 (a)** and **(b)** at 10x and 100x magnification. The AISI 440C steel flat is shown in **Figure 7.1 (c)**, and the AISI 440C steel ball is shown in **Figure 7.1 (d)**.

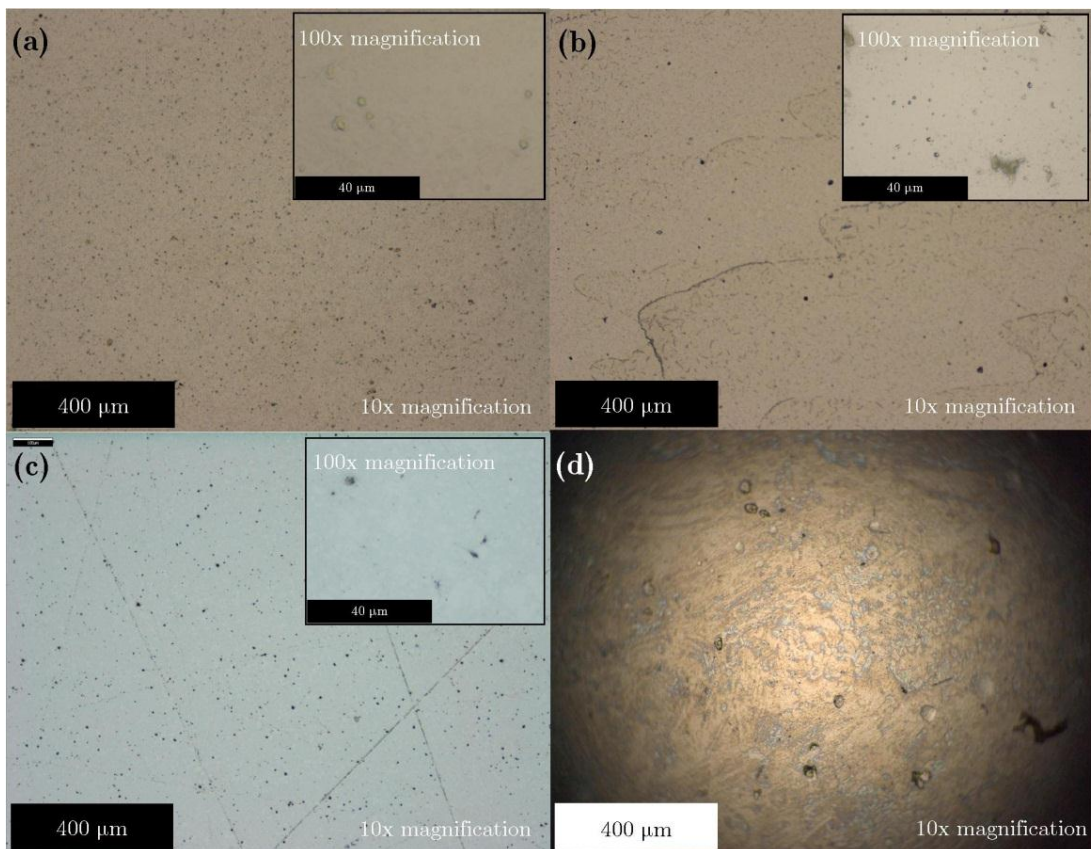


Figure 7.1. (a) Image of Adamant[®] at 10x and 100x magnification; (b) Image of BALINIT[®] DLC STAR at 10x and 100x magnification; (c) Image of the AISI 440C steel surface at 10x and 100x magnification; (d) Image of the 6 mm diameter AISI 440C ball at 10x magnification.

7.2.2. Scanning electron microscopy

Scanning electron microscopy (SEM) microscopy (see **Section 5.3.5**) can be used to identify the different layers of each DLC coating. Each DLC coating was cross-sectioned and set in Bakelite before being polished to a mirror finish for analysis on the SEM. The coating microstructure was analysed using EDX line and area spectra.

Figure 7.2 presents a secondary electron image (SEI) of the cross-section of Adamant[®]. The thickness of Adamant[®] is 6.9 μm and there are no interlayers. Two EDX area spectra (as marked in **Figure 7.2**) showed that Adamant[®] was composed (in weight percentage) of 100 % carbon, and that the AISI 440C steel was composed (in weight percentage) of 4.8 % C, 17.6 % Cr, and 77.6 % Fe. When using EDX spectroscopy, the weight percentages of C may only be taken qualitatively.

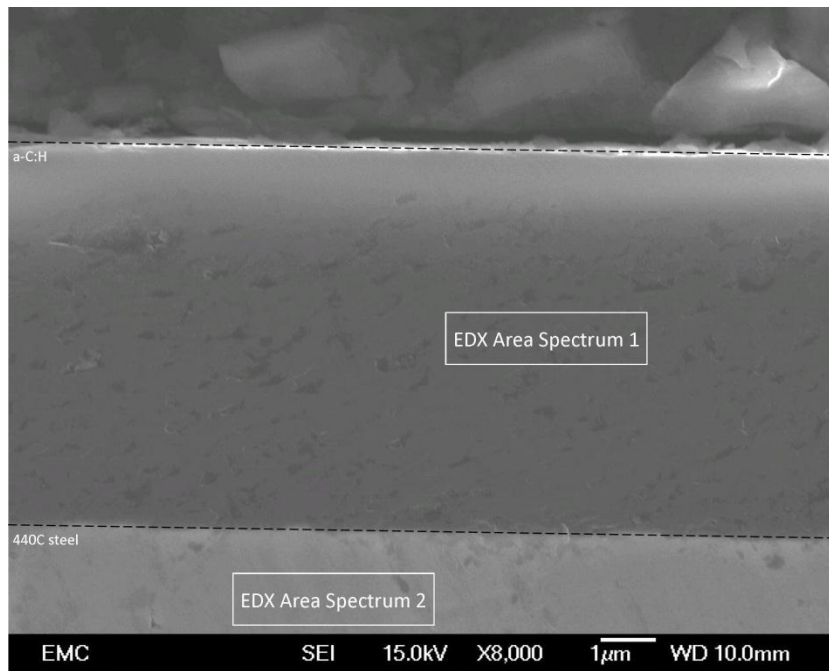


Figure 7.2. A cross-section of Adamant[®] as observed by secondary electron imaging at 8,000x magnification. The locations of two EDX area spectra are marked in white.

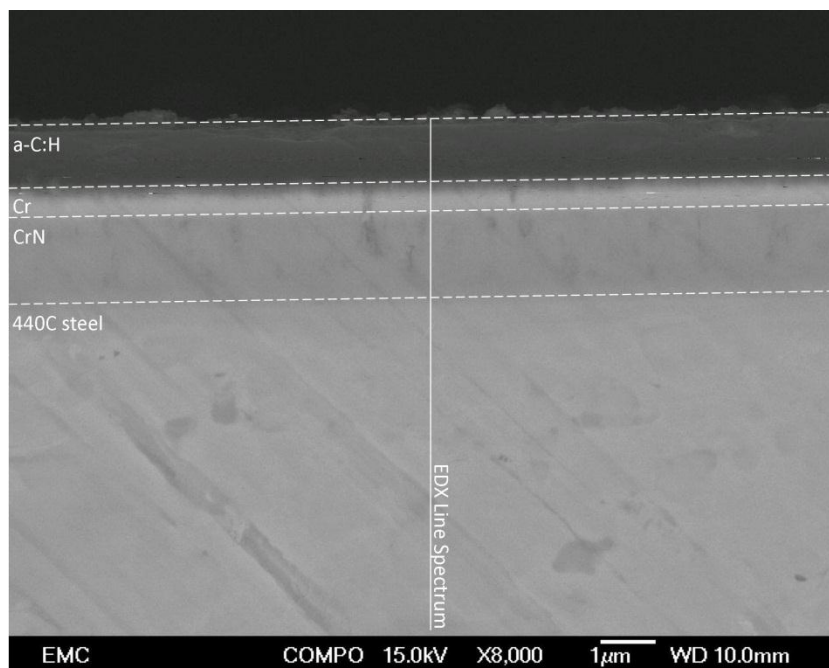


Figure 7.3. A cross-section of BALINIT[®] DLC STAR as observed using backscatter electron imaging at 8,000x magnification. The location of an EDX line spectrum is marked in white.

Figure 7.3 presents a cross-section of BALINIT[®] DLC STAR using backscatter electron imaging (BEI). When using BEI, elements with a high atomic number are brighter than those with a low atomic number. BALINIT[®] DLC STAR is observed to be composed of three distinct layers. This was confirmed by an EDX line spectrum that was taken through the depth of the coating (the location of which is shown in **Figure 7.3**) with the aim to identify the chemical constituents of each layer.

BALINIT[®] DLC STAR is composed of three distinct layers; a 1.1 μm thick a-C:H/Cr top-layer, followed by a 0.5 μm Cr layer, which is followed by a 1.5 μm CrN layer, which is adhered to the AISI 440C steel substrate.

The weight percentage of C, N, Fe, and Cr through the depth of the coating are plotted in **Figure 7.4 (a) – (d)**. The approximate boundaries between layers are shown by dashed lines. The top layer is mainly C, with 5 – 10 % Cr. The presence of N in **Figure 7.4 (b)** is found to be only significant in the CrN layer. Fe was only observed in the AISI 440C steel substrate (see **Figure 7.4 (c)**). The weight percentage of Cr is shown in **Figure 7.4 (d)** and is present throughout all layers of the coating, but is highest in the Cr layer and CrN layer. The AISI 440C steel contains 17 % Cr (as observed from the EDX area spectrum in **Figure 7.2**) but this content varies throughout the steel perhaps to the presence of eutectic carbides.

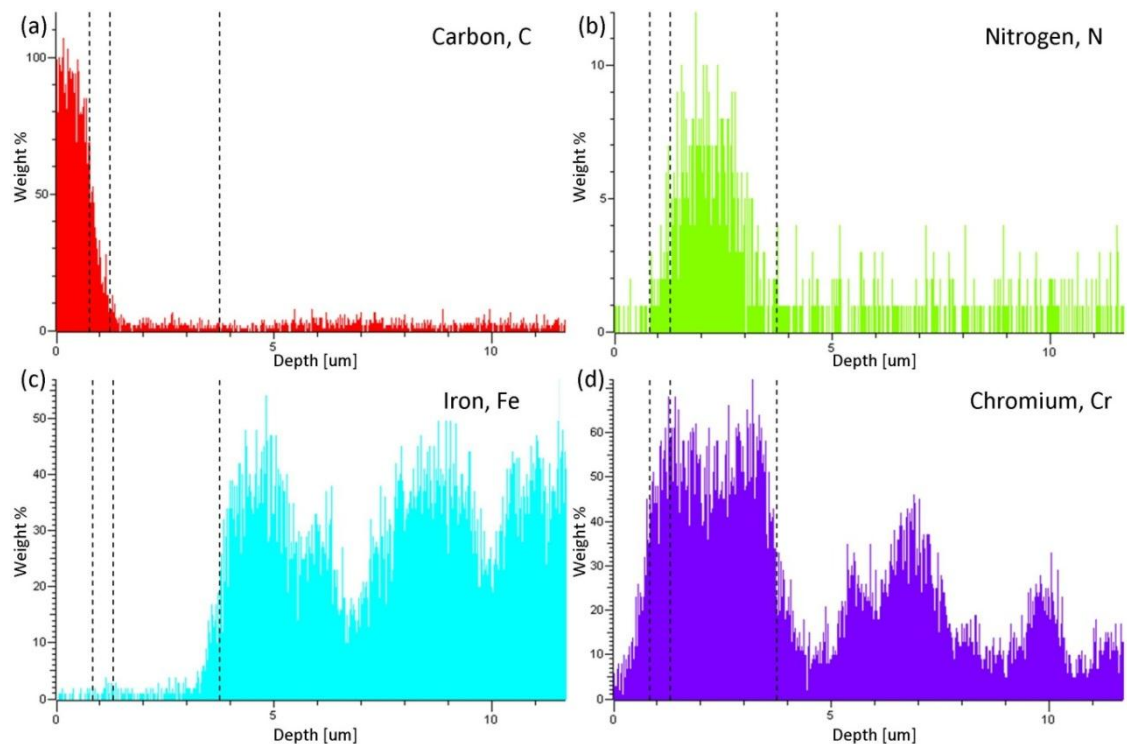


Figure 7.4. The weight percentage of (a) C, (b) N, (c) Fe, and (d) Cr, along the EDX line spectrum for BALINIT[®] DLC STAR. The x-axis represents depth from the top of the coating.

7.3. Reciprocating test matrix

Each reciprocating friction test runs according to the methodology described in **Chapter 6**. Each test is a reciprocating ball-on-flat contact of an AISI 440C ball sliding against a DLC coated AISI 440C steel flat in deionised water. Each test uses a 2 mm stroke.

A test schedule was designed to apply every combination of normal load (5 N, 10 N, and 20 N) and sliding frequency (5 Hz, 10 Hz, and 20 Hz) over nine 5 minute intervals, according to **Figure 7.5**. The aim of this experiment was to see how the coefficient of friction varied as a function of test parameters – and to see if a repeat of the test schedule would yield repeatable frictional behaviour. Additionally, one test ran in reverse to analyse whether the same frictional data would be observed.

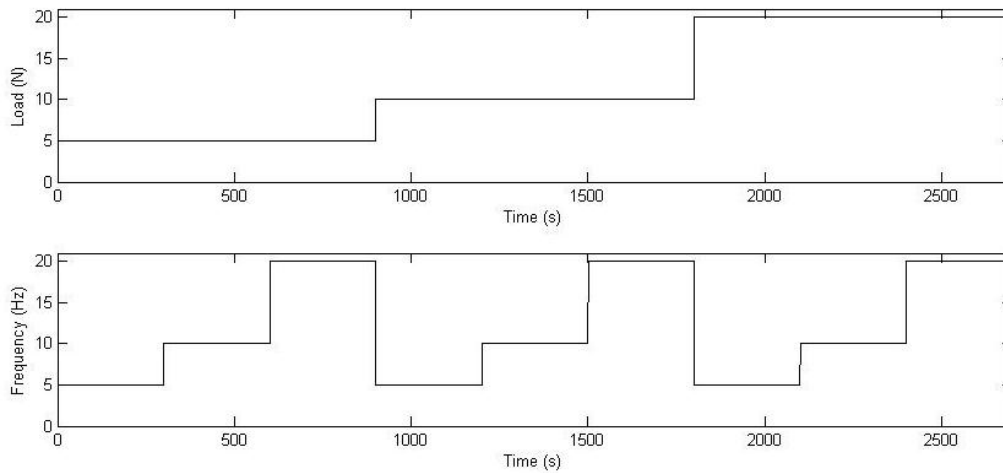


Figure 7.5. Test schedule for wear testing of BALINIT[®] DLC STAR and Adamant[®] against a 6 mm diameter AISI 440C ball on the TE77 reciprocating tribometer using a 2 mm stroke.

To obtain wear data, individual tests ran at a constant normal load, and sliding frequency, for varying test time. All tests ran at room temperature (23 °C). The test matrix is detailed in **Table 7.1**.

Table 7.1. Parameters for wear testing of BALINIT[®] DLC STAR and Adamant[®] against 6 mm diameter AISI 440C steel balls on the TE77 reciprocating tribometer using a 2 mm stroke.

Parameter	Values	Equivalent Machine Parameter Values
Mean Contact Pressure	0.73 GPa*, 0.93 GPa*, 1.17 GPa*	5 N, 10 N, 20 N
Sliding Velocity	0.02 m/s, 0.04 m/s, 0.08 m/s	5 Hz, 10 Hz, 20 Hz
Time	120 s, 600 s, 3600 s	N/A

*Contact pressure calculated using a Hertzian analysis.

7.4. Results

This section presents the results from the reciprocating sliding of BALINIT[®] DLC STAR and Adamant[®] against an AISI 440C steel ball in deionised water. **Section 7.4.1** presents analytical relations for the coefficient of friction of each DLC coating. **Section 7.4.2** examines the wear depth of Adamant[®] and BALINIT[®] DLC STAR as a function of normal load and sliding frequency.

7.4.1. Coefficient of friction

This section begins by presenting the results obtained from the test schedule (shown in **Figure 7.5**) where the normal load (5 N, 10 N, and 20 N) and sliding frequency (5 Hz, 10 Hz, and 20 Hz) change cyclically over 5 minute intervals through all 9 combinations. For both Adamant[®] and BALINIT[®] DLC STAR, when the test schedule ran a second time, entirely repeatable frictional behaviour was observed. When a test schedule ran in reverse, the same values for the coefficient of friction were obtained at each normal load and sliding frequency combination. This suggested that the changes in friction were reversible and were not due to tribological changes at the interface.

i. Adamant[®]

For Adamant[®], the coefficient of friction is plotted against normal load in **Figure 7.6**, for a sliding frequency of 5 Hz (red circles), 10 Hz (green circles), and 20 Hz (blue circles). The minimum coefficient of friction was $0.015 (\pm 0.01)$ at a normal load of 20 N and a sliding frequency of 5 Hz. The maximum coefficient of friction was $0.190 (\pm 0.05)$ at a normal load of 5 N and a sliding frequency of 20 Hz.

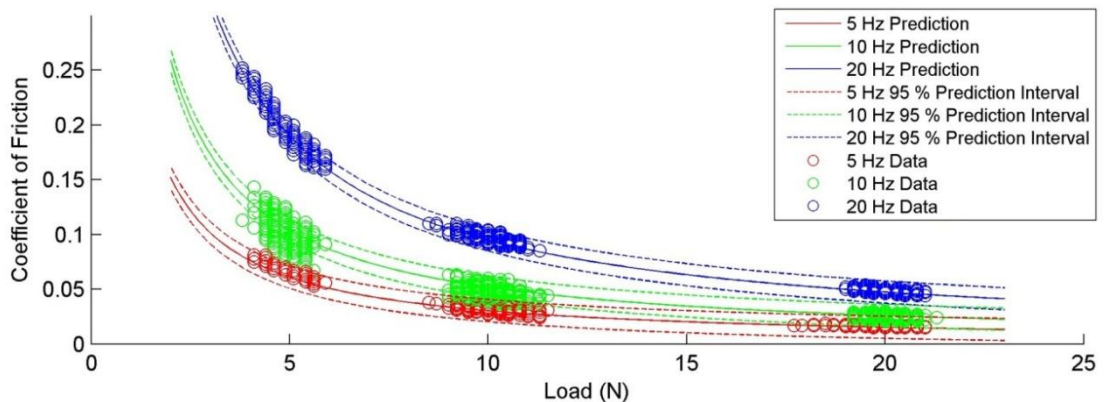


Figure 7.6. The coefficient of friction of Adamant[®] plotted against the normal load, at a frequency of 5 Hz (red circles), 10 Hz (green circles), and 20 Hz (blue circles). The predictions of the linear model (solid line) and associated 95 % prediction intervals (dashed lines) are plotted for each sliding frequency.

A linear model was fitted to the friction data of Adamant[®] to describe the dependence of the coefficient of friction on the normal load and sliding frequency. Assuming that the coefficient of friction μ was inversely proportional to the normal load N and proportional to the sliding frequency f , the linear model provided the following analytical relationship (see **Equation 7.1**).

$$\mu = \frac{0.090}{N} (1 + 0.480f) \quad (7.1)$$

The predictions of the linear model (solid line) and associated 95 % prediction intervals (dashed lines) are shown in **Figure 7.6** for a sliding frequency of 5 Hz (red), 10 Hz (green), and 20 Hz (blue). The prediction intervals are small, and allow us to have confidence in the fit of the linear model.

An assumption made in the fitting of the linear model is that the variance of the coefficient of friction is constant. The experimental data suggests that the variance increases with sliding frequency and decreases with normal load. The model predictions will not be affected by this assumption, but the model may underestimate the 95 % prediction intervals as a result.

To apply a physical understanding to the constants in **Equation 7.1**, one might consider the work of Bowden and Tabor [44] (see **Section 3.1.1**) who define the frictional force as the sum of an adhesive contribution due real contact between surfaces and an abrasive contribution due to surface deformation or ploughing (see **Equation 7.2**).

$$F \equiv A_r \tau + F_{Abr} = 0.090 + 0.043f \quad (7.2)$$

The adhesive force is the product of the real area of contact A_r and the shear strength of an asperity contact τ , and since the changes in friction were shown to be reversible and not a result of tribochemical changes at the interface, this might be considered to be constant. The abrasive component of friction is related to plastic deformation and is mechanical in nature. An increase in the sliding frequency (or equivalently sliding velocity) may affect the protection of the transfer layer and alter the abrasive component of friction.

ii. BALINIT[®] DLC STAR

For BALINIT[®] DLC STAR, the coefficient of friction is plotted against normal load in **Figure 7.7**. The coefficient of friction was independent of the sliding frequency. The minimum coefficient of friction was 0.008 (± 0.005) at a normal load of 20 N. The maximum coefficient of friction was 0.034 (± 0.02) at a normal load of 5 N.

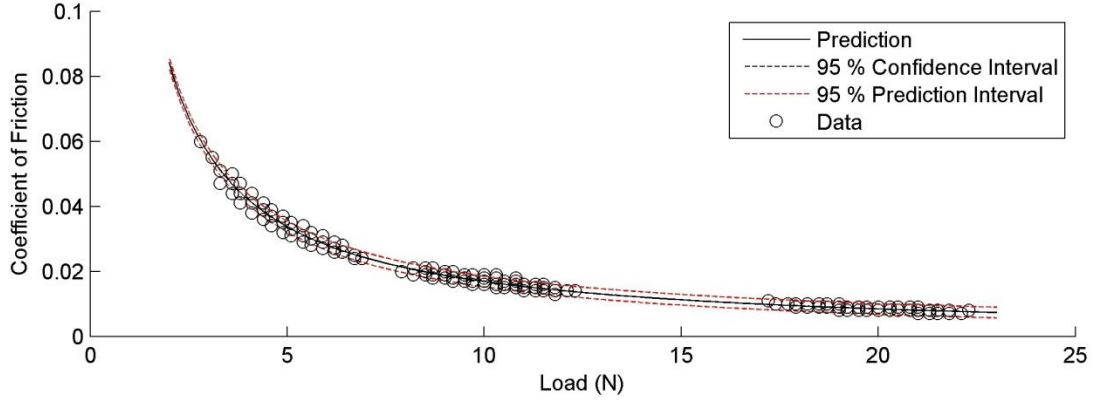


Figure 7.7. The coefficient of friction of BALINIT[®] DLC STAR plotted against the normal load for all frequency combinations (black circles). The predictions of the linear model (solid line) and associated 95 % prediction intervals (dashed lines) are shown as labelled.

A linear model was fitted to the friction data of BALINIT[®] DLC STAR to describe the dependence of the coefficient of friction on the normal load. Assuming that the coefficient of friction μ was inversely proportional to the normal load N , the linear model provided the following analytical relationship (see **Equation 7.3**).

$$\mu = \frac{0.169}{N} \quad (7.3)$$

The predictions of the linear model (solid line) and associated 95 % prediction intervals (dashed lines) are shown in **Figure 7.7**. The prediction intervals are small, and allow us to have confidence in the fit of the linear model. An assumption made in the fitting of the linear model is that the variance of the coefficient of friction is constant. The experimental data suggests that the variance decreases with normal load. The model predictions will not be affected by this assumption, but the model may underestimate the 95 % prediction intervals as a result.

To apply a physical understanding to the constant in **Equation 7.3**, one may consider that the frictional force required to continue sliding is 0.169 N, independent of the normal load or sliding velocity. This suggests that both the adhesive and abrasive components of friction are constant. For BALINIT[®] DLC STAR, the abrasive component of friction is constant – from which it is concluded that for the dynamics of the transfer layer are invariant to changes in frequency.

iii. Discussion

The friction observed for each DLC coating in this chapter can be compared to the observations discussed in **Chapter 6**. In the current chapter, an AISI 440C stainless steel ball is used instead of an AISI 52100 steel ball, and as a result the effect of iron

oxide species on the coefficient of friction will be reduced. This is reflected in the fact that in this chapter the coefficient of friction is constant throughout each test.

In **Chapter 6**, the normal load was 5 N and the sliding velocity was 0.076 m/s, and therefore **Equation 7.1** and **Equation 7.3** predict that the coefficient of friction observed for Adamant[®] and BALINIT[®] DLC STAR, respectively, should have been approximately 0.18 and 0.03, respectively. The observed coefficient of friction in **Chapter 6** for Adamant[®] was 0.19 (in very good comparison to the predicted value) which suggests that the tribology of Adamant[®] was not affected by the formation of iron oxide species. The observed coefficient of friction in **Chapter 6** for BALINIT[®] DLC STAR was in excess of 0.20 throughout the test (in poor comparison to the predicted value), and varied according to the proportion of iron oxide species at the interface. The coefficient of friction of BALINIT[®] DLC STAR observed in the current chapter is clearly very different – and this is associated to the reduction in iron oxide species.

In this chapter, at the same normal load and sliding frequency, the coefficient of friction was lower for BALINIT[®] DLC STAR than it was for Adamant[®]. The reason for this is unknown but must be related to the deposition process and the resulting mechanical properties. A potential reason could be that BALINIT[®] DLC STAR contains a higher hydrogen content than Adamant[®] (the hydrogen content of the coatings have not been measured in this work), and as a result the surface would be passivated by hydrogen atoms which would reduce the potential for adhesive interactions [5, 58], but this is conjecture.

A final point to discuss is that the coefficient of friction of BALINIT[®] DLC STAR was observed to be independent of sliding frequency, in contrast to the coefficient of friction of Adamant[®]. The SEM analysis in **Section 7.2.2** shows that there is some Cr present in the a-C:H top-layer of BALINIT[®] DLC STAR, and this could alter the tribochemistry.

The coefficient of friction of Adamant[®] sliding against AISI 440C steel in deionised water varied over the range 0.015 – 0.190 as a function of normal load and sliding frequency, according to Equation 7.1.

The coefficient of friction of BALINIT[®] DLC STAR sliding against AISI 440C steel in deionised water varied over the range 0.008 – 0.034 as a function of normal load (and independent of sliding velocity) according to Equation 7.3.

The tribology of BALINIT[®] DLC STAR was disrupted by the presence of iron oxide species, relating to loss of the carbonaceous transfer layer. The tribology of Adamant[®] was not affected by the presence of iron oxide species at the sliding interface.

7.4.2. Wear depth

To analyse the change in wear depth over time, individual tests at each combination of normal load (5 N, 10 N, and 20 N) and sliding frequency (5 Hz, 10 Hz, and 20 Hz) ran for 120 s, 600 s, and 3600 s. The wear scar of each individual test was scanned using TaiCaan laser profilometry, before being analysed in MATLAB[®] to extract the average wear depth, using the methodology presented in **Section 5.3.2**. The wear depth of the AISI 440C ball was calculated from the spherical cap formulae [157].

i. Adamant[®]

For Adamant[®], the wear depth of each individual test is plotted against sliding distance in **Figure 7.8 (a) – (c)**, for a normal load of 5 N, 10 N, and 20 N, respectively. Tests that ran at 5 Hz are shown in red, tests that ran at 10 Hz are shown in green, and tests that ran at 20 Hz are shown in blue. Error bars denote the error in the experimental measurements.

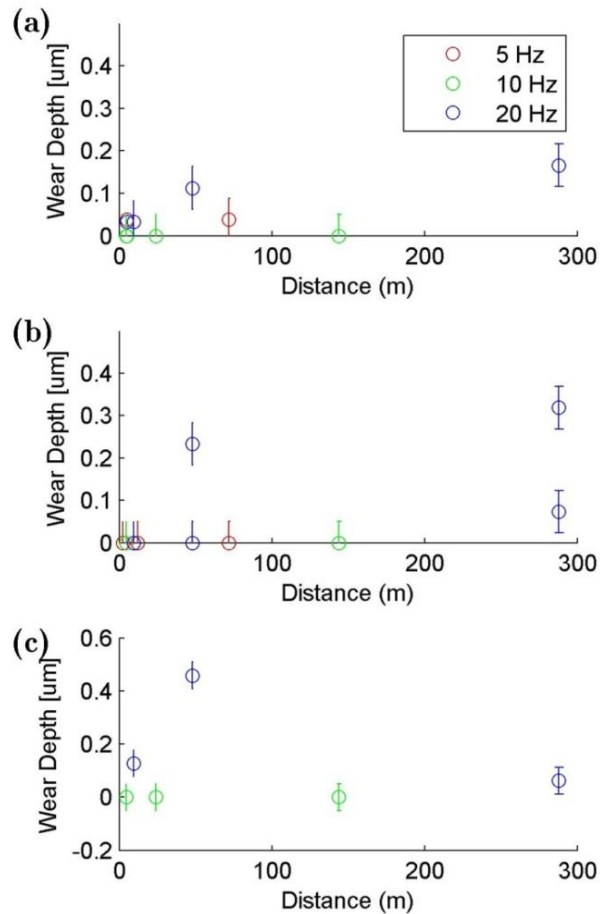


Figure 7.8. The average wear depth of Adamant[®] plotted against sliding distance, at a normal load of (a) 5 N, (b) 10 N, and (c) 20 N. Tests that ran at 5 Hz are shown in red, tests that ran at 10 Hz are shown in green, and tests that ran at 20 Hz are shown in blue. Error bars denote the error in the experimental measurements.

An inaccuracy in the set-up of some tests meant that the reciprocating motion was not precisely parallel to the surface of the flat DLC coating. As a result, the AISI 440C steel ball was forced into the DLC coating resulting in a coefficient of friction which was higher than that expected by **Equation 7.1**. These tests were removed from the dataset. The consequence of this is an incomplete test matrix, with only 22 data points instead of 27.

The maximum wear depth of Adamant[®] was 0.46 (± 0.05) μm after a sliding distance of 48 m, at a normal load of 20 N and a sliding frequency of 20 Hz. Several test runs showed an immeasurable wear depth for Adamant[®] (to an accuracy of $\pm 0.05 \mu\text{m}$) in the same way as observed previously in **Section 6.4**.

A statistical analysis of the wear data of Adamant[®] using MATLAB[®] was performed to describe the relationship between the wear depth and the normal load, sliding frequency, and sliding distance. A loose dependence of wear depth on the frequency was evident (with a coefficient of correlation of 0.297), but the effects of normal load and sliding distance were statistically insignificant.

The wear data has a large variance – and this is the reason behind the poor findings of the statistical model. In reality it is clear that the wear depth of Adamant[®] should increase monotonically with sliding distance. In addition, Archard’s wear law [110, 111] suggests that wear depth should increase with normal load. To investigate this, further testing was required. To limit the number of test runs to a sensible amount, two specific load / frequency combinations were chosen; namely, 5 Hz and 5 N, and 5 Hz and 20 N. These combinations were chosen so that the dependence of wear depth on normal load could be analysed further. To minimise the variance between each test run, a running-in period of 120 seconds at a load of 5 N and a frequency of 5 Hz was included at the start of each test to prevent initially high contact pressures leading to high variance in the test data at a high normal load.

The wear depth of Adamant[®] (see **Figure 7.9 (a)**) and the AISI 440C steel counterface (see **Figure 7.9 (b)**) is plotted against sliding distance at a normal load of 5 N (red circles) and 20 N (blue circles). Tests were subject to a running-in period of 120 seconds, and three experimental data points (black circles) are shown to identify the wear depth at this point in the test. The use of a running-in period at the beginning of the test reduced the magnitude of the variance considerably.

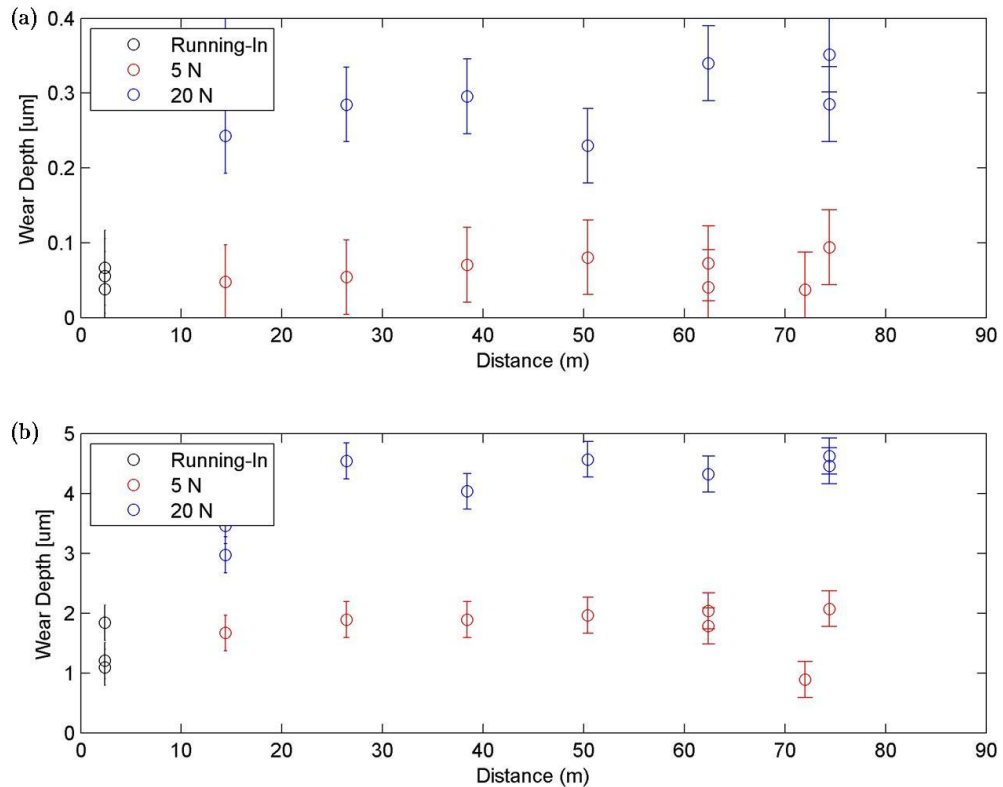


Figure 7.9. The average wear depth of (a) Adamant[®] and (b) AISI 440C steel plotted against sliding distance at a frequency of 5 Hz. Tests that ran at 5 N are shown in red, and tests that ran at 20 N are shown in blue. Error bars denote the error in the experimental measurements.

The wear data for both Adamant[®] and the AISI 440C steel ball clearly shows an increase of wear depth with an increase in sliding distance, and the relationship is non-linear. The majority of wear appears to occur in the first 15 metres of sliding. In addition, more wear occurs at a normal load of 20 N than it does at a normal load of 5 N, but the functional form of this relationship is unknown.

To fit a statistical model to the wear data in **Figure 7.9**, a linear model is not sufficient. Instead, the relationship between wear depth and sliding distance at a specific load and velocity combination must be understood. To analyse the relationship between wear depth and sliding distance, two complementary wear models have been developed in **Chapter 8** and **Chapter 9**.

ii. BALINIT[®] DLC STAR

For BALINIT[®] DLC STAR, the wear depth of each individual test is plotted against sliding distance in **Figure 7.10 (a) – (c)** for a normal load of 5 N, 10 N, and 20 N, respectively. Tests that ran at 5 Hz are shown in red, tests that ran at 10 Hz are shown in green, and tests that ran at 20 Hz are shown in blue. Error bars denote the error in the experimental measurements.

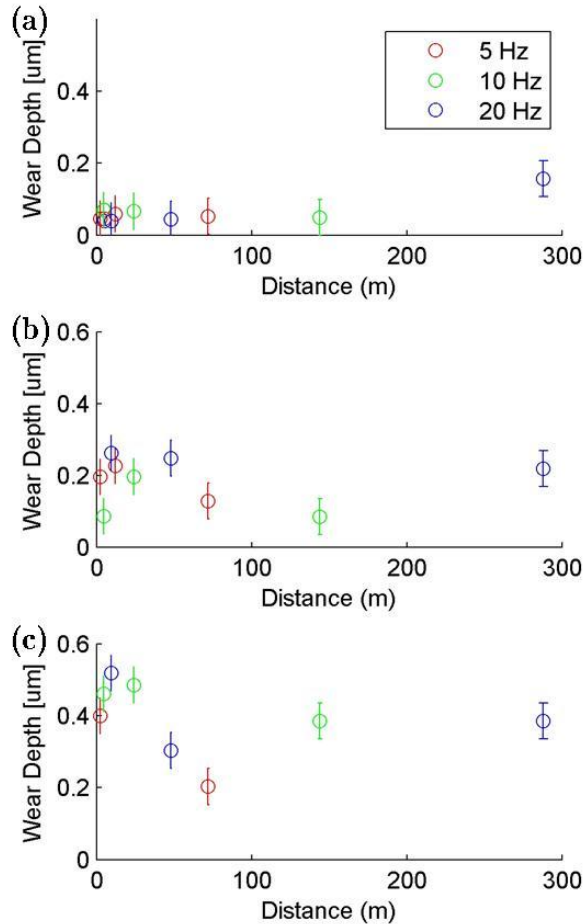


Figure 7.10. The average wear depth of BALINIT® DLC STAR plotted against sliding distance, at a normal load of (a) 5 N, (b) 10 N, and (c) 20 N. Tests that ran at 5 Hz are shown in red, tests that ran at 10 Hz are shown in green, and tests that ran at 20 Hz are shown in blue. Error bars denote the error in the experimental measurements.

The maximum wear depth of BALINIT® DLC STAR was $0.52 (\pm 0.05) \mu\text{m}$ after a sliding distance of 9.6 m, at a normal load of 20 N and a sliding frequency of 20 Hz, whereas the minimum wear depth was $0.04 (\pm 0.05) \mu\text{m}$ after a sliding distance of 9.6 m, at a normal load of 5 N and a sliding frequency of 20 Hz.

A statistical analysis of the wear data of BALINIT® DLC STAR using MATLAB® was performed to investigate the relationship between the wear depth and the normal load, sliding frequency, and sliding distance. A linear model identified that wear depth increased significantly with normal load (with a coefficient of correlation of 0.784), but the effects of sliding frequency and sliding distance were statistically insignificant.

Figure 7.11 shows the predicted wear depth of BALINIT® DLC STAR (solid line) in comparison to the experimental data (black circles), when plotted against normal load. The predicted wear depth is plotted alongside a 95 % confidence interval (dashed black lines) and a 95 % prediction interval (dashed red lines). The model appears to predict the wear depth accurately; however the variance in the wear data clearly increases with

normal load. An assumption made in the fitting of the linear model is that the variance of the wear depth is constant, and as a result the model underestimates the 95 % prediction intervals at a normal load of 20 N.

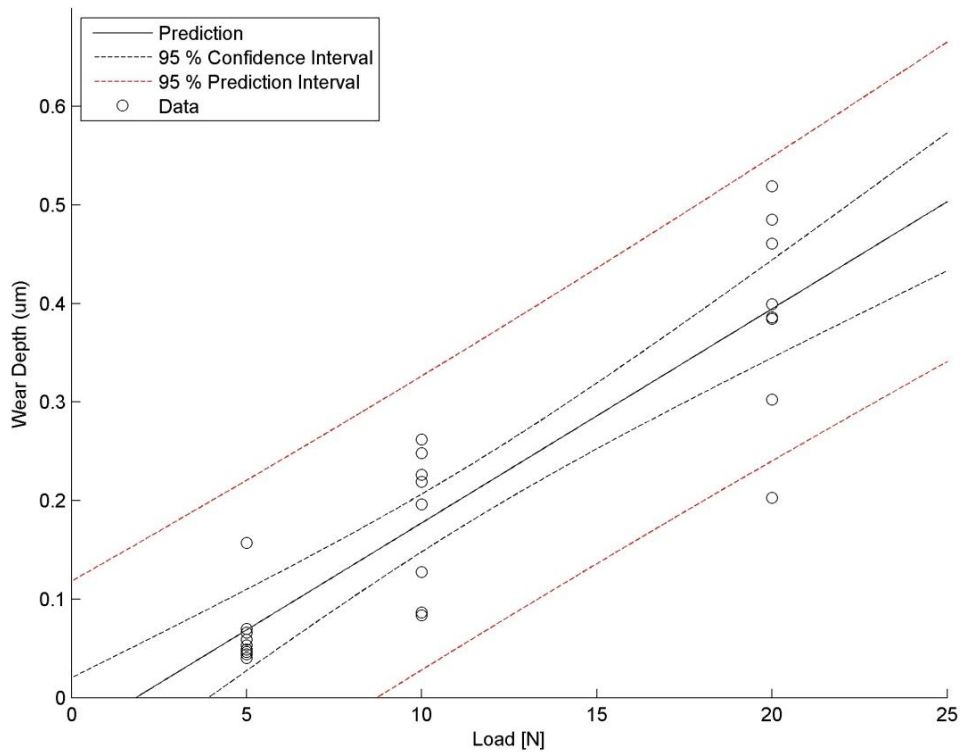


Figure 7.11. Predicted wear depth for BALINIT[®] DLC STAR (black line) and the associated 95 % confidence intervals (black dashed lines) and 95 % prediction interval (red dashed lines) plotted against load. Experimental data is plotted with a black circle.

The current statistical analysis suggests that the wear depth of BALINIT[®] DLC STAR is independent of sliding distance, which intuitively cannot be true. The reason for this inference is that the dataset has a high variance. To further investigate this, more testing was required. To limit the number of test runs to a sensible amount, two specific load / frequency combinations were chosen; namely, 5 Hz and 5 N, and 5 Hz and 20 N. These combinations were chosen so that the dependence of wear depth on load could be analysed further. To minimise the variance between each test run, a running-in period of 120 seconds at a load of 5 N and a frequency of 5 Hz was included at the start of each test to prevent initially high contact pressures leading to high variance in the test data at a high normal load.

The wear depth of BALINIT[®] DLC STAR (see **Figure 7.12 (a)**) and the AISI 440C steel counterface (see **Figure 7.12 (b)**) is plotted against sliding distance at a normal load of 5 N (red circles) and 20 N (blue circles). Tests were subject to a running-in period of 120 seconds, and three experimental data points (black circles) are shown to identify the wear depth at this point in the test. The use of a running-in period at the beginning of the test reduced the magnitude of the variance considerably.

The wear data for both BALINIT® DLC STAR and the AISI 440C steel ball clearly shows an increase of wear depth with an increase in sliding distance, and the relationship is non-linear. The majority of wear appears to occur in the first 15 metres of sliding. In addition, more wear occurs at a normal load of 20 N than it does at a normal load of 5 N, but the functional form of this relationship is unknown.

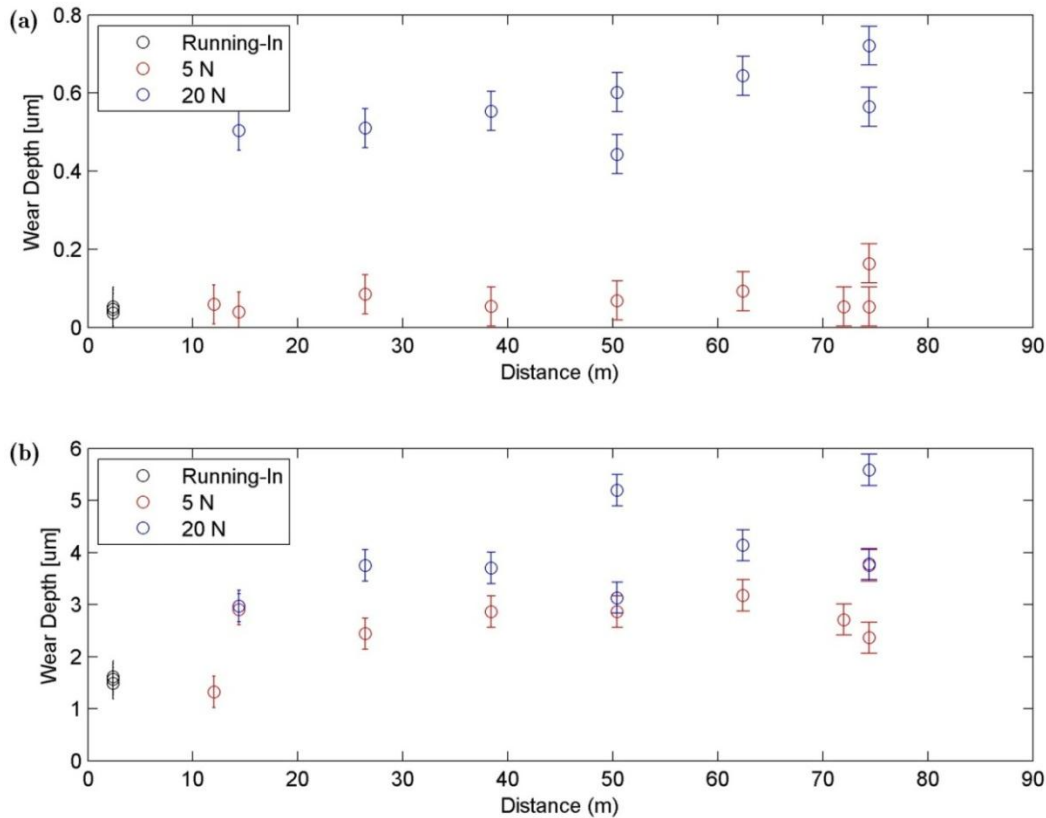


Figure 7.12. The average wear depth of (a) BALINIT® DLC STAR and (b) AISI 440C steel plotted against sliding distance at a frequency of 5 Hz. Tests that ran at 5 N are shown in red, and tests that ran at 20 N are shown in blue. Error bars denote the error in the experimental measurements.

To fit a statistical model to the wear data in **Figure 7.12** the relationship between wear depth and sliding distance at a specific load and velocity combination must be understood. To analyse the relationship between wear depth and sliding distance, two complementary wear models have been developed in **Chapter 8** and **Chapter 9**.

iii. Discussion

This section has focussed on the prediction of wear depth for Adamant® and BALINIT® DLC STAR. The three variables considered were normal load, sliding distance, and sliding frequency. **Table 7.2** presents a summary of the range of expected values for wear depth and specific wear rate of each DLC coating, and the dependence of wear depth on normal load, sliding frequency, and sliding distance.

Table 7.2. The observed range for the wear depth and specific wear rate across all load and frequency combinations, and the dependence of wear depth on normal load, sliding distance, and sliding frequency.

	Wear Depth	Specific Wear Rate ($\times 10^{-7}$)	Normal Load	Sliding Distance	Sliding Frequency
	[μm]	[mm^3/Nm]	[N]	[m]	[Hz]
Adamant[®]	0.00 – 0.46	0.00 – 23.3	Significant	Non-linear	Unknown
AISI 440C Steel	0.3 – 2.4	0.02 – 26.5	Significant	Non-linear	Unknown
BALINIT[®] DLC STAR	0.04 – 0.52	0.27 – 43.1	Significant	Non-linear	Unknown
AISI 440C Steel	1.3 – 4.1	0.27 – 20.5	Significant	Non-linear	Unknown

The wear depth of both Adamant[®] and BALINIT[®] DLC STAR sliding against AISI 440C steel in deionised water varied over the range 0.0 – 0.5 μm , for varying normal load, sliding frequency, and sliding distance. This equates to a specific wear rate below $4.3 \times 10^{-6} \text{ mm}^3/\text{Nm}$. The wear depth of each AISI 440C steel counterface varied over the range 0.3 – 4.1 μm , for varying normal load, sliding frequency, and sliding distance. This equates to a specific wear rate below $2.7 \times 10^{-6} \text{ mm}^3/\text{Nm}$.

A relationship between wear depth and normal load was shown to exist by the wear data in Figure 7.9 and Figure 7.12. For both Adamant[®] and BALINIT[®] DLC STAR, wear depth increased with normal load. In addition, the wear depth of each AISI 440C steel counterface increased with normal load.

The relationship between wear depth and sliding distance was shown to be non-linear by the wear data in Figure 7.9 and Figure 7.12, for Adamant[®] and BALINIT[®] DLC STAR, respectively. This relationship is crucial to the prediction of wear, and is the focus of the wear models presented in Chapter 8 and Chapter 9.

The relationship between wear depth and sliding frequency could not be determined due to the high variance of the dataset. It was theorised that the reciprocating frequency might affect the formation of a transfer layer, although no evidence for this was observed in this work. Further tests to examine this could be a subject for future exploration.

An important point to note is that the specific wear rate of each DLC coating varied over several orders of magnitude, when it is meant to be a constant for any material

pairing. This suggests that Archard's wear law alone is not suitable to predict the wear depth of DLC coatings against steel in deionised water. To resolve this issue, a wear model is presented in **Chapter 8** which allows the specific wear rate to vary as a function of time, or equivalently sliding distance. This is justified by the variations in the specific wear rate over several orders of magnitude.

7.5. Conclusion

This chapter examined the coefficient of friction and wear depth of Adamant[®] and BALINIT[®] DLC STAR as a function of normal load (5 N, 10 N, and 20 N), sliding velocity (5 Hz, 10 Hz, and 20 Hz), and sliding distance (2.4 – 288 metres). This analysis is of value of further the prediction of the tribological behaviour of DLC coatings in a deionised water environment.

The conclusions from this chapter are as follows:

- **The coefficient of friction of Adamant[®] varied over the range 0.015 – 0.190 as a function of normal load and sliding frequency, according to Equation 7.1.**
- **The coefficient of friction of BALINIT[®] DLC STAR varied over the range 0.008 – 0.034 as a function of normal load, according to Equation 7.3.**
- **Interfacial sliding was the dominant VAM in all tests. This was due to the higher oxidation resistance of AISI 440C steel in comparison to AISI 52100 steel. The presence of iron oxide species severely affected the tribology of BALINIT[®] DLC STAR.**
- **The wear depth of Adamant[®] and BALINIT[®] DLC STAR increased with normal load, and varied non-linearly with sliding distance. A relationship between wear depth and sliding frequency could not be obtained due to the high variance of the dataset.**
- **The specific wear rate of each DLC coating varied across several orders of magnitude for different combinations of normal load, sliding frequency, and sliding distance. Any model developed to predict the wear depth of a DLC coating will have to take this into account.**
- **A topic for future work might be to examine the relationship between wear depth and contact pressure using AISI 440C steel balls of differing radii.**

Chapter 8. A Functional Form for the Wear Depth of a Ball and a Flat Surface

In this chapter, formulae are derived from geometric principles to predict the wear depth of a ball and a flat surface through time as they slide against each other, in relation to any phenomenological law for wear volume, and taking into account the component geometry. The equations can be fit using wear volume data from ball-on-flat tribometers, and are fit to the experimental data obtained in **Chapter 7** for BALINIT[®] DLC STAR. The formulae remove previous limiting approximations made in the literature, and extend to the prediction of the wear depth of the flat surface also.

Section 8.1 presents a general discussion on the aims of wear modelling in the context of the thesis. **Section 8.2** discusses the motivation for the wear model, and **Section 8.3** derives formulae to predict the wear depth of a ball and a flat surface based on experimental data. **Section 8.4** presents a validation of the methodology, and **Section 8.5** presents a semi-empirical model to predict the wear depth of BALINIT[®] DLC STAR and an AISI 440C steel ball as they slide against each other in deionised water.

8.1. Aims

The modelling aims of the thesis are to provide a tool that is able to increase the current predictive capabilities of DLC coating lifetime.

Two independent wear models are introduced in this thesis:

- i. **This chapter presents an analytical relationship to convert wear volume measurements from traditional ball-on-flat laboratory testing into wear depth measurements that relate to changes in tolerance (that are of interest to the design engineer). In the context of the reciprocating wear of BALINIT[®] DLC STAR and an AISI 440C steel ball, a semi-empirical form of Archard's wear law is used as an input to the model.**
- ii. **Chapter 9 presents an incremental wear model developed using COMSOL Multiphysics 4.3 and LiveLink[™] for MATLAB[®] to predict the evolution of contact surfaces due to the phenomenon of wear. The formulation can be applied to components of a generalised geometry.**

Both wear models are validated by ball-on-flat reciprocating wear tests between a DLC coating and an AISI 440C steel ball in deionised water (see **Chapter 7**).

8.2. Introduction

Estimations of wear in real life applications are often based on experimental testing in the laboratory, under accelerated test conditions and on idealised test geometries. Whilst accelerated test conditions are necessary to provide data in an allowable time frame, the use of an idealised geometry such as a ball-on-flat contact may provide an erroneous assessment of wear by disregarding geometric effects on the evolution of wear depth, and as such care needs to be taken in the interpretation of experimental data.

A common assessment of wear is Archard's wear law (**Section 4.2**) which estimates the total volume of wear as a function of sliding distance d and normal load N . Assuming that wear occurs in hemispherical volumes at each asperity contact, that the contact pressure at an asperity contact equals the yield pressure of the softer material, and that the area of contact is constant, Archard derived the following expression for the wear volume w_V of either surface.

$$w_V = kNd \quad (8.1)$$

In **Equation 8.1**, the specific wear rate k is a constant which is unique to every tribological scenario and material pair. In the case of mild wear, the specific wear rate is usually given over the range $10^{-8} - 10^{-4} \text{ mm}^3/\text{Nm}$.

Archard's wear law [110, 111] predicts linearity between the wear volume and the product of load and sliding distance, but for many materials this has been shown not to be the case. For example, transitions between wear mechanisms or changes in surface chemistry may affect the evolution of wear volume with respect to time. In the case of DLC coatings, a transfer layer composed of wear debris from the DLC coating is known to develop on the counterface material, which limits contact between the DLC coating and the counterface, and thus lowers the specific wear rate as the contact ensues [3].

An important consideration is that wear depth is dependent on the area of contact between surfaces, and whilst the microscopic wear volume of an asperity contact may occur at some fixed pace according to a fundamental wear law, the wear depth may vary non-linearly due to a larger number of asperity contacts as the apparent contact area increases. For example, in a pin-on-disk test, once the head has worn away, the area of contact must remain constant, and so linearity might be assumed between wear depth and sliding distance, but in a ball-on-flat contact, the area of contact will increase monotonically from the initial Hertzian value upwards [158], and so a non-linear prediction of wear depth with time may be more appropriate.

Prior to Archard's estimation of wear volume in a tribological contact, Preston [112] suggested that the rate of change of wear depth w_D should vary proportionally to the contact pressure P and the sliding velocity v .

$$\frac{dw_D}{dt} = kPv \quad (8.2)$$

In order to compare the wear models of Archard and Preston, the relationship between wear depth and wear volume must be known. In this paper a general formulation is considered where wear volume $w_V = w_V(w_D, A)$ is written as a function of wear depth and contact area A . The rate of change of wear volume (see **Equation 8.3**) is then

determined by two terms; the first is related to the rate of change of wear depth, and the second is related to the rate of change of the contact area (which is ignored in the Archard's and Preston's formulation of wear).

$$\frac{dw_V}{dt} = \frac{\partial w_V}{\partial w_D} \frac{dw_D}{dt} + \frac{\partial w_V}{\partial A} \frac{dA}{dt} \quad (8.3)$$

If wear volume is considered to be a function of wear depth only, i.e. the contact area is assumed to be a constant, then the second term of **Equation 8.3** vanishes, and Archard's and Preston's formulations can be expressed in a comparable rate form. Of course, in many real life applications and in many common test geometries such as a ball-on-flat contact, the area of contact cannot be assumed constant, and this has an effect on the prediction of the wear of both surfaces.

For a range of component geometries, Kauzlarich and Williams [159] presented an equation to link wear depth and sliding distance for a ball sliding against a flat surface. For a ball-on-flat contact, they assumed that the radius of the wear scar was small in relation to the radius of the ball, and derived approximate relations for the wear depth of the ball. Furthermore, Kauzlarich and Williams [159] highlight that wear depth does not necessarily conform to a linear relationship with sliding distance, and that the effects of geometry on the wear depth must not be ignored.

This chapter provides formulae to link wear depth and wear volume of a ball-on-flat contact according to some fundamental law such as Archard's wear law, based on no underlying assumptions other than the surfaces wear uniformly and obey the governing law to predict wear volume. The proposed formulation removes the asymptotic approximation made in the work of Kauzlarich and Williams [159] that the radius of the wear scar is small in relation to the radius of the ball. Additionally, the phenomenological model is extended to predict the wear depth of the flat surface as a function of the contact area.

The wear model derived in the next section to predict the wear depth of the ball is shown to compare favourably to the work of Kauzlarich and Williams [159], who validated their model against experimental data from pin-on-disk testing of a steel / steel contact [129]. Experimental data from the ball-on-flat contact between BALINIT® DLC STAR and an AISI 440C steel ball in deionised water is used to validate the model. Since the wear of a DLC coating does not obey Archard's wear law due to the growth of a carbonaceous transfer layer, a time dependent specific wear rate is used to predict the wear depth of both surfaces.

8.3. Derivation of the equations

A schematic of a ball-on-flat contact including the relevant geometric parameters is shown in **Figure 8.1**.

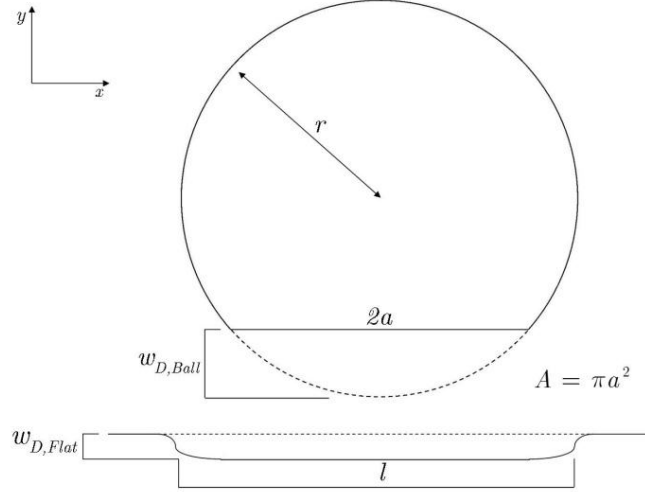


Figure 8.1. A schematic of a ball-on-flat contact. The wear depth of the ball $w_{D,Ball}$ and the wear depth of the flat surface $w_{D,Flat}$ are labelled, as are the geometric parameters (namely stroke length l , contact radius a , ball radius r , and contact area A). Dashed lines represent the original unworn geometry.

For a ball sliding against a flat surface, the actual wear volume of the ball $w_{V,Ball}$ can be given as a function of the wear depth of the ball $w_{D,Ball}$ and the contact radius a , by the spherical cap formula [8], as follows.

$$w_{V,Ball} = \frac{\pi w_{D,Ball}}{6} (3a^2 + w_{D,Ball}^2) \quad (8.4)$$

Similarly, the wear depth of the ball can be written as a function of the radius of contact a and the radius of the ball r [157].

$$w_{D,Ball} = r - \sqrt{r^2 - a^2} \quad (8.5)$$

In this manner, wear depth and wear volume of a ball may be related using geometric parameters. Assuming that the initial contact radius a_0 is Hertzian (where E^* is the reduced modulus, given as a function of the Young's modulus E and Poisson's ratio ν of the ball and flat surfaces);

$$a_0 = \left(\frac{3Nr}{2E^*} \right)^{1/3} \quad (8.6)$$

$$\frac{1}{E^*} = \left(\frac{1 - \nu_{Ball}^2}{E_{Ball}} + \frac{1 - \nu_{Flat}^2}{E_{Flat}} \right)$$

And that the average contact pressure may be given as a ratio of normal load to contact area;

$$P = \frac{N}{A} = \frac{N}{\pi a^2} \quad (8.7)$$

Then through substitution of **Equations 8.4, 8.5,** and **8.7** into **Equation 8.3,** the following first-order non-linear ordinary differential equation is derived for the contact radius.

$$\frac{da}{dt} = \frac{dw_v}{dt} \frac{\sqrt{r^2 - a^2}}{\pi a^3} \quad (8.8)$$

This equation describes the rate of change of contact radius a as a product of the rate of change of wear volume w_v (determined by experiments and provided by a law such as Archard's wear law) and a function determined by geometric considerations. The same differential equation may be derived from either Archard's or Preston's formulation of wear. Using **Equation 8.4** and **Equation 8.5,** the wear depth and wear volume of the ball can be extracted once a is known.

An analytical solution for the contact radius may be found. Integrating with respect to time yields the general solution to the differential equation, where w_v is estimated using Archard's wear law, or some equivalent phenomenological wear law [42].

$$\frac{-\pi}{3} \sqrt{r^2 - a^2} (a^2 + 2r^2) = w_v \quad (8.9)$$

Equation 8.9 can be re-arranged to give the contact radius explicitly in terms of geometric parameters and the wear volume of the ball.

$$a = r \sqrt{\xi^{1/3} + \xi^{-1/3} - 1} \quad (8.10)$$

$$\xi = 1 - \frac{3w_v}{2\pi^2 r^6} \sqrt{9w_v^2 - 4\pi^2 r^6} + 3w_v$$

Supposing that $w_v = kNvt + C_0$ (by integration of Archard's wear law), where C_0 is the initial volume shrinkage of the sphere (due to elastic deformation), then based on the initial conditions (see **Equation 8.6**) the constant C_0 is given by **Equation 8.11.**

$$C_0 = \frac{-\pi}{3} \sqrt{r^2 - a_0^2} (a_0^2 + 2r^2) \quad (8.11)$$

Using the theory developed here, the wear volume and wear depth of the flat surface can also be evaluated. Assuming that the area of the wear scar is given by the product

of the stroke length and the contact diameter then the wear volume of the flat $w_{V,Flat}$ and the average wear depth of the flat $w_{D,Flat}$ can be related by **Equation 8.12**, where l denotes the stroke length.

$$w_{V,Flat} = 2alw_{D,Flat} \quad (8.12)$$

The wear depth of the flat surface $w_{D,Flat}$ may be expressed in terms of a measured experimental wear volume W_V .

$$w_{D,Flat} = \frac{W_V}{2al} \quad (8.13)$$

Estimation of the wear volume of the flat W_V allows for extraction of wear depth of the flat surface as a function of time taking into account the changing contact area according to **Equation 8.13**. The advantage of this new theory for the wear depth of each surface is that from a single test run from which wear volume may be calculated, the theory allows for an entire description of wear depth as a function of time, which is of great importance to the design engineer interested in changes in tolerance.

8.4. Results

A focus is placed on wear between BALINIT[®] DLC STAR and an AISI 440C steel ball (see **Chapter 7**) at a normal load of 5 N and a frequency of 5 Hz (relating to a sliding velocity of 0.02 m/s). The wear depth as a function of sliding distance is plotted in **Figure 7.12 (a)** for the flat DLC coating, and in **Figure 7.12 (b)** for the AISI 440C ball. The specific wear rate input to the model (an average of the specific wear rate at a sliding distance of 2.4 meters) is $1.02 \times 10^{-6} \text{ mm}^3/\text{Nm}$ for the DLC coating, and $1.91 \times 10^{-6} \text{ mm}^3/\text{Nm}$ for the AISI 440C ball, and this data is used as an input to the wear model described in the previous section.

Figure 8.2 shows the predicted contact radius (**Equation 8.10** and **Equation 8.11**), contact pressure (**Equation 8.7**), wear depth and wear volume of the AISI 440C ball (**Equation 8.4** and **Equation 8.5**), and wear depth and volume of BALINIT[®] DLC STAR (**Equation 8.12** and **Equation 8.13**), plotted against sliding distance, based on the average specific wear rate at 120 seconds. The results are compared to the analytical results of Kauzlarich and Williams [6].

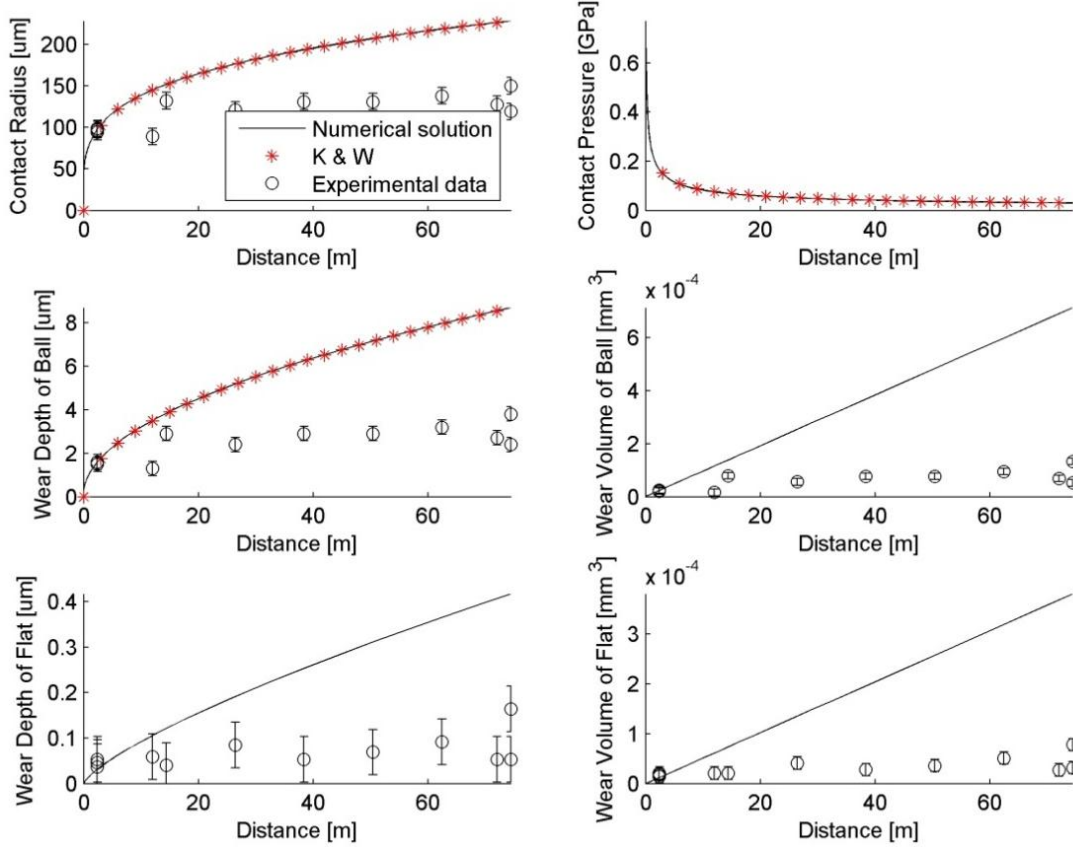


Figure 8.2. Contact radius (top-left), contact pressure (top-right), wear depth of the ball (middle-left), wear volume of the ball (middle-right), wear depth of the DLC coating (bottom-left), wear volume of the DLC coating (bottom-right), plotted against sliding distance. The black line represents the numerical solution, the red asterisks represent the model of Kauzlarich and Williams [159], and the black circles represent experimental data. Error bars are shown by black vertical lines and represent the error in measurement.

The contact radius (top-left) is predicted by the new model to increase from the initial Hertzian value of $46.5 \mu\text{m}$ to $228 \mu\text{m}$ after a sliding distance of 74.4 meters. The model of Kauzlarich and Williams [159] shows a near identical prediction to our model in this case since the assumption that the contact radius is small in relation to the radius of the ball is valid. Since our model compares well to the Kauzlarich and Williams model under different load and sliding velocity – and the Kauzlarich and Williams model was validated against the general case of a steel / steel contact – it is concluded that our model is validated in the general case of a steel / steel contact. Indeed the model can be trusted in any ball-on-flat contact which obeys Archard’s wear law.

In the context of the DLC coating / steel contact, the experimental data for the contact area matches the model well initially, but deviates as the sliding distance increases. This is suggested to be due to the growth of a carbonaceous transfer layer as is known for DLC coatings [28] which reduces the rate of wear to both surfaces. As a result of the changing contact area, the contact pressure (top-right) is shown to decrease from an initial Hertzian value of 0.73 GPa to a final value of 0.03 GPa after a sliding distance of 74.4 meters. The wear depth of the ball (middle-left) is predicted by

the new model to be $8.7 \mu\text{m}$ after a sliding distance of 74.4 meters. The model overestimates the wear depth considerably, when compared to the average experimental value of $3.1 \mu\text{m}$. The model fits the data well initially. Similarly, the wear volume of the ball (middle-right) is overestimated by the new model (since this is directly related to the wear depth). A final wear volume of $7.12 \times 10^{-4} \text{mm}^3$ is predicted by the new model, in comparison to the experimental observation of $0.93 \times 10^{-4} \text{mm}^3$.

The prediction of wear volume and wear depth of the ball by the model of Kauzlarich and Williams is the same as the prediction of the new model. However, the new model can be extended to predict the wear depth of the DLC coating also. The wear depth of the DLC coating is predicted by the new model to be $0.42 \mu\text{m}$ after a sliding distance of 74.4 metres, whereas physical tests suggest that it averages $0.11 \mu\text{m}$ in reality. Similarly, the wear volume of the DLC coating is over-predicted by the new model in the latter part of the test. Again, this is suggested to be due to the growth of a transfer layer in the contact.

An observation from the model presented in this work is that the wear depth of the ball is initially calculated to be non-zero ($0.36 \mu\text{m}$) by Hertzian calculations and this is due to the elastic deformation of the ball which **Equation 8.5** interprets as wear (since the contact width is non-zero initially). The supposed wear depth of the ball calculated by the differential equation is actually a sum of the wear depth plus the elastic deformation of the ball. Since the elastic deformation of the ball tends to zero as the pressure tends to zero, this approximation becomes less important as the test goes on.

The wear model is able to predict the wear depth and wear volume of a ball and a flat surface as they slide against each other. However, an input to this model is the specific wear rate of each surface, which must be calculated directly from experiments, and an issue arises in the context of DLC coatings since the experimental specific wear rate varies with time, and as such a formulation based on Archard's wear law cannot predict the evolution of wear accurately. A physical interpretation for this is thought to be related to the growth of a transfer layer – which is known to reduce the specific wear rate of a DLC coating [3, 28]. For example, if the development of a transfer layer prevents contact between the DLC coating and steel – then the contact develops from a DLC coating / steel contact with a high specific wear rate to a DLC coating / transfer layer contact with a low specific wear rate as the transfer layer grows across the contact.

To account for the growth of a transfer layer during the wear of a DLC coating against steel, the model can be extended to include a non-constant specific wear rate. This extension is also of interest in a general case for any tribological scenario when Archard's wear law does not hold, for example due to a transition between wear mechanisms or due to chemical changes at the interface.

8.5. Extension to a time-dependent specific wear rate

A general case where the specific wear rate depends on time is considered. If wear volume is estimated by Archard's wear law and the specific wear rate is given as $k = k(t)$ then the differential equation for contact area (**Equation 8.8**) can be written as follows.

$$\frac{da}{dt} = Nv \left[k + \left(\frac{dk}{dt} \right) t \right] \frac{\sqrt{r^2 - a^2}}{\pi a^3} \quad (8.14)$$

A numerical solution to **Equation 8.14** will yield estimations of the wear depth and wear volume of a ball and a flat surface (using **Equations 8.4, 8.5, 8.12, and 8.13**). The numerical solutions presented in this paper have been obtained using the implicit scheme `ode15s` in MATLAB®.

The functional form which is chosen for the specific wear rate is conditioned by the experimental findings. It may be the case that a constant specific wear rate is found for tests of varying sliding distance, suggesting that the analytic results of the previous section are sufficient to describe the evolution of wear. For more complex cases, where the specific wear rate is a function of time, it must be emphasised that care needs to be taken when choosing a functional form for $k(t)$, especially when only a few data points are available. Table 8.1 considers two special cases for $k(t)$. In these cases, care must be taken when extrapolating the data – since a negative gradient may lead to unrealistic negative wear rates.

Table 8.1. Two special cases of **Equation 8.14**, where specific wear rates vary linearly and exponentially with time.

Functional Form	Contact Area Temporal Gradient
Linear , $k(t) = \alpha_1 t + \alpha_2$	$\frac{da}{dt} = Nv [2\alpha_1 t + \alpha_2] \frac{\sqrt{r^2 - a^2}}{\pi a^3}$
Exponential , $k(t) = \beta_1 e^{\beta_2 t}$	$\frac{da}{dt} = Nv \beta_1 [1 + \beta_2 t] e^{\beta_2 t} \frac{\sqrt{r^2 - a^2}}{\pi a^3}$

Figure 8.3 shows how the specific wear rate varies with time for the AISI 440C steel ball and BALINIT® DLC STAR. A linear regression (black line) and an exponential regression (red line) are used to fit the model to the data. For both the ball and BALINIT® DLC STAR, an exponential curve provides the best fit. The wear model can now be fitted to the data, by numerically solving the appropriate ordinary differential equation (**Equation 8.14**) using an exponential form for $k(t)$.

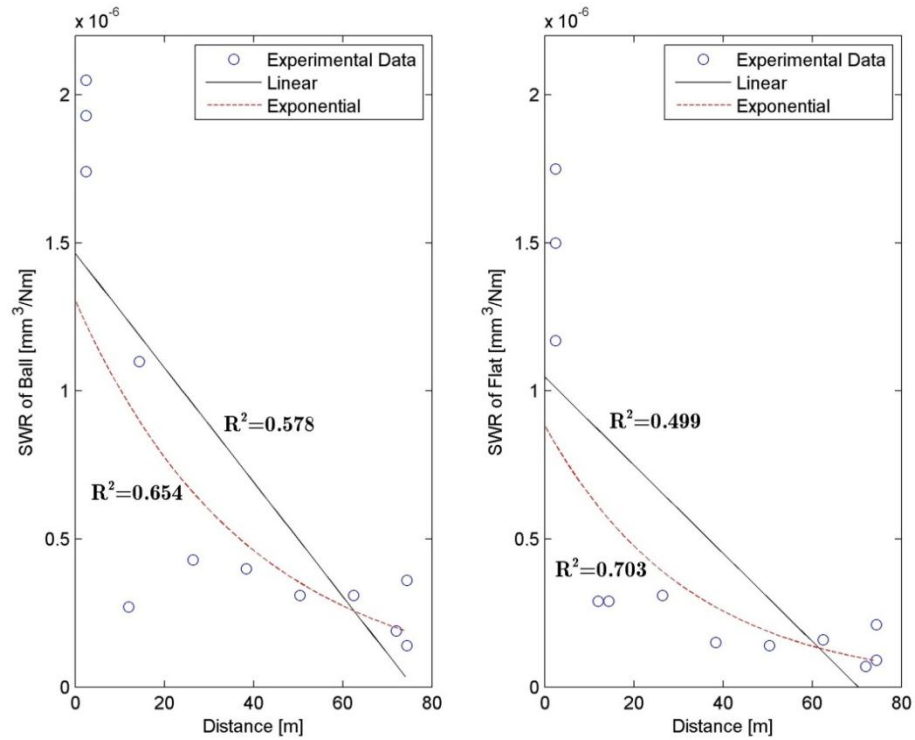


Figure 8.3. The specific wear rate (SWR) plotted against sliding distance for the ball (left), and BALINIT[®] DLC STAR (right). Experimental data is indicated by blue circles. The linear regression is given as a black line, and the exponential regression is given as a dashed red line.

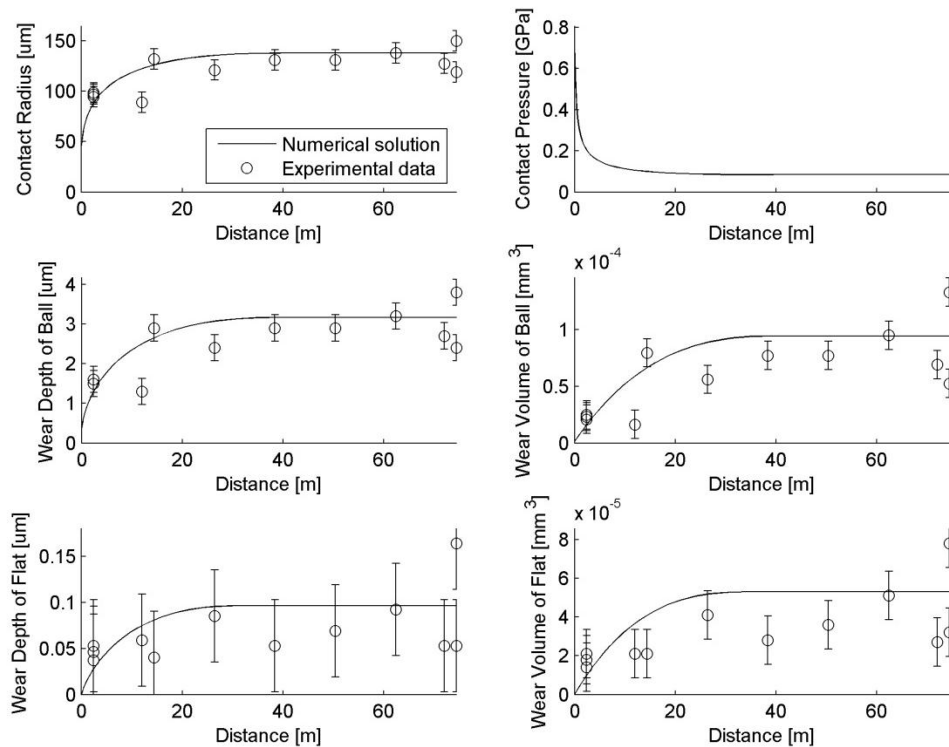


Figure 8.4. Contact radius (top-left), contact pressure (top-right), wear depth of the ball (middle-left), wear volume of the ball (middle-right), wear depth of BALINIT[®] DLC STAR (bottom-left), wear volume of BALINIT[®] DLC STAR (bottom-right), at a normal load of 5 N, plotted against sliding distance. The specific wear rate of the ball and BALINIT[®] DLC STAR is assumed to decrease exponentially. The black line represents the numerical solution, and the black circles represent experimental data. Error bars, shown by black vertical lines, represent the error in measurement.

Figure 8.4 shows the numerical solution of the new semi-empirical wear model (black line) fitted to the experimental data (black circles). The change in contact radius (top-left) fits very well with the experimental data, predicting a final contact radius of 138 μm suggesting a mean contact pressure of 0.08 GPa. The final wear depth of the AISI 440C steel ball is predicted to be 3.17 μm in comparison to the observed average of 3.1 μm from the experiments. The wear depth of BALINIT[®] DLC STAR is estimated as 0.096 μm in comparison to the observed average of 0.11 μm from the experiments.

A time dependent specific wear rate leads to an excellent fit for the data at a normal load of 5 N and a frequency of 5 Hz. The wear depth of each surface is predicted accurately since the time-dependent specific wear rate leads to an accurate prediction of wear volume as a function of sliding distance. In the general case, for any given phenomenological law that accurately predicts wear volume as a function of input parameters such as normal load or reciprocating frequency, the wear depth can be predicted accurately as a function of sliding distance.

8.6. Conclusion

This chapter derived formulae from first principles to predict the wear depth of a ball and a flat surface through time as they slide against each other, in relation to any phenomenological law for wear volume, and taking into account the component geometry.

The conclusions from this chapter are as follows:

- **Archard's and Preston's formulations were generalised to include the change in contact area as a ball-on-flat test progressed. An equation was derived to predict the change in contact radius with time for any phenomenological wear law (see Equation 8.10). From this, wear depth of a ball and a flat surface were extracted.**
- **The formulation presented provides a robust methodology to convert from any accurate prediction of wear volume as a function of sliding distance and test parameters to an accurate prediction of wear depth as a function of sliding distance and test parameters.**
- **The model features a high degree of modularity as it can accommodate arbitrary functional forms to calculate wear volume. It is hoped that the**

flexibility of the model presented in the paper will be exploited by tribologists to further put its descriptive and predictive power to the test.

- Experimental tests of BALINIT[®] DLC STAR against an AISI 440C steel ball showed that a constant specific wear rate did not allow for accurate prediction of the wear depth. Experimentally, the specific wear rate was observed to vary with time. This was due to the formation of a transfer layer, the effects of which are not included for in Archard's wear law.
- Assuming a specific wear rate varies in time, an exponential model was fitted to the data for the ball and flat surfaces based on experimental observations. Wear volume and wear depth was predicted accurately with less than a 5 % deviation from the experimental data. The assumption that the specific wear rate varies in time may, in a general case, be due to a transition between wear mechanisms or due to chemical changes.
- Care should be taken when fitting functional forms for the specific wear rate. Critically, a need for several data points was highlighted to allow confidence in the choice of fitting a functional form for the specific wear rate.
- Possible extensions to this work include a consideration of a line contact or elliptic contact following a similar methodology to the point contact discussed in this work.

Chapter 9. An Incremental Wear Model for Diamond-Like Carbon Coatings

An incremental finite element wear model based on Archard's wear law is developed for BALINIT[®] DLC STAR and an AISI 440C steel ball in deionised water. Under a ball-on-flat reciprocating contact, a transfer layer was observed to develop, causing a decrease in the rate of wear. A transfer layer is incorporated in the finite element model, and the growth of the transfer layer is prescribed according to a logistic function. A logistic formulation has been applied previously to model the growth of biological films, and describe population dynamics, and is presented here to describe the growth of a transfer layer. The mechanical properties of the transfer layer were identified previously using nanoindentation (see **Section 6.5.4**).

Dispersive numerical error is common in incremental wear models due to discretisation of the contact surfaces as a finite element mesh. A unique formulation is presented that reduces the magnitude of numerical error by integration of a diffusion equation on the contact surfaces which enforces continuity. Additionally, the number of finite element solutions is minimised by imposing a minimum wear depth condition. The wear model is fitted to the experimental data presented in **Chapter 7**.

Section 9.1 provides an introduction to the chapter. Next, in **Section 9.2**, the methodology of the incremental wear model is presented. **Section 9.3** presents the model predictions for the wear depth of BALINIT[®] DLC STAR and an AISI 440C steel ball at a sliding velocity of 0.02 m/s and a normal load of 5 N in deionised water. **Section 9.4** presents a discussion of the results, and a comparison to the wear model of **Chapter 8**.

9.1. Introduction

In any mechanical system, contacting surfaces moving in relative motion to each other experience wear, which after time may lead to a loss in geometric tolerance and a decline in performance. As a result, the phenomena of wear must be readily understood, and predictive solutions implemented into the design of systems and system components.

The implementation of a DLC coating as a material solution requires understanding of the coating tribology. Crucial to this is the development of a transfer layer which is known to control the specific wear rate (SWR) of a DLC coating [3, 50]. Under reciprocating sliding of BALINIT[®] DLC STAR and AISI 440C steel in deionised water, the growth of a transfer layer was observed in all tests (see **Chapter 6**). Therefore, to accurately predict wear, the growth of a transfer layer needs to be incorporated into such a wear model. In **Chapter 8**, this was included in the form of an exponential decay of the specific wear rate as a transfer layer developed. In this chapter, a new approach is presented.

An increasingly common methodology for the prediction of wear is the incremental wear model (see **Section 4.4**), where surfaces are assumed to wear according to some phenomenological wear law such as Archard's wear law [110-112]. The incremental wear model invokes an iterative procedure where the pressure distribution between contact surfaces is evaluated, and used to calculate the depth of wear along each surface. The geometry of the contact surfaces is updated, allowing the computation of a new pressure distribution. In this manner, the iterative procedure steps forwards through time.

Many incremental wear models in the literature show artificial spikes in the pressure distribution. Hegadekatte et al. [132] describe these numerical instabilities in terms of the dispersive components of the integrated pressure distribution. It is suggested that these numerical errors develop due to the discretisation of the contact surfaces into a finite element mesh [133]. A limitation on the maximum wear depth in any one time-step was suggested to reduce the magnitude of the numerical error [128, 129].

In this chapter, an incremental finite element wear model is developed using COMSOL Multiphysics 4.3 and LiveLink™ for MATLAB® which enforces continuity along the contact surfaces by integration of a diffusion equation.

- A diffusion coefficient can be adjusted to allow a large time-step whilst minimising the magnitude of numerical instabilities in the pressure distribution.
- The number of finite element solutions is minimised by imposing a minimum wear depth condition.

The 2D growth of a transfer layer is prescribed according to a logistic equation, and this leads to a reduction in the SWR.

The adaptive wear model is validated against a physical experiment consisting of a ball-on-flat reciprocating contact between a 6 µm thick BALINIT® DLC STAR and an AISI 440C steel ball in deionised water (using the data from **Chapter 7**).

9.2. Methodology

The wear model presented uses COMSOL Multiphysics 4.3 finite element software in combination with LiveLink™ for MATLAB®. The LiveLink™ interface is based upon a COMSOL client running within MATLAB®, allowing creation and alteration of a COMSOL model by communicating with the COMSOL server. In this capacity, LiveLink™ for MATLAB® allows for the implementation of an incremental wear model by alteration of the COMSOL model geometry.

The first subsection presents the finite element model. **Section 9.2.2** presents the methodology by which wear is evaluated.

9.2.1. Finite element model

A quasistatic finite element contact model, implemented in COMSOL Multiphysics 4.3, is used to solve the equations of linear elasticity and evaluate the pressure distribution between an AISI 440C steel ball and a nominally flat DLC coating (deposited on an AISI 440C steel substrate). The Young's modulus and Poisson's ratio used for the DLC coating and AISI 440C steel ball are provided in **Table 5.1** and **Table 5.2**, respectively. The elastic properties of the transfer layer were found using nanoindentation (see **Section 6.5.4**). The finite element model is 2D, and uses a plane strain approximation to evaluate the contact pressure distribution based upon a linear elastic model. The DLC coating is modelled as a single, homogenous layer, and is assumed to be perfectly

adhered to the AISI 440C steel substrate. Residual stress within a DLC coating (which arises during the coating deposition process) is neglected in this work.

The geometry of the finite element model is shown in **Figure 9.1**. The model geometry is a 1 mm^2 cross-section of a point contact between an AISI 440C steel ball and a DLC coating. An active region is defined on the ball, near the area of contact, where a transfer layer can develop, and the implementation of this is discussed below. A normal load is applied to the top boundary, while the bottom boundary is fixed in place. A contact pair is defined between the DLC coating and the AISI 440C steel ball, with a Coulomb friction model which results in a tangential stress when a horizontal displacement is applied to the ball to simulate sliding.

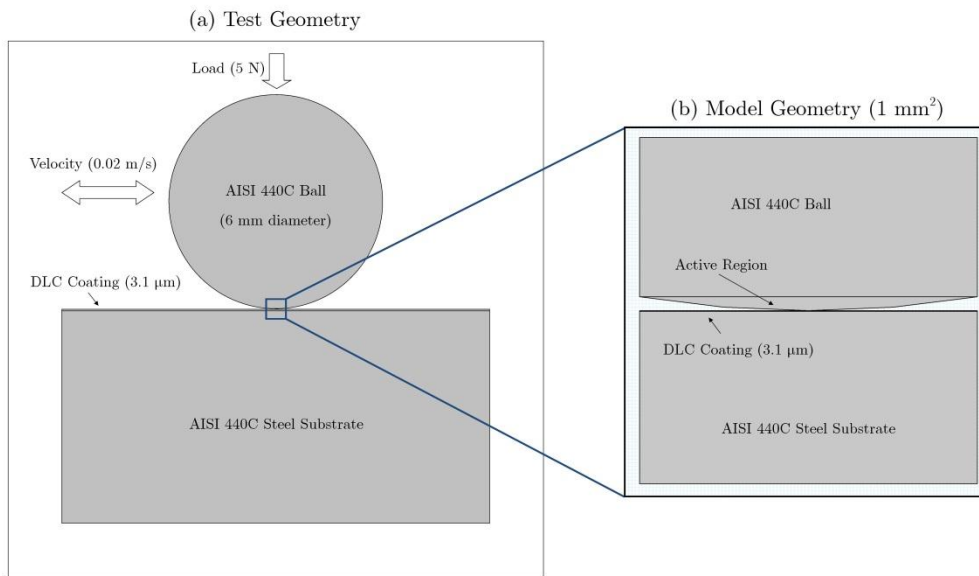


Figure 9.1. (a) The actual test geometry, and (b) the model geometry, including the active region.

In two dimensions, COMSOL can only approximate a line contact since axial symmetry is not supported. Therefore to model the contact problem in two dimensions the length of the line contact must be defined. There is no ideal choice – but the obvious choice is to set the contact area identical to that of the equivalent Hertzian point contact. Therefore the depth chosen is $\pi a_p^2 / 2a_l$ (where a_p is the radius of a point contact, and a_l is the width of a line contact). This results in an approximately 20 % lower average contact pressure than the associated point contact. This is a required simplification for a 2D point contact model.

The initial mesh uses 140,000 quadratic triangular elements with a maximum element size of 1 μm in the active region. This provides a high resolution around the contact region, and is optimised so that further refinement does not significantly alter the results. The mesh is coarser away from the contact region to prevent needless computation.

The growth of a transfer layer is implemented within an active region (see **Figure 9.2**) where the material properties are defined according to a polynomial $h(s,t)$ which describes the thickness of the transfer layer across the contact. The parameter s refers to the material coordinate system. The polynomial $h(s,t)$ is interpolated from the local value of the transfer layer height $h(n_i,t)$ at every mesh node n_i along the destination (top) boundary of the contact pair. A polynomial $C(s,t)$ defines the surface of the ball. The material properties are defined such that above $C(s,t) + h(s,t)$, the surface is defined as AISI 440C steel, and below it, the surface is defined as transfer layer.

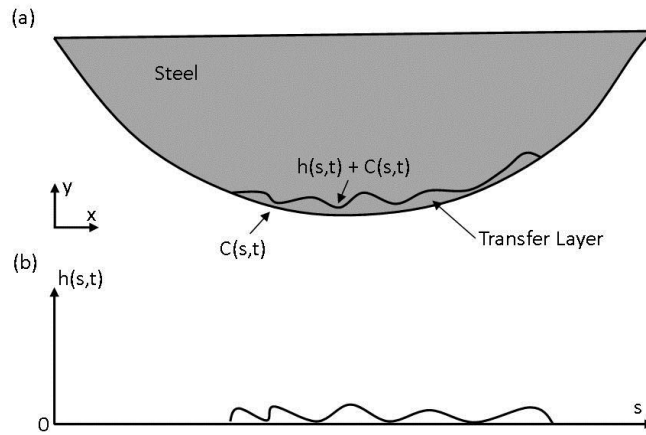


Figure 9.2. (a) A sketch of the active region of the ball, where the contact surface and the transfer layer height are defined by polynomials $C(s,t)$ and $h(s,t)$, and (b) the polynomial $h(s,t)$ which defines transfer layer thickness.

Initially, the transfer layer height is zero across the contact. The minimum element size in the active region is $0.125 \mu\text{m}$ so that the region has a reasonable resolution; however it cannot describe the growth of a transfer layer in detail. The local presence of a transfer layer will affect the pressure distribution. The finite element model is presented in detail in **Appendix A**.

9.2.2. Implementation of wear

To model the wear of a DLC coating and AISI 440C steel ball, the finite element model described above is used to evaluate the pressure distribution at each time step. The wear depth at each mesh node is calculated based upon the local pressure, by integration of Preston's wear law (see **Equation 4.3**). To minimise the magnitude of numerical instabilities whilst still using a large time-step, the contact surfaces are forced to be sufficiently smooth through integration of a diffusion equation (described below). An iterative procedure is used to integrate forwards in time and is detailed in **Figure 9.3**. The MATLAB[®] script to implement the modelling routine within LiveLink[™] for MATLAB[®] is provided in **Appendix B**.

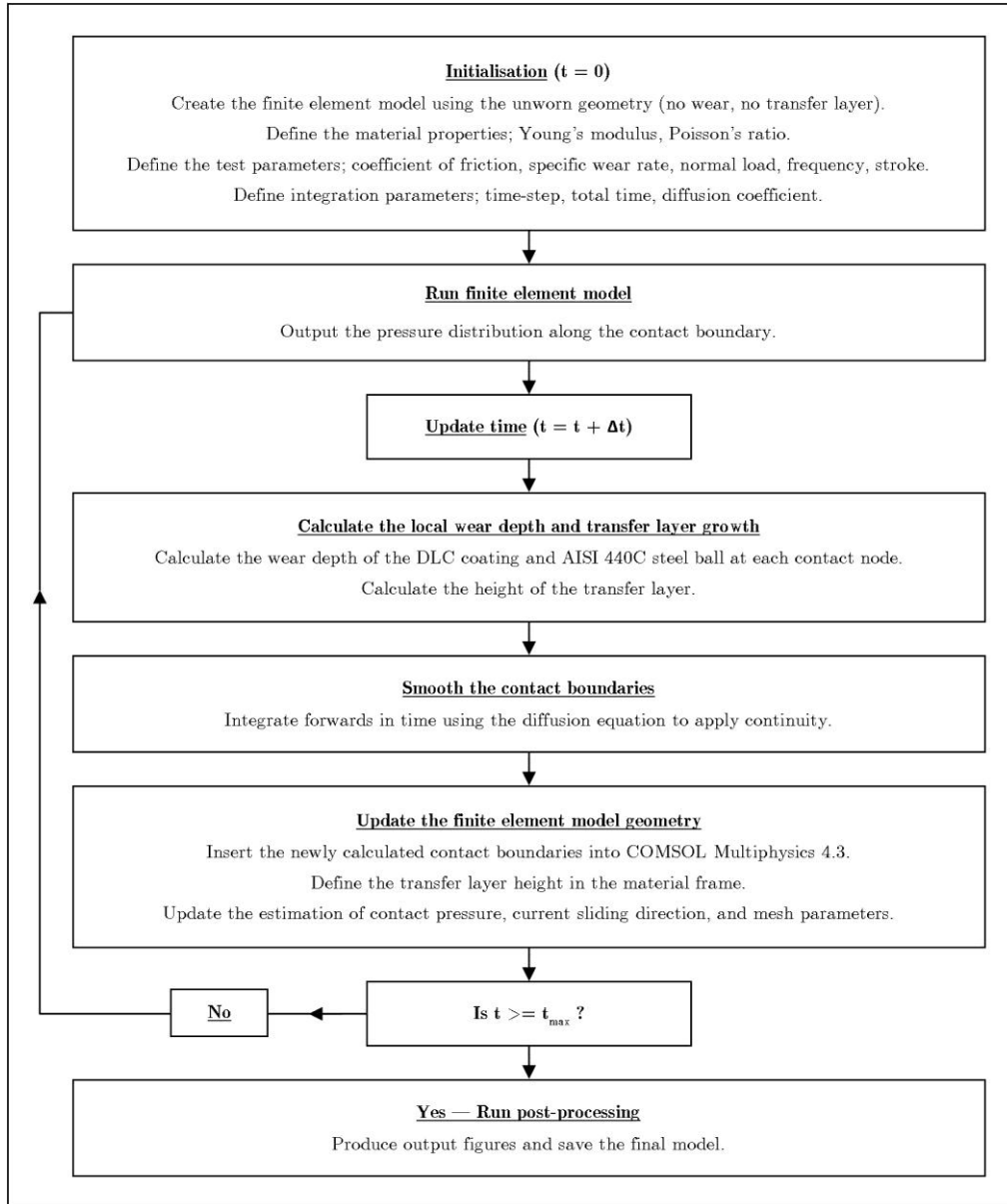


Figure 9.3. The procedure for modelling the wear of BALINIT® DLC STAR and AISI 440C steel ball using COMSOL Multiphysics 4.3 and LiveLink™ for MATLAB®.

i. Initialisation

The unworn geometry is created or imported into COMSOL Multiphysics 4.3. In this case, a 2D ball-on-flat contact is created. The finite element model is detailed in **Section 9.2.1**. A script in MATLAB® is used to initialise LiveLink™ for MATLAB®, and define the material properties, test parameters, and integration parameters. The material parameters are the Young’s modulus and Poisson’s ratio of the DLC coating, AISI 440C steel ball, and transfer layer. The test parameters are the coefficient of friction, the specific wear rate of each surface, the normal load, frequency, and stroke. The integration parameters are the total integration time, the time-step, and the diffusion coefficient. A diffusion coefficient is required to solve the diffusion equation,

and smooth the contact surfaces. For a given time-step, a diffusion coefficient much be chosen which is large enough to minimise dispersive numerical instabilities in the pressure distribution, but small enough such that the macroscopic geometry of the contact surfaces is preserved.

ii. Run finite element model

The finite element model simulates the stresses induced by static Coulomb friction at a predefined normal load. The finite element model takes less than 10 minutes to solve on a PC equipped with 12.0 GB of RAM – the solution time is dependent on the number of elements, and the accuracy of the initial guess for the contact pressure (which aids convergence of the finite element solution). The main output of the linear elastic model is the pressure distribution $P(s, t)$.

A finite element model is not solved every iteration – rather, the likelihood a finite element model is solved for any given iteration is proportional to the magnitude of the specific wear rate, and controlled by the parameter *opt*. When a finite element model is not solved, the pressure distribution from the previous iteration is used instead. This formulation is intuitively correct, since when the specific wear rate is small, less wear has occurred, and the pressure distribution is unlikely to have varied as much. Using this formulation, the number of finite element solutions can be reduced enormously.

iii. Calculate the local wear depth and transfer layer growth

The surfaces of the DLC coating and the AISI 440C steel ball are defined by a piecewise cubic interpolation of the contact coordinates $C(n_i, t)$ and $D(n_i, t)$. The contact coordinates of the unworn surfaces of the AISI 440C steel ball and DLC coating are denoted by $C(n_i, 0)$ and $D(n_i, 0)$, respectively. The wear depth of the surfaces of the DLC coating and AISI 440C steel ball are denoted by $w_{DLC}(n_i, t)$ and $w_{Ball}(n_i, t)$, respectively.

$$\begin{aligned} C(n_i, t) &= C(n_i, 0) + w_{DLC}(n_i, t) \\ D(n_i, t) &= D(n_i, 0) - w_{Ball}(n_i, t) \end{aligned} \tag{9.1}$$

To evaluate the wear depth of each surface, the forward Euler method is used to integrate Preston’s formulation of Archard’s law [112] (see **Equation 4.3**) forward in time. A subroutine controls the integration in time from t to $t + \Delta t$ using a smaller time-step $\Delta\tau \ll \Delta t$ defined such that the cyclic movement of the ball relative to the surface of the DLC coating can be resolved even when Δt is large. For a ball sliding with velocity v and a time-step $\Delta\tau$, the horizontal displacement of the ball is given as

$x_d = v\Delta\tau$. The MATLAB[®] script controls the position and direction of the ball on the DLC coating surface at each time-step.

The wear depth of the DLC coating at contact node n_i at time $t + \Delta\tau$ is given by **Equation 9.2**, where $k_{DLC}(t)$ is the specific wear rate of the DLC coating.

$$w_{DLC}(n_i, t + \Delta\tau) = w_{DLC}(n_i, t) + k_{DLC}(t)P(n_i, t)v\Delta\tau \quad (9.2)$$

The wear depth of the AISI 440C steel ball at contact node n_i at time $t + \Delta\tau$ is given by **Equation 9.3**, where $k_{Ball}(t)$ is the specific wear rate of the AISI 440C steel ball.

$$w_{Ball}(n_i, t + \Delta\tau) = w_{Ball}(n_i, t) + k_{Ball}(t)P(n_i, t)v\Delta\tau \quad (9.3)$$

Based on the experimental data for the reciprocating sliding of a DLC coating and an AISI 440C steel ball from **Chapter 7**, the SWR is postulated to decrease from an initially high wear rate to a steady-state wear rate as a transfer layer grows in the contact region [3, 50]. If the height of a transfer layer is denoted h and prescribed to increase from 0 to h_{max} as sliding wear occurs, then the SWR for the DLC coating and the AISI 440 steel ball can be given as functions of h by **Equation 9.4**, where $k_{DLC}(0)$, $k_{DLC}(t_{max})$, $k_{Ball}(0)$, and $k_{Ball}(t_{max})$, are the initial and final specific wear rate of the DLC coating and AISI 440 steel ball. These values are provided from the experimental data reported in **Figure 7.8**.

$$\begin{aligned} k_{DLC} &= k_{DLC}(0) + k_{DLC}(t_{max}) - k_{DLC}(0) \frac{h(t)}{h_{max}} \\ k_{Ball} &= k_{Ball}(0) + k_{Ball}(t_{max}) - k_{Ball}(0) \frac{h(t)}{h_{max}} \end{aligned} \quad (9.4)$$

In order to describe the growth of a transfer layer, a functional form for h needs to be provided. Analysis of the wear data (see **Figure 8.3**) suggests that the SWR decreased at an exponential rate, and therefore a logistic function was suggested to describe the growth of a transfer layer (see **Equation 9.5**). A logistic formulation has been applied previously to model the growth of biological films, and describe population dynamics, and is presented here to describe the growth of a transfer layer. Growth begins slowly, and then increases rapidly, until saturation at which point the growth rate decays to zero (see **Figure 9.4**). The logistic growth parameter κ is used to fit the incremental wear model to the experimental data. The maximum transfer layer height is given by h_{max} and is estimated to be 0.3 μm based on the literature [3].

$$h(t) = h_{max} \frac{1 - e^{-\kappa t}}{1 - e^{-\kappa t_{max}}} \quad (9.5)$$

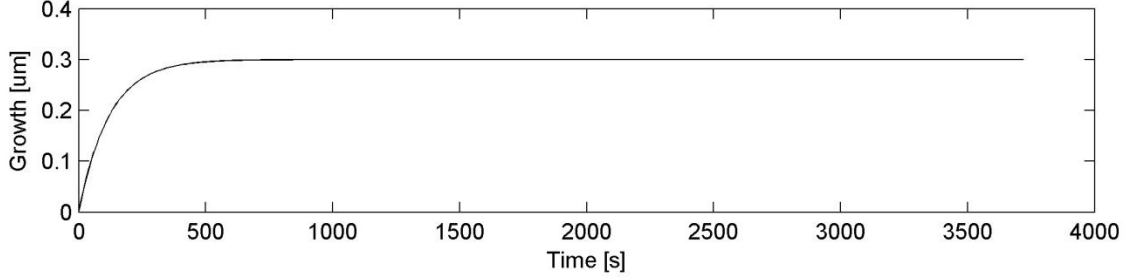


Figure 9.4. The prescribed growth of the transfer layer with time, according to a logistic function (see **Equation 9.5**) with logistic growth parameter $\kappa = 1/120 \text{ s}^{-1}$.

iv. Smooth the contact boundaries

The wear depth at each node is evaluated independently of the height of the surrounding nodes, resulting in the generation of artificially rough contact boundaries when too large a time-step is used. The forward Euler method is derived from a linear truncation of a Taylor series, where continuity is a requirement. Therefore, integration of discontinuous quantities (such as the contact surfaces) will lead to the generation of dispersive numerical error [132]. One method to avoid numerical instability is to keep the time-step relatively small, however this increases the time it takes to solve an incremental wear model. An alternative solution, unique to the present formulation, is to artificially smooth the contact boundaries to enforce continuity.

Equation 9.6 gives a diffusion equation used for each contact boundary and the transfer layer height. It is known that the initial contact boundaries $C(n_i, 0)$ and $D(n_i, 0)$ are smooth, so the requirement is that a diffusion coefficient d_c is chosen such that w_{DLC} , w_{Ball} , and h , are sufficiently smooth. The forward Euler finite difference formulation is used to integrate **Equation 9.6** from time t to time $t + \Delta t$.

$$\begin{aligned}
 \frac{dw_{DLC}}{dt} &= d_c \frac{d^2 w_{DLC}}{dt^2} \\
 \frac{dw_{Ball}}{dt} &= d_c \frac{d^2 w_{Ball}}{dt^2} \\
 \frac{dh}{dt} &= d_c \frac{d^2 h}{dt^2}
 \end{aligned} \tag{9.6}$$

For a given time-step, a diffusion coefficient is chosen which is large enough to minimise dispersive numerical instabilities in the pressure distribution, but small enough such that the macroscopic geometry of the contact surfaces is preserved. Importantly, this formulation conserves wear volume.

v. Update the finite element model geometry

The smoothed contact boundary coordinates, and the current transfer layer height, are updated and loaded into COMSOL Multiphysics 4.3. The model geometry is updated and meshed. The updated new finite element model is run, and the current time is updated. Steps (ii) to (v) are repeated until the time is equal to the integration time.

vi. Run post-processing

The model results are plotted and saved as high resolution jpegs. The solution time of each finite element model is recorded. The MATLAB[®] workspace is saved so that the finite element model can be reloaded and post-processed at a later stage.

9.3. Results

The incremental wear model was integrated for 3720 seconds (the time-span of the experimental data acquisition) with a time-step of 10 seconds. The normal load was 5 N, and the sliding velocity was 0.02 m/s (equivalent to a reciprocating frequency of 5 Hz). The entire model took 96 minutes to solve, during which time 5 finite element models were solved. The initial and final SWR for each surface was taken from the average of the experimental data at 120 seconds and 3720 seconds, respectively. For BALINIT[®] DLC STAR, the initial SWR was $5.67 \times 10^{-7} \text{ mm}^3/\text{Nm}$, and the final SWR was $0.18 \times 10^{-7} \text{ mm}^3/\text{Nm}$. For the AISI 440C steel ball, the initial SWR was $16.0 \times 10^{-7} \text{ mm}^3/\text{Nm}$, and the final SWR was $0.48 \times 10^{-7} \text{ mm}^3/\text{Nm}$. The logistic growth parameter ($\kappa = 0.0083 \text{ s}^{-1}$) was chosen such that the decline in the SWR of each surface fitted the experimental data. The diffusion coefficient ($d_c = 5 \times 10^{-11} \text{ m}^2\text{s}^{-1}$) was optimised by trial and error (see **Section 9.4.1**).

The wear depth predictions of the incremental wear model, shown in **Figure 9.5**, are compared to the experimental wear data measurements (from **Figure 7.12**). The model prediction for the wear depth of BALINIT[®] DLC STAR (see **Figure 9.5 (a)**) is in good agreement with the experimental data. The final predicted wear depth is $0.107 \text{ }\mu\text{m}$. Similarly, the model prediction for the wear depth of the AISI 440C steel ball (see **Figure 9.5 (b)**) is in good agreement with the experimental data. The final predicted wear depth is $3.161 \text{ }\mu\text{m}$. For each surface, the rate at which the SWR transitions from a high initial value to a low final value is controlled by the logistic growth of the transfer layer (see **Figure 9.4**). This empirical fit is required since the growth of a transfer layer causes a transition in the rate of wear, which cannot be described by a single SWR.

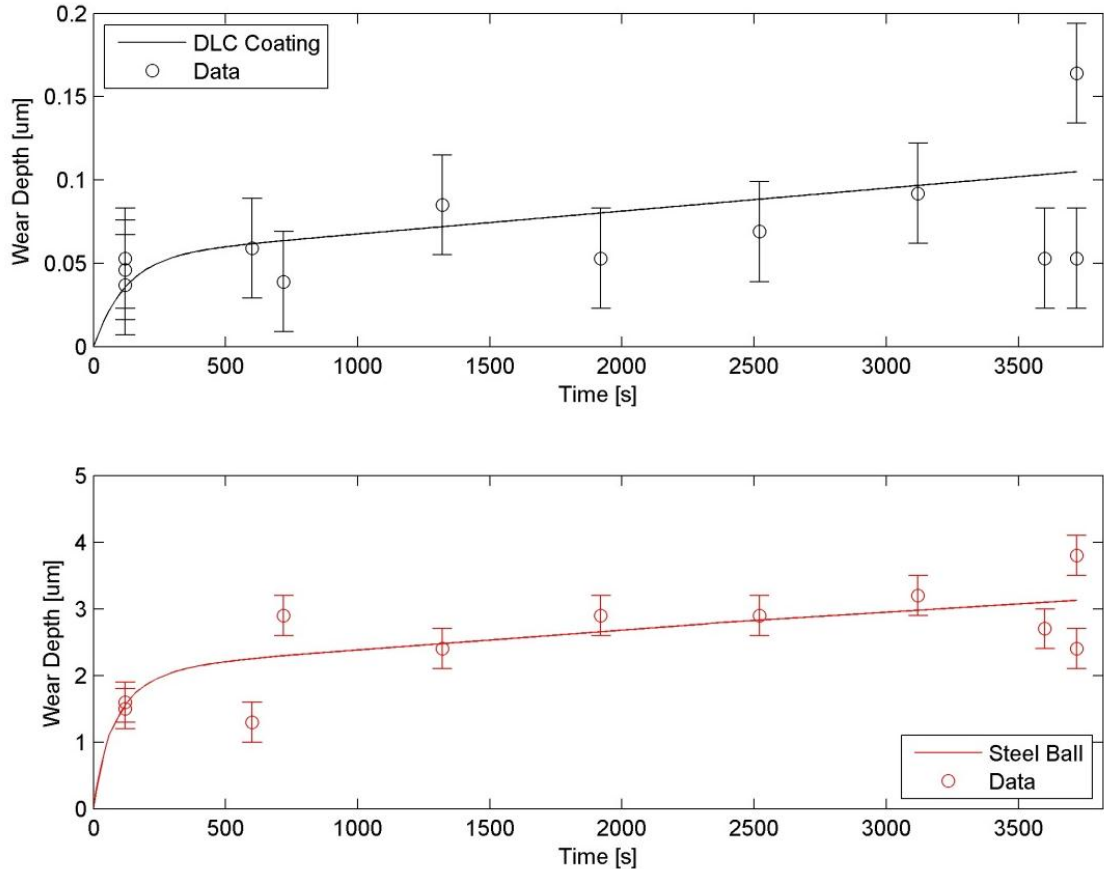


Figure 9.5. The model prediction of wear depth of (top) BALINIT[®] DLC STAR, and (bottom) an AISI 440C steel ball, during reciprocating sliding at a frequency of 5 Hz and a normal load of 5 N. Growth of the transfer layer is prescribed, with a growth parameter of 0.0083. Error bars are shown by vertical lines and represent the error in measurement.

The wear profile of the AISI 440C steel ball is shown in **Figure 9.6 (a) – (l)** as time advances from 10 seconds to 3720 seconds (as labelled). Initially, wear occurs at a fast rate and the tip of the AISI 440C steel ball is worn away. The transfer layer (green line) is observed to develop in the contact region. After 50 seconds, a small sinusoidal perturbation is recognisable in the contact boundary of the AISI 440C steel ball, and this is a result of damped numerical instabilities. This sinusoidal perturbation increases in magnitude as time increases, however the final perturbation has an amplitude of only 200 – 300 nm (which averages to zero across the contact), and as such does not significantly affect the averaged wear results.

The wear profile of BALINIT[®] DLC STAR is analogous to those shown elsewhere in the literature for incremental wear models [129, 132, 143, 144], and is not explicitly shown. Numerical instability did not affect the wear profile of BALINIT[®] DLC STAR.

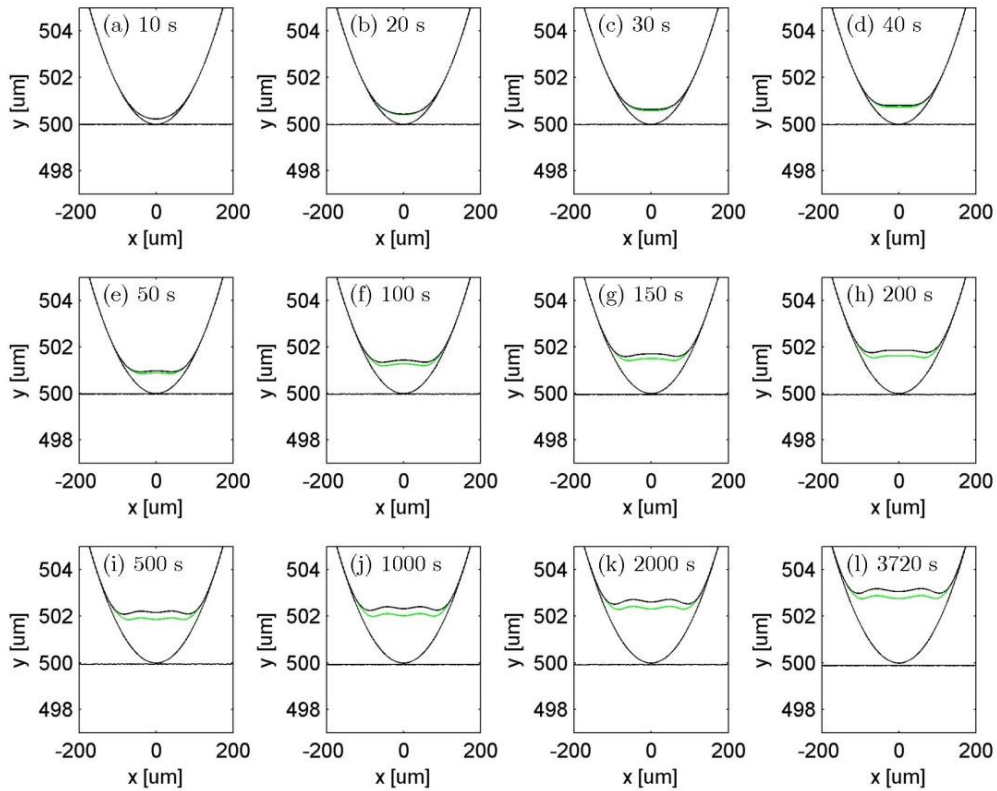


Figure 9.6. The model geometry during reciprocating sliding between BALINIT[®] DLC STAR and an AISI 440C steel ball at a frequency of 5 Hz and a normal load of 5 N. The surface of the DLC coating and AISI 440C steel ball are shown by a solid black line. The transfer layer is shown by a solid green line.

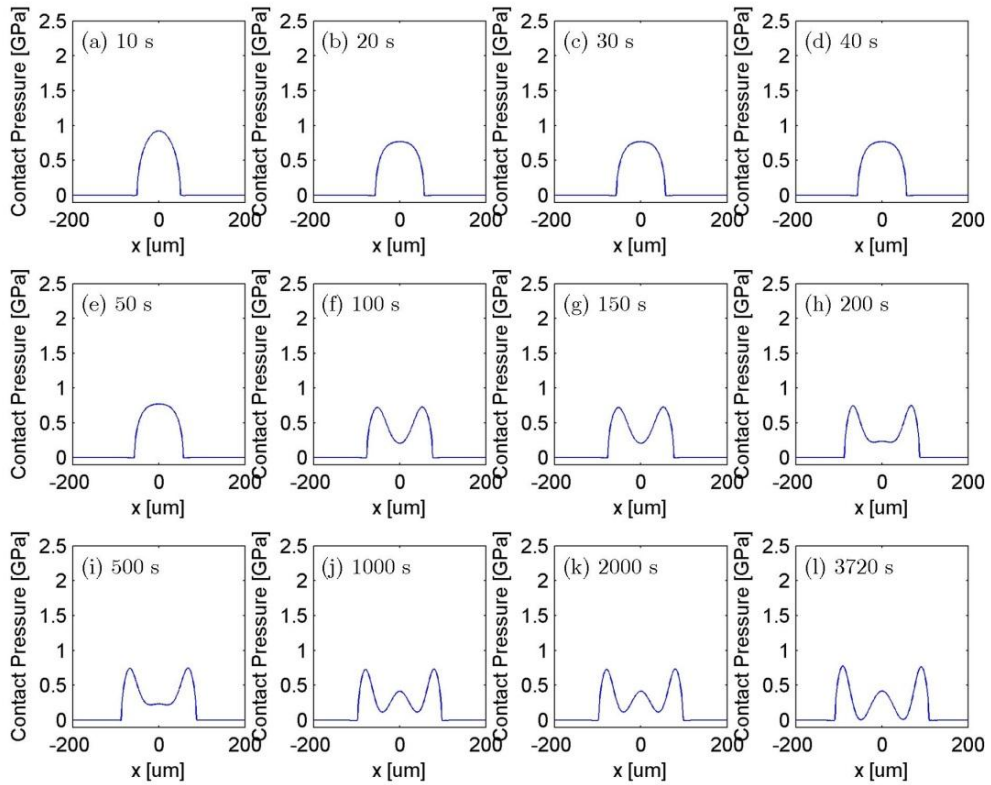


Figure 9.7. The numerical solution for contact pressure between BALINIT[®] DLC STAR and an AISI 440C steel ball, during reciprocating sliding at a frequency of 5 Hz and a normal load of 5 N.

The contact pressure distribution between BALINIT[®] DLC STAR and the AISI 440C steel ball is shown in **Figure 9.7 (a) – (l)** as time advances from 10 seconds to 3720 seconds (as labelled). Initially, the contact pressure distribution is Hertzian in appearance, and decreases in magnitude from 10 seconds to 50 seconds. At 100 seconds, two artificial spikes in the contact pressure distribution are observed, as a result of the sinusoidal perturbation in the contact boundary of the AISI 440C steel ball. The artificial spikes in each contact pressure distribution increase in magnitude as time increases, however the averaged wear results (discussed above) are not significantly affected.

9.4. Discussion

The incremental wear model described uses a time-dependent SWR which decreases in magnitude as a transfer layer is prescribed to grow in the contact (see **Figure 9.5**). For each surface, the rate at which the SWR transitions from a high initial value to a low final value is controlled by the logistic growth parameter. In addition to the empirical fit of the logistic growth parameter, there are two main routines used in this model which are implemented to provide a fast and accurate numerical solution of the wear model. First, a diffusion equation is used to artificially smooth the contact boundaries and damp numerical instabilities. Second, the number of finite element solutions is minimised by imposing a minimum wear depth condition between each finite element solution [133]. The implementation of these routines and their effect on the model predictions are examined in the following two subsections.

9.4.1. Diffusion of the contact boundaries

Numerical instability in finite difference schemes arises due to spatial and temporal discretisation. Most finite difference schemes are based on a Taylor series expansion (in time and/or space) which relies on the continuity of the conserved quantity. The integration of a discontinuous quantity will lead to the generation of numerical error [132]. In the context of finite element models, many authors have noted the presence of numerical instabilities as spikes in the pressure distribution [133]. One method to avoid numerical instability is to keep the time-step relatively small, however this increases the time it takes to solve an incremental wear model. The current work implements a new methodology where continuity is enforced by integration of a diffusion equation to smooth the contact boundaries of each surface.

The selection of an appropriate diffusion coefficient is critical to the evaluation of wear. A diffusion coefficient must be chosen that is large enough to smooth the artificial

roughness of the contact boundaries, but small enough that the macroscopic geometry of the contact boundaries remains unchanged. The diffusion coefficient used in the current model ($d_C = 5 \times 10^{-11} \text{ m}^2/\text{s}$) was optimised by trial and error such that the forward Euler integration scheme using a time-step of 10 seconds is stable.

Table 9.1 presents the total solution time, the average wear depth of each contact surface, and the relative error (in comparison to the wear depth of the ball using a diffusion coefficient of $5 \times 10^{-11} \text{ m}^2/\text{s}$), for a range of diffusion coefficients.

- The optimum value for the diffusion coefficient was $5 \times 10^{-11} \text{ m}^2/\text{s}$.
- When the diffusion coefficient was relatively small, the total solution time and the average wear depth of each contact surface increase. This is due to numerical instability, and the additional time required for a finite element model to converge to a solution when the contact boundaries are rough.
- When the diffusion coefficient was relatively large, the total solution time and the average wear depth of each contact surface increase. This is due to over-smoothing, which inhibits the growth of a transfer layer and leads to a larger SWR than expected.

Table 9.1. A parametric sweep of d_C to assess the total solution time of the incremental wear model in comparison to the relative error of the averaged predictions for wear depth of BALINIT[®] DLC STAR and an AISI 440C steel ball.

d_C ($\times 10^{-11} \text{ m}^2\text{s}^{-1}$)	Solution Time (minutes)	Wear Depth of DLC Coating (μm)	Wear Depth of Ball (μm)	Relative Error (%)
1	119	0.154	4.062	28.5
2.5	93	0.120	3.441	8.9
5	86	0.107	3.161	0.0
10	93	0.134	3.674	16.2
15	102	0.176	4.378	38.5

9.4.2. The minimum wear depth condition

A finite element model is not necessarily solved every iteration. Towards the end of the integration time, the SWR is much lower than at the beginning, and therefore less wear occurs during an individual time-step. To reduce the total solution time, fewer finite element models are solved towards the end of the integration period. Equivalently, it can be stated that a finite element model is only solved after a certain wear depth has been reached since the last finite element solution. The magnitude of the wear depth

that is worn between each finite element solution is controlled by a dimensionless parameter, opt . When opt is large, more finite element models will be solved, and when opt is small, the number of finite element solutions is reduced.

Table 9.2 presents the number of finite element solutions, the total solution time, the average wear depth of each contact surface, and the relative error (in comparison to the wear depth of the ball using $opt = 1.5$), for a range of values of opt .

- As opt increases in magnitude, the number of finite element solutions and the total solution time increase. The wear depth of the AISI 440C steel ball tends towards 3.126 μm .
- The value for opt in the current model is 0.2. This provided numerical solutions which show a relative error in the wear depth of the AISI 440C steel ball of 1.1 % (in comparison to the wear depth of the ball using $opt = 1.5$). This is an acceptable approximation to reduce the solution time by 50 %.
- The average wear depth of the DLC coating is invariant to changes in opt , since the numerical instabilities average out across the wear scar.

Table 9.2. A parametric sweep of opt to assess the total solution time of the incremental wear model in comparison to the relative error of the averaged predictions for wear depth of BALINIT[®] DLC STAR and an AISI 440C steel ball.

opt	Number of Finite Element Solutions	Solution Time (minutes)	Wear Depth of DLC Coating (μm)	Wear Depth of Ball (μm)	Relative Error (%)
0.1	3	75	0.107	3.370	7.8
0.2	5	96	0.107	3.161	1.1
0.5	13	128	0.107	3.139	0.4
1.0	25	152	0.107	3.129	0.01
1.5	37	177	0.107	3.126	0.0

9.4.3. Comparison to the predictions of Chapter 8

It is interesting to compare the predictions of the current computational model to the analytical differential equation presented in **Chapter 8**. To compare both wear models, the same logistic equation (described in **Section 9.2.2**) is used to control the decline in the SWR.

Figure 9.8 displays a comparison of the predictions of the incremental wear model (solid line) to the analytical differential equation (dashed line), for the wear depth of

BALINIT[®] DLC STAR (top) and the AISI 440C steel ball (bottom). For BALINIT[®] DLC STAR, both models accurately predict the transition from a high specific wear rate to a low specific wear rate, and appear to fit the data well. The incremental wear model provides a higher estimation of wear depth (after 3720 seconds) than the differential equation by 4.7 %. This can be attributed to numerical error obtained due to the large time-steps used in the forward Euler integration. For the AISI 440C steel ball, both models accurately predict the transition from a high specific wear rate to a low specific wear rate, and appear to fit the data well. The incremental wear model initially provides a higher estimation of wear depth than the differential equation. The final rate of wear is lower for the incremental wear model than the differential equation. This might be due to numerical error obtained due to the large time-steps used in the forward Euler integration, or due to the approximation of the ball-on-flat contact as a line contact in the 2D finite element model.

The incremental wear model has a constant SWR near the end of the test, and therefore a trustworthy lifetime prediction can be obtained by extrapolation.

At a normal load of 5 N and a sliding velocity of 0.02 m/s (relating to a sliding frequency of 5 Hz), BALINIT[®] DLC STAR is estimated to wear through after 25.4 hours, or a total sliding distance of 1.83 km.

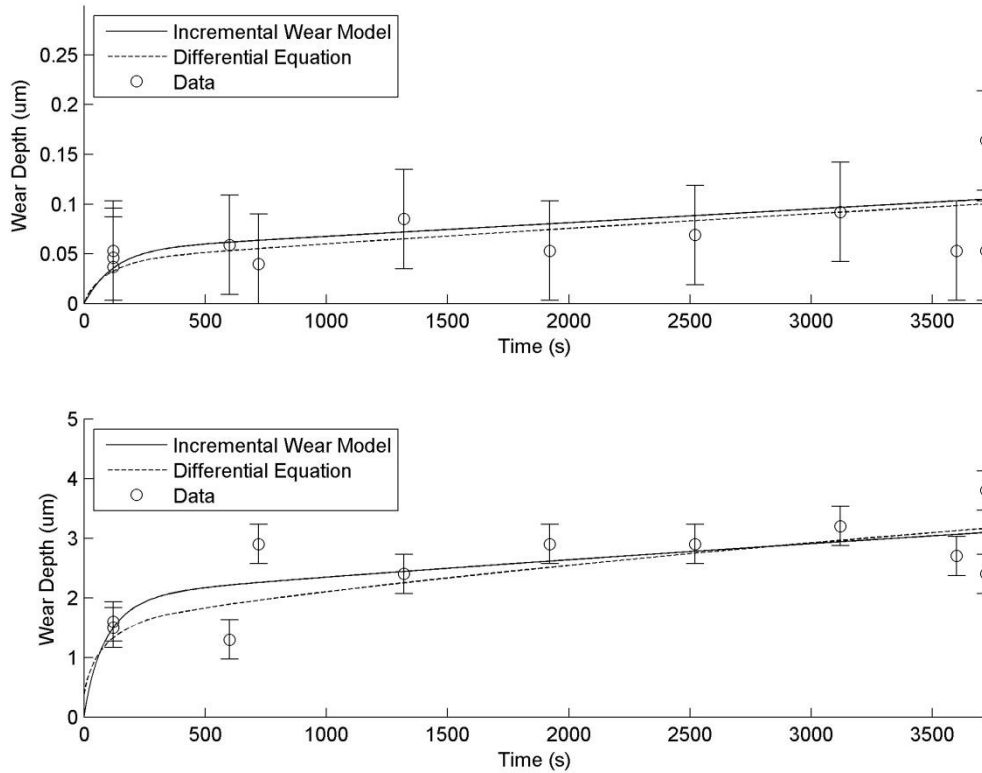


Figure 9.8. The incremental wear model prediction of wear depth (solid line) compared to the differential equation of Chapter 8 (dashed line) for (top) BALINIT[®] DLC STAR and (bottom) an AISI 440C steel ball, during reciprocating sliding at a frequency of 5 Hz and a normal load of 5 N.

The lifetime prediction of BALINIT[®] DLC STAR applies only to tests under reciprocating sliding against an AISI 440C steel ball in deionised water. The prediction applies to the mild wear regime observed in the experiments, assuming that tensile fracture is unlikely to occur, and that the coating shows strong adhesion to the substrate [143, 144]. The reality is that the once the coating wears to a critical thickness it will delaminate. The critical thickness will depend on the strength of adhesion of the coating to the substrate, and the stresses induced by sliding and intensified by friction.

9.4.4. Prediction of wear under different test conditions

The incremental wear model considered in this chapter was fitted to experimental data at a normal load of 5 N and a sliding frequency of 5 Hz. The wear model was successful in the prediction of the wear depth of BALINIT[®] DLC STAR and AISI 440C steel under reciprocating sliding conditions. An important consideration is the prediction of wear depth for a range of different test conditions. This is particularly challenging due to the development of the transfer layer, for which an empirical formulation for the SWR of a DLC coating is required.

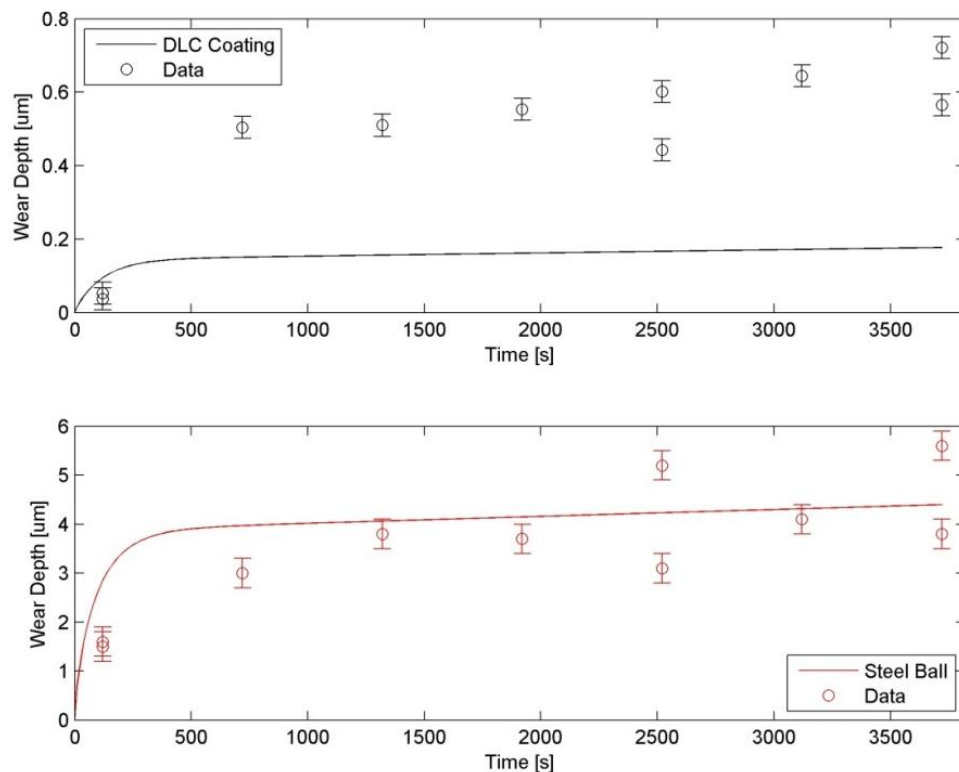


Figure 9.9. The model prediction for wear depth of (top) BALINIT[®] DLC STAR, and (bottom) an AISI 440C steel ball, during reciprocating sliding at a frequency of 5 Hz and a normal load of 20 N. The model was fitted to the data at a normal load of 5 N.

Figure 9.9 presents the computational model prediction for wear depth of BALINIT[®] DLC STAR (top) and an AISI 440C steel ball (bottom) at a normal load of 20 N and a sliding frequency of 5 Hz. The wear model predictions are compared to experimental data obtained in **Chapter 7**. The wear depth of BALINIT[®] DLC STAR is under-predicted, and does not compare well to the experimental data. This may be due to a change in wear mechanism, or a change in the VAM of the transfer layer. Optical analysis of the worn surfaces did not identify a reason behind the non-linear increase in the wear rate of BALINIT[®] DLC STAR at a normal load of 20 N. The wear depth of the AISI 440C steel ball compares well to the numerical prediction. The final predicted wear depth is 4.40 μm in comparison of 4.68 μm .

9.5. Conclusion

In this chapter, the development of an incremental wear model which integrated Preston's equation [112] and evaluated the wear depth of BALINIT[®] DLC STAR and an AISI 440C steel ball, under reciprocating sliding conditions in deionised water, was presented. An important input was the pressure distribution between surfaces, which was evaluated using a 2D finite element model (COMSOL Multiphysics 4.3). The model routine was controlled in MATLAB[®] using LiveLink[™] for MATLAB[®].

The conclusions from this chapter are as follows:

- **Implementation of a diffusion equation that enforced smooth contact boundaries and damped the growth of numerical instabilities, allowed for a fast and accurate integration of the wear model. A diffusion coefficient was chosen optimally to preserve the macroscopic geometry whilst minimising numerical error.**
- **A transfer layer was prescribed to grow according to a logistic equation (Equation 9.5). This resulted in a smooth transition from a high initial SWR to a low final SWR, in agreement to the experimental observations of Chapter 7.**
- **The number of finite element model solutions required was minimised by implementation of a minimum wear depth criterion. Only 5 finite element models were solved, and the numerical error in the average wear results was limited to approximately 1.1 %.**

- The incremental wear model accurately predicted the wear depth of BALINIT[®] DLC STAR and an AISI 440C steel ball in deionised water at a normal load of 5 N and a sliding velocity of 0.02 m/s (see Figure 9.5). The model predicted that BALINIT[®] DLC STAR would wear through after a sliding distance of 1.83 km.
- The incremental wear model was unable to accurately predict the wear depth of BALINIT[®] DLC STAR at a normal load of 20 N and a sliding velocity of 0.02 m/s. This may have been due to a change in wear mechanism, or a change in the VAM of the transfer layer, although no cause for this was observed optically.
- An excellent comparison was drawn between the predictions of the incremental wear model of the current chapter, and the analytical differential equation derived in Chapter 8.
- Further work will extend the current 2D formulation of the wear model (which approximates a line contact) into a 3D finite element model which simulates a point contact. Additionally, the semi-empirical model presented (in terms of a prescribed transfer layer growth) will be extended into a more realistic description of transfer layer growth including oxidative processes and plastic deformation.

Chapter 10. Conclusions and Future Work

This chapter compares the work presented in each previous chapter of this thesis, and presents a general discussion of the experimental and modelling outcomes in the context of current literature. Experimentally, unique contributions to knowledge regarding the tribology of DLC coatings in water, and the dependence of the tribology on test parameters and environmental species, are discussed. In the context of modelling, two distinct wear models were presented in **Chapter 8** and **Chapter 9**, and each provided an important extension to current state-of-the-art wear models available in the literature. Each wear model was used to predict the wear depth of BALINIT[®] DLC STAR as a function of sliding distance. This chapter concludes with a discussion of potential avenues for future work.

Section 10.1 begins by reviewing the main objectives in the context of Rolls-Royce research and development activities. Following this, the experimental and modelling conclusions of the thesis are discussed. **Section 10.2** suggests future directions for additional research.

10.1. Conclusions

One of the primary aims of this work was to provide a predictive model for the wear of DLC coatings in a water environment. Wear models for DLC coatings in water were missing from the literature, and before the tribology of a DLC coating in an environment as complex as a pressurised water reactor could be assessed, a simple predictive model needed to be developed for DLC coatings in a water environment. Additionally, Rolls-Royce were interested in the effect of iron oxide species on the tribology of DLC coatings – an initial question was whether the development of a transfer layer would be affected by iron oxide species – and so the tribology of DLC coatings against steel in water was set as the focus of the work.

Rolls-Royce were interested in the tribological testing of DLC coatings from manufacturers in the UK, since any future use of DLC coatings in pressurised water reactors would need to be from a reliable supplier. An understanding of the link between the tribology of a DLC coating and the deposition method was required however, since if a coating manufacturer of a certain DLC coating was to cease trading, the DLC coating (and its good tribology) would need to be reproduced. Three DLC coatings were obtained from coating manufacturers within the UK; Graphit-iC™ from Teer Coatings, BALINIT® DLC STAR from Oerlikon Balzers, and Adamant® from Diamond Hard Surfaces.

Initially, a literature review [160] was undertaken, in terms of the mechanical and tribological properties of DLC coatings against steel in water, and the current modelling capability. Subsequently, reciprocating wear tests of each DLC coating against steel in water were run to understand the tribology in this environment. **Section 10.1.1** presents the conclusions from the mechanical and tribological testing of the commercial DLC coatings (see **Chapter 6** and **Chapter 7**). Finally, two distinct wear models were developed (see **Chapter 8** and **Chapter 9**) to predict the tribology of a DLC coating against steel in water. Each model is a valuable extension to the current literature regarding the modelling of wear, outside the context of DLC coatings. **Section 10.1.2** discusses the conclusions regarding each predictive wear model.

10.1.1. Experimental conclusions

Chapter 6 examined the tribology of three commercial DLC coatings (Graphit-iC™, BALINIT® DLC STAR, and Adamant®) against AISI 52100 steel in distilled water [161]. Reciprocating sliding tests ran at a normal load of 5 N and a sliding velocity of 0.076 m/s for varying test time (30 – 3600 seconds). The focus of the sliding wear tests was to compare the tribology of the commercial DLC coatings, and to examine the effect of iron oxide species on the formation of a transfer layer.

- **Adamant® showed the lowest and least varied coefficient of friction (0.17 – 0.19) throughout the sliding wear test. In comparison, the coefficient of friction of Graphit-iC™ and BALINIT® DLC STAR varied over the range 0.2 – 0.5.**
- **The specific wear rate (SWR) of Adamant® was immeasurable and estimated to be of order 10^{-8} mm³/Nm. For BALINIT® DLC STAR and Graphit-iC®, the SWR was 1.8×10^{-7} mm³/Nm and 2.2×10^{-7} mm³/Nm, respectively.**

Recent work by Scharf and Singer [48, 79-81] has suggested that the tribology of a DLC coating can be controlled by the **velocity accommodation mode (VAM)** of the transfer layer (see **Figure 3.5**) – either interfacial sliding, or shear and re-circulation of debris. The VAM of the transfer layer of each DLC coating was defined based on optical microscopy.

- **Interfacial sliding was the dominant VAM for Adamant®. A carbonaceous transfer layer was present at all times (as identified by Raman spectra), and low friction and low SWR were observed as a result.**
- **Shear was the dominant VAM for BALINIT® DLC STAR and Graphit-iC®. The carbonaceous transfer layer which was initially present was replaced by iron oxide species (as identified by Raman spectra), and high friction and high SWR were observed as a result.**
- **A three-body abrasive wear mechanism involving hematite particles was suggested to be responsible for the high specific wear rate of Graphit-iC™ and BALINIT® DLC STAR in comparison to Adamant®.**

Of the three commercial DLC coatings examined, Adamant® showed the best tribology at the given test conditions. In addition, the tribology of Adamant® was unaffected by

the presence of iron oxide species. The work presented in **Chapter 6** identified the importance of the VAM of the transfer layer on the subsequent tribology.

Further study was required to analyse the critical factors that control the VAM – and govern whether or not interfacial sliding would occur in any given tribological scenario. Adamant[®] showed the best tribology of the commercial coatings examined; however would this good behaviour be affected by changes in test conditions, such as variations in normal load or sliding velocity, or use of a different counterface material. This was the motivation for the work presented in **Chapter 7**, which assessed the effect of varying test parameters such as **normal load** (5 N, 10 N, and 20 N), **sliding frequency** (5 Hz, 10 Hz, and 20 Hz), and **sliding distance** (2.4 – 288 metres) on the tribology of BALINIT[®] DLC STAR and Adamant[®] against AISI 440C steel in deionised water.

- **Interfacial sliding was the dominant VAM observed in all tests, for both Adamant[®] and BALINIT[®] DLC STAR. This was due to the higher oxidation resistance of AISI 440C steel in comparison to AISI 52100 steel, resulting in a reduction in the proportion of iron oxide species.**
- **The coefficient of friction of Adamant[®] varied over the range 0.015 – 0.190 as a function of normal load and sliding frequency according to Equation 7.1.**
- **The coefficient of friction of BALINIT[®] DLC STAR varied over the range 0.008 – 0.034 as a function of normal load according to Equation 7.3.**
- **The coefficient of friction of BALINIT[®] DLC STAR was smaller than the coefficient of friction of Adamant[®], under identical test conditions.**
- **The SWR of Adamant[®] and BALINIT[®] DLC STAR varied across several orders of magnitude for different combinations of normal load, sliding frequency, and sliding distance.**

The importance of the VAM of a transfer layer is shown by examination of the tribological behaviour of BALINIT[®] DLC STAR in the presence of iron oxide species. In **Chapter 6**, the tribology of BALINIT[®] DLC STAR was affected by the presence of iron oxide species, resulting in a high SWR in comparison to Adamant[®]. The identified VAM of BALINIT[®] DLC STAR was shear and extrusion of debris. When the proportion of iron oxide species was reduced (through use of a stainless steel counterface), the coefficient of friction of BALINIT[®] DLC STAR was lower than Adamant[®], and both coatings showed a similar SWR under identical test conditions. The identified VAM of both DLC coatings was interfacial sliding.

To develop a wear model capable of predicting wear depth accurately for a given set of test conditions, an understanding of the dependencies between **wear depth** and **normal load**, **sliding frequency**, and **sliding distance**, were required. The work presented in **Chapter 7** provided these relationships, which added to the predictive power of the wear model.

- **Wear depth of Adamant[®] and BALINIT[®] DLC STAR increased with normal load, and increased non-linearly with sliding distance.**
- **A relationship between wear depth and sliding frequency was not obtained due to the high variance of the dataset.**
- **Wear depth is known to increase monotonically with sliding distance; however the precise relationship is a function of both the SWR (calculated from wear volume) and the component geometry.**

In **Chapter 7**, the nature of the relationship between wear depth and sliding distance was unknown. The relationship was shown to be non-linear, but the precise functional form of the relationship was not identified. This motivated the development of the first wear model (see **Chapter 8**) which provided an explicit formula to describe the evolution of wear depth with respect to sliding distance for a ball-on-flat geometry. To extend this work to an arbitrary geometry, **Chapter 9** developed a more generalised wear model based on the solution of a number of finite element models, which provided predictions of wear depth for any component geometry, but at higher computational expense.

10.1.2. Modelling conclusions

From fundamental geometric roots, **Chapter 8** derived an analytical relation to describe the relationship between wear depth and sliding distance for a ball-on-flat geometry [162]. The theory was utilised to calculate the wear depth of a ball and a flat surface based on wear volume measurements from experiments in combination with Archard's wear law. Wear depth measurements are of concern to the design engineer interested in changes in geometric tolerance.

- **The formulae (see Section 8.3) describe the relationship between wear depth and sliding distance. Wear data for BALINIT[®] DLC STAR (see Chapter 7) was used to validate the wear model.**

- Experimentally, the SWR of each surface was observed to decrease exponentially with sliding distance – due to the formation of a carbonaceous transfer layer – and as a result, a time-dependent SWR was used to fit a semi-empirical model.
- Wear depth of both surfaces was predicted accurately to less than a 5 % deviation from the experimental data.

The predictions of the wear model were validated by the experimental data – although an empirical description for the SWR was required, since the wear data did not align with the predictions of Archard’s wear law. This was due to the growth of a transfer layer in the reciprocating contact, resulting in a transition from a high initial wear rate to a low final wear rate. The wear model shows a high degree of modularity, as it can accommodate arbitrary descriptions for the specific wear rate.

The quality of the wear depth predictions of the model can only be as good as the quality of the input (in terms of a specific wear rate, or a phenomenological law for wear volume). To develop a wear model that provided accurate predictions for wear depth, an understanding of the dependencies between wear depth and normal load were required. Specifically, sufficient experiment data was required to be confident in the quality of the model inputs. This was the focus of **Chapter 7**, however the precise relationship between wear depth and normal load was not obtained due to the high variance in the wear data.

The wear model was derived for a ball-on-flat geometry, and further derivations for differing geometries (such as a line or elliptic contacts) are obvious extensions to the work. The wear model presented in **Chapter 9**, however, was inspired by the requirement to predict wear depth for more complex geometries.

- An incremental wear model was presented using COMSOL Multiphysics 4.3 to predict wear depth between contact surfaces. The wear model was computationally expensive, but the formulation can be applied to components of an arbitrary geometry.
- A unique and efficient methodology was presented to allow fast integration of the equations whilst damping numerical instabilities through integration of a continuity condition along the contact surfaces.

It was observed previously that an empirical description for the SWR was required. In **Chapter 8**, a time-dependent SWR was utilised to predict wear depth as a function of sliding distance (or equivalently time). In **Chapter 9**, a logistic growth of the transfer

layer was prescribed (according to **Equation 9.5**) and this directly controlled the SWR. The development of the transfer layer was included in the finite element model; using mechanical properties obtained from nanoindentation (see **Section 6.5.4**).

- **At a normal load of 5 N and a sliding frequency of 5 Hz, the average wear depth predicted by the model for BALINIT[®] DLC STAR and the AISI 440C steel ball compared well with the experimental data.**
- **The wear depth predictions of the incremental wear model compared excellently to the predictions of the wear model in Chapter 8 (see Figure 9.8).**
- **Extrapolation of the wear data suggested that BALINIT[®] DLC STAR would wear through after a sliding distance of 1.83 km. In reality, the coating would be expected to delaminate once it had worn to some critical thickness.**

Both wear models were unable to predict the wear depth of BALINIT[®] DLC STAR and an AISI 440C steel ball at a normal load of 20 N. This is because the precise relationship between wear depth and normal load was not obtained from the wear data in **Chapter 7**, and the wear data did not follow Archard's wear law. It has been mentioned that the quality of the wear depth predictions of a model can only be as good as the quality of the input, and to develop accurate predictions for the wear depth, the relationship between wear depth and normal load must be obtained. This is a subject for future work.

The wear models derived in this thesis both represent a considerable extension to current wear modelling techniques in the literature.

- (i) **A unique analytical wear model was derived to describe the relationship between wear depth and sliding distance for a ball-on-flat geometry.**
- (ii) **An incremental wear model was developed to describe the relationship between wear depth and sliding distance for arbitrary component geometry.**

Both wear models showed an excellent comparison in their predictions for wear for a ball-on-flat contact, validating the use of the incremental wear model for more complex model geometries.

10.2. Future work

Considerable experimental research has been carried out regarding the tribology of DLC coatings, yet of this knowledge base, a small percentage concern the tribology of a DLC coating against steel in water. Of the papers which have considered this tribological scenario, two approaches were taken: (i) ranking a range of DLC coatings tested in terms of the SWR, or (ii) a tribochemical analysis of worn surfaces. The work that was presented in this thesis considered the mechanical motions of the third-body, and the prevailing dynamics in terms of VAMs – which were shown to govern the subsequent tribology.

(i) Exploration of the key deposition and test parameters which affect the VAM, and govern whether or not interfacial sliding will occur.

The deposition method (and deposition parameters such as bias voltage, source gas, dopant, etc.) is known to be an important factor that controls the mechanical and tribological properties of a DLC coating. Adamant[®] was unaffected by the presence of iron oxide species and showed interfacial sliding in all tests, whereas the tribology of BALINIT[®] DLC STAR was sensitive to the presence of iron oxide species, and the reason for this differing behaviour lies in differences between the deposition processes. The hardness, density, elastic modulus, thickness, and surface roughness, of the DLC coating, are all important factors that affect the tribology – and can be related to the method of deposition.

It has been mentioned previously that if a surface engineering company stopped producing a certain DLC coating, it would be useful to be able to replicate the tribological properties of the coating based on knowledge of the important variables. As a result, a larger focus must be placed on deposition processes, and the link between deposition methods and the subsequent tribology in terms of VAMs. Future work should examine a range of well-defined DLC coatings (from the viewpoint of deposition method / parameters) and run tribological tests to examine the VAM of the transfer layer and the subsequent tribology.

Extrinsic considerations that can affect the VAM are the counterface material used in tribological testing (e.g. grade of steel, hardness, roughness, etc.), the test geometry and test environment, and the subsequent tribochemical reactions. The test parameters in terms of normal load and sliding velocity are also important variables, and this was the focus of the thesis. Further study into the link between all these considerations and the VAM of the transfer layer could lead to a developed understanding of whether a DLC coating will show good tribology in a specific test environment.

(ii) Exploration of the effect of iron oxide species on the VAM of a transfer layer.

The work presented in **Chapter 6** showed the destabilising effect of iron oxide species on the transfer layer. Shear and extrusion of carbonaceous debris led to poor tribology for BALINIT[®] DLC STAR in the presence of abrasive iron oxide particles. An interesting future study would be an in-depth examination of the effect of the type of iron oxide species on the subsequent tribology. In the work presented in this thesis, Raman spectra were unable to show any correlation between the type of iron oxide present (hematite, magnetite, or maghemite) and the governing interfacial motion.

In a PWR, an oxide layer would grow on the steel counterface, so a topic for future work could be to allow an oxide layer to grow artificially and to examine the effects this has on the tribology. In addition, several different grades of steel could be examined to see the effect on the VAM of the transfer layer. Raman spectra could be used to examine the relationship between the type of iron oxide species present at the interface and the VAM of the transfer layer.

Further study to examine the effect of iron oxide species on the VAM in varying test conditions would be useful. For example, variations in contact pressure or sliding velocity could affect the distribution of species on the steel counterface, and affect the tribology as a result. To move to a more realistic test environment, to simulate that of a PWR, a custom tribometer could be designed inside an autoclave such that the effects of pressure, and temperature, could be examined simultaneously.

(iii) Implementation of experimental design techniques concerning the prediction of wear depth. Due to the large number of factors which affect wear, a statistical analysis is essential to draw meaningful conclusions.

The dependence of wear depth on normal load, sliding frequency, and sliding distance, was analysed in **Chapter 7**. Whilst a large number of experimental tests were run, it was difficult to obtain reliable data over a large parameter space. The non-linear dependence between wear depth and sliding distance was assessed successfully; however the functional form of the relationship between wear depth and normal load, for example, could not be assessed. For this reason, implementation of experimental design techniques is suggested to dictate future testing, to explore the parameter space more efficiently. An avenue for future exploration is neural networking, perhaps using Bayesian inference to select an optimal model.

In addition to exploration of the relationship between wear depth, and normal load and sliding distance, the relationship between wear depth and specific iron oxide species could be examined.

Regarding general improvements to the wear modelling presented in the thesis, there are several logical extensions to improve the current capability to predict wear. The requirement for an understanding of the relationship between wear depth and test parameters such as normal load and sliding distance is underlined, since the quality of the wear depth predictions can only be as good as the quality of the input.

- (iv) The analytical model of Chapter 8 was specific to a ball-on-flat geometry, and an extension would be to consider a line contact or an elliptic contact following a similar derivation.**

The extension of the point contact model to a different geometry would be a valuable extension to the literature. The analytical relation would provide a fast evaluation of wear depth with respect to sliding distance, and avoid the computational expense of using an incremental wear model.

- (v) The incremental wear model of Chapter 9 could be extended to three dimensions, providing a useful tool for more complex geometries.**

Extension of the incremental wear model to three dimensions would remove the plane strain approximation made in the current work. Once validated, the incremental wear model could be applied to a variety of complex three-dimensional geometries.

- (vi) The finite element model could extend to consider a more realistic description of the contact problem with regards to plasticity of the transfer layer, surface roughness of each surface, and the interlayers of the DLC coating.**

The plastic deformation of the transfer layer could be included as opposed to the current linear elastic description. In addition, the real surface profile of each surface could be used (based on surface profilometry measurements) to assess the effect of surface roughness of the averaged model predictions. The interlayers of the DLC coating could be included in the model instead of the currently homogenous properties, where nanoindentation could be used to assess the mechanical properties of each layer.

- (vii) Advanced level set methods could be applied to consider transfer layer growth using a thermodynamically consistent constitutive model of chemo-mechanical behaviour.**

To extend the analysis to a more realistic description of transfer layer growth, a thermodynamically consistent model of the chemo-mechanical behaviour of the transfer layer could be explored, instead of the logistic formulation suggested in this thesis.

Appendix A

This appendix contains two COMSOL Multiphysics 4.3 finite element models in relation to the wear model presented in **Chapter 9**; the initial model prior to wear, and the completed model after 3720 seconds of wear. Both models are saved as m-files. The first m-file is the finite element model used as an input to the control script in **Appendix B**.

```
function out = model

% Finite Element Model.m
% Model exported on Nov 22 2013, 15:09 by COMSOL 4.3.0.184.

import com.comsol.model.*
import com.comsol.model.util.*

model = ModelUtil.create('Model');
model.modelPath('C:\Local\Dropbox\Incremental Wear Model\v25');
model.name('Transfer_Model.mph');

model.param.set('W', '2*sqrt((2*hmax)*(2*R-(2*hmax)))', 'Width of the domain');
model.param.set('H', '500[um]', 'Half the height of the domain');
model.param.set('hmax', '20[um]', 'Height of the active region');
model.param.set('R', '3[mm]', 'Ball-bearing radius');
model.param.set('h_DLC', '3.1[um]', 'DLC coating thickness');
model.param.set('E_DLC', '21200000000[Pa]', 'Youngs modulus of DLC');
model.param.set('E_Steel', '200000000000[Pa]', 'Youngs modulus of steel');
model.param.set('E_TF', '415000000000[Pa]', 'Youngs modulus of transfer layer');
model.param.set('nu_DLC', '0.22', 'Poissons ratio of DLC');
model.param.set('nu_Steel', '0.3', 'Poissons ratio of steel');
model.param.set('nu_TF', '0.22', 'Poissons ratio of transfer layer');
model.param.set('rho_DLC', '2.5[g/cm^3]', 'Density of DLC');
model.param.set('rho_Steel', '7.65[g/cm^3]', 'Density of steel');
model.param.set('rho_TF', '2.5[g/cm^3]', 'Density of transfer layer');
model.param.set('dispx', '1e-005[m]', 'x-displacement');
model.param.set('Fn', '5[N]', 'Normal load');
model.param.set('velocity', '0.02[m/s]', 'Sliding velocity');
model.param.set('meshnumber', '900', 'Number of element along contact pair boundaries');
model.param.set('a', '50.437[um]', 'Best guess of contact radius');
model.param.set('depth', '6.7858e-005[m]', 'Depth of domain');
model.param.set('angle', 'asin(W/2/R)', 'Geometric parameter');
model.param.set('direction', '1', 'Sliding direction (1=left to right, -1=right to left)');
model.param.set('frictioncoeff', '0.0388', 'Coefficient of friction');

model.modelNode.create('mod1');

model.func.create('an1', 'Analytic');
model.func.create('an2', 'Analytic');
model.func.create('int3', 'Interpolation');
model.func.create('int5', 'Interpolation');
model.func('an1').model('mod1');
model.func('an1').set('funcname', 'f_E');
model.func('an1').set('expr', '(Y<coords(X)+h(X)-1.00001[um])*(h(X)>0.01[um])*(E_TF-E_Steel) + E_Steel');
model.func('an1').set('args', {'X' 'Y'});
model.func('an1').set('plotargs', {'X' ' ' ' '; 'Y' ' ' ' '});
model.func('an2').model('mod1');
model.func('an2').set('funcname', 'f_nu');
model.func('an2').set('expr', '(Y<coords(X)+h(X)-1.00001[um])*(h(X)>0.01[um])*(nu_TF-nu_Steel) + nu_Steel');
model.func('an2').set('args', {'X' 'Y'});
model.func('an2').set('plotargs', {'X' ' ' ' '; 'Y' ' ' ' '});
model.func('int3').model('mod1');
model.func('int3').set('funcname', 'h');
```

```

model.func('int3').set('table', {'-W/2' '0'; '-W/4' '0'; '-W/8' '0'; '0' '0'; 'W/8' '0';
'W/4' '0'; 'W/2' '0'});
model.func('int3').set('interp', 'piecewise cubic');
model.func('int3').set('argunit', 'm');
model.func('int3').set('fununit', 'um');
model.func('int5').model('mod1');
model.func('int5').name('Interpolation 4');
model.func('int5').set('funcname', 'coords');
model.func('int5').set('table', {'-W/2' '500'; '-W/4' '500'; '-W/8' '500'; '0' '500';
'W/8' '500'; 'W/4' '500'; 'W/2' '500'});
model.func('int5').set('interp', 'piecewise cubic');
model.func('int5').set('argunit', 'm');
model.func('int5').set('fununit', 'um');

model.geom.create('geom1', 2);
model.geom('geom1').angularUnit('rad');
model.geom('geom1').lengthUnit([native2unicode(hex2dec('00b5'), 'Cp1252') 'm']);
model.geom('geom1').feature.create('r2', 'Rectangle');
model.geom('geom1').feature.create('pc1', 'ParametricCurve');
model.geom('geom1').feature.create('csol2', 'ConvertToSolid');
model.geom('geom1').feature.create('del1', 'Delete');
model.geom('geom1').feature.create('mov3', 'Move');
model.geom('geom1').feature.create('b1', 'BezierPolygon');
model.geom('geom1').feature.create('csol1', 'ConvertToSolid');
model.geom('geom1').feature.create('r4', 'Rectangle');
model.geom('geom1').feature.create('pc2', 'ParametricCurve');
model.geom('geom1').feature.create('pc3', 'ParametricCurve');
model.geom('geom1').feature.create('pc4', 'ParametricCurve');
model.geom('geom1').feature.create('csol3', 'ConvertToSolid');
model.geom('geom1').feature.create('uni1', 'Union');
model.geom('geom1').feature.create('uni2', 'Union');
model.geom('geom1').feature('r2').set('pos', {'-W/2' 'H'});
model.geom('geom1').feature('r2').set('layername', {''});
model.geom('geom1').feature('r2').set('layerbottom', false);
model.geom('geom1').feature('r2').set('size', {'W' 'H + 1[um]'});
model.geom('geom1').feature('pc1').set('pos', {'0' 'H+R+1[um]'});
model.geom('geom1').feature('pc1').set('parmin', 'pi-angle');
model.geom('geom1').feature('pc1').set('parmax', 'pi+angle');
model.geom('geom1').feature('pc1').set('coord', {'R*sin(s)' 'R*cos(s)'});
model.geom('geom1').feature('pc1').set('rtol', '1.0E-10');
model.geom('geom1').feature('csol2').set('repairtol', '1.0E-10');
model.geom('geom1').feature('csol2').selection('input').set({'pc1' 'r2'});
model.geom('geom1').feature('del1').selection('input').set({'csol2(1)', [1 2 5]});
model.geom('geom1').feature('mov3').set('disply', '-1[um]');
model.geom('geom1').feature('mov3').selection('input').set({'del1'});
model.geom('geom1').feature('b1').set('p', {'-W/2' 'W/2'; '5[um]+H+2*hmax'
'5[um]+H+2*hmax'});
model.geom('geom1').feature('b1').set('degree', {'1'});
model.geom('geom1').feature('b1').set('w', {'1' '1'});
model.geom('geom1').feature('csol1').set('repairtol', '1.0E-10');
model.geom('geom1').feature('csol1').selection('input').set({'b1' 'mov3'});
model.geom('geom1').feature('r4').set('pos', {'-W/2' '0'});
model.geom('geom1').feature('r4').set('layerbottom', false);
model.geom('geom1').feature('r4').set('size', {'W' 'H-h_DLC'});
model.geom('geom1').feature('pc2').set('pos', {'-W/2' 'H-h_DLC'});
model.geom('geom1').feature('pc2').set('parmax', 'h_DLC');
model.geom('geom1').feature('pc2').set('coord', {'0' 's'});
model.geom('geom1').feature('pc2').set('rtol', '1.0E-15');
model.geom('geom1').feature('pc3').set('pos', {'W/2' 'H-h_DLC'});
model.geom('geom1').feature('pc3').set('parmax', 'h_DLC');
model.geom('geom1').feature('pc3').set('coord', {'0' 's'});
model.geom('geom1').feature('pc3').set('rtol', '1.0E-15');
model.geom('geom1').feature('pc4').set('pos', {'0' 'H'});
model.geom('geom1').feature('pc4').set('parmin', '-W/2');
model.geom('geom1').feature('pc4').set('parmax', 'W/2');
model.geom('geom1').feature('pc4').set('coord', {'s' '0'});
model.geom('geom1').feature('pc4').set('rtol', '1.0E-10');
model.geom('geom1').feature('csol3').set('repairtol', '1.0E-10');
model.geom('geom1').feature('csol3').selection('input').set({'pc2' 'pc3' 'pc4' 'r4'});
model.geom('geom1').feature('uni1').set('repairtol', '1.0E-15');
model.geom('geom1').feature('uni1').selection('input').set({'csol3'});
model.geom('geom1').feature('uni2').set('repairtol', '1.0E-15');
model.geom('geom1').feature('uni2').selection('input').set({'csol1'});
model.geom('geom1').feature('fin').name('Form Assembly');
model.geom('geom1').feature('fin').set('action', 'assembly');
model.geom('geom1').feature('fin').set('pairtype', 'contact');
model.geom('geom1').feature('fin').set('repairtol', '1.0E-10');

```

```

model.geom('geom1').run;

model.view.create('view3', 2);
model.view.create('view4', 2);
model.view.create('view5', 2);
model.view.create('view6', 2);
model.view.create('view7', 2);
model.view.create('view8', 2);
model.view.create('view9', 2);

model.pair.create('ap2', 'Contact', 'geom1');
model.pair('ap2').source.set([6]);
model.pair('ap2').destination.set([14]);

model.material.create('mat2');
model.material('mat2').selection.set([3]);
model.material.create('mat1');
model.material('mat1').selection.set([2]);
model.material.create('mat3');
model.material('mat3').selection.set([1 4]);

model.physics.create('solid', 'SolidMechanics', 'geom1');
model.physics('solid').feature.create('displ', 'Displacement1', 1);
model.physics('solid').feature('displ').selection.set([2]);
model.physics('solid').feature.create('bll1', 'BodyLoad', 2);
model.physics('solid').feature('bll1').selection.set([3 4]);
model.physics('solid').feature.create('disp3', 'Displacement1', 1);
model.physics('solid').feature('disp3').selection.set([8 9 12 13]);
model.physics('solid').feature.create('cnt1', 'Contact', 1);
model.physics('solid').feature('cnt1').feature.create('fric1', 'Friction', 1);

model.mesh.create('mesh1', 'geom1');
model.mesh('mesh1').feature.create('ftril', 'FreeTri');
model.mesh('mesh1').feature('ftril').selection.geom('geom1', 2);
model.mesh('mesh1').feature('ftril').selection.set([2 3]);
model.mesh('mesh1').feature('ftril').feature.create('dis1', 'Distribution');
model.mesh('mesh1').feature('ftril').feature('dis1').selection.set([14]);
model.mesh('mesh1').feature('ftril').feature.create('dis2', 'Distribution');
model.mesh('mesh1').feature('ftril').feature('dis2').selection.set([6]);
model.mesh('mesh1').feature('ftril').feature.create('siz1', 'Size');
model.mesh('mesh1').feature.create('ftri2', 'FreeTri');
model.mesh('mesh1').feature('ftri2').feature.create('siz1', 'Size');

model.result.table.create('evl2', 'Table');
model.result.table.create('tbl1', 'Table');

model.view('view1').axis.set('xmin', '-860.8243408203125');
model.view('view1').axis.set('xmax', '1601.3817138671875');
model.view('view1').axis.set('ymin', '-466.4554443359375');
model.view('view1').axis.set('ymax', '1243.2620849609375');
model.view('view3').axis.set('xmin', '-669.54833984375');
model.view('view3').axis.set('xmax', '1516.958740234375');
model.view('view3').axis.set('ymin', '-404.3259582519531');
model.view('view3').axis.set('ymax', '1162.2950439453125');
model.view('view6').axis.set('xmin', '-1.6572504043579102');
model.view('view6').axis.set('xmax', '1.6572504043579102');
model.view('view7').axis.set('xmin', '-1.5255906581878662');
model.view('view7').axis.set('xmax', '1.5255906581878662');
model.view('view8').axis.set('xmin', '-1.5255906581878662');
model.view('view8').axis.set('xmax', '1.5255906581878662');
model.view('view9').axis.set('xmin', '-1.5255906581878662');
model.view('view9').axis.set('xmax', '1.5255906581878662');

model.material('mat2').name('Steel/TF');
model.material('mat2').propertyGroup('def').func.name('Functions');
model.material('mat2').propertyGroup('def').set('youngsmodulus', 'f_E(X[1/m],Y[1/m])');
model.material('mat2').propertyGroup('def').set('poissonsratio', 'f_nu(X[1/m],Y[1/m])');
model.material('mat2').propertyGroup('def').set('density', 'f_rho(X[1/m],Y[1/m])');
model.material('mat2').propertyGroup('def').set('heatcapacity', '');
model.material('mat2').propertyGroup('def').set('thermalconductivity', {' '0' '0' '0'
' '0' '0' '0' ''});
model.material('mat1').name('DLC');
model.material('mat1').propertyGroup('def').func.name('Functions');
model.material('mat1').propertyGroup('def').set('youngsmodulus', 'E_DLC');
model.material('mat1').propertyGroup('def').set('poissonsratio', 'nu_DLC');
model.material('mat1').propertyGroup('def').set('density', 'rho_DLC');

```

```

model.material('mat1').propertyGroup('def').set('thermalconductivity', {' ' '0' '0' '0'
' ' '0' '0' '0' ' '});
model.material('mat1').propertyGroup('def').set('heatcapacity', '');
model.material('mat3').name('AISI 440C Steel');
model.material('mat3').propertyGroup('def').func.name('Functions');
model.material('mat3').propertyGroup('def').set('youngsmodulus', 'E_Steel');
model.material('mat3').propertyGroup('def').set('poissonsratio', 'nu_Steel');
model.material('mat3').propertyGroup('def').set('density', 'rho_Steel');
model.material('mat3').propertyGroup('def').set('thermalconductivity', {' ' '0' '0' '0'
' ' '0' '0' '0' ' '});
model.material('mat3').propertyGroup('def').set('heatcapacity', '');

model.physics('solid').prop('d').set('d', 'depth');
model.physics('solid').feature('lemm1').set('ForceLinearStrainRes', '1');
model.physics('solid').feature('lemm1').set('editModelInputs', '1');
model.physics('solid').feature('lemm1').name('Linear Elastic Material Model 1');
model.physics('solid').feature('init1').set('u', {'u'; 'v'; '0'});
model.physics('solid').feature('displ').set('Direction', {'1'; '1'; '0'});
model.physics('solid').feature('b11').set('FperVol', {'0'; '-Fn/Vsph'; '0'});
model.physics('solid').feature('b11').set('LoadType', 'TotalForce');
model.physics('solid').feature('b11').set('Ftot', {'0'; '-Fn'; '0'});
model.physics('solid').feature('disp3').set('U0', {'dispX'; '0'; '0'});
model.physics('solid').feature('disp3').set('Direction', {'1'; '0'; '0'});
model.physics('solid').feature('cnt1').set('pairs', 'ap2');
model.physics('solid').feature('cnt1').set('Tn_init', '0.8[GPa]');
model.physics('solid').feature('cnt1').feature('fric1').set('mustat', 'frictioncoeff');
model.physics('solid').feature('cnt1').feature('fric1').set('Tt_init', {'solid.Ttx_ap2';
'solid.Tty_ap2'; '0'});
model.physics('solid').feature('cnt1').feature('fric1').set('cm_old_init', {'X'; 'Y';
'0'});
model.physics('solid').feature('cnt1').feature('fric1').set('ContactPreviousStep',
'InContact');

model.mesh('mesh1').feature('size').set('hauto', 2);
model.mesh('mesh1').feature('ftri1').feature('dis1').set('numelem', 'meshnumber*2');
model.mesh('mesh1').feature('ftri1').feature('dis2').set('numelem', 'meshnumber');
model.mesh('mesh1').feature('ftri1').feature('size1').set('hmax', '1[um]');
model.mesh('mesh1').feature('ftri1').feature('size1').set('hmin', '0.02');
model.mesh('mesh1').feature('ftri1').feature('size1').set('hminactive', false);
model.mesh('mesh1').feature('ftri1').feature('size1').set('hcurve', '0.2');
model.mesh('mesh1').feature('ftri1').feature('size1').set('hcurveactive', false);
model.mesh('mesh1').feature('ftri1').feature('size1').set('hnarrowactive', false);
model.mesh('mesh1').feature('ftri1').feature('size1').set('hgrad', '1.1');
model.mesh('mesh1').feature('ftri1').feature('size1').set('hgradactive', false);
model.mesh('mesh1').feature('ftri1').feature('size1').set('hauto', '1');
model.mesh('mesh1').feature('ftri1').feature('size1').set('hmax', '1[um]');
model.mesh('mesh1').feature('ftri1').feature('size1').set('hminactive', false);
model.mesh('mesh1').feature('ftri1').feature('size1').set('hcurveactive', false);
model.mesh('mesh1').feature('ftri1').feature('size1').set('hnarrowactive', false);
model.mesh('mesh1').feature('ftri1').feature('size1').set('hgradactive', false);
model.mesh('mesh1').feature('ftri2').feature('size1').set('hmax', '37');
model.mesh('mesh1').feature('ftri2').feature('size1').set('hmaxactive', false);
model.mesh('mesh1').feature('ftri2').feature('size1').set('hmin', '0.125');
model.mesh('mesh1').feature('ftri2').feature('size1').set('hminactive', false);
model.mesh('mesh1').feature('ftri2').feature('size1').set('hcurve', '0.25');
model.mesh('mesh1').feature('ftri2').feature('size1').set('hcurveactive', false);
model.mesh('mesh1').feature('ftri2').feature('size1').set('hnarrowactive', false);
model.mesh('mesh1').feature('ftri2').feature('size1').set('hgrad', '1.1');
model.mesh('mesh1').feature('ftri2').feature('size1').set('hauto', '3');
model.mesh('mesh1').feature('ftri2').feature('size1').set('hmaxactive', false);
model.mesh('mesh1').feature('ftri2').feature('size1').set('hminactive', false);
model.mesh('mesh1').feature('ftri2').feature('size1').set('hcurveactive', false);
model.mesh('mesh1').feature('ftri2').feature('size1').set('hnarrowactive', false);
model.mesh('mesh1').feature('ftri2').feature('size1').set('hgrad', '1.1');
model.mesh('mesh1').run();

model.result.table('evl2').name('Evaluation 2D');
model.result.table('evl2').comments('Interactive 2D values');
model.result.table('tbl1').comments('Surface Maximum 1 (solid.p)');

model.study.create('std1');
model.study('std1').feature.create('param', 'Parametric');
model.study('std1').feature.create('stat', 'Stationary');

model.sol.create('soll');
model.sol('soll').study('std1');
model.sol('soll').attach('std1');

```

```

model.sol('soll').feature.create('st1', 'StudyStep');
model.sol('soll').feature.create('v1', 'Variables');
model.sol('soll').feature.create('s1', 'Stationary');
model.sol('soll').feature('s1').feature.create('p1', 'Parametric');
model.sol('soll').feature('s1').feature('p1').feature.create('ps1', 'PreviousSolution');
model.sol('soll').feature('s1').feature.create('sel', 'Segregated');
model.sol('soll').feature('s1').feature('sel').feature.create('ss1', 'SegregatedStep');
model.sol('soll').feature('s1').feature('sel').feature.create('lsl', 'LumpedStep');
model.sol('soll').feature('s1').feature('sel').feature.remove('ssDef');
model.sol('soll').feature('s1').feature.remove('fcDef');

model.result.create('pg1', 'PlotGroup2D');
model.result('pg1').feature.create('surfl', 'Surface');
model.result('pg1').feature('surfl').feature.create('def', 'Deform');
model.result.create('pg5', 'PlotGroup2D');
model.result('pg5').feature.create('surfl', 'Surface');
model.result('pg5').feature('surfl').feature.create('def', 'Deform');
model.result.create('pg2', 'PlotGroup1D');
model.result('pg2').set('probetag', 'none');
model.result('pg2').feature.create('lngr1', 'LineGraph');
model.result('pg2').feature('lngr1').selection.set([14]);
model.result.create('pg3', 'PlotGroup1D');
model.result('pg3').set('probetag', 'none');
model.result('pg3').feature.create('lngr1', 'LineGraph');
model.result('pg3').feature('lngr1').selection.set([14]);
model.result('pg3').feature.create('lngr2', 'LineGraph');
model.result('pg3').feature('lngr2').selection.set([6]);
model.result('pg3').feature.create('lngr3', 'LineGraph');
model.result('pg3').feature('lngr3').selection.set([3]);
model.result('pg3').feature.create('lngr4', 'LineGraph');
model.result('pg3').feature('lngr4').selection.set([14]);
model.result.create('pg4', 'PlotGroup1D');
model.result('pg4').set('probetag', 'none');
model.result('pg4').feature.create('lngr1', 'LineGraph');
model.result('pg4').feature('lngr1').selection.set([14]);
model.result('pg4').feature.create('lngr2', 'LineGraph');
model.result('pg4').feature('lngr2').selection.set([6]);
model.result('pg4').feature.create('lngr3', 'LineGraph');
model.result('pg4').feature('lngr3').selection.set([3]);
model.result('pg4').feature.create('lngr4', 'LineGraph');
model.result('pg4').feature('lngr4').selection.set([14]);
model.result.create('pg6', 'PlotGroup1D');
model.result('pg6').set('probetag', 'none');
model.result('pg6').feature.create('lngr1', 'LineGraph');
model.result('pg6').feature('lngr1').selection.set([14]);
model.result('pg6').feature.create('lngr2', 'LineGraph');
model.result('pg6').feature('lngr2').selection.set([14]);

model.study('std1').name('Study 1 (TF)');
model.study('std1').feature('param').set('pname', {'dispX'});
model.study('std1').feature('param').set('plistarr', {'0[um] 10[um]'});

model.sol('soll').attach('std1');
model.sol('soll').feature('st1').name('Compile Equations: Stationary');
model.sol('soll').feature('st1').set('studystep', 'stat');
model.sol('soll').feature('v1').set('control', 'stat');
model.sol('soll').feature('v1').feature('modl_u').set('scalemethod', 'manual');
model.sol('soll').feature('v1').feature('modl_u').set('scaleval', '1e-2*0.0013977124167724923');
model.sol('soll').feature('v1').feature('modl_solid_Tn_ap2').set('scalemethod', 'manual');
model.sol('soll').feature('v1').feature('modl_solid_Tn_ap2').set('scaleval', '10000000');
model.sol('soll').feature('v1').feature('modl_solid_Tt_ap2').set('scalemethod', 'manual');
model.sol('soll').feature('v1').feature('modl_solid_Tt_ap2').set('scaleval', '10000000');
model.sol('soll').feature('s1').set('control', 'stat');
model.sol('soll').feature('s1').feature('p1').set('control', 'param');
model.sol('soll').feature('s1').feature('p1').set('pname', {'dispX'});
model.sol('soll').feature('s1').feature('p1').set('plistarr', {'0[um] 10[um]'});
model.sol('soll').feature('s1').feature('p1').set('porder', 'linear');
model.sol('soll').feature('s1').feature('p1').feature('ps1').set('prevcomp', {'modl_solid_contact_ap2_old' 'modl_solid_cm_ap2_old'});
model.sol('soll').feature('s1').feature('sel').set('maxsegiter', '15');
model.sol('soll').feature('s1').feature('sel').feature('ss1').set('segvar', {'modl_u'});
model.sol('soll').feature('s1').feature('sel').feature('ss1').set('subdtech', 'ddog');

```

```

model.sol('sol1').feature('s1').feature('se1').feature('ss1').set('subtermauto',
'itertol');
model.sol('sol1').feature('s1').feature('se1').feature('ss1').set('subntolfact', '1');
model.sol('sol1').feature('s1').feature('se1').feature('ss1').set('subiter', '7');
model.sol('sol1').feature('s1').feature('se1').feature('ls1').set('segvar',
{'modl_solid_Tn_ap2' 'modl_solid_Tt_ap2' 'modl_solid_contact_ap2_old'
'modl_solid_cm_ap2_old'});
model.sol('sol1').runAll;

model.result('pg1').name('Stress (solid)');
model.result('pg1').feature('surf1').set('expr', 'solid.p');
model.result('pg1').feature('surf1').set('unit', 'GPa');
model.result('pg1').feature('surf1').set('descr', 'Pressure');
model.result('pg1').feature('surf1').feature('def').set('scaleactive', true);
model.result('pg5').name('Elastic Modulus');
model.result('pg5').setIndex('looplevel', '1', 0);
model.result('pg5').feature('surf1').set('expr', 'solid.E');
model.result('pg5').feature('surf1').set('unit', 'GPa');
model.result('pg5').feature('surf1').set('descr', 'Young's modulus');
model.result('pg5').feature('surf1').feature('def').set('scaleactive', true);
model.result('pg2').set('xlabel', ['x-coordinate (' native2unicode(hex2dec('00b5'),
'Cp1252') 'm)']);
model.result('pg2').set('ylabel', 'Contact pressure, contact pair ap2 (GPa)');
model.result('pg2').set('axislimits', 'on');
model.result('pg2').set('xmin', '-165.2027587890625');
model.result('pg2').set('xmax', '241.5543975830078');
model.result('pg2').set('ymin', '-2.231545925140381');
model.result('pg2').set('ymax', '3.056295156478882');
model.result('pg2').set('xlabelactive', false);
model.result('pg2').set('ylabelactive', false);
model.result('pg2').feature('lngr1').set('expr', 'solid.Tn_ap2');
model.result('pg2').feature('lngr1').set('unit', 'GPa');
model.result('pg2').feature('lngr1').set('descr', 'Contact pressure, contact pair ap2');
model.result('pg2').feature('lngr1').set('xdata', 'expr');
model.result('pg2').feature('lngr1').set('xdataexpr', 'x');
model.result('pg2').feature('lngr1').set('xdatadescr', 'x-coordinate');
model.result('pg3').name('Not Deformed');
model.result('pg3').set('looplevelinput', {'last'});
model.result('pg3').set('xlabel', ['X-coordinate (' native2unicode(hex2dec('00b5'),
'Cp1252') 'm)']);
model.result('pg3').set('axislimits', 'on');
model.result('pg3').set('xmin', '-250');
model.result('pg3').set('xmax', '250');
model.result('pg3').set('ymin', '497');
model.result('pg3').set('ymax', '510');
model.result('pg3').set('xlabelactive', false);
model.result('pg3').feature('lngr1').set('expr', 'Y');
model.result('pg3').feature('lngr1').set('descr', 'Y-coordinate');
model.result('pg3').feature('lngr1').set('xdata', 'expr');
model.result('pg3').feature('lngr1').set('xdataexpr', 'X');
model.result('pg3').feature('lngr1').set('xdatadescr', 'X-coordinate');
model.result('pg3').feature('lngr2').set('expr', 'Y');
model.result('pg3').feature('lngr2').set('descr', 'Y-coordinate');
model.result('pg3').feature('lngr2').set('xdata', 'expr');
model.result('pg3').feature('lngr2').set('xdataexpr', 'X');
model.result('pg3').feature('lngr2').set('xdatadescr', 'X-coordinate');
model.result('pg3').feature('lngr3').set('expr', 'Y');
model.result('pg3').feature('lngr3').set('descr', 'Y-coordinate');
model.result('pg3').feature('lngr3').set('xdata', 'expr');
model.result('pg3').feature('lngr3').set('xdataexpr', 'X');
model.result('pg3').feature('lngr3').set('xdatadescr', 'X-coordinate');
model.result('pg3').feature('lngr4').set('expr', 'Y+h(X)');
model.result('pg3').feature('lngr4').set('descr', 'Y+h(X)');
model.result('pg3').feature('lngr4').set('xdata', 'expr');
model.result('pg3').feature('lngr4').set('xdataexpr', 'X');
model.result('pg3').feature('lngr4').set('xdatadescr', 'X-coordinate');
model.result('pg4').name('Deformed');
model.result('pg4').set('looplevelinput', {'last'});
model.result('pg4').set('xlabel', ['x-coordinate (' native2unicode(hex2dec('00b5'),
'Cp1252') 'm)']);
model.result('pg4').set('axislimits', 'on');
model.result('pg4').set('xmin', '-250');
model.result('pg4').set('xmax', '250');
model.result('pg4').set('ymin', '497');
model.result('pg4').set('ymax', '510');
model.result('pg4').set('xlabelactive', false);
model.result('pg4').feature('lngr1').set('expr', 'y');

```

```

model.result('pg4').feature('lngr1').set('descr', 'y-coordinate');
model.result('pg4').feature('lngr1').set('xdata', 'expr');
model.result('pg4').feature('lngr1').set('xdataexpr', 'x');
model.result('pg4').feature('lngr1').set('xdatadescr', 'x-coordinate');
model.result('pg4').feature('lngr2').set('expr', 'y');
model.result('pg4').feature('lngr2').set('descr', 'y-coordinate');
model.result('pg4').feature('lngr2').set('xdata', 'expr');
model.result('pg4').feature('lngr2').set('xdataexpr', 'x');
model.result('pg4').feature('lngr2').set('xdatadescr', 'x-coordinate');
model.result('pg4').feature('lngr3').set('expr', 'y');
model.result('pg4').feature('lngr3').set('descr', 'y-coordinate');
model.result('pg4').feature('lngr3').set('xdata', 'expr');
model.result('pg4').feature('lngr3').set('xdataexpr', 'x');
model.result('pg4').feature('lngr3').set('xdatadescr', 'x-coordinate');
model.result('pg4').feature('lngr4').set('expr', 'y+h(X)');
model.result('pg4').feature('lngr4').set('descr', 'y+h(X)');
model.result('pg4').feature('lngr4').set('xdata', 'expr');
model.result('pg4').feature('lngr4').set('xdataexpr', 'x');
model.result('pg4').feature('lngr4').set('xdatadescr', 'x-coordinate');
model.result('pg6').set('xlabel', ['X-coordinate (' native2unicode(hex2dec('00b5'),
'Cpl252') 'm)']);
model.result('pg6').set('xlabelactive', false);
model.result('pg6').feature('lngr1').set('expr', '(solid.E-E_Steel)/E_Steel*0.01[um]');
model.result('pg6').feature('lngr1').set('descr', '(solid.E-E_Steel)/E_Steel*0.01[um]');
model.result('pg6').feature('lngr1').set('xdata', 'expr');
model.result('pg6').feature('lngr1').set('xdataexpr', 'X');
model.result('pg6').feature('lngr1').set('xdatadescr', 'X-coordinate');
model.result('pg6').feature('lngr2').set('expr', 'h(X)');
model.result('pg6').feature('lngr2').set('descr', 'h(X)');
model.result('pg6').feature('lngr2').set('xdata', 'expr');
model.result('pg6').feature('lngr2').set('xdataexpr', 'X');
model.result('pg6').feature('lngr2').set('xdatadescr', 'X-coordinate');

out = model;

```

The second m-file is a finite element model which was saved after 3720 seconds of wear.

```

function out = model
%
% v25i_iter_372_of_372.m
%
% Model exported on Nov 22 2013, 14:51 by COMSOL 4.3.0.184.

import com.comsol.model.*
import com.comsol.model.util.*

model = ModelUtil.create('Model');
model.modelPath('C:\Local\Dropbox\Incremental Wear Model\v25');
model.name('v25i_iter_372_of_372.mph');

model.param.set('W', '2*sqrt((2*hmax)*(2*R-(2*hmax)))', 'Width of the domain');
model.param.set('H', '500[um]', 'Half the height of the domain');
model.param.set('hmax', '20[um]', 'Height of the active region');
model.param.set('R', '3[mm]', 'Ball-bearing radius');
model.param.set('h_DLC', '3.1[um]', 'DLC coating thickness');
model.param.set('E_DLC', '21200000000[Pa]', 'Youngs modulus of DLC');
model.param.set('E_Steel', '20000000000[Pa]', 'Youngs modulus of steel');
model.param.set('E_TF', '41500000000[Pa]', 'Youngs modulus of transfer layer');
model.param.set('nu_DLC', '0.22', 'Poissons ratio of DLC');
model.param.set('nu_Steel', '0.3', 'Poissons ratio of steel');
model.param.set('nu_TF', '0.22', 'Poissons ratio of transfer layer');
model.param.set('rho_DLC', '2.5[g/cm^3]', 'Density of DLC');
model.param.set('rho_Steel', '7.65[g/cm^3]', 'Density of steel');
model.param.set('rho_TF', '2.5[g/cm^3]', 'Density of transfer layer');
model.param.set('dispx', '1e-005[m]', 'x-displacement');
model.param.set('Fn', '5[N]', 'Normal load');
model.param.set('velocity', '0.02[m/s]', 'Sliding velocity');
model.param.set('meshnumber', '500', 'Number of element along contact pair boundaries');
model.param.set('a', '120.1126[um]', 'Best guess of contact radius');
model.param.set('depth', '6.7858e-005[m]', 'Depth of domain');
model.param.set('angle', 'asin(W/2/R)', 'Geometric parameter');
model.param.set('direction', '1', 'Sliding direction (1=left to right, -1=right to left)');
model.param.set('frictioncoeff', '0.0338', 'Coefficient of friction');

```

```

model.modelNode.create('mod1');

model.file.create('res743');
model.file.create('res744');

model.func.create('an1', 'Analytic');
model.func.create('an2', 'Analytic');
model.func.create('int3', 'Interpolation');
model.func.create('int5', 'Interpolation');
model.func('an1').model('mod1');
model.func('an1').set('funcname', 'f_E');
model.func('an1').set('expr', '(Y<coords(X)+h(X)-1.00001[um])* (h(X)>0.01[um]) * (E_TF-
E_Steel) + E_Steel');
model.func('an1').set('args', {'X' 'Y'});
model.func('an1').set('plotargs', {'X' ' ' ' '; 'Y' ' ' ' '});
model.func('an2').model('mod1');
model.func('an2').set('funcname', 'f_nu');
model.func('an2').set('expr', '(Y<coords(X)+h(X)-1.00001[um])* (h(X)>0.01[um]) * (nu_TF-
nu_Steel) + nu_Steel');
model.func('an2').set('args', {'X' 'Y'});
model.func('an2').set('plotargs', {'X' ' ' ' '; 'Y' ' ' ' '});
model.func('int3').model('mod1');
model.func('int3').set('sourcetype', 'model');
model.func('int3').set('modelres', 'res743');
model.func('int3').set('importedname', 'h_data_v25i.txt');
model.func('int3').set('importedstruct', 'Spreadsheet');
model.func('int3').set('importeddim', '1D');
model.func('int3').set('funcs', {'h' '1'});
model.func('int3').set('interp', 'piecewisecubic');
model.func('int3').set('argunit', 'um');
model.func('int3').set('fununit', 'um');

model.file('res743').resource('C:\Users\ds6c10\AppData\Local\Temp\cs079241\tmp5006102951
835801837_copy');

model.func('int3').set('struct', 'spreadsheet');
model.func('int5').model('mod1');
model.func('int5').name('Interpolation 4');
model.func('int5').set('sourcetype', 'model');
model.func('int5').set('modelres', 'res744');
model.func('int5').set('importedname', 'D_data_v25i.txt');
model.func('int5').set('importedstruct', 'Spreadsheet');
model.func('int5').set('importeddim', '1D');
model.func('int5').set('funcs', {'coords' '1'});
model.func('int5').set('interp', 'piecewisecubic');
model.func('int5').set('argunit', 'um');
model.func('int5').set('fununit', 'um');

model.file('res744').resource('C:\Users\ds6c10\AppData\Local\Temp\cs079241\tmp6705564239
288293925_copy');

model.func('int5').set('struct', 'spreadsheet');

model.geom.create('geom1', 2);
model.geom('geom1').angularUnit('rad');
model.geom('geom1').lengthUnit([native2unicode(hex2dec('00b5'), 'Cp1252') 'm']);
model.geom('geom1').feature.create('r2', 'Rectangle');
model.geom('geom1').feature.create('ic1', 'InterpolationCurve');
model.geom('geom1').feature.create('csol2', 'ConvertToSolid');
model.geom('geom1').feature.create('dell', 'Delete');
model.geom('geom1').feature.create('mov3', 'Move');
model.geom('geom1').feature.create('b1', 'BezierPolygon');
model.geom('geom1').feature.create('csol1', 'ConvertToSolid');
model.geom('geom1').feature.create('r4', 'Rectangle');
model.geom('geom1').feature.create('pc2', 'ParametricCurve');
model.geom('geom1').feature.create('pc3', 'ParametricCurve');
model.geom('geom1').feature.create('ic2', 'InterpolationCurve');
model.geom('geom1').feature.create('csol3', 'ConvertToSolid');
model.geom('geom1').feature.create('uni1', 'Union');
model.geom('geom1').feature.create('uni2', 'Union');
model.geom('geom1').feature.create('mov4', 'Move');
model.geom('geom1').feature('r2').set('pos', {'-W/2' 'H'});
model.geom('geom1').feature('r2').set('layername', {''});
model.geom('geom1').feature('r2').set('layerbottom', false);
model.geom('geom1').feature('r2').set('size', {'W' 'H + 1[um]'});
model.geom('geom1').feature('ic1').set('source', 'file');

```

```

model.geom('geom1').feature('ic1').set('filename', 'C:\Local\Non-Dropbox
Documents\COMSOL with MATLAB®\Test 12\v25\D_data_v25i.txt');
model.geom('geom1').feature('ic1').set('rtol', '1.0E-10');
model.geom('geom1').feature('csol2').set('repairtol', '1.0E-10');
model.geom('geom1').feature('csol2').selection('input').set({'ic1' 'r2'});
model.geom('geom1').feature('dell1').selection('input').set({'csol2(1)', [1 2 5]});
model.geom('geom1').feature('mov3').set('disply', '-1[um]');
model.geom('geom1').feature('mov3').selection('input').set({'dell1'});
model.geom('geom1').feature('b1').set('p', {'-W/2' 'W/2'; '5[um]+H+2*hmax'
'5[um]+H+2*hmax'});
model.geom('geom1').feature('b1').set('degree', {'1'});
model.geom('geom1').feature('b1').set('w', {'1' '1'});
model.geom('geom1').feature('csol1').set('repairtol', '1.0E-10');
model.geom('geom1').feature('csol1').selection('input').set({'b1' 'mov3'});
model.geom('geom1').feature('r4').set('pos', {'-W/2' '0'});
model.geom('geom1').feature('r4').set('layerbottom', false);
model.geom('geom1').feature('r4').set('size', {'W' 'H-h_DLC'});
model.geom('geom1').feature('pc2').set('pos', {'-W/2' 'H-h_DLC'});
model.geom('geom1').feature('pc2').set('parmax', 'h_DLC');
model.geom('geom1').feature('pc2').set('coord', {'0' 's'});
model.geom('geom1').feature('pc2').set('rtol', '1.0E-15');
model.geom('geom1').feature('pc3').set('pos', {'W/2' 'H-h_DLC'});
model.geom('geom1').feature('pc3').set('parmax', 'h_DLC');
model.geom('geom1').feature('pc3').set('coord', {'0' 's'});
model.geom('geom1').feature('pc3').set('rtol', '1.0E-15');
model.geom('geom1').feature('ic2').set('source', 'file');
model.geom('geom1').feature('ic2').set('filename', 'C:\Local\Non-Dropbox
Documents\COMSOL with MATLAB®\Test 12\v25\C_data_v25i.txt');
model.geom('geom1').feature('ic2').set('rtol', '1.0E-10');
model.geom('geom1').feature('csol3').set('repairtol', '1.0E-10');
model.geom('geom1').feature('csol3').selection('input').set({'pc2' 'pc3' 'r4' 'ic2'});
model.geom('geom1').feature('uni1').set('repairtol', '1.0E-15');
model.geom('geom1').feature('uni1').selection('input').set({'csol3'});
model.geom('geom1').feature('uni2').set('repairtol', '1.0E-15');
model.geom('geom1').feature('uni2').selection('input').set({'csol1'});
model.geom('geom1').feature('mov4').set('disply', '3.116[um]');
model.geom('geom1').feature('mov4').selection('input').set({'uni1'});
model.geom('geom1').feature('fin').name('Form Assembly');
model.geom('geom1').feature('fin').set('action', 'assembly');
model.geom('geom1').feature('fin').set('pairtype', 'contact');
model.geom('geom1').feature('fin').set('repairtol', '1.0E-10');
model.geom('geom1').run;

model.view.create('view3', 2);
model.view.create('view4', 2);
model.view.create('view5', 2);
model.view.create('view6', 2);
model.view.create('view7', 2);
model.view.create('view8', 2);
model.view.create('view9', 2);

model.pair.create('ap2', 'Contact', 'geom1');
model.pair('ap2').source.set([6]);
model.pair('ap2').destination.set([14]);

model.material.create('mat2');
model.material('mat2').selection.set([3]);
model.material.create('mat1');
model.material('mat1').selection.set([2]);
model.material.create('mat3');
model.material('mat3').selection.set([1 4]);

model.physics.create('solid', 'SolidMechanics', 'geom1');
model.physics('solid').feature.create('displ', 'Displacement1', 1);
model.physics('solid').feature('displ').selection.set([2]);
model.physics('solid').feature.create('b11', 'BodyLoad', 2);
model.physics('solid').feature('b11').selection.set([3 4]);
model.physics('solid').feature.create('disp3', 'Displacement1', 1);
model.physics('solid').feature('disp3').selection.set([8 9 12 13]);
model.physics('solid').feature.create('cnt1', 'Contact', 1);
model.physics('solid').feature('cnt1').feature.create('fric1', 'Friction', 1);

model.mesh.create('mesh1', 'geom1');
model.mesh('mesh1').feature.create('ftril', 'FreeTri');
model.mesh('mesh1').feature('ftril').selection.geom('geom1', 2);
model.mesh('mesh1').feature('ftril').selection.set([2 3]);
model.mesh('mesh1').feature('ftril').feature.create('dis1', 'Distribution');

```

```

model.mesh('mesh1').feature('ftri1').feature('dis1').selection.set([14]);
model.mesh('mesh1').feature('ftri1').feature.create('dis2', 'Distribution');
model.mesh('mesh1').feature('ftri1').feature('dis2').selection.set([6]);
model.mesh('mesh1').feature('ftri1').feature.create('size1', 'Size');
model.mesh('mesh1').feature.create('ftri2', 'FreeTri');
model.mesh('mesh1').feature('ftri2').feature.create('size1', 'Size');

model.result.table.create('evl2', 'Table');
model.result.table.create('tbl1', 'Table');

model.view('view1').axis.set('xmin', '-840.8500366210938');
model.view('view1').axis.set('xmax', '840.8500366210938');
model.view('view1').axis.set('ymin', '-46.72823715209961');
model.view('view1').axis.set('ymax', '1049.84423828125');
model.view('view3').axis.set('xmin', '-669.54833984375');
model.view('view3').axis.set('xmax', '1516.958740234375');
model.view('view3').axis.set('ymin', '-404.3259582519531');
model.view('view3').axis.set('ymax', '1162.2950439453125');
model.view('view6').axis.set('xmin', '-1.6572504043579102');
model.view('view6').axis.set('xmax', '1.6572504043579102');
model.view('view7').axis.set('xmin', '-1.5255906581878662');
model.view('view7').axis.set('xmax', '1.5255906581878662');
model.view('view8').axis.set('xmin', '-1.5255906581878662');
model.view('view8').axis.set('xmax', '1.5255906581878662');
model.view('view9').axis.set('xmin', '-1.5255906581878662');
model.view('view9').axis.set('xmax', '1.5255906581878662');

model.material('mat2').name('Steel/TF');
model.material('mat2').propertyGroup('def').func.name('Functions');
model.material('mat2').propertyGroup('def').set('youngsmodulus', 'f_E(X[1/m],Y[1/m])');
model.material('mat2').propertyGroup('def').set('poissonsratio', 'f_nu(X[1/m],Y[1/m])');
model.material('mat2').propertyGroup('def').set('density', 'f_rho(X[1/m],Y[1/m])');
model.material('mat2').propertyGroup('def').set('heatcapacity', '');
model.material('mat2').propertyGroup('def').set('thermalconductivity', {'0' '0' '0'
'0' '0' '0' ''});
model.material('mat1').name('DLC');
model.material('mat1').propertyGroup('def').func.name('Functions');
model.material('mat1').propertyGroup('def').set('youngsmodulus', 'E_DLC');
model.material('mat1').propertyGroup('def').set('poissonsratio', 'nu_DLC');
model.material('mat1').propertyGroup('def').set('density', 'rho_DLC');
model.material('mat1').propertyGroup('def').set('thermalconductivity', {'0' '0' '0'
'0' '0' '0' ''});
model.material('mat1').propertyGroup('def').set('heatcapacity', '');
model.material('mat3').name('AISI 440C Steel');
model.material('mat3').propertyGroup('def').func.name('Functions');
model.material('mat3').propertyGroup('def').set('youngsmodulus', 'E_Steel');
model.material('mat3').propertyGroup('def').set('poissonsratio', 'nu_Steel');
model.material('mat3').propertyGroup('def').set('density', 'rho_Steel');
model.material('mat3').propertyGroup('def').set('thermalconductivity', {'0' '0' '0'
'0' '0' '0' ''});
model.material('mat3').propertyGroup('def').set('heatcapacity', '');

model.physics('solid').prop('d').set('d', 'depth');
model.physics('solid').feature('lemm1').set('ForceLinearStrainRes', '1');
model.physics('solid').feature('lemm1').set('editModelInputs', '1');
model.physics('solid').feature('lemm1').name('Linear Elastic Material Model 1');
model.physics('solid').feature('init1').set('u', {'u'; 'v'; '0'});
model.physics('solid').feature('displ').set('Direction', {'1'; '1'; '0'});
model.physics('solid').feature('bll1').set('FperVol', {'0'; '-Fn/Vsph'; '0'});
model.physics('solid').feature('bll1').set('LoadType', 'TotalForce');
model.physics('solid').feature('bll1').set('Ftot', {'0'; '-Fn'; '0'});
model.physics('solid').feature('disp3').set('U0', {'dispx'; '0'; '0'});
model.physics('solid').feature('disp3').set('Direction', {'1'; '0'; '0'});
model.physics('solid').feature('cntl').set('pairs', 'ap2');
model.physics('solid').feature('cntl').set('Tn_init', '0.5[GPa]');
model.physics('solid').feature('cntl').feature('fric1').set('mustat', 'frictioncoeff');
model.physics('solid').feature('cntl').feature('fric1').set('Tt_init', {'solid.Ttx_ap2';
'solid.Tty_ap2'; '0'});
model.physics('solid').feature('cntl').feature('fric1').set('cm_old_init', {'X'; 'Y';
'0'});
model.physics('solid').feature('cntl').feature('fric1').set('ContactPreviousStep',
'InContact');

model.mesh('mesh1').feature('size').set('hauto', 2);
model.mesh('mesh1').feature('ftri1').feature('dis1').set('numelem', 'meshnumber*2');
model.mesh('mesh1').feature('ftri1').feature('dis2').set('numelem', 'meshnumber');
model.mesh('mesh1').feature('ftri1').feature('size1').set('hmax', '2[um]');

```

```

model.mesh('mesh1').feature('ftril').feature('size1').set('hmin', '0.02');
model.mesh('mesh1').feature('ftril').feature('size1').set('hminactive', false);
model.mesh('mesh1').feature('ftril').feature('size1').set('hcurve', '0.2');
model.mesh('mesh1').feature('ftril').feature('size1').set('hcurveactive', false);
model.mesh('mesh1').feature('ftril').feature('size1').set('harrowactive', false);
model.mesh('mesh1').feature('ftril').feature('size1').set('hgrad', '1.1');
model.mesh('mesh1').feature('ftril').feature('size1').set('hgradactive', false);
model.mesh('mesh1').feature('ftril').feature('size1').set('hauto', '1');
model.mesh('mesh1').feature('ftril').feature('size1').set('hmax', '2[um]');
model.mesh('mesh1').feature('ftril').feature('size1').set('hmin', '0.02');
model.mesh('mesh1').feature('ftril').feature('size1').set('hminactive', false);
model.mesh('mesh1').feature('ftril').feature('size1').set('hcurveactive', false);
model.mesh('mesh1').feature('ftril').feature('size1').set('harrowactive', false);
model.mesh('mesh1').feature('ftril').feature('size1').set('hgradactive', false);
model.mesh('mesh1').feature('ftri2').feature('size1').set('hmax', '37');
model.mesh('mesh1').feature('ftri2').feature('size1').set('hmaxactive', false);
model.mesh('mesh1').feature('ftri2').feature('size1').set('hmin', '0.125');
model.mesh('mesh1').feature('ftri2').feature('size1').set('hminactive', false);
model.mesh('mesh1').feature('ftri2').feature('size1').set('hcurve', '0.25');
model.mesh('mesh1').feature('ftri2').feature('size1').set('hcurveactive', false);
model.mesh('mesh1').feature('ftri2').feature('size1').set('harrowactive', false);
model.mesh('mesh1').feature('ftri2').feature('size1').set('hgrad', '1.1');
model.mesh('mesh1').feature('ftri2').feature('size1').set('hauto', '3');
model.mesh('mesh1').feature('ftri2').feature('size1').set('hmax', '37');
model.mesh('mesh1').feature('ftri2').feature('size1').set('hmaxactive', false);
model.mesh('mesh1').feature('ftri2').feature('size1').set('hminactive', false);
model.mesh('mesh1').feature('ftri2').feature('size1').set('hcurveactive', false);
model.mesh('mesh1').feature('ftri2').feature('size1').set('harrowactive', false);
model.mesh('mesh1').feature('ftri2').feature('size1').set('hgrad', '1.1');
model.mesh('mesh1').run;

model.result.table('evl2').name('Evaluation 2D');
model.result.table('evl2').comments('Interactive 2D values');
model.result.table('tbl1').comments('Surface Maximum 1 (solid.p)');

model.study.create('std1');
model.study('std1').feature.create('param', 'Parametric');
model.study('std1').feature.create('stat', 'Stationary');

model.sol.create('soll');
model.sol('soll').study('std1');
model.sol('soll').attach('std1');
model.sol('soll').feature.create('st1', 'StudyStep');
model.sol('soll').feature.create('v1', 'Variables');
model.sol('soll').feature.create('s1', 'Stationary');
model.sol('soll').feature('s1').feature.create('p1', 'Parametric');
model.sol('soll').feature('s1').feature('p1').feature.create('ps1', 'PreviousSolution');
model.sol('soll').feature('s1').feature.create('sel', 'Segregated');
model.sol('soll').feature('s1').feature('sel').feature.create('ss1', 'SegregatedStep');
model.sol('soll').feature('s1').feature('sel').feature.create('ls1', 'LumpedStep');
model.sol('soll').feature('s1').feature('sel').feature.remove('ssDef');
model.sol('soll').feature('s1').feature.remove('fcDef');

model.result.create('pg1', 'PlotGroup2D');
model.result('pg1').feature.create('surfl', 'Surface');
model.result('pg1').feature('surfl').feature.create('def', 'Deform');
model.result.create('pg5', 'PlotGroup2D');
model.result('pg5').feature.create('surfl', 'Surface');
model.result('pg5').feature('surfl').feature.create('def', 'Deform');
model.result.create('pg2', 'PlotGroup1D');
model.result('pg2').set('probetag', 'none');
model.result('pg2').feature.create('lngr1', 'LineGraph');
model.result('pg2').feature('lngr1').selection.set([14]);
model.result.create('pg3', 'PlotGroup1D');
model.result('pg3').set('probetag', 'none');
model.result('pg3').feature.create('lngr1', 'LineGraph');
model.result('pg3').feature('lngr1').selection.set([14]);
model.result('pg3').feature.create('lngr2', 'LineGraph');
model.result('pg3').feature('lngr2').selection.set([6]);
model.result('pg3').feature.create('lngr3', 'LineGraph');
model.result('pg3').feature('lngr3').selection.set([3]);
model.result('pg3').feature.create('lngr4', 'LineGraph');
model.result('pg3').feature('lngr4').selection.set([14]);
model.result.create('pg4', 'PlotGroup1D');
model.result('pg4').set('probetag', 'none');
model.result('pg4').feature.create('lngr1', 'LineGraph');
model.result('pg4').feature('lngr1').selection.set([14]);

```

```

model.result('pg4').feature.create('lngr2', 'LineGraph');
model.result('pg4').feature('lngr2').selection.set([6]);
model.result('pg4').feature.create('lngr3', 'LineGraph');
model.result('pg4').feature('lngr3').selection.set([3]);
model.result('pg4').feature.create('lngr4', 'LineGraph');
model.result('pg4').feature('lngr4').selection.set([14]);
model.result.create('pg6', 'PlotGroup1D');
model.result('pg6').set('probetag', 'none');
model.result('pg6').feature.create('lngr1', 'LineGraph');
model.result('pg6').feature('lngr1').selection.set([14]);
model.result('pg6').feature.create('lngr2', 'LineGraph');
model.result('pg6').feature('lngr2').selection.set([14]);

model.study('std1').name('Study 1 (TF)');
model.study('std1').feature('param').set('pname', {'dispX'});
model.study('std1').feature('param').set('plistarr', {'10[um]'});

model.sol('sol1').attach('std1');
model.sol('sol1').feature('st1').name('Compile Equations: Stationary');
model.sol('sol1').feature('st1').set('studystep', 'stat');
model.sol('sol1').feature('v1').set('control', 'stat');
model.sol('sol1').feature('v1').feature('mod1_u').set('scalemethod', 'manual');
model.sol('sol1').feature('v1').feature('mod1_u').set('scaleval', '1e-
2*0.001397712416724923');
model.sol('sol1').feature('v1').feature('mod1_solid_Tn_ap2').set('scalemethod',
'manual');
model.sol('sol1').feature('v1').feature('mod1_solid_Tn_ap2').set('scaleval',
'100000000');
model.sol('sol1').feature('v1').feature('mod1_solid_Tt_ap2').set('scalemethod',
'manual');
model.sol('sol1').feature('v1').feature('mod1_solid_Tt_ap2').set('scaleval', '1000000');
model.sol('sol1').feature('s1').set('control', 'stat');
model.sol('sol1').feature('s1').feature('p1').set('control', 'param');
model.sol('sol1').feature('s1').feature('p1').set('pname', {'dispX'});
model.sol('sol1').feature('s1').feature('p1').set('plistarr', {'10[um]'});
model.sol('sol1').feature('s1').feature('p1').set('porder', 'linear');
model.sol('sol1').feature('s1').feature('p1').feature('ps1').set('prevcomp',
{'mod1_solid_contact_ap2_old' 'mod1_solid_cm_ap2_old'});
model.sol('sol1').feature('s1').feature('sel').set('maxsegiter', '15');
model.sol('sol1').feature('s1').feature('sel').feature('ss1').set('segvar', {'mod1_u'});
model.sol('sol1').feature('s1').feature('sel').feature('ss1').set('subdtech', 'ddog');
model.sol('sol1').feature('s1').feature('sel').feature('ss1').set('subtermauto',
'itertol');
model.sol('sol1').feature('s1').feature('sel').feature('ss1').set('subntolfact', '1');
model.sol('sol1').feature('s1').feature('sel').feature('ss1').set('subiter', '7');
model.sol('sol1').feature('s1').feature('sel').feature('ls1').set('segvar',
{'mod1_solid_Tn_ap2' 'mod1_solid_Tt_ap2' 'mod1_solid_contact_ap2_old'
'mod1_solid_cm_ap2_old'});
model.sol('sol1').runAll();

model.result('pg1').name('Stress (solid)');
model.result('pg1').feature('surf1').set('expr', 'solid.p');
model.result('pg1').feature('surf1').set('unit', 'GPa');
model.result('pg1').feature('surf1').set('descr', 'Pressure');
model.result('pg1').feature('surf1').feature('def').set('scaleactive', true);
model.result('pg5').name('Elastic Modulus');
model.result('pg5').feature('surf1').set('expr', 'solid.E');
model.result('pg5').feature('surf1').set('unit', 'GPa');
model.result('pg5').feature('surf1').set('descr', 'Young's modulus');
model.result('pg5').feature('surf1').feature('def').set('scaleactive', true);
model.result('pg2').set('xlabel', ['x-coordinate (' native2unicode(hex2dec('00b5'),
'Cp1252') 'm)']);
model.result('pg2').set('ylabel', 'Contact pressure, contact pair ap2 (GPa)');
model.result('pg2').set('axislimits', 'on');
model.result('pg2').set('xmin', '-165.2027587890625');
model.result('pg2').set('xmax', '241.5543975830078');
model.result('pg2').set('ymin', '-2.231545925140381');
model.result('pg2').set('ymax', '3.056295394897461');
model.result('pg2').set('xlabelactive', false);
model.result('pg2').set('ylabelactive', false);
model.result('pg2').feature('lngr1').set('expr', 'solid.Tn_ap2');
model.result('pg2').feature('lngr1').set('unit', 'GPa');
model.result('pg2').feature('lngr1').set('descr', 'Contact pressure, contact pair ap2');
model.result('pg2').feature('lngr1').set('xdata', 'expr');
model.result('pg2').feature('lngr1').set('xdataexpr', 'x');
model.result('pg2').feature('lngr1').set('xdatadescr', 'x-coordinate');
model.result('pg3').name('Not Deformed');

```

```

model.result('pg3').set('looplevelinput', {'last'});
model.result('pg3').set('xlabel', ['X-coordinate (' native2unicode(hex2dec('00b5'),
' Cp1252') 'm')]);
model.result('pg3').set('axislimits', 'on');
model.result('pg3').set('xmin', '-250');
model.result('pg3').set('xmax', '250');
model.result('pg3').set('ymin', '497');
model.result('pg3').set('ymax', '510');
model.result('pg3').set('xlabelactive', false);
model.result('pg3').feature('lngr1').set('expr', 'Y');
model.result('pg3').feature('lngr1').set('descr', 'Y-coordinate');
model.result('pg3').feature('lngr1').set('xdata', 'expr');
model.result('pg3').feature('lngr1').set('xdataexpr', 'X');
model.result('pg3').feature('lngr1').set('xdatadescr', 'X-coordinate');
model.result('pg3').feature('lngr2').set('expr', 'Y');
model.result('pg3').feature('lngr2').set('descr', 'Y-coordinate');
model.result('pg3').feature('lngr2').set('xdata', 'expr');
model.result('pg3').feature('lngr2').set('xdataexpr', 'X');
model.result('pg3').feature('lngr2').set('xdatadescr', 'X-coordinate');
model.result('pg3').feature('lngr3').set('expr', 'Y');
model.result('pg3').feature('lngr3').set('descr', 'Y-coordinate');
model.result('pg3').feature('lngr3').set('xdata', 'expr');
model.result('pg3').feature('lngr3').set('xdataexpr', 'X');
model.result('pg3').feature('lngr3').set('xdatadescr', 'X-coordinate');
model.result('pg3').feature('lngr4').set('expr', 'Y+h(X)');
model.result('pg3').feature('lngr4').set('descr', 'Y+h(X)');
model.result('pg3').feature('lngr4').set('xdata', 'expr');
model.result('pg3').feature('lngr4').set('xdataexpr', 'X');
model.result('pg3').feature('lngr4').set('xdatadescr', 'X-coordinate');
model.result('pg4').name('Deformed');
model.result('pg4').set('looplevelinput', {'last'});
model.result('pg4').set('xlabel', ['x-coordinate (' native2unicode(hex2dec('00b5'),
' Cp1252') 'm')]);
model.result('pg4').set('axislimits', 'on');
model.result('pg4').set('xmin', '-652.8642578125');
model.result('pg4').set('xmax', '786.2227783203125');
model.result('pg4').set('ymin', '488.59320068359375');
model.result('pg4').set('ymax', '526.0096435546875');
model.result('pg4').set('xlabelactive', false);
model.result('pg4').feature('lngr1').set('expr', 'y');
model.result('pg4').feature('lngr1').set('descr', 'y-coordinate');
model.result('pg4').feature('lngr1').set('xdata', 'expr');
model.result('pg4').feature('lngr1').set('xdataexpr', 'x');
model.result('pg4').feature('lngr1').set('xdatadescr', 'x-coordinate');
model.result('pg4').feature('lngr2').set('expr', 'y');
model.result('pg4').feature('lngr2').set('descr', 'y-coordinate');
model.result('pg4').feature('lngr2').set('xdata', 'expr');
model.result('pg4').feature('lngr2').set('xdataexpr', 'x');
model.result('pg4').feature('lngr2').set('xdatadescr', 'x-coordinate');
model.result('pg4').feature('lngr3').set('expr', 'y');
model.result('pg4').feature('lngr3').set('descr', 'y-coordinate');
model.result('pg4').feature('lngr3').set('xdata', 'expr');
model.result('pg4').feature('lngr3').set('xdataexpr', 'x');
model.result('pg4').feature('lngr3').set('xdatadescr', 'x-coordinate');
model.result('pg4').feature('lngr4').set('expr', 'y+h(X)');
model.result('pg4').feature('lngr4').set('descr', 'y+h(X)');
model.result('pg4').feature('lngr4').set('xdata', 'expr');
model.result('pg4').feature('lngr4').set('xdataexpr', 'x');
model.result('pg4').feature('lngr4').set('xdatadescr', 'x-coordinate');
model.result('pg6').set('xlabel', ['X-coordinate (' native2unicode(hex2dec('00b5'),
' Cp1252') 'm')]);
model.result('pg6').set('xlabelactive', false);
model.result('pg6').feature('lngr1').set('expr', '(solid.E-E_Steel)/(E_TF-
E_Steel)*0.3[um]');
model.result('pg6').feature('lngr1').set('descr', '(solid.E-E_Steel)/(E_TF-
E_Steel)*0.3[um]');
model.result('pg6').feature('lngr1').set('xdata', 'expr');
model.result('pg6').feature('lngr1').set('xdataexpr', 'X');
model.result('pg6').feature('lngr1').set('xdatadescr', 'X-coordinate');
model.result('pg6').feature('lngr2').set('expr', 'h(X)');
model.result('pg6').feature('lngr2').set('descr', 'h(X)');
model.result('pg6').feature('lngr2').set('xdata', 'expr');
model.result('pg6').feature('lngr2').set('xdataexpr', 'X');
model.result('pg6').feature('lngr2').set('xdatadescr', 'X-coordinate');

```

```
out = model;
```


Appendix B

This appendix contains the MATLAB[®] coding to run the incremental wear model described in **Section 9.2**. The wear model runs through a control script which calls to the other script and function files as indicated in **Figure B.1**.

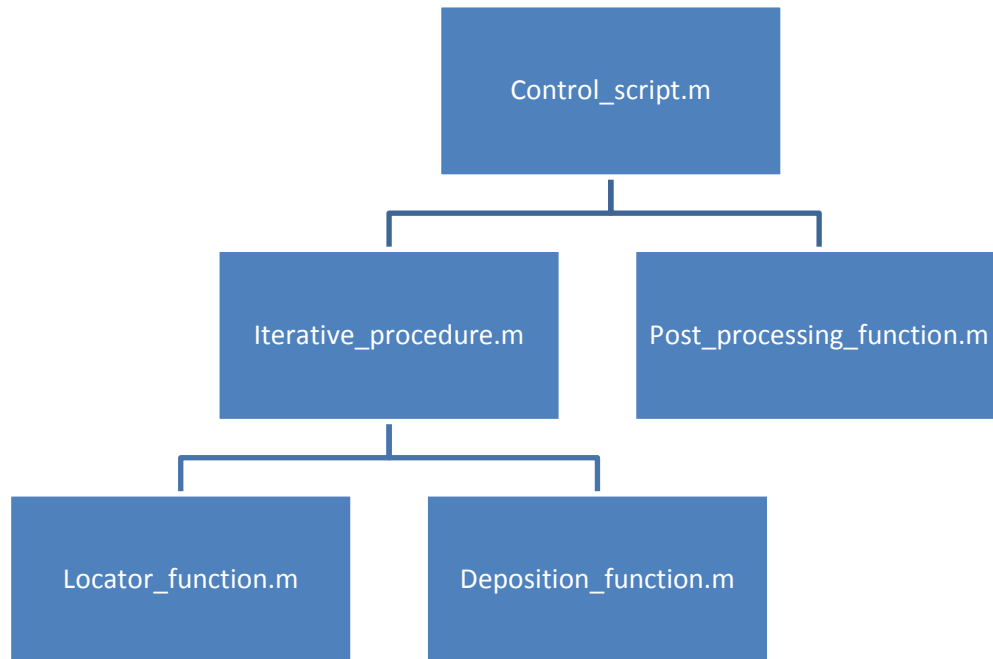


Figure B.1. A flowchart to describe the dependencies of each script and function file within the incremental wear model.

The first script is the control script. This initialises the wear model, defines the model geometry, test parameters, integration parameters, and material parameters, runs the iterative procedure to integrate forward in time, and post-processes the data. The script is presented below.

```
% Control_script.m
% An Incremental Wear Model for a DLC Coating and an AISI 440C Steel Ball
% LiveLink for MATLAB® and COMSOL Multiphysics 4.3
% D. C. Sutton, 21/11/2013

%% Initialisation

clear % Clear the workspace
close all % Close all figures
clc % Clear command window

IRIDIS = 0; % 1 if solving on IRIDIS, 0 otherwise
if IRIDIS == 1
    addpath('/local/software/rh53/comsol/4.3/mli') % For solving on IRIDIS
    mphstart % Initialise LiveLink for MATLAB®
end

import com.comsol.model.* % Load the LiveLink model
import com.comsol.model.util.* % Load the LiveLink model utility
model = mphload('Finite Element Model'); % Load the 2D quasistatic model

testname = 'v1'; % Define a unique test name
```

```

disp(['Test name is ',testname,'.']) % Print the test name to command window

%% Geometric parameters

thickness = 3.1; % DLC coating thickness [um]
ball_rad = 3e-3; % AISI 440C steel ball radius [m]

model.param.set('h_DLC', [num2str(thickness),'[um]'], 'DLC coating thickness'); % Set
the DLC coating thickness in COMSOL

%% Define the test parameters

stroke = 2e-3; % Stroke of TE77 [m]
force = 5; % Load of TE77 [N]
freq = 5; % Frequency of TE77 [1/s]
velocity = freq * stroke * 2; % Sliding velocity [m/s]
t_input = 3720; % Test time [s]
frictioncoeff = 0.169/force; % Coefficient of friction for BALINIT DLC STAR

model.param.set('frictioncoeff', num2str(frictioncoeff), 'Coefficient of friction'); %
Set coefficient of friction in COMSOL
model.param.set('Fn', [num2str(force),'[N]'], 'Normal load'); % Set normal load in
COMSOL
model.param.set('velocity', [num2str(velocity),'[m/s]'], 'Sliding velocity'); % Set
sliding velocity in COMSOL

%% Define integration parameters

dispx = 10e-6; % Displacement in x-direction each time-step [m]
para = 2 * stroke / dispx; % Number of time-steps per cycle of motion [.]
dt = dispx / velocity; % Time-step [s]

relaxation = 20000; % Relaxation [.]
N = relaxation * ceil(t_input / (dt * relaxation)); % Number of time-steps per iteration
timestep = dt * relaxation; % Timestep each iteration [s]
no_iter = N / relaxation; % Number of iterations [.]

model.param.set('dispx',[num2str(dispx),'[m]']); % Set x-displacement in COMSOL

disp(['Number of iterations is ',num2str(no_iter,3),'.']); % Print the number of
iterations to command window

vCF = 5e-11; % Diffusion coefficient of the contact pair [m^2/s]
vTF = 1e-11; % Diffusion coefficient of transfer layer [m^2/s]

%% Load the data from experiments, and calculate the specific wear rate (SWR)

% Load the wear data from experiments
load(fullfile(cd,'data_STAR_5N_5Hz.mat'));

% Calculate the average initial and final specific wear rate
swr_DLC = weardatavol_DLC ./ (force * velocity .* timedata); % Specific wear rate of DLC
coating
swr_CF = weardatavol_CF ./ (force * velocity .* timedata); % Specific wear rate of ball
count = 0; countb = 0;
for i = 1:length(timedata)
    if timedata(i) == min(timedata)
        count = count + 1;
        store(1, count) = swr_DLC(i);
        store(2, count) = swr_CF(i);
        store_wv(1, count) = weardatavol_DLC(i);
        store_wv(2, count) = weardatavol_CF(i);
    end
    if timedata(i) == max(timedata)
        countb = countb + 1;
        storeb(1, countb) = swr_DLC(i);
        storeb(2, countb) = swr_CF(i);
        storeb_wv(1, countb) = weardatavol_DLC(i);
        storeb_wv(2, countb) = weardatavol_CF(i);
    end
end
final_SWR_DLC = (mean(storeb_wv(1,:)) - mean(store_wv(1,:))) / (force * velocity *
(max(timedata) - min(timedata)));
final_SWR_CF = (mean(storeb_wv(2,:)) - mean(store_wv(2,:))) / (force * velocity *
(max(timedata) - min(timedata)));
SWR_DLC_vec = [0.38 * mean(store(1,:)), 0.18 * final_SWR_DLC]; % Vector of the initial
and final specific wear rate for the DLC coating

```

```

SWR_CF_vec = [0.85 * mean(store(2,:)), 0.25 * final_SWR_CF]; % Vector of the initial and
final specific wear rate for the ball
clear store storeb_wv storeb_wv count countb swr_DLC swr_CF final_SWR_DLC
final_SWR_CF fac

% Prescribe the logistic growth of the transfer layer
ttt = 0:timestep:t_input;
tfmax = 0.3; % Maximum transfer layer height
logistic = 0.0067; % Logistic growth parameter (1 / kappa)
fctn = tfmax * (1 - exp(-ttt * logistic)) / (1 - exp(-t_input * logistic)); % Logistic
growth function

% Define on which iterations to solve a finite element model
opt = 1; % Tune to solve more or less finite element models (0 < opt < 1)
ccc = 0; % A finite element model runs when ccc >= 1

% Define on which iterations to save the finite element model and workspace
selection = [1, 2, 3, 4, 5, 10, 15, 20, 50, 100, 200, t_input / timestep];
for i=1:length(selection)
    if selection(i) > no_iter
        selection(i) = no_iter;
    end
end

%% Define material parameters

E_DLC = 212e9; % Elastic modulus of the DLC coating
E_Steel = 200e9; % Elastic modulus of the AISI 440C steel ball
E_TF = 415e9; % Elastic modulus of the transfer layer

nu_DLC = 0.22; % Poisson's ratio of each surface of the DLC coating
nu_Steel = 0.30; % Poisson's ratio of the AISI 440C steel ball
nu_TF = 0.22; % Poisson's ratio of the transfer layer

rho_DLC = 2.5; % Density of the DLC coating
rho_Steel = 7.65; % Density of the AISI 440C steel ball
rho_TF = 2.5; % Density of the transfer layer

% Set the material parameters in COMSOL
model.param.set('E_DLC', [num2str(E_DLC)], '[Pa]', 'Youngs modulus of DLC');
model.param.set('E_Steel', [num2str(E_Steel)], '[Pa]', 'Youngs modulus of steel');
model.param.set('E_TF', [num2str(E_TF)], '[Pa]', 'Youngs modulus of transfer layer');
model.param.set('nu_DLC', [num2str(nu_DLC)], 'Poissons ratio of DLC');
model.param.set('nu_Steel', [num2str(nu_Steel)], 'Poissons ratio of steel');
model.param.set('nu_TF', [num2str(nu_TF)], 'Poissons ratio of transfer layer');
model.param.set('rho_DLC', [num2str(rho_DLC)], '[g/cm^3]', 'Density of DLC');
model.param.set('rho_Steel', [num2str(rho_Steel)], '[g/cm^3]', 'Density of steel');
model.param.set('rho_TF', [num2str(rho_TF)], '[g/cm^3]', 'Density of transfer layer');

%% Hertzian calculations

E_star = 2 * E_Steel * E_DLC / (E_Steel * (1 - nu_DLC^2) + E_DLC * (1 - nu_Steel^2)); %
Reduced modulus
a_point = (3 * force * ball_rad / (2 * E_star))^(1/3); % Hertzian point contact radius

% Optimisation of the model depth
a_guess = 50e-6; % Initial guess of contact radius
a_line = 0; % Hertzian line contact radius
while norm(a_line - a_guess) > 0.01e-6
    a_guess = a_guess + 0.01e-6; % Update guess of contact radius
    depth = pi * a_point^2 / (2 * a_guess); % Inferred model depth
    a_line = sqrt(8 * force * ball_rad / (pi * E_star * depth)); % Inferred Hertzian line
contact radius
end
adj = 0.1 * ceil(10 * force / (pi * a_line^2) * 1e-9); % Prediction of contact pressure

model.param.set('depth', [num2str(depth)], '[m]'); % Set the model depth in COMSOL
model.param.set('a', [num2str(a_line)], '[m]'); % Set the line contact radius in COMSOL

%% Integrate forwards in time

model.hist.disable; % Disable model history
totaltime = tic; % Start a timer for total time to solve model

for i = 1:relaxation:N
    run(fullfile(cd, 'Iterative_procedure.m')) % Runs model
end

```

```

toc(totaltime); % End the timer for total time to solve model

%% Post-processing

% Save the finite element model
modelName = fullfile(cd,[testname,'_iter_',num2str(iter +
1),'_of_',num2str(no_iter),'.mph']);
model.save(modelName);

% Save the workspace
warning off all
workspaceName = fullfile(cd,[testname,'_iter_',num2str(iter +
1),'_of_',num2str(no_iter),'_workspace.mat']);
save(workspaceName);
warning on all

% Run post-processing
if IRIDIS == 0
    Post_processing_function(testname, no_iter, no_iter, selection, 3, 4, timedata,
weardata_DLC, weardata_CF)
end

delete('junk.txt') % Delete output file
disp('Model finished.') % Print to command window

```

The second script is the iterative procedure that must run during each time-step. This saves back-ups of the finite element model and MATLAB® workspace, runs the finite element model, transforms from the finite element mesh to a uniform mesh, calculates wear of each surface and the growth of the transfer layer, smooth's the surfaces to prevent numerical error, stores the outputs, provides output plots as the model solves, and provides COMSOL Multiphysics with new interpolation data for the contact boundaries. The script is given below.

```

% Iterative_procedure.m
% An Incremental Wear Model for a DLC Coating and an AISI 440C Steel Ball
% LiveLink for MATLAB® and COMSOL Multiphysics 4.3
% D. C. Sutton, 21/11/2013

%% Save the finite element model and workspace if required

steptime = tic; % Start a timer for this iteration time
iter = (i-1) / relaxation; % Set the current iteration

% Save the model and workspace if required
if i > 1
    for j = 1:length(selection)
        if iter == selection(j)
            % Save the finite element model
            modelName =
fullfile(cd,[testname,'_iter_',num2str(iter),'_of_',num2str(no_iter),'.mph']);
            model.save(modelName);

            % Save the workspace
            warning off all
            workspaceName =
fullfile(cd,[testname,'_iter_',num2str(iter),'_of_',num2str(no_iter),'_workspace.mat']);
            save(workspaceName);
            warning on all
        end
    end
end

% Save the most recent finite element model as a backup
backupName = fullfile(cd,'backup.mph');
model.save(backupName);

% Save the most recent workspace as a backup
warning off all

```

```

backupNameworkspace = fullfile(cd, 'backup_workspace.mat');
save (backupNameworkspace);
warning on all

%% Run the finite element model

% Calculate on which iterations to solve a finite element model
if opt == 0 || i == 1
    ccc = 0.99;
else
    ccc = ccc + opt * (SWR_CF / SWR_CF_vec(1)); % ccc increases proportionally to the
specific wear rate
end

% Solve the finite element model
if ccc >= 1
    ccc = ccc - 1; % Reduce ccc to less than one again
    if i > 1
        attempts = 0; % Number of attempts to solve the finite element model
        shift = [0, -0.1, 0.1, -0.2, -0.3, 0.2]; % Deviations from the guess for initial
pressure
        while attempts < length(shift)
            try
                % Define the temporary guess for initial pressure
                attempts = attempts + 1;
                temp_adj = adj + shift(attempts); % New initial guess

                % Set the new initial guess in COMSOL
                model.physics('solid').feature('cnt1').set('Tn_init', 1,
[num2str(temp_adj), 'GPa']);

                % Solve in COMSOL and display progress if solves
                if IRIDIS == 0
                    ModelUtil.showProgress(true);
                end
                pause(1)
                model.geom('geom1').runAll; % Build geometry
                model.study('std1').run; % Run model
                fprintf('Solved for %3.2f GPa.\n', temp_adj) % Print output
                break
            catch err
                % Print output if the model fails to solve
                fprintf('Failed for %3.2f GPa.\n', temp_adj)
            end
        end

        % Keep the new initial guess for the next iteration
        adj = temp_adj;
    end
end

% Increase the current test time
testtime = (i - 1 + relaxation) * dt;

%% Set-up the interpolation files for the first iteration

if i == 1
    % Move the geometry according to the amount of wear
    modelgeom = model.geom('geom1');
    modelgeom.runAll;
    modelgeom.feature.create('mov4', 'Move');
    modelgeom.feature('mov4').selection('input').set({'unil'});
    modelgeom.feature('mov4').set('disply', '0[um]');
    modelgeom.run

    % Create an interpolation curve 'C' for the DLC surface
    modelgeom.run('pc4');
    modelgeom.feature.create('ic2', 'InterpolationCurve');
    modelgeom.feature('ic2').set('source', 'file');
    filenameC = fullfile(cd, ['C data ', testname, '.txt']);
    modelgeom.feature('ic2').set('filename', filenameC);
    modelgeom.feature('ic2').set('rtol', 1e-10);
    mgf=modelgeom.feature('csol3');
    mgf.selection('input').set({'pc2' 'pc3' 'r4' 'ic2'});
    modelgeom.feature.remove('pc4');

```

```

% Create an interpolation curve 'D' for the ball-bearing surface
modelgeom.run('pcl');
modelgeom.feature.create('ic1', 'InterpolationCurve');
modelgeom.feature('ic1').set('source', 'file');
filenameD = fullfile(cd,['D_data_',testname,'.txt']);
modelgeom.feature('ic1').set('filename', filenameD);
modelgeom.feature('ic1').set('rtol',1e-10);
modelgeom.feature('csol2').selection('input').set({'ic1' 'r2'});
modelgeom.feature.remove('pcl');

% Create a file input for transfer film height (called 'h_data')
h = model.func('int3');
h.model('mod1');
h.set('source', 'file');
filenameh = fullfile(cd,['h_data_',testname,'.txt']);
h.set('filename', filenameh);
h.set('funcs', {'h','1'});
model.func('int3').set('argunit', 'um');

% Create a file input for ball-bearing coordinates (using 'D_data')
coords = model.func('int5');
coords.model('mod1');
coords.set('source', 'file');
filename_coords=fullfile(cd,['D_data_',testname,'.txt']);
coords.set('filename', filename_coords);
coords.set('funcs', {'coords','1'});
model.func('int5').set('argunit', 'um');

% Define the parametric sweep
model.study('std1').feature('param').setIndex('plistarr', '10[um]', 0);
end

%% Define the model parameters for the first iteration

if i == 1
% Create a uniform grid
W = 9.76525e-4; % Length of geometry [m]
L = 1001; % Number of nodes
dx = 1e6 * W / (L - 1); % Spacing in uniform grid [um]

% Extract the original coordinates from COMSOL for the top boundary
dataInitD = mpheval(model,{'X' 'Y'}, 'dataset','dset1','edim', 'boundary', 'selection',
14);
initX = dataInitD.d1(1,:);
initial_Dpos = dataInitD.d2(1,:);

% Extract the original coordinates from COMSOL for the bottom boundary
dataInitC = mpheval(model,{'X' 'Y'}, 'dataset','dset1','edim', 'boundary', 'selection',
6);
initXX = dataInitC.d1(1,:);
initial_Cpos = dataInitC.d2(1,:);

% Convert from initial grid to the uniform grid with spacing dx and length L
X = 1e6 * W / 2:-dx:-1e6 * W / 2;
initial_Cpos = interp1(initXX, initial_Cpos, X, 'spline');
initial_Dpos = interp1(initX, initial_Dpos, X, 'spline');

% Define empty vectors for output (spatial)
sum_w_DLC = zeros(1,L); % Total wear depth of DLC coating
sum_w_CF = zeros(1,L); % Total wear depth of ball

% Define empty vectors for output (temporal)
mean_h = zeros(1,no_iter); % Average transfer film height.
mean_P = zeros(1,no_iter); % Mean contact pressure
max_P = zeros(1,no_iter); % Maximum contact pressure
initP = zeros(1,no_iter); % Initial condition for each model.
solvertime = zeros(1,no_iter); % Solution time for each model.
end

%% Extract the data from finite element model and interpolate to uniform grid

% Extract the data from COMSOL
data = mpheval(model,{'solid.Tn_ap2' 'solid.gap_ap2'
'X'}, 'dataset','dset1','edim','boundary','selection',14);
P1 = data.d1(1,:); % Contact pressure (direction = 1)
P2 = fliplr(P1); % Contact pressure (direction = -1)
contact1=data.d2(1,:); % Contact gap distance (material frame, direction = 1)

```

```

contact2=fliplr(contact1); % Contact gap distance (material frame, direction = -1)
meshX = data.d3(1,:); % Output the initial X coordinates

% Interpolate from the non-uniform mesh to uniform grid with spacing dx and length L
P1 = interp1(meshX, P1, X, 'spline');
P2 = interp1(meshX, P2, X, 'spline');
for m = 1:length(contact1)
    if contact1(m) > 50
        contact1(m) = 50;
    end
    if contact2(m) > 50
        contact2(m) = 50;
    end
end
contact1 = interp1(meshX, contact1, X, 'spline');
contact2 = interp1(meshX, contact2, X, 'spline');

%% Adjust the geometry for the DLC coating is the stroke is too large

% Average the DLC coating wear depth if the stroke is larger than 2/3 * model geometry
if stroke > 2/3*W
    if i == 1
        W0 = 2 * stroke; % Store W
        L0 = 1 + ceil(1e6 * W0 / dx); % Store L
        W0 = dx * (L0 - 1) / 1e6; % Adjust W0
        X0 = 1e6 * W0 / 2:-1e6 * W0 / (L0 - 1):-1e6* W0 / 2; % Save new X
    end
    var = 1;
else
    var = 0;
end

% Transform the finite element output data P1, P2, contact1, contact2, and sum_w_DLC
if var == 1
    P10 = interp1(X, P1, X0);
    for j = 1:length(P10)
        if isnan(P10(j)) == 1
            P10(j) = 0;
        end
    end
    P20 = interp1(X, P2, X0);
    for j = 1:length(P20)
        if isnan(P20(j)) == 1
            P20(j) = 0;
        end
    end
    contact10 = interp1(X, contact1, X0);
    for j = 1:length(contact10)
        if isnan(contact10(j)) == 1
            contact10(j) = 0;
        end
    end
    contact20 = interp1(X, contact2, X0);
    for j = 1:length(contact20)
        if isnan(contact20(j)) == 1
            contact20(j) = 0;
        end
    end
    sum_w_DLC = interp1(X, sum_w_DLC, X0);
    for j = 1:length(sum_w_DLC)
        if isnan(sum_w_DLC(j)) == 1
            sum_w_DLC(j) = 0;
        end
    end
else
    W0 = W;
    L0 = L;
    X0 = X;
    P10 = P1;
    P20 = P2;
    contact10 = contact1;
    contact20 = contact2;
end

%% Calculate the wear depth of the DLC coating

% Ensure the pressure distribution is always positive

```

```

for m = 1:L0
    if P10(m) <= 0 || P20(m) <= 0
        P10(m) = 0;
        P20(m) = 0;
    end
end
for m = 1:L
    if P1(m) <= 0 || P2(m) <= 0
        P1(m) = 0;
        P2(m) = 0;
    end
end

% Initialise empty vectors
if i == 1
    wearscar = zeros(1,L0);
    contactbottom0 = zeros(1, L0);
    contactbottom = zeros(1, L);
end

% Calculate wear depth for each cycle (there are 'para' movements in one cycle of
motion)
w_DLC_cycle = zeros(1, L0);
for k = 1:para
    % Tracks direction of sliding
    if k <= para / 4
        upper = k;
        P0 = P10; % Slides right to left
        P = P1;
        contacttop0 = contact10;
        contacttop = contact1;
    elseif k <= 3 * para / 4
        upper = para / 2 - k;
        P0 = P20; % Slides right to left
        P = P2;
        contacttop0 = contact20;
        contacttop = contact2;
    else
        upper = k - para;
        P0 = P10; % Slides left to right
        P = P1;
        contacttop0 = contact10;
        contacttop = contact1;
    end

    % Tracks position on surface
    dd = upper * dispX; % Position on surface [m]
    dX = round(dd * (L0 - 1) / W0); % Position on surface [number of elements]

    % Define the nodes where the ball is "in contact"
    for m = 1:L0
        dj = mod(m+dX, L0);
        if dj == 0
            dj = L0;
        end
        if contacttop0(m) < 0.005
            contactbottom0(dj) = 1;
            contacttop0(m) = 1;
        else
            contactbottom0(dj) = 0;
            contacttop0(m) = 0;
        end
    end
    for m = 1:L
        dj = mod(m+dX, L);
        if dj == 0
            dj = L;
        end
        if contacttop(m) < 0.005
            contactbottom(dj) = 1;
            contacttop(m) = 1;
        else
            contactbottom(dj) = 0;
            contacttop(m) = 0;
        end
    end
end

```

```

    % Calculate the length of the contact region
    d = find(contacttop, 1, 'last') - find(contacttop, 1, 'first'); % Length of contact
region [gridpoints]
    d_length = 1e6 * W0 * d / (L0 - 1); % Length of contact region [um]

    % Set the current specific wear rate of the DLC coating based on the current transfer
layer height
    if i == 1
        SWR_DLC = SWR_DLC_vec(1);
    else
        SWR_DLC = SWR_DLC_vec(1) * (tfmax - mean_h(iter)) / tfmax +
SWR_DLC_vec(length(SWR_DLC_vec)) * mean_h(iter) / tfmax;
    end

    % Calculate the wear depth of the DLC coating
    w_DLC = zeros(1,L0);
    for m = 1:L0
        dj = mod(m+dX, L0);
        if dj == 0
            dj = L0;
        end
        w_DLC(dj) = 1e-3 * relaxation / para * SWR_DLC * P0(m) * velocity * dt *
contactbottom0(dj);
    end

    % Store the wear of the DLC coating
    w_DLC_cycle = w_DLC_cycle + w_DLC;
    sum_w_DLC = wearscar + w_DLC;
    wearscar = wearscar + w_DLC;
end

% Store the wear of DLC this iteration
wear_cycle = sum(w_DLC_cycle);

% Interpolate back from the new coordinates for the surface of the DLC coating to the
uniform grid
w_DLC = interp1(X0, w_DLC, X);
w_DLC_cycle = interp1(X0, w_DLC_cycle, X);
sum_w_DLC = interp1(X0, sum_w_DLC, X);

% Average the wear data if the wear scar is too long relative to the model geometry
if var == 1
    w_DLC_cycle = mean(w_DLC_cycle) * ones(1, L);
    sum_w_DLC = mean(sum_w_DLC) * ones(1, L);
end

%% Calculate the wear depth of the ball

% Set the current specific wear rate of the ball based on the current transfer layer
height
if i==1
    SWR_CF = SWR_CF_vec(1);
else
    SWR_CF = SWR_CF_vec(1) * (tfmax - mean_h(iter)) / tfmax +
SWR_CF_vec(length(SWR_CF_vec)) * mean_h(iter) / tfmax;
end
sum_dh = ones(1, L) * fctn(iter + 1) .* contacttop;

% Calculate the wear depth of the ball
w_CF = zeros(1,L);
for m = 1:L
    w_CF(m) = 1e-3 * relaxation * SWR_CF * P(m) * velocity * dt * contacttop(m);
end

% Smooth the wear depth of the ball using Deposition_function.m
for k = 1:relaxation
    w_CF = Deposition_function(W, L, dt, w_CF, vCF);
end

% Store the wear of the ball
sum_w_CF = sum_w_CF + w_CF;

%% Calculate the growth of the transfer layer

% Smooth the growth of the transfer layer using Deposition_function.m
for k = 1:relaxation
    sum_dh = Deposition_function(W, L, dt, sum_dh, vTF);

```

```

end

%% Continuity check and smoothing

% First derivative of the ball surface
gr = zeros(1,L);
for m = 2:L-1
    gr(m) = (sum_w_CF(m-1) - sum_w_CF(m+1))/(2*dx) - (sum_dh(m-1) - sum_dh(m+1)) / (2 *
dx);
end

% Second derivative of the ball surface
gr2 = zeros(1,L);
for m=2:L-1
    gr2(m) = (gr(m-1) - gr(m+1)) / (2 * dx);
end
gr2_init = gr2;

% Smooth the surfaces locally with bandwidth smfac if the second derivative of the ball
surface is smaller than delta
smfac = 10; % Bandwidth
delta = 0.01; % Allowed discontinuity in gradient (-ve => maxima)

% Locate the points where the second derivative of the ball surface is smaller than
delta
counter = 0;
location = 0;
for m = 5:L-5
    if gr2(m) < -delta || gr2(m) > delta
        counter = counter + 1;
        location(counter) = m;
    end
end

% If the points lie next to each other then delete the repeats to prevent excess
smoothing
coord = Locator_function(location, smfac);

% Smooths the points until the second derivative of the ball surface is greater than
delta
storage = zeros(1, length(coord));
for m = 1:length(coord)
    point = coord(m);
    while gr2(point) < -delta || gr2(point) > delta
        % Smooth the point chosen
        storage(m) = storage(m) + 1;
        temp = sum_w_CF(point - 2 * smfac:point + 2 * smfac);
        temp = smooth(temp, smfac)';
        sum_w_CF(point - 2 * smfac:point + 2 * smfac) = temp;

        % Calculate the new second derivative
        for n = 2:length(sum_w_CF)-1
            gr(n)=(sum_w_CF(n-1) - sum_w_CF(n+1))/(2*dx);
        end
        for n = 2:length(sum_w_CF)-1
            gr2(n)=(gr(n-1)-gr(n+1))/(2*dx);
        end
    end
end

%% Store the output data for this iteration

mean_h(iter + 1) = max(sum_dh((L - 1) / 2 + ceil(-d / 2):(L - 1) / 2 + ceil(d / 2))); %
Average transfer layer height
mean_w_DLC(iter + 1) = mean(sum_w_DLC((L - 1) / 2 + ceil(-d / 2):(L - 1) / 2 + ceil(d /
2))); % Average wear depth of DLC coating
mean_w_CF(iter + 1) = mean(initial_Dpos((L - 1) / 2 + ceil(-d / 4):(L - 1) / 2 + ceil(d
/ 4)) - 500 + sum_w_CF((L - 1) / 2 + ceil(-d / 4):(L - 1) / 2 + ceil(d / 4))); % Average
wear depth of ball
mean_wv_DLC(iter + 1) = 1e-3 * mean_w_DLC(iter + 1) * stroke * 2 * sqrt(mean_w_CF(iter +
1) * (2 * ball_rad * 1e6 - mean_w_CF(iter + 1))); % Total wear volume of DLC coating
mean_wv_CF(iter + 1) = 1e-9 * pi / 3 * mean_w_CF(iter + 1)^2 * (3 * ball_rad * 1e6 -
mean_w_CF(iter + 1)); % Total wear volume of ball
mean_P(iter + 1) = mean(P((L - 1) / 2 + ceil(-d / 2):(L - 1) / 2 + ceil(d / 2))); %
Average contact pressure
max_P(iter + 1) = max(P); % Maximum contact pressure

```

```

%% Update plots of data each iteration

if IRIDIS == 0
    figure(1)
    % Plot the mean wear depth of the DLC coating against experimental data
    subplot(2,3,1); hold on
    plot(testtime, mean_w_DLC(iter + 1), 'ok', 0, 0, 'ok');
    plot(timedata, weardata_DLC, 'ko')
    hold on
    xlim([0, testtime]);
    legend('DLC Coating', 'Location', 'SouthEast')
    xlabel('Time [s]')
    ylabel('Wear Depth [um]')

    % Plot the mean wear depth of the ball against experimental data
    subplot(2,3,2); hold on
    plot(testtime, mean_w_CF(iter + 1), 'or', 0, 0, 'or');
    plot(timedata, weardata_CF, 'ro')
    hold on
    xlim([0, testtime]);
    legend('Steel', 'Location', 'SouthEast')
    xlabel('Time [s]')
    ylabel('Wear Depth [um]')

    % Plot the mean transfer layer height against experimental data
    subplot(2,3,3); hold on
    plot(testtime, mean_h(iter + 1), 'og', 0, 0, 'og');
    hold on
    xlim([0, testtime]);
    ylim([0, 0.1 + 1.1 * max(sum_dh)])
    legend('Transfer Layer')
    xlabel('Time [s]')
    ylabel('Growth [um]')

    % Plot the mean wear volume of the DLC coating against experimental data
    subplot(2,3,4); hold on
    plot(testtime, mean_wv_DLC(iter + 1), 'ok', 0, 0, 'ok');
    plot(timedata, weardata_vol_DLC, 'ko')
    hold on
    xlim([0, testtime]);
    legend('DLC Coating', 'Location', 'SouthEast')
    xlabel('Time [s]')
    ylabel('Wear Volume [mm^3]')

    % Plot the mean wear volume of the ball against experimental data
    subplot(2,3,5); hold on
    plot(testtime, mean_wv_CF(iter + 1), 'or', 0, 0, 'or');
    plot(timedata, weardata_vol_CF, 'ro')
    hold on
    xlim([0, testtime]);
    legend('Steel', 'Location', 'SouthEast')
    xlabel('Time [s]')
    ylabel('Wear Volume [mm^3]')
end

%% Calculate new interpolation files for input to the finite element model

% Export the data currently loaded for interpolation
if i > 1
    model.func('int3').exportData(fullfile(cd, 'junk.txt'));
    model.func('int5').exportData(fullfile(cd, 'junk.txt'));
    model.func('int3').set('filename', filenameh);
    model.func('int5').set('filename', filename_coords);
end

% Save C as an interpolation file
fid = fopen(filenameC, 'w');
for m = 1:L
    fprintf(fid, ' %10.10f %10.10f\n', X(m), initial_Cpos(m) - sum_w_DLC(m));
end
fclose(fid);

% Save D as an interpolation file
fid = fopen(filenameD, 'w');
for m = 1:L
    fprintf(fid, ' %10.10f %10.10f\n', X(m), initial_Dpos(m) + sum_w_CF(m) - sum_dh(m) +
1);

```

```

end
fclose(fid);

% Save h as an interpolation file
fid = fopen(filenameh, 'w');
for m = 1:L
    fprintf(fid, ' %10.10f %10.10f\n', X(m), sum_dh(m));
end
fclose(fid);

% Import the data currently loaded for interpolation
model.func('int3').importData;
model.func('int5').importData;
model.geom('geom1').feature('ic2').importData;
model.geom('geom1').feature('ic1').importData;

%% Calculate new parameters for input to the finite element model

% Set an initial guess for contact pressure in COMSOL
initP(iter + 1) = adj;

% Define the mesh density based on the contact pressure
if i == 1
    meshnumber=900;
end
if max_P(iter + 1) < 1e9
    meshnumber = roundn((L-1) * adj,2);
end
if meshnumber > 0.9 * (L-1)
    meshnumber = 900;
elseif meshnumber < 0.5 * (L-1)
    meshnumber = 500;
end
meshdensity=round(1e6*W/meshnumber*10)/10;

% Define the displacement so that the contact pair are touching
disply=min((initial_Dpos + sum_w_CF-sum_dh)-(initial_Cpos - sum_w_DLC));

% Save the time taken for this iteration
solvertime(iter + 1) = toc(stepstime);

% Set the model parameters in COMSOL
model.physics('solid').feature('cnt1').set('Tn_init', 1, [num2str(adj), '[GPa]']);
model.param.set('meshnumber', num2str(meshnumber));
model.mesh('mesh1').feature('ftril').feature('size1').set('hmax', [num2str(meshdensity),
' [um]']);
model.param.set('a', [num2str(d_length/2), ' [um]']);
model.geom.feature('mov4').set('disply', [num2str(disply), ' [um]']);
model.sol('sol1').feature('s1').feature('sel').set('maxsegiter', '15');

%% Update plots of data each iteration
if IRIDIS == 0
    % Plot the model geometry
    figure(1)
    subplot(2,3,6)
    plot(X,initial_Dpos, 'k--')
    hold on
    plot(X,initial_Cpos - sum_w_DLC, 'k')
    plot(X,initial_Cpos - 2, 'k')
    plot(X,initial_Dpos + sum_w_CF, 'k')
    plot(X,initial_Dpos + sum_w_CF - sum_dh, 'g')
    hold off
    if i > 1
        xlim([-d_length/1.5 d_length/1.5]); ylim([500 - ceil(5*mean_w_DLC(iter)) 500 +
ceil(5*mean_w_CF(iter))]);
    else
        xlim([-d_length/1.5 d_length/1.5]); ylim([499 501]);
    end
    xlabel('x [um]');
    ylabel('y [um]');
    title(['Surfaces at t = ', num2str(testtime,3), ' seconds.']);

% Plot the contact pressure distribution
figure(2)
subplot(1,2,1+mod(iter+2,2))
plot(X, P*1e-9)

```

```

xlim([-d_length d_length]); ylim([-0.1 2.5]);
xlabel('x [um]'); ylabel('Contact Pressure [GPa]');
title(['Pressure at t = ',num2str(testtime-timestep,4),' seconds.']);

pause(1)
end

%% Display informative text
fprintf('End of iteration No. %d. Current time is %5.2f seconds. There were %d smoothing
operations.\n',iter + 1,testtime, sum(storage))

```

The locator function controls smoothing, and automatically locates regions where the second derivative of the contact boundaries is large. The function is given below.

```

% Locator_function.m
% An Incremental Wear Model for a DLC Coating and an AISI 440C Steel Ball
% LiveLink for MATLAB® and COMSOL Multiphysics 4.3
% D. C. Sutton, 21/11/2013

function sm = Locator_function(location, smfac)

% Add zero values to the vector
location = [zeros(1, smfac) location zeros(1, smfac)];

% Locate the points with a large second derivative
if length(location) > 1

response = 1;
while response > 0
response = 0;
for m = 1:length(location) - smfac
vec = zeros(1, smfac);
dr = 1;
vec(dr) = 1;
while location(m + dr) - location(m) == dr
if dr <= smfac - 1
vec(dr + 1) = 1;
response = response + 1;
dr = dr + 1;
else
location(m + dr) = location(m);
end
end
save = ceil(sum(vec) / 2);
for dr = 1:sum(vec)
if dr ~= save
location(m + dr - 1) = 0;
end
end
end
end

% Remove all the zero values in the vector
temp2 = zeros(1, nnz(location));
counter = 0;
for n = 1:length(location)
if location(n) > 0
counter = counter + 1;
temp2(counter) = location(n);
end
end
location = temp2;
end
sm = location;

```

The deposition function controls the smoothing of the contact boundaries using a diffusion equation. The function is presented below.

```

% Deposition_function.m
% An Incremental Wear Model for a DLC Coating and an AISI 440C Steel Ball

```

```

% LiveLink for MATLAB® and COMSOL Multiphysics 4.3
% D. C. Sutton, 21/11/2013

function y_temp = Deposition_function(x, xn, dt, y, v)

% Calculate spacing between nodes
dx = x / (xn - 1);

% Initialise empty vectors
grad2 = zeros(1, xn);
y_temp = zeros(1, xn);

% Solve the diffusion equation
grad2(1) = (y(2) - 2 * y(1) + y(xn)) / dx^2;
y_temp(1) = y(1) + dt * (v * grad2(1));
for j = 2:xn - 1
    grad2(j) = (y(j+1) - 2 * y(j) + y(j-1)) / dx^2;
    y_temp(j) = y(j) + dt * (v * grad2(j));
end
grad2(xn) = (y(1) - 2 * y(xn) + y(xn-1)) / dx^2;
y_temp(xn) = y(xn) + dt * (v * grad2(xn));

```

The post-processing function concerns the post-processing of data. It creates and saves the model predictions in comparison to the experimental data. It also plots the solution time for each finite element model to aid in tuning of the model. The function is given below.

```

% Post_processing.m
% An Incremental Wear Model for a DLC Coating and an AISI 440C Steel Ball
% LiveLink for MATLAB® and COMSOL Multiphysics 4.3
% D. C. Sutton, 21/11/2013

function Post_processing(testname, iteration, totaliteration, selection, aa, bb,
timedata, weardata_DLC, weardata_CF)

% Close current figures
figure(1); close
figure(2); close
figure(3); close
figure(4); close
figure(5); close

% Load the correct workspace and experimental data
load([cd, '\', testname, '_iter_', num2str(iteration), '_of_', num2str(totaliteration), '_works
pace.mat'])
load(fullfile(cd, 'data_STAR_5N_5Hz.mat'));

% Define the time vector
t = 0:timestep:t_input;

% Define the experimental error
ebdlc = 0.03;
Ebdlc = 1.25e-5;
ebcf = 0.30;
Ebcf = 1.25e-5;

% Plot the wear depth of the DLC coating against the experimental data
figure(1)
subplot(2,3,1)
plot(t, [0 mean_w_DLC], 'k')
hold on
errorbar(timedata, weardata_DLC, ebdlc*ones(1, length(timedata)), 'ko')
xlim([0 t_input]);
legend('DLC Coating', 'Data', 'Location', 'NorthWest')
xlabel('Time [s]')
ylabel('Wear Depth [um]')
yl=yylim; ylim([0 yl(2)]);
xlim([0 3820])

% Plot the wear depth of the ball against the experimental data
subplot(2,3,2)
plot(t, [0 mean_w_CF], 'r')

```

```

hold on
errorbar(timedata,weardata_CF,ebcf*ones(1,length(timedata)),'ro')
xlim([0 t_input]);
legend('Steel Ball','Data','Location','SouthEast')
xlabel('Time [s]')
ylabel('Wear Depth [um]')
yl=yylim; ylim([0 yl(2)]);
xlim([0 3820])

% Plot the transfer layer height against the experimental data
subplot(2,3,3)
plot(t, [0 mean_h], 'g')
xlim([0,t_input])
ylim([0, 0.1 + 1.1 * max(sum_dh)])
legend('Transfer Layer','Location','NorthWest')
xlabel('Time [s]')
ylabel('Growth [um]')
yl=yylim; ylim([0 yl(2)]);
xlim([0 3820])

% Plot the wear volume of the DLC coating against the experimental data
subplot(2,3,4)
plot(t, [0 mean_wv_DLC], 'k')
hold on
errorbar(timedata, weardatavol_DLC, Ebdlc * ones(1, length(timedata)),'ko')
xlim([0 t_input]);
legend('DLC Coating','Data','Location','NorthWest')
xlabel('Time [s]')
ylabel('Wear Volume [mm^3]')
yl=yylim; ylim([0 yl(2)]);
xlim([0 3820])

% Plot the wear volume of the ball against the experimental data
subplot(2,3,5)
plot(t, [0 mean_wv_CF], 'r')
hold on
errorbar(timedata,weardatavol_CF,Ebcf * ones(1, length(timedata)),'ro')
xlim([0 t_input]);
legend('Steel Ball','Data','Location','SouthEast')
xlabel('Time [s]')
ylabel('Wear Volume [mm^3]')
yl=yylim; ylim([0 yl(2)]);
xlim([0 3820])

% Plot the model geometry at the final time
subplot(2,3,6)
hold on
plot(X,initial_Dpos,'r--')
plot(X,initial_Cpos - sum_w_DLC,'k')
plot(X,initial_Cpos - thickness,'k')
plot(X,initial_Cpos,'k--')
plot(X,initial_Dpos + sum_w_CF - sum_dh,'g')
plot(X,initial_Dpos + sum_w_CF,'r')
xlim([-300 300])
ylim([490 510]);
xlabel('x [um]')
ylabel('y [um]')

% Save Figure 1
print([testname,'_image_wear.jpg'],'-r300','-djpeg100')

% Plot the solution time for each iteration
figure(2)
hold on
plot(t(2:length(t)), solvertime,'ro')
xlim([0,t_input])
ylim([0 1.1 * max(solvertime)])
xlabel('Time [s]')
ylabel('Solution Time [s]')

% Save Figure 2
print([testname,'_image_solntime.jpg'],'-r300','-djpeg100')

% Plot and save the contact pressure distribution each selection
figure(3)
plot_pressure(testname,aa,bb,selection,totaliteration)

```

```

% Plot and save the contact geometry each selection
figure(4)
plot_picture(testname,aa,bb,selection,totaliteration)

% Plot and save the transfer layer height each selection
figure(5)
plot_TF(testname,aa,bb,selection,totaliteration)

% Save the wear depth of the DLC coating and the ball against the experimental data
figure(6)
subplot(2,1,1)
plot(t, [0 mean_w_DLC], 'k')
hold on
errorbar(timedata, weardata_DLC, ebdlc*ones(1,length(timedata)), 'ko')
xlim([0 3820]);
legend('DLC Coating','Data','Location','NorthWest')
xlabel('Time [s]')
ylabel('Wear Depth [um]')

subplot(2,1,2)
plot(t, [0 mean_w_CF], 'r')
hold on
errorbar(timedata, weardata_CF, ebcf*ones(1,length(timedata)), 'ro')
xlim([0 3820]);
legend('Steel Ball','Data','Location','SouthEast')
xlabel('Time [s]')
ylabel('Wear Depth [um]')

% Save Figure 6
print([testname,'_image_weardepth.jpg'],'-r300','-djpeg100')

% plot_pressure
function plot_pressure(testname,aa,bb,selection,totaliteration)

for ii=1:aa*bb

load(fullfile(cd,[testname,'_iter_',num2str(selection(ii)),'_of_',num2str(totaliteration)
),'_workspace.mat']));
pause(0.1)
subplot(aa,bb,ii)
plot(X, P*1e-9)
xlim([-200 200]);
ylim([-0.1 2.5]);
xlabel('x [um]');
ylabel('Contact Pressure [GPa]');
end
print([testname,'_image_pressure.jpg'],'-r300','-djpeg100')

% plot_picture
function plot_picture(testname,aa,bb,selection,totaliteration)

for ii=1:aa*bb

load(fullfile(cd,[testname,'_iter_',num2str(selection(ii)),'_of_',num2str(totaliteration)
),'_workspace.mat']));
pause(0.1)
subplot(aa,bb,ii)
plot(X,initial_Dpos + sum_w_CF - sum_dh,'g')
hold on
plot(X,initial_Dpos,'k-')
plot(X,initial_Cpos - sum_w_DLC,'k')
plot(X,initial_Dpos + sum_w_CF,'k')
hold off
xlim([-200 200]);
ylim([497 505]);
xlabel('x [um]');
ylabel('y [um]');
end
print([testname,'_image_geom.jpg'],'-r300','-djpeg100')

% plot_TF
function plot_TF(testname,aa,bb,selection,totaliteration)

for ii=1:aa*bb

load(fullfile(cd,[testname,'_iter_',num2str(selection(ii)),'_of_',num2str(totaliteration)
),'_workspace.mat']));

```

```
pause(0.1)
subplot(aa,bb,ii)
plot(X,sum_dh)
xlim([-200 200]);
ylim([0 0.1 + 1.1*max(sum_dh)]);
xlabel('x [um]');
ylabel('Transfer Layer Height [um]');
end
print([testname, '_image_TF.jpg'], '-r300', '-djpeg100')
```

Bibliography

1. *Nuclear Industrial Strategy - The UK's Nuclear Future.* Department for Business, Innovation, and Skills, 2013.
2. *Pressurised Water Reactor; United States Nuclear Regulatory Commission.* 2012; Available from: <http://www.nrc.gov/reading-rm/basic-ref/teachers/pwr-schematic.html>.
3. Erdemir, A. and C. Donnet, *Tribology of Diamond-Like Carbon Films.* 2008: Springer.
4. Robertson, J., *Diamond-like amorphous carbon.* Materials Science & Engineering R-Reports, 2002. **37**(4-6): p. 129-281.
5. Erdemir, A., *The role of hydrogen in tribological properties of diamond-like carbon films.* Surface & Coatings Technology, 2001. **146**: p. 292-297.
6. *Allotropes of Carbon.* 2012; Available from: http://upload.wikimedia.org/wikipedia/commons/f/f8/Eight_Allotropes_of_Carbon.png.
7. Jacob, W. and W. Moller, *On the Structure of Thin Hydrocarbon Films.* Applied Physics Letters, 1993. **63**(13): p. 1771-1773.
8. Lemoine, P.Q., J.P.; Maguire, P.D.; McLaughlin, J.A., *Mechanical Characterisation and Properties of DLC Films,* in *Tribology of Diamond-Like Carbon Films,* A.D. Erdemir, C., Editor. 2008, Springer. p. 83-101.
9. Ferrari, A.C., *Non-destructive Characterisation of Carbon Films,* in *Tribology of Diamond-Like Carbon Films,* A.D. Erdemir, C., Editor. 2008, Springer. p. 25 - 82.
10. Robertson, J., *The Deposition Mechanism of Diamond-Like a-C and a-C:H.* Diamond and Related Materials, 1994. **3**(4-6): p. 361-368.
11. Mattox, D.M., *Handbook of Physical Vapor Deposition (PVD) Processing.* 1998: William Andrew Publishing.
12. Field, S.K., M. Jarratt, and D.G. Teer, *Tribological properties of graphite-like and diamond-like carbon coatings.* Tribology International, 2004. **37**(11-12): p. 949-956.
13. Bonelli, M., et al., *Structural and mechanical properties of diamond-like carbon films prepared by pulsed laser deposition with varying laser intensity.* Amorphous and Nanostructured Carbon, 2000. **593**: p. 359-364.
14. Morrison, N.A., et al., *The preparation, characterization and tribological properties of ta-C:H deposited using an electron cyclotron wave resonance*

- plasma beam source*. Physica Status Solidi a-Applied Research, 1999. **172**(1): p. 79-90.
15. Bull, S.J., *Nanoindentation of Coatings*. Journal of Physics D-Applied Physics, 2005. **38**(24): p. 393-413.
 16. Oliver, W.C. and G.M. Pharr, *An Improved Technique for Determining Hardness and Elastic-Modulus Using Load and Displacement Sensing Indentation Experiments*. Journal of Materials Research, 1992. **7**(6): p. 1564-1583.
 17. Ferrari, A.C., et al., *Density, $sp(3)$ fraction, and cross-sectional structure of amorphous carbon films determined by x-ray reflectivity and electron energy-loss spectroscopy*. Physical Review B, 2000. **62**(16): p. 11089-11103.
 18. Lemoine, P., et al., *Intrinsic mechanical properties of ultra-thin amorphous carbon layers*. Applied Surface Science, 2007. **253**(14): p. 6165-6175.
 19. Lemoine, P., et al., *Hardness measurements at shallow depths on ultra-thin amorphous carbon films deposited onto silicon and Al₂O₃-TiC substrates*. Thin Solid Films, 2000. **379**(1-2): p. 166-172.
 20. Ferrari, A.C., *Diamond-like carbon for magnetic storage disks*. Surface & Coatings Technology, 2004. **180-81**: p. 190-206.
 21. Pauleau, Y., *Residual Stresses in DLC Films and Adhesion to Various Substrates*, in *Tribology of Diamond-Like Carbon Films*, A.D. Erdemir, C., Editor. 2008, Springer. p. 102-136.
 22. Holmberg, K., et al., *Residual stresses in TiN, DLC and MoS₂ coated surfaces with regard to their tribological fracture behaviour*. Wear, 2009. **267**(12): p. 2142-2156.
 23. Ban, M., et al., *Stress and structural properties of diamond-like carbon films deposited by electron beam excited plasma CVD*. Diamond and Related Materials, 2003. **12**(1): p. 47-56.
 24. Oka, Y., et al., *Measurement of residual stress in DLC films prepared by plasma-based ion implantation and deposition*. Surface & Coatings Technology, 2004. **186**(1-2): p. 141-145.
 25. Kumar, S., et al., *Diamond-like carbon films with extremely low stress*. Thin Solid Films, 1999. **346**(1-2): p. 130-137.
 26. Yamada, H. and O. Tsuji, *Characteristics of diamondlike carbon thin films prepared by rf plasma pulsed deposition method - Effect of annealing temperature*. Journal of the Ceramic Society of Japan, 1997. **105**(1): p. 62-67.

27. Damasceno, J.C., et al., *Deposition of Si-DLC films with high hardness, low stress and high deposition rates*. Surface & Coatings Technology, 2000. **133**: p. 247-252.
28. Erdemir, A. and C. Donnet, *Tribology of diamond-like carbon films: recent progress and future prospects*. Journal of Physics D-Applied Physics, 2006. **39**(18): p. 311-327.
29. Grischke, M., et al., *Application-oriented modifications of deposition processes for diamond-like-carbon-based coatings*. Surface & Coatings Technology, 1995. **74-75**(1-3): p. 739-745.
30. Sanchez-Lopez, J.C.F., A., *Doping and Alloying Effects on DLC Coatings*, in *Tribology of Diamond-Like Carbon Films*, A.D. Erdemir, C., Editor. 2008, Springer. p. 311 - 338.
31. Love, C.A.C., R. B.; Harvey, P. A.; Wood, R. J. K., *Diamond like carbon coatings for potential application in biological implants—a review*. Tribology International, 2012.
32. Wu, W.J., T.M. Pai, and M.H. Hon, *Wear behavior of silicon-containing diamond-like carbon coatings*. Diamond and Related Materials, 1998. **7**(10): p. 1478-1484.
33. Khurshudov, A., K. Kato, and S. Daisuke, *Comparison of tribological properties of carbon and carbon nitride protective coatings over magnetic media*. Journal of Vacuum Science & Technology a-Vacuum Surfaces and Films, 1996. **14**(5): p. 2935-2939.
34. Franceschini, D.F., C.A. Achete, and F.L. Freire, *Internal-Stress Reduction by Nitrogen Incorporation in Hard Amorphous-Carbon Thin-Films*. Applied Physics Letters, 1992. **60**(26): p. 3229-3231.
35. Hauert, R., et al., *Influence of nitrogen doping on different properties of a-C:H*. Thin Solid Films, 1995. **268**(1-2): p. 22-29.
36. Wang, P., et al., *Comparing internal stress in diamond-like carbon films with different structure*. Thin Solid Films, 2007. **515**(17): p. 6899-6903.
37. Dearnley, P.A., et al., *Coatings tribology drivers for high density plasma technologies*. Surface Engineering, 2010. **26**(1-2): p. 80-96.
38. Tagawa, M., et al., *Effect of water adsorption on microtribological properties of hydrogenated diamond-like carbon films*. Tribology Letters, 2004. **17**(3): p. 575-580.
39. Paul, R., et al., *Synthesis of DLC films with different $sp(2)/sp(3)$ ratios and their hydrophobic behaviour*. Journal of Physics D-Applied Physics, 2008. **41**(5).

40. Ali, N., et al., *Human micro-vascular endothelial cell seeding on Cr-DLC thin films for mechanical heart valve applications*. *Thin Solid Films*, 2006. **515**(1): p. 59-65.
41. Persson, B.N.J., *Area of Real Contact: Elastic and Plastic Deformations*. *Sliding Friction: Physical Principles and Applications*. 2000: Springer.
42. Bryant, M.D., M.M. Khonsari, and F.F. Ling, *On the thermodynamics of degradation*. *Proceedings of the Royal Society a-Mathematical Physical and Engineering Sciences*, 2008. **464**(2096): p. 2001-2014.
43. Amiri, M. and M.M. Khonsari, *On the Thermodynamics of Friction and Wear-A Review*. *Entropy*, 2010. **12**(5): p. 1021-1049.
44. Bowden, F.P. and D. Tabor, *The Friction and Lubrication of Solids*. New edition of Revised edition ed. 2001, Oxford: Oxford University Press. 424.
45. Fontaine, J.E., A.; Donnet, C., *Fundamentals of the Tribology of DLC Coatings*, in *Tribology of Diamond-Like Carbon Films*, C. V, Editor. 2008, Springer.
46. Erdemir, A., et al., *Friction and Wear Performance of Ion-Beam-Deposited Diamond-Like Carbon-Films on Steel Substrates*. *Diamond and Related Materials*, 1994. **3**(1-2): p. 119-125.
47. Voevodin, A.A., et al., *Friction induced phase transformation of pulsed laser deposited diamond-like carbon*. *Diamond and Related Materials*, 1996. **5**(11): p. 1264-1269.
48. Scharf, T.W. and I.L. Singer, *Monitoring transfer films and friction instabilities with in situ Raman tribometry*. *Tribology Letters*, 2003. **14**(1): p. 3-8.
49. Low, M.B.J., *Effect of the Transfer Film on the Friction and Wear of Dry Bearing Materials for a Power-Plant Application*. *Wear*, 1979. **52**(2): p. 347-363.
50. Bull, S.J., *Tribology of Carbon Coatings - DLC, Diamond and Beyond*. *Diamond and Related Materials*, 1995. **4**(5-6): p. 827-836.
51. Grill, A., *Review of the Tribology of Diamond-Like Carbon*. *Wear*, 1993. **168**(1-2): p. 143-153.
52. Grill, A., *Tribology of diamondlike carbon and related materials: an updated review*. *Surface & Coatings Technology*, 1997. **94-5**(1-3): p. 507-513.
53. Ronkainen, H., Holmberg, K., *Environmental and Thermal Effects on the Tribological Performance of DLC Coatings*, in *Tribology of Diamond-Like Carbon Films*, A.D. Erdemir, C., Editor. 2008, Springer. p. 155 - 200.
54. Meunier, C., et al., *Friction properties of ta-C and a-C : H coatings under high vacuum*. *Surface & Coatings Technology*, 2005. **200**(5-6): p. 1976-1981.
55. Enke, K., H. Dimigen, and H. Hubsch, *Frictional-Properties of Diamond-Like Carbon Layers*. *Applied Physics Letters*, 1980. **36**(4): p. 291-292.

56. Voevodin, A.A., et al., *Mechanical and tribological properties of diamond-like carbon coatings prepared by pulsed laser deposition*. Surface & Coatings Technology, 1995. **76-77**(1-3): p. 534-539.
57. Andersson, J., R.A. Erck, and A. Erdemir, *Friction of diamond-like carbon films in different atmospheres*. Wear, 2003. **254**(11): p. 1070-1075.
58. Erdemir, A., *Genesis of superlow friction and wear in diamondlike carbon films*. Tribology International, 2004. **37**(11-12): p. 1005-1012.
59. Ronkainen, H., S. Varjus, and K. Holmberg, *Tribological performance of different DLC coatings in water-lubricated conditions*. Wear, 2001. **249**(3-4): p. 267-271.
60. Andersson, J., R.A. Erck, and A. Erdemir, *Frictional behavior of diamondlike carbon films in vacuum and under varying water vapor pressure*. Surface & Coatings Technology, 2003. **163**: p. 535-540.
61. Fontaine, J., et al., *Achieving superlow friction with hydrogenated amorphous carbon: some key requirements*. Thin Solid Films, 2005. **482**(1-2): p. 99-108.
62. Heimberg, J.A., et al., *Superlow friction behavior of diamond-like carbon coatings: Time and speed effects*. Applied Physics Letters, 2001. **78**(17): p. 2449-2451.
63. Donnet, C., *Recent progress on the tribology of doped diamond-like and carbon alloy coatings: a review*. Surface & Coatings Technology, 1998. **100**(1-3): p. 180-186.
64. Oguri, K. and T. Arai, *Tribological Properties and Characterization of Diamond-Like Carbon Coatings with Silicon Prepared by Plasma-Assisted Chemical Vapor-Deposition*. Surface & Coatings Technology, 1991. **47**(1-3): p. 710-721.
65. Gilmore, R. and R. Hauert, *Comparative study of the tribological moisture sensitivity of Si-free and Si-containing diamond-like carbon films*. Surface & Coatings Technology, 2000. **133**: p. 437-442.
66. Hioki, T., et al., *Tribology of Carbonaceous Films Formed by Ion-Beam-Assisted Deposition of Organic Material*. Surface & Coatings Technology, 1991. **46**(2): p. 233-243.
67. Miyamoto, T., R. Kaneko, and S. Miyake, *Tribological Characteristics of Amorphous-Carbon Films Investigated by Point Contact Microscopy*. Journal of Vacuum Science & Technology B, 1991. **9**(2): p. 1336-1339.
68. Konca, E., et al., *Effect of test atmosphere on the tribological behaviour of the non-hydrogenated diamond-like carbon coatings against 319 aluminum alloy and tungsten carbide*. Surface & Coatings Technology, 2005. **200**(5-6): p. 1783-1791.

69. Dai, W., et al., *Investigation of the microstructure, mechanical properties and tribological behaviors of Ti-containing diamond-like carbon films fabricated by a hybrid ion beam method*. Thin Solid Films, 2012. **520**(19): p. 6057-6063.
70. Dai, W. and A.Y. Wang, *Deposition and properties of Al-containing diamond-like carbon films by a hybrid ion beam sources*. Journal of Alloys and Compounds, 2011. **509**(13): p. 4626-4631.
71. Holmberg, K., A. Matthews, and H. Ronkainen, *Coatings tribology - contact mechanisms and surface design*. Tribology International, 1998. **31**(1-3): p. 107-120.
72. Sanchez-Lopez, J.C., et al., *Friction-induced structural transformations of diamondlike carbon coatings under various atmospheres*. Surface & Coatings Technology, 2003. **163**: p. 444-450.
73. Ferrari, A.C. and J. Robertson, *Raman spectroscopy of amorphous, nanostructured, diamond-like carbon, and nanodiamond*. Philosophical Transactions of the Royal Society a-Mathematical Physical and Engineering Sciences, 2004. **362**(1824): p. 2477-2512.
74. Ronkainen, H., et al., *Differentiating the tribological performance of hydrogenated and hydrogen-free DLC coatings*. Wear, 2001. **249**(3-4): p. 260-266.
75. Miyoshi, K., *Studies of Mechanochemical Interactions in the Tribological Behavior of Materials*. Surface & Coatings Technology, 1990. **43-4**(1-3): p. 799-812.
76. Bhushan, B. and B.K. Gupta, *Friction and Wear of Ion-Implanted Diamond-Like Carbon and Fullerene Films for Thin-Film Rigid Disks*. Journal of Applied Physics, 1994. **75**(10): p. 6156-6158.
77. Erdemir, A., et al., *Characterization of transfer layers forming on surfaces sliding against diamond-like carbon*. Surface & Coatings Technology, 1996. **86-7**(1-3): p. 692-697.
78. Jiang, J.R. and R.D. Arnell, *On the running-in behaviour of diamond-like carbon coatings under the ball-on-disk contact geometry*. Wear, 1998. **217**(2): p. 190-199.
79. Singer, I.L., et al., *Role of third bodies in friction and wear of protective coatings*. Journal of Vacuum Science & Technology A, 2003. **21**(5): p. S232-S240.
80. Scharf, T.W. and I.L. Singer, *Third Bodies and Tribochemistry of DLC Coatings*, in *Tribology of Diamond-Like Carbon Films*, A.D. Erdemir, C., Editor. 2008, Springer. p. 201-236.

81. Scharf, T.W. and I.L. Singer, *Role of the Transfer Film on the Friction and Wear of Metal Carbide Reinforced Amorphous Carbon Coatings During Run-in*. Tribology Letters, 2009. **36**(1): p. 43-53.
82. Shaha, K.P., et al., *Influence of hardness and roughness on the tribological performance of TiC/a-C nanocomposite coatings*. Surface & Coatings Technology, 2010. **205**(7): p. 2624-2632.
83. Shaha, K.P., et al., *Influence of Surface Roughness on the Transfer Film Formation and Frictional Behavior of TiC/a-C Nanocomposite Coatings*. Tribology Letters, 2011. **41**(1): p. 97-101.
84. Ito, H., K. Yamamoto, and M. Masuko, *Thermal stability of UBM sputtered DLC coatings with various hydrogen contents*. Thin Solid Films, 2008. **517**(3): p. 1115-1119.
85. Liu, Y., A. Erdemir, and E.I. Meletis, *A study of the wear mechanism of diamond-like carbon films*. Surface and Coatings Technology, 1996. **82**(1-2): p. 48-56.
86. Batchelor, A.W.S., G. W., *Engineering Tribology*. 2005, Oxford: Elsevier.
87. Krumpiegl, T., et al., *Amorphous carbon coatings and their tribological behaviour at high temperatures and in high vacuum*. Surface & Coatings Technology, 1999. **121**: p. 555-560.
88. Vanhulsel, A., et al., *Study of the wear behaviour of diamond-like coatings at elevated temperatures*. Surface & Coatings Technology, 1998. **98**(1-3): p. 1047-1052.
89. Konca, E., et al., *Elevated temperature tribological behavior of non-hydrogenated diamond-like carbon coatings against 319 aluminum alloy*. Surface & Coatings Technology, 2006. **200**(12-13): p. 3996-4005.
90. Wang, D.Y., C.L. Chang, and W.Y. Ho, *Oxidation behavior of diamond-like carbon films*. Surface & Coatings Technology, 1999. **120**: p. 138-144.
91. Hsu, S.M., E.E. Klaus, and H.S. Cheng, *A Mechano-Chemical Descriptive Model for Wear under Mixed Lubrication Conditions*. Wear, 1988. **128**(3): p. 307-323.
92. Donnet, C., et al., *The respective role of oxygen and water vapor on the tribology of hydrogenated diamond-like carbon coatings*. Tribology Letters, 1998. **4**(3-4): p. 259-265.
93. Kim, H.I., et al., *Environmental effects on the friction of hydrogenated DLC films*. Tribology Letters, 2006. **21**(1): p. 53-58.

94. Yamamoto, K. and K. Matsukado, *Effect of hydrogenated DLC coating hardness on the tribological properties under water lubrication*. Tribology International, 2006. **39**(12): p. 1609-1614.
95. Jiang, J.R., S. Zhang, and R.D. Arnell, *The effect of relative humidity on wear of a diamond-like carbon coating*. Surface & Coatings Technology, 2003. **167**(2-3): p. 221-225.
96. Rabinowicz, E., *Practical uses of the surface energy criterion*. Wear, 1964. **7**(1): p. 9-22.
97. Uchidate, M., et al., *Effects of water environment on tribological properties of DLC rubbed against stainless steel*. Wear, 2007. **263**: p. 1335-1340.
98. Park, S.J., K.R. Lee, and D.H. Ko, *Tribochemical reaction of hydrogenated diamond-like carbon films: a clue to understand the environmental dependence*. Tribology International, 2004. **37**(11-12): p. 913-921.
99. Li, H.X., et al., *Friction-induced physical and chemical interactions among diamond-like carbon film, steel ball and water and/or oxygen molecules*. Diamond and Related Materials, 2006. **15**(9): p. 1228-1234.
100. Li, H., et al., *Tribochemical effects on the friction and wear behaviors of diamond-like carbon film under high relative humidity condition*. Tribology Letters, 2005. **19**(3): p. 231-238.
101. Hutchings, I.M., *Tribology: Friction and Wear of Engineering Materials*. Metallurgy & Materials Science. 1992: Edward Arnold. 273.
102. Goto, Y., *The Effect of Squeezing on the Phase Transformation and Magnetic Properties of γ -Fe₂O₃*. Jpn. J. Appl. Phys., 1964. **3**: p. 739-744.
103. Fukui, H., et al., *An investigation of the wear track on DLC (a-C : H) film by time-of-flight secondary ion mass spectroscopy*. Surface & Coatings Technology, 2001. **146**: p. 378-383.
104. Wu, X., et al., *Tribochemical investigation of DLC coating in water using stable isotopic tracers*. Applied Surface Science, 2008. **254**(11): p. 3397-3402.
105. Holmberg, K., et al., *Tribological contact analysis of a rigid ball sliding on a hard coated surface Part I: Modelling stresses and strains*. Surface & Coatings Technology, 2006. **200**(12-13): p. 3793-3809.
106. Holmberg, K., et al., *Tribological contact analysis of a rigid ball sliding on a hard coated surface Part II: Material deformations, influence of coating thickness and Young's modulus*. Surface & Coatings Technology, 2006. **200**(12-13): p. 3810-3823.
107. Laukkanen, A., et al., *Tribological contact analysis of a rigid ball sliding on a hard coated surface, Part III: Fracture toughness calculation and influence of*

- residual stresses*. Surface & Coatings Technology, 2006. **200**(12-13): p. 3824-3844.
108. Holmberg, K.L., A.; Ronkainen, H.; Wallin, K.; Varjus, S., *A model for stresses, crack generation and fracture toughness calculation in scratched TiN-coated steel surfaces*. Wear, 2003. **254**: p. 278-291.
 109. Fan, X. and D.F. Diao, *Contact Mechanisms of Transfer Layered Surface During Sliding Wear of Amorphous Carbon Film*. Journal of Tribology-Transactions of the Asme, 2011. **133**(4).
 110. Archard, J.F., *Contact and rubbing of flat surfaces*. Journal of Applied Physics, 1953. **24**(8): p. 981-988.
 111. Archard, J.F.H., W., *The wear of materials under lubricated conditions*. Proceedings of the Royal Society of Mechanical Engineers, 1956. **A-236**: p. 397-410.
 112. Preston, F.W., *The Theory and Design of Plate Glass polishing Machines*. J. Soc. Glass Technol., 1927. **11**: p. 214-256.
 113. Matveesky, R.M., *The critical temperature of oil with point and line contact machines*. ASME Transactions, 1965. **87**: p. 754.
 114. Plint, M.A. and A.F. Alliston-Greiner, *The energy pulse: A new wear criterion and its relevance to wear in gear teeth and automotive engine valve trains*. Lubrication Science, 1996. **8**(3): p. 233-251.
 115. Fouvry, S., et al., *Wear analysis in fretting of hard coatings through a dissipated energy concept*. Wear, 1997. **203**: p. 393-403.
 116. Huq, M.Z. and J.P. Celis, *Expressing wear rate in sliding contacts based on dissipated energy*. Wear, 2002. **252**(5-6): p. 375-383.
 117. Klamecki, B.E., *A Thermodynamic Model of Friction*. Wear, 1980. **63**(1): p. 113-120.
 118. Klamecki, B.E., *Wear - Entropy Production-Model*. Wear, 1980. **58**(2): p. 325-330.
 119. Klamecki, B.E., *Energy-Dissipation in Sliding*. Wear, 1982. **77**(1): p. 115-128.
 120. Klamecki, B.E., *An Entropy-Based Model of Plastic-Deformation Energy-Dissipation in Sliding*. Wear, 1984. **96**(3): p. 319-329.
 121. Zmitrowicz, A., *A Thermodynamical Model of Contact, Friction and Wear .1. Governing Equations*. Wear, 1987. **114**(2): p. 135-168.
 122. Zmitrowicz, A., *A Thermodynamical Model of Contact, Friction and Wear .2. Constitutive-Equations for Materials and Linearized Theories*. Wear, 1987. **114**(2): p. 169-197.

123. Zmitrowicz, A., *A Thermodynamical Model of Contact, Friction and Wear .3. Constitutive-Equations for Friction, Wear and Frictional Heat.* *Wear*, 1987. **114**(2): p. 199-221.
124. Doelling, K.L., et al., *An experimental study of the correlation between wear and entropy flow in machinery components.* *Journal of Applied Physics*, 2000. **88**(5): p. 2999-3003.
125. Bryant, M.D., *Entropy and Dissipative processes of Friction and Wear.* 2009.
126. Onsager, L., *Reciprocal Relations in Irreversible Processes. I.* *Physical Review*, 1931. **37**.
127. de Groot, S.R., *Thermodynamics of irreversible processes*, ed. J.B. de Boer, H.; Casimir, H. B. G. 1951: North Holland Publishing Company.
128. Johansson, L., *Numerical-Simulation of Contact Pressure Evolution in Fretting.* *Journal of Tribology-Transactions of the Asme*, 1994. **116**(2): p. 247-254.
129. Podra, P. and S. Andersson, *Simulating sliding wear with finite element method.* *Tribology International*, 1999. **32**(2): p. 71-81.
130. Oqvist, M., *Numerical simulations of mild wear using updated geometry with different step size approaches.* *Wear*, 2001. **249**(1-2): p. 6-11.
131. Hegadekatte, V., N. Huber, and O. Kraft, *Finite element based simulation of dry sliding wear.* *Modelling and Simulation in Materials Science and Engineering*, 2005. **13**(1): p. 57-75.
132. Hegadekatte, V., N. Huber, and O. Kraft, *Modeling and simulation of wear in a pin on disc tribometer.* *Tribology Letters*, 2006. **24**(1): p. 51-60.
133. Mukras, S., et al., *Numerical integration schemes and parallel computation for wear prediction using finite element method.* *Wear*, 2009. **266**(7-8): p. 822-831.
134. Kim, T.W., S.M. Moon, and Y.J. Cho, *Prediction of fretting wear using boundary element method.* *Tribology International*, 2011. **44**(11): p. 1571-1576.
135. Rodriguez-Tembleque, L., R. Abascal, and M.H. Aliabadi, *Anisotropic Fretting Wear Simulation Using the Boundary Element Method.* *Cmes-Computer Modeling in Engineering & Sciences*, 2012. **87**(2): p. 127-156.
136. Podra, P. and S. Andersson, *Wear simulation with the winkler surface model.* *Wear*, 1997. **207**(1-2): p. 79-85.
137. Choi, K.Y., S.S. Kim, and I.A. Soldatenkov, *Modeling of Fretting Wear Based on Solution of Wear Contact Problem.* *Tribology Letters*, 2010. **37**(1): p. 69-74.
138. Flodin, A. and S. Andersson, *A simplified model for wear prediction in helical gears.* *Wear*, 2001. **249**(3-4): p. 285-292.

139. Steiner, L., et al., *Modelling of unlubricated oscillating sliding wear of DLC-coatings considering surface topography, oxidation and graphitisation*. *Wear*, 2010. **268**(9-10): p. 1184-1194.
140. Quinn, T.F.J., *The role of oxidation in the mild wear of steel*. *Br. J. Appl. Phys.*, 1962. **13**: p. 33-37.
141. Lim, S.C. and M.F. Ashby, *Wear-mechanism maps*. *Acta Metallurgica*, 1987. **35**(1): p. 1-24.
142. LeHuu, T., et al., *Transformation of $sp(3)$ to $sp(2)$ sites of diamond like carbon coatings during friction in vacuum and under water vapour environment*. *Thin Solid Films*, 1996. **290**: p. 126-130.
143. Mohd Tobi, A.L., et al., *The effect of gross sliding fretting wear on stress distributions in thin W-DLC coating systems*. *Tribology International*, 2010. **43**(10): p. 1917-1932.
144. Mohd Tobi, A.L., P.H. Shipway, and S.B. Leen, *Gross slip fretting wear performance of a layered thin W-DLC coating: Damage mechanisms and life modelling*. *Wear*, 2011. **271**(9-10): p. 1572-1584.
145. Stallard, J., et al., *A study of the tribological behaviour of three carbon-based coatings, tested in air, water and oil environments at high loads*. *Surface & Coatings Technology*, 2004. **177**: p. 545-551.
146. Cho, S.J., et al., *Determination of elastic modulus and Poisson's ratio of diamond-like carbon films*. *Thin Solid Films*, 1999. **341**(1-2): p. 207-210.
147. Zhou, Z.F., et al., *Study of tribological performance of ECR-CVD diamond-like carbon coatings on steel substrates Part 2. The analysis of wear mechanism*. *Wear*, 2005. **258**(10): p. 1589-1599.
148. Moelle, C.W., M.; Szucs, F; Wittorf, D.; Sellschopp, M.; von Borany, J, *Specific heat of single-, poly- and nanocrystalline diamond*. *Diamond and Related Materials*, 1997. **7**: p. 499-503.
149. Bein, B.K., et al., *Photothermal characterization of amorphous thin films*. *Surface & Coatings Technology*, 1999. **116**: p. 147-154.
150. *Specifications of Alloy Steel: AISI 52100*. Available from: <http://www.m3tubecomponents.com/images/AISI%2052100%20SPECIFICATIONS.pdf>.
151. Irmer, G. and A. Dorner-Reisel, *Micro-Raman studies on DLC coatings*. *Advanced Engineering Materials*, 2005. **7**(8): p. 694-705.
152. Hamrock, B.J.D., D., *The Elastohydrodynamics of Elliptical Contacts*. 1981: John Wiley and Sons.

153. Fontaine, J., et al., *Tribochemistry between hydrogen and diamond-like carbon films*. Surface & Coatings Technology, 2001. **146**: p. 286-291.
154. deFaria, D.L.A., S.V. Silva, and M.T. deOliveira, *Raman microspectroscopy of some iron oxides and oxyhydroxides*. Journal of Raman Spectroscopy, 1997. **28**(11): p. 873-878.
155. Oh, S.J., D.C. Cook, and H.E. Townsend, *Characterization of iron oxides commonly formed as corrosion products on steel*. Hyperfine Interactions, 1998. **112**(1-4): p. 59-65.
156. Chin, K.J., H. Zaidi, and T. Mathia, *Oxide film formation in magnetized sliding steel/steel contact - analysis of the contact stress field and film failure mode*. Wear, 2005. **259**(1-6): p. 477-481.
157. Harris, J.W. and H. Stocker, *Spherical Segment (Spherical Cap)*, in *Handbook of Mathematics and Computational Science*. 1998, Springer-Verlag: New York. p. 107.
158. Hertz, H., *Über die berührung fester elastischer Körper (On the contact of rigid elastic solids)*, in *Miscellaneous Papers*, J.a. Schott, Editor. 1896, Macmillan: London.
159. Kauzlarich, J.J. and J.A. Williams, *Archard wear and component geometry*. Proceedings of the Institution of Mechanical Engineers Part J-Journal of Engineering Tribology, 2001. **215**(J4): p. 387-403.
160. Sutton, D.C., et al., *The friction of diamond-like carbon coatings in a water environment*. Friction, 2013. **1**(3): p. 210-221.
161. Sutton, D.C., et al., *Interpreting the effects of interfacial chemistry on the tribology of diamond-like carbon coatings against steel in distilled water*. Wear, 2013. **302**(1-2): p. 918-928.
162. Sutton, D.C., et al., *A functional form for wear depth of a ball and a flat surface*. Tribology Letters, 2013. **53**(1): p. 173-179.